MOMENTUM AND PARTICLE TRANSPORT IN A NONHOMOGENOUS CANOPY

by

Andrew W. Gould

A thesis submitted to the faculty of
The University of Utah
in partial fulfillment of the requirements for the degree of

Master of Science

Department of Mechanical Engineering

The University of Utah

May 2013

The University of Utah Graduate School

STATEMENT OF THESIS APPROVAL

The thesis of **Andrew W. Gould**

has been approved by the following supervisory committee members:

James Robert Stoll II	, Chair	**13 March 2013** Date Approved
Meredith M. Metzger	, Member	**11 March 2013** Date Approved
Eric R. Pardyjak	, Member	**13 March 2013** Date Approved

and by **Tim Ameel**, Chair of the Department of **Mechanical Engineering**

and by Donna M. White, Interim Dean of The Graduate School.

ABSTRACT

Turbulent particle transport through the air plays an important role in the life cycle of many plant pathogens. In this study, data from a field experiment was analyzed to explore momentum and particle transport within a grape vineyard. The overall goal of these experiments was to understand how the architecture of a sparse agricultural canopy interacts with turbulent flow and ultimately determines the dispersion of airborne fungal plant pathogens. Turbulence in the vineyard canopy was measured using an array of four sonic anemometers deployed at heights $z/H \sim 0.4$, 0.9, 1.45, and 1.95 where z is the height of the each sonic and H is the canopy height. In addition to turbulence measurements from the sonic anemometers, particle dispersion was measured using inert particles with the approximate size and density of powdery mildew spores and a roto-rod impaction trap array. Measurements from the sonic anemometers demonstrate that first and second order statistics of the wind field are dependent on wind direction orientation with respect to vineyard row direction. This dependence is a result of wind channeling which transfers energy between the velocity components when the wind direction is not aligned with the rows. Although the winds have a strong directional dependence, spectra analysis indicates that the structure of the turbulent flow is not fundamentally altered by the interaction between wind direction and row direction. Examination of a limited number of particle release events indicates that the wind turning and channeling observed in the momentum field impacts particle dispersion. For row-aligned flow, particle dispersion in the direction normal to the flow is decreased relative to the plume spread predicted by a standard Gaussian plume model. For flow that is not aligned with the row direction, the plume is found to rotate in the same manner as the momentum field.

For my wife, Michelle, for always being by my side.

And my parents, for pushing me to do my best.

CONTENTS

ABSTRACT iii

LIST OF FIGURES vii

LIST OF TABLES xxii

ACKNOWLEDGEMENTS xxiv

CHAPTERS

1. INTRODUCTION 1

2. EXPERIMENTAL SETUP: MOMENTUM TRANSPORT 6

2.1 Experiment Site 6
2.2 Data Collection 6
2.3 Momentum Statistics 7

3. MOMENTUM TRANSPORT 13

3.1 Wind Rose 13
3.2 Deviation of w-component of Wind vs. Stability 14
3.3 Data Selection 15
3.4 Wind Profile 15
3.5 Profiles of Wind Component Deviations 16
3.6 Vertical Kinematic Flux 18
3.7 Turbulent Spectra 19

4. PARTICLE SETUP 70

4.1 Particle Releases 70
4.2 Test Array 70
4.3 Particles 71
4.4 Roto-Rod Impaction Traps 71
4.5 Particle Analysis 72

5. PARTICLE TRANSPORT 85

5.1 Vertical Concentrations 85
5.2 Gaussian Plume 87
5.3 Error of the Gaussian Plume 88

6. CONCLUSION **117**
6.1 Future Work 117

APPENDICES

A. WIND PROFILES FOR EACH 30-MINUTE PERIOD **119**

B. PROFILES OF WIND COMPONENT DEVIATIONS **125**

C. PROFILES OF VERTICAL KINEMATIC FLUXES **141**

D. RELEASE AND TRAP DESIGN **157**

E. VERTICAL CONCENTRATION PLOTS **159**

F. GAUSSIAN PLUME PLOTS **167**

G. ERROR PLOTS OF THE GAUSSIAN PLUME **188**

REFERENCES **193**

LIST OF FIGURES

2.1 An aerial view taken from Google Earth™ mapping service of the test vineyard *(44° 49' 28.35" N 123° 14' 16.04" W)*. Important features and locations have been marked. 10

2.2 Cross section view of a row in the canopy. It shows the heights of the sonic anemometer and roto-rod impaction traps along with the average height of the canopy and the location of the fruiting wire. *(Not drawn to scale)* 11

2.3 Plan view of the vineyard. The rows are 0.3 m wide and are 2 m apart. The rows run from North to South. Wind direction was measured by where the wind originated from with the wind out of the North defined as a positive u-component and wind out of the West defined as a positive v-component. *(Not drawn to scale)* 12

3.1 Wind rose representing all convective 30-minute data sets collected between 11 Aug. 2010 to 12 Aug. 2010 at sonic 4. Each bin represents 10°. The bins are then subdivided by the percentage of time the winds are at a magnitude range. 21

3.2 Wind rose representing all convective 30-minute data sets collected between 11 Aug. 2010 to 12 Aug. 2010 at sonic 3. Each bin represents 10°. The bins are then subdivided by the percentage of time the winds are at a magnitude range. 22

3.3 Wind rose representing all convective 30-minute data sets collected between 11 Aug. 2010 to 12 Aug. 2010 at sonic 2. Each bin represents 10°. The bins are then subdivided by the percentage of time the winds are at a magnitude range. 23

3.4 Wind rose representing all convective 30-minute data sets collected between 11 Aug. 2010 to 12 Aug. 2010 at sonic 1. Each bin represents 10°. The bins are then subdivided by the percentage of time the winds are at a magnitude range. 24

3.5 Wind rose representing all convective 30-minute data sets collected during the experiment at sonic 4. Each bin represents 10°. The bins are then subdivided by the percentage of time the winds are at a magnitude range. 25

3.6 Wind rose representing all convective 30-minute data sets collected during the experiment at sonic 3. Each bin represents 10°. The bins are then subdivided by the percentage of time the winds are at a magnitude range. 26

3.7 Wind rose representing all convective 30-minute data sets collected during the experiment at sonic 2. Each bin represents 10°. The bins are then subdivided by the percentage of time the winds are at a magnitude range. 27

3.8 Wind rose representing all convective 30-minute data sets collected during the experiment at sonic 1. Each bin represents 10°. The bins are then subdivided by the percentage of time the winds are at a magnitude range. 28

3.9 Deviation of w-component of wind taken from sonic 4 normalized by u_* as a function of ζ. All 30-minute convective data sets are represented, as depicted by blue circles. A curve was then fitted to the data, as depicted by the solid line, equation 3.1. 29

3.10 Wind magnitude, U, normalized by u_* vs. height of sonic, z, normalized by the height of the rows, h; (Along flow, $0 > \zeta > -1$). Red dots show mean of the data set, and the blue lines show the 25^{th}, 50^{th}, and 75^{th} percentiles. 30

3.11 Wind magnitude, U, normalized by u_* vs. height of sonic, z, normalized by the height of the rows, h; (cross flow, $0 > \zeta > -1$). Red dots show mean of the data set, and the blue lines show the 25^{th}, 50^{th}, and 75^{th} percentiles. 31

3.12 Wind magnitude, U, normalized by u_* vs. height of sonic, z, normalized by the height of the rows, h; (along flow, $-1 > \zeta$). Red dots show mean of the data set, and the blue lines show the 25^{th}, 50^{th}, and 75^{th} percentiles. 32

3.13 Wind magnitude, U, normalized by u_* vs. height of sonic, z, normalized by the height of the rows, h; (cross flow, $-1 > \zeta$). Red dots show mean of the data set, and the blue lines show the 25^{th}, 50^{th}, and 75^{th} percentiles. 33

3.14 Deviation of u-component of wind, σ_u, normalized by u_* vs. height of sonic, z, normalized by the height of the rows, h; (Along flow, $0 > \zeta > -1$). Red dots show mean of the data set, and the blue lines show the 25^{th}, 50^{th}, and 75^{th} percentiles. 34

3.15 Deviation of u-component of wind, σ_u, normalized by u_* vs. height of sonic, z, normalized by the height of the rows, h; (cross flow, $0 > \zeta > -1$). Red dots show mean of the data set, and the blue lines show the 25^{th}, 50^{th}, and 75^{th} percentiles. 35

3.16 Deviation of u-component of wind, σ_u, normalized by u_* vs. height of sonic, z, normalized by the height of the rows, h; (along flow, $-1 > \zeta$). Red dots show mean of the data set, and the blue lines show the 25^{th}, 50^{th}, and 75^{th} percentiles. 36

3.17 Deviation of u-component of wind, σ_u, normalized by u_* vs. height of sonic, z, normalized by the height of the rows, h; (cross flow, $-1 > \zeta$). Red dots show mean of the data set, and the blue lines show the 25^{th}, 50^{th}, and 75^{th} percentiles. 37

3.18 Deviation of v-component of wind, σ_v, normalized by u_* vs. height of sonic, z, normalized by the height of the rows, h; (Along flow, $0 > \zeta > -1$). Red dots show mean of the data set, and the blue lines show the 25^{th}, 50^{th}, and 75^{th} percentiles. 38

3.19 Deviation of v-component of wind, σ_v, normalized by u_* vs. height of sonic, z, normalized by the height of the rows, h; (cross flow, $0 > \zeta > -1$). Red dots show mean of the data set, and the blue lines show the 25^{th}, 50^{th}, and 75^{th} percentiles. 39

3.20 Deviation of v-component of wind, σ_v, normalized by u_* vs. height of sonic, z, normalized by the height of the rows, h; (along flow, $-1 > \zeta$). Red dots show mean of the data set, and the blue lines show the 25^{th}, 50^{th}, and 75^{th} percentiles. 40

3.21 Deviation of v-component of wind, σ_v, normalized by u_* vs. height of sonic, z, normalized by the height of the rows, h; (cross flow, $-1 > \zeta$). Red dots show mean of the data set, and the blue lines show the 25^{th}, 50^{th}, and 75^{th} percentiles. 41

3.22 Deviation of w-component of wind, σ_w, normalized by u_* vs. height of sonic, z, normalized by the height of the rows, h; (Along flow, $0 > \zeta > -1$). Red dots show mean of the data set, and the blue lines show the 25^{th}, 50^{th}, and 75^{th} percentiles. 42

3.23 Deviation of w-component of wind, σ_w, normalized by u_* vs. height of sonic, z, normalized by the height of the rows, h; (cross flow, $0 > \zeta > -1$). Red dots show mean of the data set, and the blue lines show the 25^{th}, 50^{th}, and 75^{th} percentiles. 43

3.24 Deviation of w-component of wind, σ_w, normalized by u_* vs. height of sonic, z, normalized by the height of the rows, h; (along flow, $-1 > \zeta$). Red dots show mean of the data set, and the blue lines show the 25^{th}, 50^{th}, and 75^{th} percentiles. 44

3.25 Deviation of v-component of wind, σ_v, normalized by u_* vs. height of sonic, z, normalized by the height of the rows, h; (cross flow, $-1 > \zeta$). Red dots show mean of the data set, and the blue lines show the 25^{th}, 50^{th}, and 75^{th} percentiles. 45

3.26 Vertical kinematic eddy flux of U-momentum, $\overline{u'\,w'}$, normalized by u_*^2 vs. height of sonic, z, normalized by the height of the rows, h; (Along flow, $0 > \zeta > -1$). Red dots show mean of the data set, and the blue lines show the 25^{th}, 50^{th}, and 75^{th} percentiles. 46

3.27 Vertical kinematic eddy flux of U-momentum, $\overline{u'\,w'}$, normalized by u_*^2 vs. height of sonic, z, normalized by the height of the rows, h; (cross flow, $0 > \zeta > -1$). Red dots show mean of the data set, and the blue lines show the 25^{th}, 50^{th}, and 75^{th} percentiles. 47

3.28 Vertical kinematic eddy flux of U-momentum, $\overline{u'\,w'}$, normalized by u_*^2 vs. height of sonic, z, normalized by the height of the rows, h; (along flow, $-1 > \zeta$). Red dots show mean of the data set, and the blue lines show the 25^{th}, 50^{th}, and 75^{th} percentiles. 48

3.29 Vertical kinematic eddy flux of U-momentum, $\overline{u'\,w'}$, normalized by u_*^2 vs. height of sonic, z, normalized by the height of the rows, h; (cross flow, $-1 > \zeta$). Red dots show mean of the data set, and the blue lines show the 25^{th}, 50^{th}, and 75^{th} percentiles. 49

3.30 Vertical kinematic eddy flux of U-momentum, $\overline{v'\,w'}$, normalized by u_*^2 vs. height of sonic, z, normalized by the height of the rows, h; (Along flow, $0 > \zeta > -1$). Red dots show mean of the data set, and the blue lines show the 25^{th}, 50^{th}, and 75^{th} percentiles. 50

3.31 Vertical kinematic eddy flux of U-momentum, $\overline{v'\,w'}$, normalized by u_*^2 vs. height of sonic, z, normalized by the height of the rows, h; (cross flow, $0 > \zeta > -1$). Red dots show mean of the data set, and the blue lines show the 25^{th}, 50^{th}, and 75^{th} percentiles. 51

3.32 Vertical kinematic eddy flux of U-momentum, $\overline{v'\,w'}$, normalized by u_*^2 vs. height of sonic, z, normalized by the height of the rows, h; (along flow, $-1 > \zeta$). Red dots show mean of the data set, and the blue lines show the 25^{th}, 50^{th}, and 75^{th} percentiles. 52

3.33 Vertical kinematic eddy flux of U-momentum, $\overline{v'\,w'}$, normalized by u_*^2 vs. height of sonic, z, normalized by the height of the rows, h; (cross flow, $-1 > \zeta$). Red dots show mean of the data set, and the blue lines show the 25^{th}, 50^{th}, and 75^{th} percentiles. 53

3.34 Vertical kinematic eddy flux of U-momentum, $\overline{u'\,w'}$ and $\overline{v'\,w'}$, normalized by u_*^2 vs. height of sonic, z, normalized by the height of the rows, h; (Along flow, $0 > \zeta > -1$). Red dots show mean of the data set, and the blue lines show the 25^{th}, 50^{th}, and 75^{th} percentiles. 54

3.35 Vertical kinematic eddy flux of U-momentum, $\overline{u'\,w'}$ and $\overline{v'\,w'}$, normalized by u_*^2 vs. height of sonic, z, normalized by the height of the rows, h; (cross flow, $0 > \zeta > -1$). Red dots show mean of the data set, and the blue lines show the 25^{th}, 50^{th}, and 75^{th} percentiles. 55

3.36 Vertical kinematic eddy flux of U-momentum, $\overline{u'\,w'}$ and $\overline{v'\,w'}$, normalized by u_*^2 vs. height of sonic, z, normalized by the height of the rows, h; (along flow, $-1 > \zeta$). Red dots show mean of the data set, and the blue lines show the 25^{th}, 50^{th}, and 75^{th} percentiles. 56

3.37 Vertical kinematic eddy flux of U-momentum, $\overline{u'\,w'}$ and $\overline{v'\,w'}$, normalized by u_*^2 vs. height of sonic, z, normalized by the height of the rows, h; (cross flow, $-1 > \zeta$). Red dots show mean of the data set, and the blue lines show the 25^{th}, 50^{th}, and 75^{th} percentiles. 57

3.38 Spectra for u-component of wind. Sonic 1 was at a height of 0.8 m. Sonic 2 was at a height of 1.8 m. Sonic 3 was at a height of 2.9 m. Sonic 4 was at a height of 3.9 m; (Along flow, $0 > \zeta > -1$). 58

3.39 Spectra for u-component of wind. Sonic 1 was at a height of 0.8 m. Sonic 2 was at a height of 1.8 m. Sonic 3 was at a height of 2.9 m. Sonic 4 was at a height of 3.9 m; (cross flow, $0 > \zeta > -1$). 59

3.40 Spectra for u-component of wind. Sonic 1 was at a height of 0.8 m. Sonic 2 was at a height of 1.8 m. Sonic 3 was at a height of 2.9 m. Sonic 4 was at a height of 3.9 m; (along flow, $-1 > \zeta$). 60

3.41 Spectra for u-component of wind. Sonic 1 was at a height of 0.8 m. Sonic 2 was at a height of 1.8 m. Sonic 3 was at a height of 2.9 m. Sonic 4 was at a height of 3.9 m; (cross flow, $-1 > \zeta$). 61

3.42 Spectra for v-component of wind. Sonic 1 was at a height of 0.8 m. Sonic 2 was at a height of 1.8 m. Sonic 3 was at a height of 2.9 m. Sonic 4 was at a height of 3.9 m; (Along flow, $0 > \zeta > -1$). 62

3.43 Spectra for v-component of wind. Sonic 1 was at a height of 0.8 m. Sonic 2 was at a height of 1.8 m. Sonic 3 was at a height of 2.9 m. Sonic 4 was at a height of 3.9 m; (cross flow, $0 > \zeta > -1$). 63

3.44 Spectra for v-component of wind. Sonic 1 was at a height of 0.8 m. Sonic 2 was at a height of 1.8 m. Sonic 3 was at a height of 2.9 m. Sonic 4 was at a height of 3.9 m; (along flow, $-1 > \zeta$). 64

3.45 Spectra for v-component of wind. Sonic 1 was at a height of 0.8 m. Sonic 2 was at a height of 1.8 m. Sonic 3 was at a height of 2.9 m. Sonic 4 was at a height of 3.9 m; (cross flow, $-1 > \zeta$). 65

3.46 Spectra for w-component of wind. Sonic 1 was at a height of 0.8 m. Sonic 2 was at a height of 1.8 m. Sonic 3 was at a height of 2.9 m. Sonic 4 was at a height of 3.9 m; (Along flow, $0 > \zeta > -1$). 66

3.47 Spectra for w-component of wind. Sonic 1 was at a height of 0.8 m. Sonic 2 was at a height of 1.8 m. Sonic 3 was at a height of 2.9 m. Sonic 4 was at a height of 3.9 m; (cross flow, $0 > \zeta > -1$). 67

3.48 Spectra for w-component of wind. Sonic 1 was at a height of 0.8 m. Sonic 2 was at a height of 1.8 m. Sonic 3 was at a height of 2.9 m. Sonic 4 was at a height of 3.9 m; (along flow, $-1 > \zeta$). 68

3.49 Spectra for w-component of wind. Sonic 1 was at a height of 0.8 m. Sonic 2 was at a height of 1.8 m. Sonic 3 was at a height of 2.9 m. Sonic 4 was at a height of 3.9 m; (cross flow, $-1 > \zeta$). 69

4.1 Particle point release device. The funnel holds a reservoir of particles. There is a plug at the end of the stem to control the amount of particles being released. At the top of the funnel is a vibrating motor that causes particles to be released. 74

4.2 The funnel release mechanism is in the center of the photo. It uses a vibrating motor to oscillate particles out of a small orifices in the bottom of the funnel. 75

4.3 Roto-rod impaction traps assembled into arrays throughout the vineyard. The traps are situated to be on the edge of the row. 76

4.4 The setup for all cross flow experiments *(top view)*. The trap arrays were divided into three groups according to their distance downstream from the release point. The release point and the center trap array from each group are on the center line represented by the dashed line. Each group had different spacing in between the trap arrays in order to capture as many particles as possible from the release device. *(Not drawn to scale)* 77

4.5 The setup for all along flow experiments *(top view)*. The trap array's were divided into five groups according to their distance downstream from the release point. The release point and center trap array from each group are aligned. All trap arrays are spaced by 2 m downstream and are spaced by each row distance, roughly 2.3 m, laterally. *(Not drawn to scale)* 78

4.6 Magnified picture of the particles that were used in the release experiments. *Image taken from Cospheric's website* 79

4.7 A single roto-rod impaction trap in the canopy. The cross bar rotates on axis at high revolutions. The two vertical white polystyrene strips have been coated with a thin layer of grease, so that as the trap rotates particles are trapped. 80

4.8 Original zoomed picture of the two removed substrates. Subplot A shows several thousand particles, subplot B shows a couple hundred particles. 81

4.9 Black and white of zoomed picture of the two removed substrates. Subplot A shows several hundred particles, subplot B shows a couple of particles. 82

4.10 Cropped black and white zoomed picture of the two removed substrates. Subplot A shows several hundred particles, subplot B shows a couple of particles. 83

4.11 Binary version of zoomed picture of the two removed substrates. Subplot A shows several hundred particles, subplot B shows a couple of particles. 84

5.1 Values of concentration, $(u_* c) / q$, vs. height of sonic, z, normalized by the height of the rows, h, for Release 1 trap group 1. The blue line represents the release height normalized by row height. 90

5.2 Values of concentration, $(u_* c) / q$, vs. height of sonic, z, normalized by the height of the rows, h, for Release 1 trap group 2. The blue line represents the release height normalized by row height. 91

5.3 Values of concentration, $(u_* c) / q$, vs. height of sonic, z, normalized by the height of the rows, h, for Release 1 trap group 3. The blue line represents the release height normalized by row height. 92

5.4 Values of concentration, $(u_* c) / q$, vs. height of sonic, z, normalized by the height of the rows, h, for Release 2 trap group 1. The blue line represents the release height normalized by row height. 93

5.5 Values of concentration, $(u_* c) / q$, vs. height of sonic, z, normalized by the height of the rows, h, for Release 2 trap group 2. The blue line represents the release height normalized by row height. 94

5.6 Values of concentration, $(u_* c) / q$, vs. height of sonic, z, normalized by the height of the rows, h, for Release 2 trap group 3. The blue line represents the release height normalized by row height. 95

5.7 Values of concentration, $(u_* c) / q$, vs. height of sonic, z, normalized by the height of the rows, h, for Release 4 trap group 1. The blue line represents the release height normalized by row height. 96

5.8 Values of concentration, $(u_* c) / q$, vs. height of sonic, z, normalized by the height of the rows, h, for Release 4 trap group 2. The blue line represents the release height normalized by row height. 97

5.9 Values of concentration, $(u_* c) / q$, vs. height of sonic, z, normalized by the height of the rows, h, for Release 4 trap group 3. The blue line represents the release height normalized by row height. 98

5.10 Values of concentration, $(u_* c) / q$, vs. height of sonic, z, normalized by the height of the rows, h, for Release 4 trap group 4. The blue line represents the release height normalized by row height. 99

5.11 Values of concentration, $(u_* c) / q$, vs. height of sonic, z, normalized by the height of the rows, h, for Release 5 trap group 1. The blue line represents the release height normalized by row height. 100

5.12 Values of concentration, $(u_* c) / q$, vs. height of sonic, z, normalized by the height of the rows, h, for Release 9 trap group 2. The blue line represents the release height normalized by row height. 101

5.13 Values of concentration, $(u_* c) / q$, vs. height of sonic, z, normalized by the height of the rows, h, for Release 9 trap group 3. The blue line represents the release height normalized by row height. 102

5.14 Values of concentration, $(u_* c) / q$, vs. height of sonic, z, normalized by the height of the rows, h, for Release 9 trap group 4. The blue line represents the release height normalized by row height. 103

5.15 The normalized measured field data compared to the normalized Gaussian Plume model for release 1 at a height of 0.5 m or trap level 1. The measured field data were indicated by color filled circles. The release was located at (0.0m, 0.0m, 0.81m). Circles were omitted if data were not available at the trap location. 105

5.16 The normalized measured field data compared to the normalized Gaussian Plume model for release 1 at a height of 1.0 m or trap level 2. The measured field data were indicated by color filled circles. The release was located at (0.0m, 0.0m, 0.81m). Circles were omitted if data were not available at the trap location. 106

5.17 The normalized measured field data compared to the normalized Gaussian Plume model for release 1 at a height of 1.3 m or trap level 3. The measured field data were indicated by color filled circles. The release was located at (0.0m, 0.0m, 0.81m). Circles were omitted if data were not available at the trap location. 107

5.18 The normalized measured field data compared to the normalized Gaussian Plume model for release 1 at a height of 1.8 m or trap level 4. The measured field data were indicated by color filled circles. The release was located at (0.0m, 0.0m, 0.81m). Circles were omitted if data were not available at the trap location. 108

5.19 The normalized measured field data compared to the normalized Gaussian Plume model for release 1 at a height of 3.7 m or trap level 5. The measured field data were indicated by color filled circles. The release was located at (0.0m, 0.0m, 0.81m). Circles were omitted if data were not available at the trap location. 109

5.20 The normalized measured field data compared to the normalized Gaussian Plume model for release 6 at a height of 0.5 m or trap level 1. The measured field data were indicated by color filled circles. The release was located at (0.0m, 0.0m, 0.84m). Circles were omitted if data were not available at the trap location. 110

5.21 The normalized measured field data compared to the normalized Gaussian Plume model for release 6 at a height of 1.0 m or trap level 2. The measured field data were indicated by color filled circles. The release was located at (0.0m, 0.0m, 0.84m). Circles were omitted if data were not available at the trap location. 111

5.22 The normalized measured field data compared to the normalized Gaussian Plume model for release 6 at a height of 1.3 m or trap level 3. The measured field data were indicated by color filled circles. The release was located at (0.0m, 0.0m, 0.84m). Circles were omitted if data were not available at the trap location. 112

5.23 The normalized measured field data compared to the normalized Gaussian Plume model for release 6 at a height of 1.8 m or trap level 4. The measured field data were indicated by color filled circles. The release was located at (0.0m, 0.0m, 0.84m). Circles were omitted if data were not available at the trap location. 113

5.24 The normalized measured field data compared to the normalized Gaussian Plume model for release 6 at a height of 3.7 m or trap level 5. The measured field data were indicated by color filled circles. The release was located at (0.0m, 0.0m, 0.84m). Circles were omitted if data were not available at the trap location. 114

5.25 Depicts the amount of error between the measured data and the Gaussian Plume for the entire trap level at each trap height for release 1. . . 115

5.26 Depicts the amount of error between the measured data and the Gaussian Plume for the entire trap level at each trap height for release 6. . . 116

A.1 Wind magnitude, U, normalized by u_* vs. height of sonic, z, normalized by the height of the rows, h; (Along flow, $0 > \zeta > -1$). Red dots show mean of the data set, and the blue lines show the 25^{th}, 50^{th}, and 75^{th} percentiles. All 30-minute period profiles. 121

A.2 Wind magnitude, U, normalized by u_* vs. height of sonic, z, normalized by the height of the rows, h; (cross flow, $0 > \zeta > -1$). Red dots show mean of the data set, and the blue lines show the 25^{th}, 50^{th}, and 75^{th} percentiles. All 30-minute period profiles. 122

A.3 Wind magnitude, U, normalized by u_* vs. height of sonic, z, normalized by the height of the rows, h; (along flow, $-1 > \zeta$). Red dots show mean of the data set, and the blue lines show the 25^{th}, 50^{th}, and 75^{th} percentiles. All 30-minute period profiles. 123

A.4 Wind magnitude, U, normalized by u_* vs. height of sonic, z, normalized by the height of the rows, h; (cross flow, $-1 > \zeta$). Red dots show mean of the data set, and the blue lines show the 25^{th}, 50^{th}, and 75^{th} percentiles. All 30-minute period profiles. 124

B.1 Deviation of u-component of wind, σ_u, normalized by u_* vs. height of sonic, z, normalized by the height of the rows, h; (Along flow, $0 > \zeta > -1$). Red dots show mean of the data set, and the blue lines show the 25^{th}, 50^{th}, and 75^{th} percentiles. All 30-minute period. 127

B.2 Deviation of u-component of wind, σ_u, normalized by u_* vs. height of sonic, z, normalized by the height of the rows, h; (cross flow, $0 > \zeta > -1$). Red dots show mean of the data set, and the blue lines show the 25^{th}, 50^{th}, and 75^{th} percentiles. All 30-minute period. 128

B.3 Deviation of u-component of wind, σ_u, normalized by u_* vs. height of sonic, z, normalized by the height of the rows, h; (along flow, $-1 > \zeta$). Red dots show mean of the data set, and the blue lines show the 25^{th}, 50^{th}, and 75^{th} percentiles. All 30-minute period. 129

B.4 Deviation of u-component of wind, σ_u, normalized by u_* vs. height of sonic, z, normalized by the height of the rows, h; (cross flow, $-1 > \zeta$). Red dots show mean of the data set, and the blue lines show the 25^{th}, 50^{th}, and 75^{th} percentiles. All 30-minute period. 130

B.5 Deviation of v-component of wind, σ_v, normalized by u_* vs. height of sonic, z, normalized by the height of the rows, h; (Along flow, $0 > \zeta > -1$). Red dots show mean of the data set, and the blue lines show the 25^{th}, 50^{th}, and 75^{th} percentiles. All 30-minute period profiles. 132

B.6 Deviation of v-component of wind, σ_v, normalized by u_* vs. height of sonic, z, normalized by the height of the rows, h; (cross flow, $0 > \zeta > -1$). Red dots show mean of the data set, and the blue lines show the 25^{th}, 50^{th}, and 75^{th} percentiles. All 30-minute period profiles. 133

B.7 Deviation of v-component of wind, σ_v, normalized by u_* vs. height of sonic, z, normalized by the height of the rows, h; (along flow, $-1 > \zeta$). Red dots show mean of the data set, and the blue lines show the 25^{th}, 50^{th}, and 75^{th} percentiles. All 30-minute period profiles. 134

B.8 Deviation of v-component of wind, σ_v, normalized by u_* vs. height of sonic, z, normalized by the height of the rows, h; (cross flow, $-1 > \zeta$). Red dots show mean of the data set, and the blue lines show the 25^{th}, 50^{th}, and 75^{th} percentiles. All 30-minute period profiles. 135

B.9 Deviation of w-component of wind, σ_w, normalized by u_* vs. height of sonic, z, normalized by the height of the rows, h; (Along flow, $0 > \zeta > -1$). Red dots show mean of the data set, and the blue lines show the 25^{th}, 50^{th}, and 75^{th} percentiles. All 30-minute period. 137

B.10 Deviation of w-component of wind, σ_w, normalized by u_* vs. height of sonic, z, normalized by the height of the rows, h; (cross flow, $0 > \zeta > -1$). Red dots show mean of the data set, and the blue lines show the 25^{th}, 50^{th}, and 75^{th} percentiles. All 30-minute period. 138

B.11 Deviation of w-component of wind, σ_w, normalized by u_* vs. height of sonic, z, normalized by the height of the rows, h; (along flow, $-1 > \zeta$). Red dots show mean of the data set, and the blue lines show the 25^{th}, 50^{th}, and 75^{th} percentiles. All 30-minute period. 139

B.12 Deviation of v-component of wind, σ_v, normalized by u_* vs. height of sonic, z, normalized by the height of the rows, h; (cross flow, $-1 > \zeta$). Red dots show mean of the data set, and the blue lines show the 25^{th}, 50^{th}, and 75^{th} percentiles. All 30-minute period. 140

C.1 Vertical kinematic eddy flux of U-momentum, $\overline{u'\,w'}$, normalized by u_*^2 vs. height of sonic, z, normalized by the height of the rows, h; (Along flow, $0 > \zeta > -1$). Red dots show mean of the data set, and the blue lines show the 25^{th}, 50^{th}, and 75^{th} percentiles. All 30-minute period profiles. 143

C.2 Vertical kinematic eddy flux of U-momentum, $\overline{u'\,w'}$, normalized by u_*^2 vs. height of sonic, z, normalized by the height of the rows, h; (cross flow, $0 > \zeta > -1$). Red dots show mean of the data set, and the blue lines show the 25^{th}, 50^{th}, and 75^{th} percentiles. All 30-minute period profiles. 144

C.3 Vertical kinematic eddy flux of U-momentum, $\overline{u'\,w'}$, normalized by u_*^2 vs. height of sonic, z, normalized by the height of the rows, h; (along flow, $-1 > \zeta$). Red dots show mean of the data set, and the blue lines show the 25^{th}, 50^{th}, and 75^{th} percentiles. All 30-minute period profiles. 145

C.4 Vertical kinematic eddy flux of U-momentum, $\overline{u'\,w'}$, normalized by u_*^2 vs. height of sonic, z, normalized by the height of the rows, h; (cross flow, $-1 > \zeta$). Red dots show mean of the data set, and the blue lines show the 25^{th}, 50^{th}, and 75^{th} percentiles. All 30-minute period profiles. 146

C.5 Vertical kinematic eddy flux of U-momentum, $\overline{v'\,w'}$, normalized by u_*^2 vs. height of sonic, z, normalized by the height of the rows, h; (Along flow, $0 > \zeta > -1$). Red dots show mean of the data set, and the blue lines show the 25^{th}, 50^{th}, and 75^{th} percentiles. All 30-minute period profiles. 148

C.6 Vertical kinematic eddy flux of U-momentum, $\overline{v'\,w'}$, normalized by u_*^2 vs. height of sonic, z, normalized by the height of the rows, h; (cross flow, $0 > \zeta > -1$). Red dots show mean of the data set, and the blue lines show the 25^{th}, 50^{th}, and 75^{th} percentiles. All 30-minute period profiles. 149

C.7 Vertical kinematic eddy flux of U-momentum, $\overline{v'\,w'}$, normalized by u_*^2 vs. height of sonic, z, normalized by the height of the rows, h; (along flow, $-1 > \zeta$). Red dots show mean of the data set, and the blue lines show the 25^{th}, 50^{th}, and 75^{th} percentiles. All 30-minute period profiles. 150

C.8 Vertical kinematic eddy flux of U-momentum, $\overline{v'\,w'}$, normalized by u_*^2 vs. height of sonic, z, normalized by the height of the rows, h; (cross flow, $-1 > \zeta$). Red dots show mean of the data set, and the blue lines show the 25^{th}, 50^{th}, and 75^{th} percentiles. All 30-minute period profiles. 151

C.9 Vertical kinematic eddy flux of U-momentum, $\overline{u'\,w'}$ and $\overline{v'\,w'}$, normalized by u_*^2 vs. height of sonic, z, normalized by the height of the rows, h; (Along flow, $0 > \zeta > -1$). Red dots show mean of the data set, and the blue lines show the 25^{th}, 50^{th}, and 75^{th} percentiles. All 30-minute period profiles. 153

C.10 Vertical kinematic eddy flux of U-momentum, $\overline{u'\,w'}$ and $\overline{v'\,w'}$, normalized by u_*^2 vs. height of sonic, z, normalized by the height of the rows, h; (cross flow, $0 > \zeta > -1$). Red dots show mean of the data set, and the blue lines show the 25^{th}, 50^{th}, and 75^{th} percentiles. All 30-minute period profiles. 154

C.11 Vertical kinematic eddy flux of U-momentum, $\overline{u'\,w'}$ and $\overline{v'\,w'}$, normalized by u_*^2 vs. height of sonic, z, normalized by the height of the rows, h; (along flow, $-1 > \zeta$). Red dots show mean of the data set, and the blue lines show the 25^{th}, 50^{th}, and 75^{th} percentiles. All 30-minute period profiles. 155

C.12 Vertical kinematic eddy flux of U-momentum, $\overline{u'\,w'}$ and $\overline{v'\,w'}$, normalized by u_*^2 vs. height of sonic, z, normalized by the height of the rows, h; (cross flow, $-1 > \zeta$). Red dots show mean of the data set, and the blue lines show the 25^{th}, 50^{th}, and 75^{th} percentiles. All 30-minute period profiles. 156

E.1 Values of concentration, $(u_*\,c)\,/\,q$, vs. height of sonic, z, normalized by the height of the rows, h, for Release 3 trap group 1. The blue line represents the release height normalized by row height. 160

E.2 Values of concentration, $(u_*\,c)\,/\,q$, vs. height of sonic, z, normalized by the height of the rows, h, for Release 3 trap group 2. The blue line represents the release height normalized by row height. 161

E.3 Values of concentration, $(u_*\,c)\,/\,q$, vs. height of sonic, z, normalized by the height of the rows, h, for Release 3 trap group 3. The blue line represents the release height normalized by row height. 162

E.4 Values of concentration, $(u_*\,c)\,/\,q$, vs. height of sonic, z, normalized by the height of the rows, h, for Release 6 trap group 1. The blue line represents the release height normalized by row height. 163

E.5 Values of concentration, $(u_*\,c)\,/\,q$, vs. height of sonic, z, normalized by the height of the rows, h, for Release 6 trap group 2. The blue line represents the release height normalized by row height. 164

E.6 Values of concentration, $(u_*\,c)\,/\,q$, vs. height of sonic, z, normalized by the height of the rows, h, for Release 6 trap group 3. The blue line represents the release height normalized by row height. 165

E.7 Values of concentration, $(u_*\,c)\,/\,q$, vs. height of sonic, z, normalized by the height of the rows, h, for Release 6 trap group 4. The blue line represents the release height normalized by row height. 166

F.1 The normalized measured field data compared to the normalized Gaussian Plume model for release 2 at a height of 0.5 m or trap level 1. The measured field data were indicated by color filled circles. The release was located at (0.0m, 0.0m, 0.81m). Circles were omitted if data were not available at the trap location. 168

F.2 The normalized measured field data compared to the normalized Gaussian Plume model for release 2 at a height of 1.0 m or trap level 2. The measured field data were indicated by color filled circles. The release was located at (0.0m, 0.0m, 0.81m). Circles were omitted if data were not available at the trap location. 169

F.3 The normalized measured field data compared to the normalized Gaussian Plume model for release 2 at a height of 1.3 m or trap level 3. The measured field data were indicated by color filled circles. The release was located at (0.0m, 0.0m, 0.81m). Circles were omitted if data were not available at the trap location. 170

F.4 The normalized measured field data compared to the normalized Gaussian Plume model for release 2 at a height of 1.8 m or trap level 4. The measured field data were indicated by color filled circles. The release was located at (0.0m, 0.0m, 0.81m). Circles were omitted if data were not available at the trap location. 171

F.5 The normalized measured field data compared to the normalized Gaussian Plume model for release 2 at a height of 3.7 m or trap level 5. The measured field data were indicated by color filled circles. The release was located at (0.0m, 0.0m, 0.81m). Circles were omitted if data were not available at the trap location. 172

F.6 The normalized measured field data compared to the normalized Gaussian Plume model for release 3 at a height of 0.5 m or trap level 1. The measured field data were indicated by color filled circles. The release was located at (0.0m, 0.0m, 1.17m). Circles were omitted if data were not available at the trap location. 173

F.7 The normalized measured field data compared to the normalized Gaussian Plume model for release 3 at a height of 1.0 m or trap level 2. The measured field data were indicated by color filled circles. The release was located at (0.0m, 0.0m, 1.17m). Circles were omitted if data were not available at the trap location. 174

F.8 The normalized measured field data compared to the normalized Gaussian Plume model for release 3 at a height of 1.3 m or trap level 3. The measured field data were indicated by color filled circles. The release was located at (0.0m, 0.0m, 1.17m). Circles were omitted if data were not available at the trap location. 175

F.9 The normalized measured field data compared to the normalized Gaussian Plume model for release 3 at a height of 1.8 m or trap level 4. The measured field data were indicated by color filled circles. The release was located at (0.0m, 0.0m, 1.17m). Circles were omitted if data were not available at the trap location. 176

F.10 The normalized measured field data compared to the normalized Gaussian Plume model for release 3 at a height of 3.7 m or trap level 5. The measured field data were indicated by color filled circles. The release was located at (0.0m, 0.0m, 1.17m). Circles were omitted if data were not available at the trap location. 177

F.11 The normalized measured field data compared to the normalized Gaussian Plume model for release 4 at a height of 0.5 m or trap level 1. The measured field data were indicated by color filled circles. The release was located at (0.0m, 0.0m, 0.69m). Circles were omitted if data were not available at the trap location. 178

F.12 The normalized measured field data compared to the normalized Gaussian Plume model for release 4 at a height of 1.0 m or trap level 2. The measured field data were indicated by color filled circles. The release was located at (0.0m, 0.0m, 0.69m). Circles were omitted if data were not available at the trap location. 179

F.13 The normalized measured field data compared to the normalized Gaussian Plume model for release 4 at a height of 1.3 m or trap level 3. The measured field data were indicated by color filled circles. The release was located at (0.0m, 0.0m, 0.69m). Circles were omitted if data were not available at the trap location. 180

F.14 The normalized measured field data compared to the normalized Gaussian Plume model for release 4 at a height of 1.8 m or trap level 4. The measured field data were indicated by color filled circles. The release was located at (0.0m, 0.0m, 0.69m). Circles were omitted if data were not available at the trap location. 181

F.15 The normalized measured field data compared to the normalized Gaussian Plume model for release 4 at a height of 3.7 m or trap level 5. The measured field data were indicated by color filled circles. The release was located at (0.0m, 0.0m, 0.69m). Circles were omitted if data were not available at the trap location. 182

F.16 The normalized measured field data compared to the normalized Gaussian Plume model for release 5 at a height of 0.5 m or trap level 1. The measured field data were indicated by color filled circles. The release was located at (0.0m, 0.0m, 0.75m). Circles were omitted if data were not available at the trap location. 183

F.17 The normalized measured field data compared to the normalized Gaussian Plume model for release 5 at a height of 1.0 m or trap level 2. The measured field data were indicated by color filled circles. The release was located at (0.0m, 0.0m, 0.75m). Circles were omitted if data were not available at the trap location. 184

F.18 The normalized measured field data compared to the normalized Gaussian Plume model for release 5 at a height of 1.3 m or trap level 3. The measured field data were indicated by color filled circles. The release was located at (0.0m, 0.0m, 0.75m). Circles were omitted if data were not available at the trap location. 185

F.19 The normalized measured field data compared to the normalized Gaussian Plume model for release 5 at a height of 1.8 m or trap level 4. The measured field data were indicated by color filled circles. The release was located at (0.0m, 0.0m, 0.75m). Circles were omitted if data were not available at the trap location. 186

F.20 The normalized measured field data compared to the normalized Gaussian Plume model for release 5 at a height of 3.7 m or trap level 5. The measured field data were indicated by color filled circles. The release was located at (0.0m, 0.0m, 0.75m). Circles were omitted if data were not available at the trap location. 187

G.1 Depicts the amount of error between the measured data and the Gaussian Plume for the entire trap level at each trap height for release 2. . . 189

G.2 Depicts the amount of error between the measured data and the Gaussian Plume for the entire trap level at each trap height for release 3. . . 190

G.3 Depicts the amount of error between the measured data and the Gaussian Plume for the entire trap level at each trap height for release 4. . . 191

G.4 Depicts the amount of error between the measured data and the Gaussian Plume for the entire trap level at each trap height for release 5. . . 192

LIST OF TABLES

3.1 Number of 30-minute data sets for the set wind direction and stability criteria. 21

5.1 Release event parameters 104

5.2 Average meteorological data during release periods 104

A.1 Wind magnitude, U, normalized by u_* at sonic 1 (0.8m) 120

A.2 Wind magnitude, U, normalized by u_* at sonic 2 (1.8m) 120

A.3 Wind magnitude, U, normalized by u_* at sonic 3 (2.9m) 120

A.4 Wind magnitude, U, normalized by u_* at sonic 4 (3.9m) 120

B.1 Deviation of u-component of wind, σ_u, normalized by u_* at sonic 1 (0.8m) 126

B.2 Deviation of u-component of wind, σ_u, normalized by u_* at sonic 2 (1.8m) 126

B.3 Deviation of u-component of wind, σ_u, normalized by u_* at sonic 3 (2.9m) 126

B.4 Deviation of u-component of wind, σ_u, normalized by u_* at sonic 4 (3.9m) 126

B.5 Deviation of v-component of wind, σ_v, normalized by u_* at sonic 1 (0.8m) 131

B.6 Deviation of v-component of wind, σ_v, normalized by u_* at sonic 2 (1.8m) 131

B.7 Deviation of v-component of wind, σ_v, normalized by u_* at sonic 3 (2.9m) 131

B.8 Deviation of v-component of wind, σ_v, normalized by u_* at sonic 4 (3.9m) 131

B.9 Deviation of w-component of wind, σ_w, normalized by u_* at sonic 1 (0.8m) 136

B.10 Deviation of w-component of wind, σ_w, normalized by u_* at sonic 2 (1.8m) 136

B.11 Deviation of w-component of wind, σ_w, normalized by u_* at sonic 3 (2.9m) 136

B.12 Deviation of w-component of wind, σ_w, normalized by u_* at sonic 4 (3.9m) 136

C.1 Vertical kinematic eddy flux of U-momentum, $\overline{u'w'}$, normalized by u_*^2 at sonic 1 (0.8m) 142

C.2 Vertical kinematic eddy flux of U-momentum, $\overline{u'w'}$, normalized by u_*^2 at sonic 2 (1.8m) 142

C.3 Vertical kinematic eddy flux of U-momentum, $\overline{u'w'}$, normalized by u_*^2 at sonic 3 (2.9m) 142

C.4 Vertical kinematic eddy flux of U-momentum, $\overline{u'w'}$, normalized by u_*^2 at sonic 4 (3.9m) 142

C.5 Vertical kinematic eddy flux of U-momentum, $\overline{v'w'}$, normalized by u_*^2 at sonic 1 (0.8m) 147

C.6 Vertical kinematic eddy flux of U-momentum, $\overline{v'\,w'}$, normalized by u_*^2 at sonic 2 (1.8m) 147
C.7 Vertical kinematic eddy flux of U-momentum, $\overline{v'\,w'}$, normalized by u_*^2 at sonic 3 (2.9m) 147
C.8 Vertical kinematic eddy flux of U-momentum, $\overline{v'\,w'}$, normalized by u_*^2 at sonic 4 (3.9m) 147
C.9 Vertical kinematic eddy flux of U-momentum, $\overline{u'\,w'}$ and $\overline{v'\,w'}$, normalized by u_*^2 at sonic 1 (0.8m) 152
C.10 Vertical kinematic eddy flux of U-momentum, $\overline{u'\,w'}$ and $\overline{v'\,w'}$, normalized by u_*^2 at sonic 2 (1.8m) 152
C.11 Vertical kinematic eddy flux of U-momentum, $\overline{u'\,w'}$ and $\overline{v'\,w'}$, normalized by u_*^2 at sonic 3 (2.9m) 152
C.12 Vertical kinematic eddy flux of U-momentum, $\overline{u'\,w'}$ and $\overline{v'\,w'}$, normalized by u_*^2 at sonic 4 (3.9m) 152

ACKNOWLEDGEMENTS

Foremost I would like to thank my advisor, Rob Stoll, for his commitment in working with me over these past few years and giving me the opportunity to explore this field of study. Without his guidance I would not of been where I am today.

I would also like to thank Nate Miller for his part in the field study. He deployed the release devices, traps, and meteorological equipment as well as running all the releases during that two week period. Being able to discuss different directions and ideas with him was priceless.

Finally, I would like to thank Walt Mahafee for locating a vineyard that could be used for the release events and post-processing the trap substrates.

CHAPTER 1

INTRODUCTION

Transport through the air of chemical and biological species plays an important role in many environmental systems. These include the exchange of volatile organic compounds and heavy metals between the land and the atmosphere [49, 1], the transport of plant seeds [17, 31], the dispersion of pollens [9, 21, 22], and the dispersion of spores [2, 6, 10, 13, 11, 12, 34, 38]. In a majority of these environmental systems, the particles or chemical species originate from land surfaces that are covered partially or completely by plant canopies. These canopies contain a diverse range of vegetation types and canopy architectures. Depending on the type of plant, these architectures range from mature wheat canopies that can be assumed to be one-dimensional with dependence only on the vertical direction to natural forestry systems that are three-dimensional at similar scales. In agricultural systems, early season annual crops (e.g., corn) and an increasing number of perennial crops (e.g., grapes, cherries) are grown in row organized two-dimensional canopies that have a significant fraction of open space and are discontinuous at length scales of the order of the canopy. These canopies are an important class that resembles many important applications beyond agricultural systems (e.g., wind breaks, shelter belts, urban street canyons) and compared to one-dimensional and three-dimensional canopies, they have seen significantly less study.

This study focuses on the dispersion of heavy particles in sparse two-dimensional agricultural canopies (e.g., grape vineyards). Of particular interest to understand is how the geometrical structure of two-dimensional canopies interacts with turbulent transport to determine the distribution of particles dispersed from point sources within the canopy. Understanding the turbulent dispersion of heavy particles is of critical importance when studying the spread of of infectious diseases caused by

airborne plant pathogens [6]. Without turbulent dispersion, propagation would be limited to the next plant and epidemic severity would be limited [38]. Therefore, understanding how to formulate dispersion kernels for airborne plant pathogens from foci is of primary importance [8].

Particle distribution in and above a plant canopy is driven by the dynamics of the flow field. The flow field itself is impacted by the geometry of the plant canopy. Many studies have been performed to try to understand the momentum field of different canopies and relate it to canopy geometry. The majority have focused on continuous canopies and have found several important impacts of the presence of the canopy on momentum transport including altering the mean velocity profile with depth into the canopy, a dominant contribution of sweeps to eddy fluxes, and that the foliage causes a spectral short cut in the turbulent energy cascade within the canopy [26]. Several different impacts on the mean velocity profiles due to the presence of a canopy have been observed. Besides the well known reduction in velocity in the canopy [53, 55] other impacts have been observed. Su et al. found that the horizontal flow inside of a forest canopy flowed counter-clockwise to that of the mean wind at the canopy top. The amount of turning inside of the canopy increases with increased depth into the canopy. The turning was found to be greater in closed canopies than in open canopies and smaller under near neutral conditions than stable or unstable conditions. Tarara et al. and Weiss et al. [54, 57] both measured prevailing wind statistics in vineyards. Tarara et al. studied how traditional row alignment can be detrimental to the growing of grapes if the prevailing winds run perpendicular to the rows. If the winds are perpendicular to the row this can change the plant structure by causing them to grow parallel to the direction of the wind thus affecting the wind flow and the yield of the crop. Researchers examining turbulent intermittency and fluxes several important impacts of canopy geometry. Thomas et al. studied the flux contribution of coherent structures to the total exchange of energy and matter. They found that coherent structures are half as efficient at transporting momentum as buoyancy and that they have a greater affect on scalars than momentum. The decreased momentum transport efficiency was attributed to high-frequency turbulent wakes created by steams and leaves. The density and vertical distribution of leaf area significantly affected the

magnitude of the coherent exchange. Weiss et al. studied intermittency and vortical structures in the flow between two adjacent trellised canopies. They found that intermittent vortices on the order of the size of row spacing predominated the flow field. The vortices would last about two seconds when the wind 30 cm above the canopy was about 300 cm/s. These studies which investigated different aspects of the flow field show how the canopy affects momentum transport.

In addition to examining momentum transport, several researchers have looked at particle transport. This has been accomplished in a variety of ways including, pathogen release, artificial particle release, and numerical modeling of particles trajectories in canopies. Jarosz et al. and Klein et al. [30, 32] studied corn pollen dispersion. Jarosz et al. studied dispersion from a 400 m^2 field. Concentrations of pollen decreased by a factor of 3 from 3 to 10 m away from the source and was less than 10% at 30 m downstream. Klein et al. found that vegetation was not the major obstacle that stops pollen paths, but the settling rate of the corn pollen that controlled the distance the pollen would spread. Aylor and Raynor et al. [4, 48] studied ragweed being released over different types of homogeneous canopies. Aylor found that the deposition of pollen in a corn field varied with wind speed. For wind speeds of 1 to 2 m/s the deposition at the top and mid-point of the canopy was explained by sedimentation, but when winds increased to 3 to 4 m/s the deposition tripled. Intermittent wind tends to occur at lower speeds, which affects the streamlines by which the particles are traveling. The higher wind speeds tend to be more consistent having steadier streamlines thus increasing the amount of deposition. These particles can travel far within the canopy due to their low settling out rate and how inefficiently these particles are deposited onto the corn. Aylor et al. [7, 14] studied the effects of *Venturia inaequalis* in apple orchards by using a ground release. It was found that at heights of 3.0 m that the concentration was only 6% of the concentrations at 0.15 m above ground. Increasing height from the ground also increased the wind speed and turbulent eddy diffusivity. This caused the particles to be deposited more onto the ground than the upper canopy. Other studies were conducted releasing *Lycopodium* spores in a wheat canopy, and a barely crop [11, 12, 34]. These canopies were considered homogeneous since there are no distinct rows. The release point was

in the middle of the canopy vertically. The vertical concentration profiles show the highest amount of concentration at the top of the canopy with a lower concentration just above the canopy. The concentration decays from the top of the canopy till the half way point, then concentrations increased with decreased height.

Artificial particles have also been used to better understand flow fields. Bouvet et al. [18] studied how wind breaks affect particle transport. They found that the windbreaks have two effects, particles are directly deposited onto the windbreak, and increased particle deposition to the ground due to the formation of a quiescent zone downstream of the windbreak. The quiescent zone forms as a result of streamline displacements that result from the significant vertical velocity induced by the wind break. Walker [56] used glass beads over a rolling prairie. He released the particles at two different heights, 15 m and 7.42 m. The deposition on to the ground was found to follow a gaussian distribution, with the homogeneous surface the release took place over. An important conclusion that can be drawn from a comparison of prior experiments in homogeneous fields and windbreaks, is that the geometry of objects in the flow field (e.g., plant canopies or windbreaks) can have a strong impact on particle dispersion.

Several models have been developed, ranging from reduced order Lagrangian particle models [e.g., [5, 58]] to full three-dimensional large-eddy simulation studies [e.g., [16]], to better understand various flow fields and their affect on particle transport. Aylor used a Markov-chain random-flight model to simulate bare ground and a 1 m tall wheat canopy [3, 5]. The bare ground simulations had a peak flux at the height of the release and could be accurately described using a Lagrangian length scale L=0.5z, where z is the height above ground. The simulation with a particle release occurring inside of the wheat canopy had a peak flux at 2 m downstream from the release and well above the canopy, suggesting canopy enhanced vertical particle fluxes. Bailey and Stoll [16] modeled turbulent statistics in a sparse, row oriented canopy using the large eddy simulation technique and compared their results to homogeneous canopies. It was found that velocity moments were correlated with the row spacing and density. Vertical fluxes where stronger in the sparse canopy compared to the horizontally homogeneous canopy. In addition, they found that canopy geometry and

density both impact the ratio of sweeps to ejections.

Overall, while many different researchers have used a variety of techniques to study transport in sparse canopies, no experimental studies exist for particle transport in sparse agricultural canopies. The momentum field plays a critical role in determining the distribution of particles therefore, considerable effort is focused on the characterization of the momentum field and its relationship to canopy geometrical features. The thesis is broken into three main sections. The experimental setup section covers the layout of the vineyard and the instrumentation used for capturing meteorological and release data. The momentum transport section reports the first and second order statistics of the flow field. The particle transport section analyzes the releases and how the particles are affected by the flow field.

CHAPTER 2

EXPERIMENTAL SETUP: MOMENTUM TRANSPORT

2.1 Experiment Site

The particle dispersion and canopy momentum field experiment was conducted in a field experiment from 11 August 2010 to 22 August 2010 in a vineyard outside of Corvalis, OR. The approximate GPS coordinates of the vineyard are 44° 49' 28.35" N 123° 14' 16.04" W. The vineyard was approximately 0.53 km^2. Around the periphery of the vineyard there was a large white barn and several trees to the North (approx. 350 m away from release point), as well as a tree line to the Southeast (approx. 300 m away from the release point), as shown in Figure 2.1. The plant species was *Vitis vinifera* with a leaf area index of 1.385. Over the spatial and temporal scales of interest to this study, these obstacles should have little impact on momentum and particle field statistics. The rows in the vineyard run from North to South. The rows are oriented in this way, so that even amounts of radiation will reach both sides of the canopy giving a high quality yield of grapes [54]. There is a slight slope downward from the North to the South of less than a 2% grade. The canopy was roughly 2 m tall with a vegetation thickness of about 0.3 m. The rows are 2.3 m apart on center, and the fruiting wire, a point at which all vines are trimmed, was located about 0.45 m from the ground with the trunks the only things below the wire (see Figures 2.2 and 2.3).

2.2 Data Collection

Several meteorological instruments were deployed to measure the transport of momentum and heat in and above the vineyard canopy. This included Four Campbell Scientific CSAT3 three-dimensional sonic anemometers. Three-dimensional provides all three vectors of motion. Two of the sonic anemometers were positioned above

the canopy at 3.9 and 2.9 m above the ground and the other two anemometers were positioned inside the canopy at 1.8 and 0.8 m above the ground. The heights were chosen in order to measure statistics both inside and outside of the roughness sublayer, see Figure 2.2. All of the CSAT3s were oriented in the True North direction. Each CSAT3 measures the u, v, and w wind velocity components over a 10 cm measurement path length. Where u is the wind flowing along the North/South axis (positive being a wind from the North to the South), v is the wind flowing along the East/West axis (positive being a wind from the West to the East), and w is the wind flowing along the vertical axis (positive being a wind going straight up). The coordinate system is measured by where the wind is coming from (i.e., A Southwest wind is blowing from the Southwest to the Northeast). Collocated with the sonic anemometers were four fine wire thermocouples with a wire thickness of 0.0127 mm. These fine wires measured the temperature (θ_{fw}) at the center of each CSAT3's sensing volume. The sonic anemometers and fine wire thermocouples were connected to a Campbell Scientific CR5000 Measurement and Control Datalogger. The data were captured at a rate of 20 Hz.

2.3 Momentum Statistics

The data collected using the sonic anemometers were used to calculate first and second-order statistics relevant to momentum transport. The data were broken into 30-minute data sets over which statistics were calculated. This time span was small enough to capture the diurnal variation of the atmospheric boundary layer while still encompassing the large scale turbulent motions relevant to flow in and above the canopy.

The first momentum statistics examined in this thesis relate to the mean velocity field. In particular, the mean velocity was examined through analysis of the velocity fields' direction and magnitude. The wind direction was calculated for each 30-minute data set. To determine the wind direction each sonic's u- and v-components of wind were averaged over the 30-minute data set, represented by the overbar, and used in equation 2.1. Wind direction is defined by where the wind originated from and not where it is going. True North is 0°, East is 90°, South is 180°, and West is 270° as

shown in Figure 2.3.

$$Direction = \arctan \frac{\overline{v}}{\overline{u}}. \tag{2.1}$$

In this thesis, the wind magnitude, equation 2.2, is defined as the square root of the sum of the squares for each component of wind. Data sets that had average wind magnitudes, as recorded by the top sonic, of less than or equal to 0.2 m/s were removed. The accuracy of the CSAT3 decreases quickly when the wind speed is below 0.2 m/s

$$U = (u^2 + v^2 + w^2)^{1/2}. \tag{2.2}$$

In addition to the mean velocity field, turbulence quantities are also characterized in and above the vineyard canopy. In all of the turbulence quantities calculated in this thesis, perturbations are defined as the difference between the instantaneous value recorded from the CSAT3s (and or fine wire thermocouples) and their 30-minute mean values

$$u' = u - \overline{u}. \tag{2.3}$$

Equation 2.3 was applied to all four recorded parameters (u, v, w, θ_{fw}) when calculating turbulence statistics for each 30-minute time period.

The first turbulence statistic examined is the standard deviation of any measured quantity gives the spread of the data set

$$\sigma_u = \left(\overline{u'^2}\right)^{1/2}. \tag{2.4}$$

The main two turbulent production mechanisms in convective canopy flows, the focus of this study, are shear and buoyancy production. Because convective periods are the primary focus of this thesis, only 30-minute periods where $\overline{w'\theta'_{fw}} > 0$ were considered. Convective periods were chosen for two reasons. First, convective periods in the late afternoon should have the largest turbulent shear values and thus are the most likely periods for vigorous airborne spore movement and second most of the particle release experiments detailed in Chapters 4 and 5 where under convective

conditions. Only collected data that met this criteria were considered. Combining all of the criteria mentioned above including wind magnitude, turbulence intensity, and convective time periods resulted in 142 useable data sets each of 30-minute duration.

The level of shear was quantified by calculating the friction velocity given by equation 2.5

$$u_* = \left[\overline{u'w'}^2 + \overline{v'w'}^2\right]^{1/4}. \tag{2.5}$$

Typical values of u_* recorded during the experiment ranged from 0 to 0.4 at sonic 4. The friction velocity u_* given by equation 2.6 is used throughout this thesis to nondimensionalized turbulence statistics.

While u_* measures of the amount of shear and buoyancy, respectively, impacting the canopy flow, they do not quantify the relative contribution of each to turbulent energy production. This can be quantified using the ratio of the Obukhov length (L) and the measurement height z. This stability parameter ζ (given in equation 2.8) is the ration of shear production to buoyancy production at a given height. From this, classes of stability can be defined, with $\zeta \geq 1$ being slightly stable, $\zeta \leq -1$ being slightly unstable, and $1 > \zeta > -1$ being nearly neutral [29]

$$\zeta = \frac{z}{L} = \frac{-\kappa\, z\, g\, \overline{w'\theta'_{fw}}}{\overline{\theta_{fw}}\, {u_*}^3}. \tag{2.6}$$

In equation 2.6 z, is defined as the height of the sampling instrument and κ is the von Karman constant. Currently the range of this constant varies from 0.35 to 0.42. Researchers are trying to refine this number. It is assumed in this paper the the von Karman constant is 0.4 [51, 52]. The displacement length was not calculated causing the stability to be larger than reported values in literature.

Figure 2.1. An aerial view taken from Google Earth™ mapping service of the test vineyard *(44° 49' 28.35" N 123° 14' 16.04" W)*. Important features and locations have been marked.

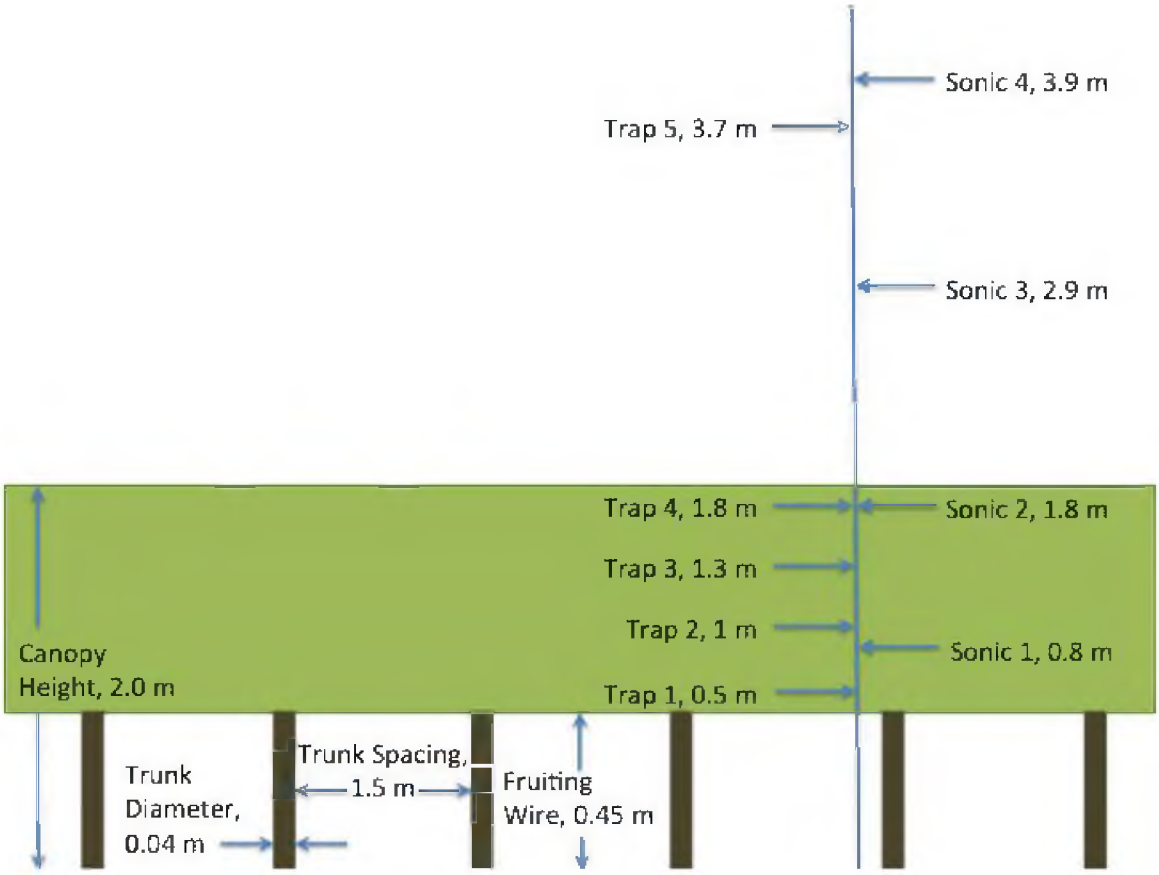

Figure 2.2. Cross section view of a row in the canopy. It shows the heights of the sonic anemometer and roto-rod impaction traps along with the average height of the canopy and the location of the fruiting wire. *(Not drawn to scale)*

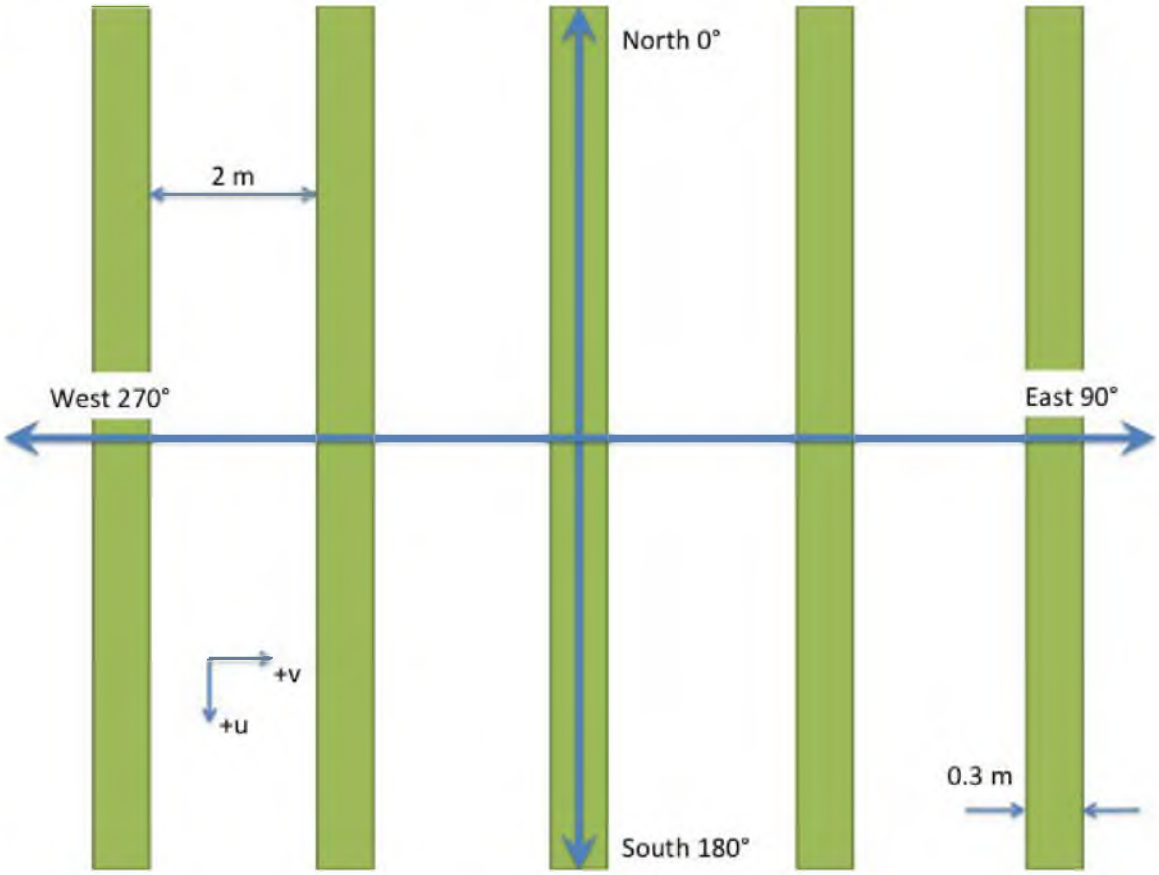

Figure 2.3. Plan view of the vineyard. The rows are 0.3 m wide and are 2 m apart. The rows run from North to South. Wind direction was measured by where the wind originated from with the wind out of the North defined as a positive u-component and wind out of the West defined as a positive v-component. *(Not drawn to scale)*

CHAPTER 3

MOMENTUM TRANSPORT

3.1 Wind Rose

Vineyard and other trellis trained canopies are sparse and have very distinct directionally dependent geometries. Therefore, it was important to understand how the magnitude and direction of the wind changes as a function of height within the canopy. This helped identify if the canopy geometry has an impact on the mean flow field within the canopy and identify similarities between trellis trained canopies and other types of canopies including urban and homogeneous canopies [40, 45]. A wind rose can characterize the percentage of time, direction, and magnitude of the entire data set.

These wind roses show the wind direction and wind speed for time periods that were convective. Figures 3.1 through 3.4 and 3.5 through 3.8 show each sonic height. These plots show both the direction, magnitude, and frequency in which the wind blows. The wind directions were binned in 10° increments. Each bin represents a wedge on the circle. Within each bin the frequency of the wind magnitude is then calculated and is represented by the different colors within the wedge.

Figures 3.1 through 3.4 show the convective time periods during a 24-hour period. The representative day shows the wind coming out of the North by Northwest. Subplots A and B show several wind directions and high wind magnitude. Descending in height shows a descending wind magnitude as expected in canopy flow as is shown in subplots C and D [60]. These plots also show a decrease in different wind directions due to wind channeling by the vineyard rows.

Figures 3.5 through 3.8 show how the wind was turned for all the recorded convective periods during the field experiment. The overall data set shows two prevailing wind directions, North by Northwest, and West by Southwest. Descending down the towers also shows the decreasing wind magnitude along with channeling.

The variation of the two prevailing winds decreases significantly as the wind was channeled down the rows. These plots suggest that the wind flow field is similar to a street canyon flow due to the semirigid structure of the rows [40, 39].

Since channeling was present, the top sonic can be used to determine what the angles are to define cross flow or along flow. Considering Figure 3.8, there was a large number of wind directions that are coming between the angles of 355° and 25°. Along row flow will then be considered as any wind direction coming from 355° to 25° or 175° to 205°. Cross flow will be considered as flow outside of these bounds. Distinguishing between cross and along row flow is critical towards identifying the signature of canopy geometry on turbulent flow statistics.

3.2 Deviation of w-component of Wind vs. Stability

Using the data from the top sonic was desired to see if vertical transport, due to shear forces, could be derived as a function of atmospheric stability [42, 59]. All of the convective periods of recorded data were used to calculate σ_w/u_* vs. ζ. These values were then plotted as shown in Figure 3.9. A curve fit was then applied to the data

$$\frac{\sigma_w}{u_*} = -0.226\,\zeta + 1.22. \tag{3.1}$$

Figure 3.9 and equation 3.1 describe the vertical transport due to shear forces. With the increase of instability, the vertical transport due to shear forces also increases. This plot and curve fit, are similar to those produced in Pahlow et al. paper on Obukhov Similarity Theory in several field experiments [42]. Wyngaard et al. described the data as following a negative one third slope over the prairie in Kansas [59]. This field experiment describes a negative slope of 0.226. The difference between the prescribed slopes could be a function of geometry changes in the flow field. It was expected as the atmosphere becomes more unstable an increase in vertical turbulence generated from shear forces would be seen.

As conditions become more unstable the cause would lead to particles being ejected out of the canopy due to the increase in deviation of vertical transport. This could

cause pathogens to travel a much greater distances than they would during a more stable condition.

3.3 Data Selection

With a large data set of raw data, data were selected in order to mimic when field releases were conducted. Only convective time periods ($\zeta < 0$) would be considered due to the same atmospheric conditions that existed when the releases occurred. The data captured by the sonic anemometers were categorized by flow direction and stability. Two stability regimes have been identified. The first stability regime was for values of ζ from 0 to -1. This regime was a weakly convective time period. The other regime had values of ζ from -1 to -∞. This regime included strong convective time periods. Each one of these stability regimes were then categorized by either along or cross flow, as identified in section 3.1. Table 3.1 shows how many 30-minute periods fit the given wind direction, along or cross row flow, and stability criteria. These data sets were used to calculate several atmospheric statistics in order to find if they are a function of flow direction or stability.

From the data that was collected, roughly 30% of it was usable for analysis. In order to determine the quality of the data sets, the wind direction of various time intervals was calculated for each individual 30-minute record. The record was then divided up into smaller time series and the wind direction was then calculated for each of those smaller time series. If the values fell outside of the established bounds for direction the entire 30-minute record was removed. It was found that the change in wind direction was sporadic and is believed to be due to localized turbulent structures. This causes some of the statistics to be skewed.

3.4 Wind Profile

The wind profile in a canopy shows how the canopy affects the magnitude of the wind speed [15, 24, 28, 44]. Endalew et al. [25] modeled canopy flow by adjusting the height of different objects in the flow field to see how it affected the the wind profile with height of an object. This experiment simulated various canopies. This experiment demonstrated that U/u_* decreased right at the dense part of the canopy, but increased in magnitude above the canopy. A similar effect can be seen in Figures

3.10 through 3.13, which show the different wind profiles for the given criteria.

Figures 3.10 through 3.13 represent the mean wind speed normalized by u_* vs. the height of the sonic normalized by the height of the rows. The average of each 30-minute data set was normalized by u_*. Then the individual averages were compiled into a larger data set for each stability regime and flow direction. The red line shows the mean of all the data set in that bin. The blue lines show the 25^{th}, 50^{th}, and 75^{th} percentiles of the data set, as is represented with two blue asterisk and a blue dot. In Appendix A, Figures 3.10 through 3.13 have been tabulated and each 30-minute profile is represented.

For all plots sonic 1 had the lowest magnitude while sonic 4 had the highest magnitude. The magnitude steadily increased in magnitude on average by 30% from sonic 1 to sonic 2 and the same for sonic 3 to sonic 4. There was a large change of magnitude, on the order of 37% from sonic 2 to 3 because of the change of drag within the canopy, meaning the flow was above the canopy.

Across all given criteria the general profile shape was the same meaning that at the canopy height there was an increase in magnitude. Sonics 3 and 4 have about a 12.5% higher magnitudes for along flow wind vs. cross flow wind. Sonics 1 and 2 also have different magnitudes based on the of flow direction of about 5% difference. Higher magnitudes were recorded from sonics 1 and 2 for all stability classes when the flow was aligned with the rows than during cross flow conditions by about 20%. This could be due to the lack of drag induced by the canopy since the flow is in line with the rows instead of against them.

3.5 Profiles of Wind Component Deviations

The standard deviation of both u- and w- components of wind show how the variability of wind changes with height [15, 26, 33, 36, 40, 46, 50, 61]. The standard deviations are expected to decay exponentially inside the canopy [15]. Finnigan also reports that there was an exponential decay once inside a plant canopy [26]. The resolution of data points recorded inside the canopy was coarse, but it can be determined that there was a rapid decay rate of σ decreasing with height.

Figures 3.14 through 3.25 present the standard deviation of each measured component normalized by u_* vs. the height of the sonic normalized by the height of

the rows. The average of each 30-minute data set was normalized by u_*. Then the individual averages were compiled into a larger data set for each stability regime and flow direction. The red line shows the mean of all the data set in that bin. The blue lines show the 25^{th}, 50^{th}, and 75^{th} percentiles of the data set, as is represented with two blue asterisk and a blue dot. In Appendix B, Figures 3.14 through 3.25 have been tabulated and each 30-minute profile is represented.

Figures 3.14 through B.4 show the standard deviation of the u-component of wind. The profiles depicted show similar profiles for stability regimes regardless of row direction. For weakly convective time periods the decay rate seems to be linear in nature, but for the strongly convective time periods the profiles seems to take on more of an exponential decay rate once inside the canopy. During the stronger convective time periods there is a higher rate of shear forces at the top of the canopy, as is seen by the rapid increase in magnitude between sonics 2 and 3 on the order of 23%.

Figures 3.18 through 3.21 show the standard deviation of the v-component of wind. There was a similar profile across all criteria, but with a change in magnitude based on flow direction and increase of convection. There appears to be more of a linear decay inside the canopy than an exponential decay as reported by Aylor [15]. As convection increases the magnitude also increases. The top two sonics, sonics 3 and 4, have similar magnitudes (≈ 5.5) regardless of flow direction for strong convective time periods, but sonics 1 and 2 show a difference in magnitude of about 50% based on flow direction for slightly convective and strongly convective time periods.

Figures 3.22 through 3.25 show the standard deviation of the w-component of wind. A similar profile was also depicted across all criteria with the exception being the increase of magnitude with the increase of convection. There was a linear decay of about 10% from sonic 4 to sonic 2 with a stronger decay rate between sonic 2 and sonic 1 of about 23%. Sonic 1 shows the lowest magnitude on each plot, due to the distance above ground the sonic was mounted at. With an increase in height the magnitudes also increase suggesting increased turbulent structures. Once outside of the canopy the fluctuations appear to be of similar magnitude for weakly convective time periods, and linearly increases during strong convective time periods.

3.6 Vertical Kinematic Flux

Vertical kinematic eddy flux of u-momentum, v-momentum, U-momentum and vertical kinematic eddy heat flux are important parameters to be considered for the momentum transport [27, 36, 43]. The flux describes if fluid particles would be transported upward or downward at that specific part of the canopy. A negative flux indicates an upward movement, while a positive flux indicates a downward movement. All vertical kinematic eddy fluxes should be constant above the canopy with a decay inside the canopy [24, 44]. A constant flux above the canopy indicates that the sonics are above the roughness sublayer and into the surface layer where Monin-Obukhov similarity holds.

Figures 3.26 through 3.37 represent the different vertical kinematic fluxes normalized by u_* vs. the height of the sonic normalized by the height of the rows. The average of each 30-minute data set was normalized by u_*. Then the individual averages were compiled into a larger data set for each stability regime and flow direction. The red line shows the mean of all the data set in that bin. The blue lines show the 25^{th}, 50^{th}, and 75^{th} percentiles of the data set, as is represented with two blue asterisk and a blue dot. In Appendix C, Figures 3.26 through 3.37 have been tabulated and each 30-minute profile is represented.

Figures 3.26 through 3.29 show the vertical kinematic eddy flux of u-momentum. Plots 3.28 and 3.29 clearly show that the flux is the greatest at the top of the canopy. The canopy is considered a momentum sink, which is shown here. There is a slight upward vertical flux at the bottom sonic because of radiative heating of the ground causing the air at the surface to warm and rise due to buoyancy.

Figures 3.30 through 3.33 show the vertical kinematic eddy flux of v-momentum. These profiles show an expected profile. With flux being highest at the top to the canopy and then approaching zero descending in height to the ground.

Figures 3.34 through 3.37 show the vertical kinematic eddy flux of U-momentum. Since this was using both vertical kinematic eddy flux of u- and v-momentum to calculate magnitudes it cannot be determined if the flux was up or down. Since u_* was calculated using data recorded from the top sonic it was expected to have a value of one. Sonic 2 still has the highest magnitude of flux for most of the criteria while

sonic 1 has the lowest expected value of flux. There appears to be a constant flux across all profiles. This would indicate that for the magnitude of fluxes that for all stability classes cross flow cases the top sonic was in the Surface Layer.

3.7 Turbulent Spectra

Another way of characterizing the flow field was by using turbulent spectra analysis. This has been done over several types of surfaces [19]. Cava et al. studied this in the trunk space of an alpine hardwood forest [20]. Nelson et al. studied the spectra in an urban environment [39]. Each study found that the cascade of energy followed Kolmogorov's law of a -5/3 slope.

Each 30-minute data set was used to calculate the turbulent spectra. The resolution of the sonic anemometer was on the order of 10 cm, so turbulent scales that were smaller than 10 cm cannot be accurately measured. MatLAB's Fast Fourier transform (fft) and the equations found in Stull [52] were used to calculate the spectra for u', v', w', and θ' for each data set. Each data set was then averaged based on flow and stability criteria to determine any trends that might be present.

Both axes had to be normalized in order to compare the different criteria to one another. The frequency was normalized by equation 3.2, and the spectra were premultiplied by equation 3.3

$$\frac{f\, z_{sonic}}{\overline{U}_{sonic}}. \tag{3.2}$$

The frequency, f, was normalized by the height, z, and the wind magnitude, $\overline{U}$, was calculated from the top sonic. The wind magnitude was calculated for each 30-minute data set, and then averaged across all the data sets based on the flow and stability criteria

$$\frac{f\, S_u(f)}{\sigma_u^2}. \tag{3.3}$$

The spectra were premultiplied as laid out in equation 3.3 to more easily identify the production range. Before being premultiplied the production range follows a -1 slope while the cascade of energy was a -5/3 slope. Performing this operation caused the production range to have a slope of zero, or horizontal, and the cascade of energy

to have a -2/3 slope. This identifies the production range more easily in order to correlate the frequency to a length scale as identified in Taylor's Hypothesis [52].

Figures 3.38 through 3.49 show the spectra for the given criteria at all sonic heights. A -2/3 slope line was placed on each plot to be able to help identify the slope of the cascade of energy. In each plot at the higher frequencies the data starts to deviate from the -2/3 slope. This was due to the inability of the sonic to resolve scales smaller than 10 cm, approaching the Nyquist frequency and signal noise associated with the measurements [39].

Finnigan found in a moga forest canopy that the slope of the cascade of energy increased as the height decreased into the canopy [26]. Large-eddy simulations models have shown this same phenomena occurring in a vineyard canopy [16]. This was not observed during the field experiments.

From calculated spectra, length scales of turbulence generation were found using Taylor's Frozen Hypothesis and the Raupach et al. Mixing-layer analogy [47]. The spectral frequency was multiplied by the top sonic height then divided by the average wind magnitude. It was found that the length scale for turbulence generation for u- and v-component of wind were on the order of the canopy height ($\approx$2 m). The w-component of wind was found to have a turbulence production length scale of approximately 1 m. The production range for the calculated spectra occurs at similar normalized frequency values found in aforementioned articles.

Table 3.1. Number of 30-minute data sets for the set wind direction and stability criteria.

Stability	Along Flow	Cross Flow
$0 > \zeta > -1$	45	67
$-1 > \zeta$	12	23

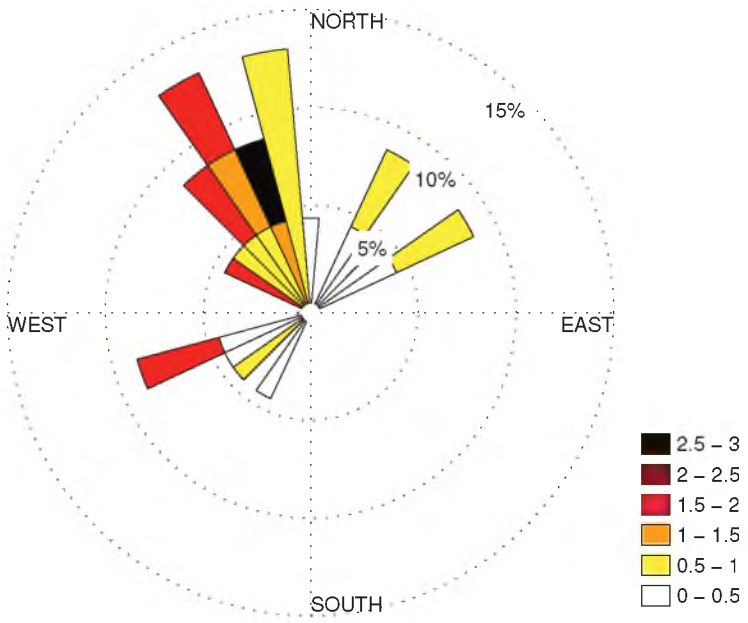

Figure 3.1. Wind rose representing all convective 30-minute data sets collected between 11 Aug. 2010 to 12 Aug. 2010 at sonic 4. Each bin represents 10°. The bins are then subdivided by the percentage of time the winds are at a magnitude range.

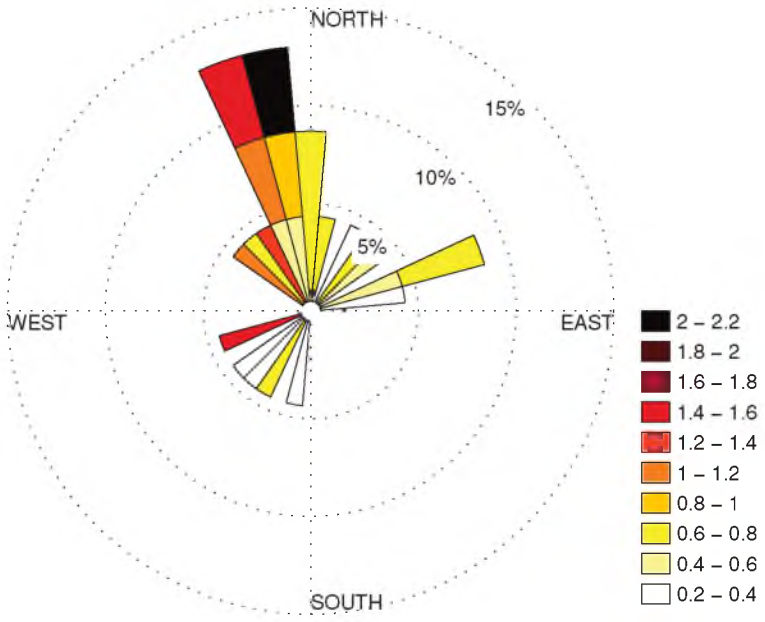

Figure 3.2. Wind rose representing all convective 30-minute data sets collected between 11 Aug. 2010 to 12 Aug. 2010 at sonic 3. Each bin represents 10°. The bins are then subdivided by the percentage of time the winds are at a magnitude range.

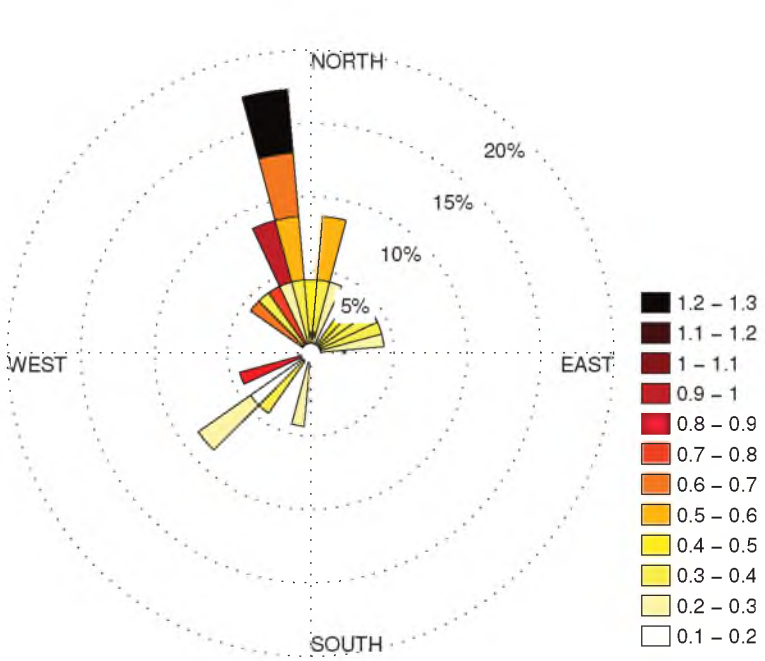

Figure 3.3. Wind rose representing all convective 30-minute data sets collected between 11 Aug. 2010 to 12 Aug. 2010 at sonic 2. Each bin represents 10°. The bins are then subdivided by the percentage of time the winds are at a magnitude range.

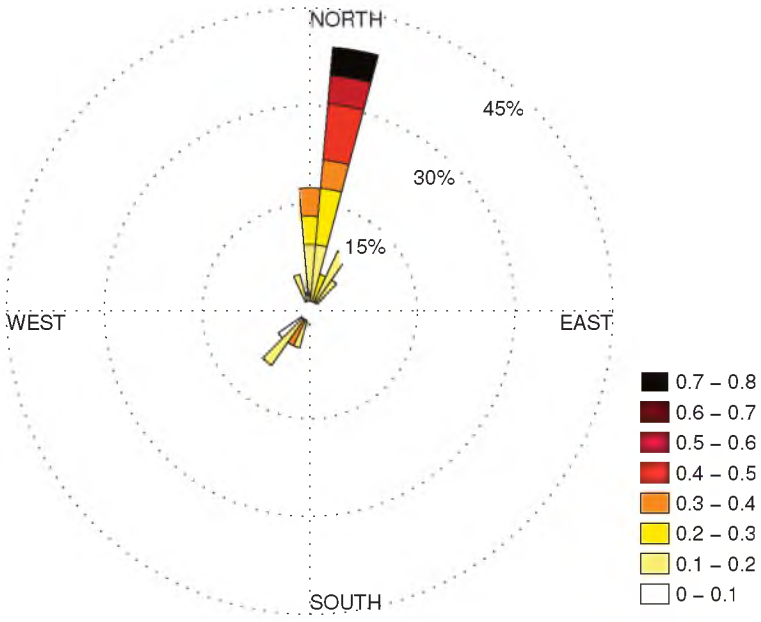

Figure 3.4. Wind rose representing all convective 30-minute data sets collected between 11 Aug. 2010 to 12 Aug. 2010 at sonic 1. Each bin represents 10°. The bins are then subdivided by the percentage of time the winds are at a magnitude range.

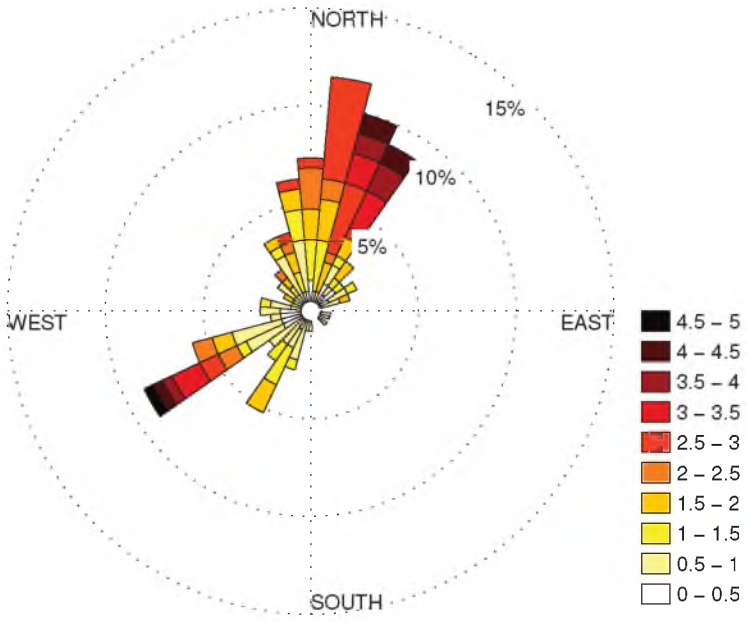

Figure 3.5. Wind rose representing all convective 30-minute data sets collected during the experiment at sonic 4. Each bin represents 10°. The bins are then subdivided by the percentage of time the winds are at a magnitude range.

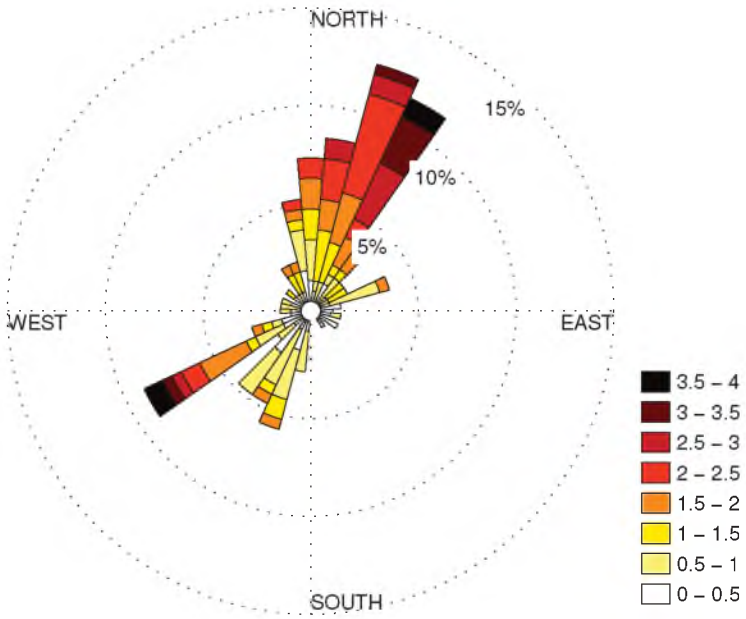

Figure 3.6. Wind rose representing all convective 30-minute data sets collected during the experiment at sonic 3. Each bin represents 10°. The bins are then subdivided by the percentage of time the winds are at a magnitude range.

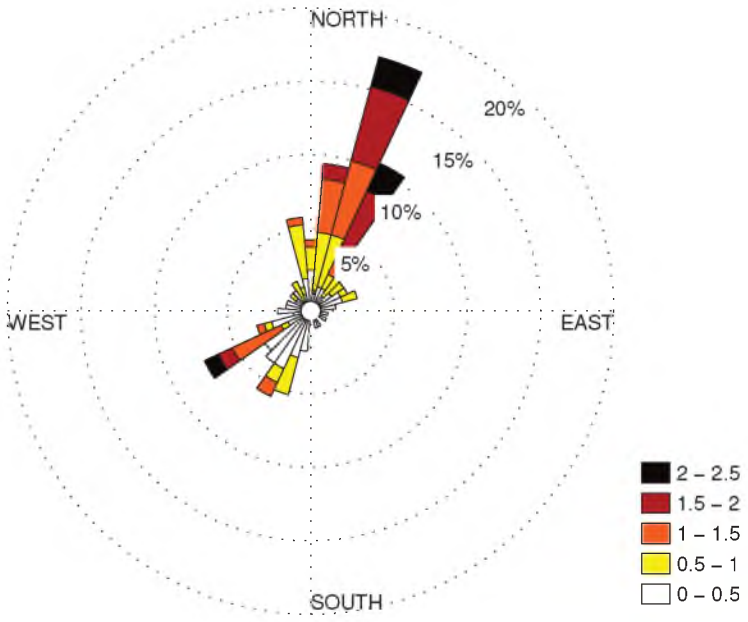

Figure 3.7. Wind rose representing all convective 30-minute data sets collected during the experiment at sonic 2. Each bin represents 10°. The bins are then subdivided by the percentage of time the winds are at a magnitude range.

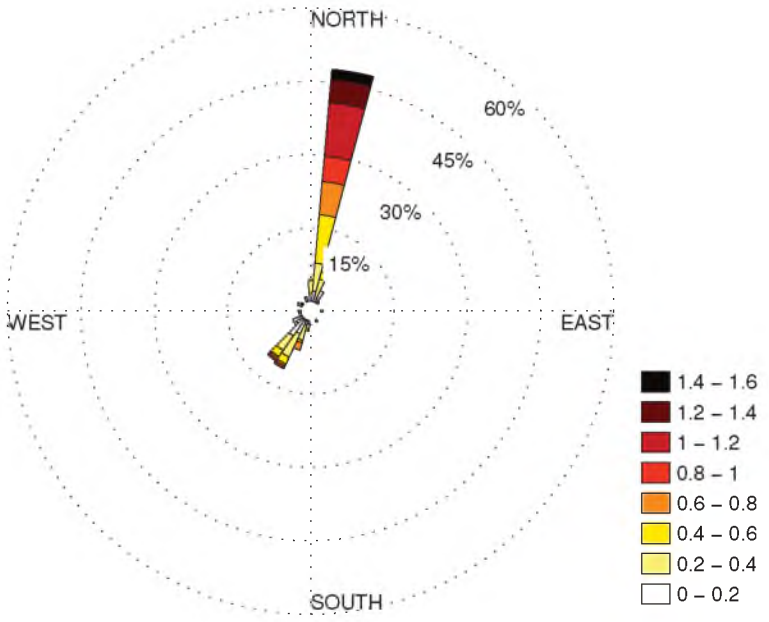

Figure 3.8. Wind rose representing all convective 30-minute data sets collected during the experiment at sonic 1. Each bin represents 10°. The bins are then subdivided by the percentage of time the winds are at a magnitude range.

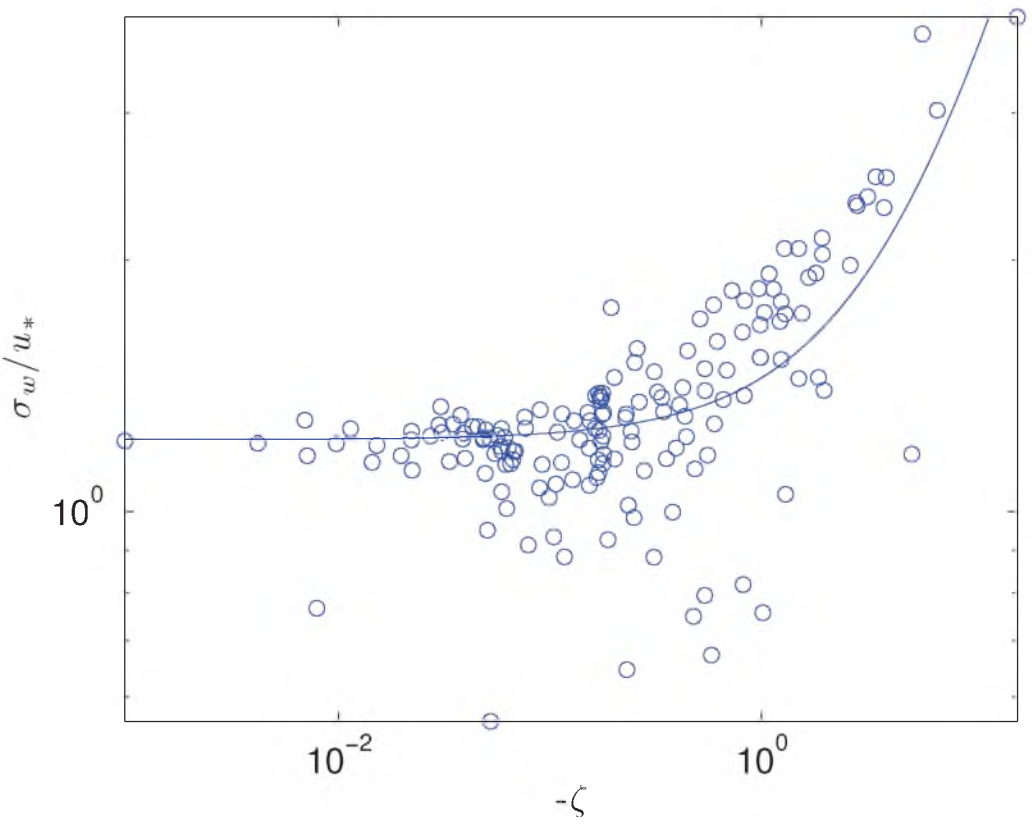

Figure 3.9. Deviation of w-component of wind taken from sonic 4 normalized by u_* as a function of ζ. All 30-minute convective data sets are represented, as depicted by blue circles. A curve was then fitted to the data, as depicted by the solid line, equation 3.1.

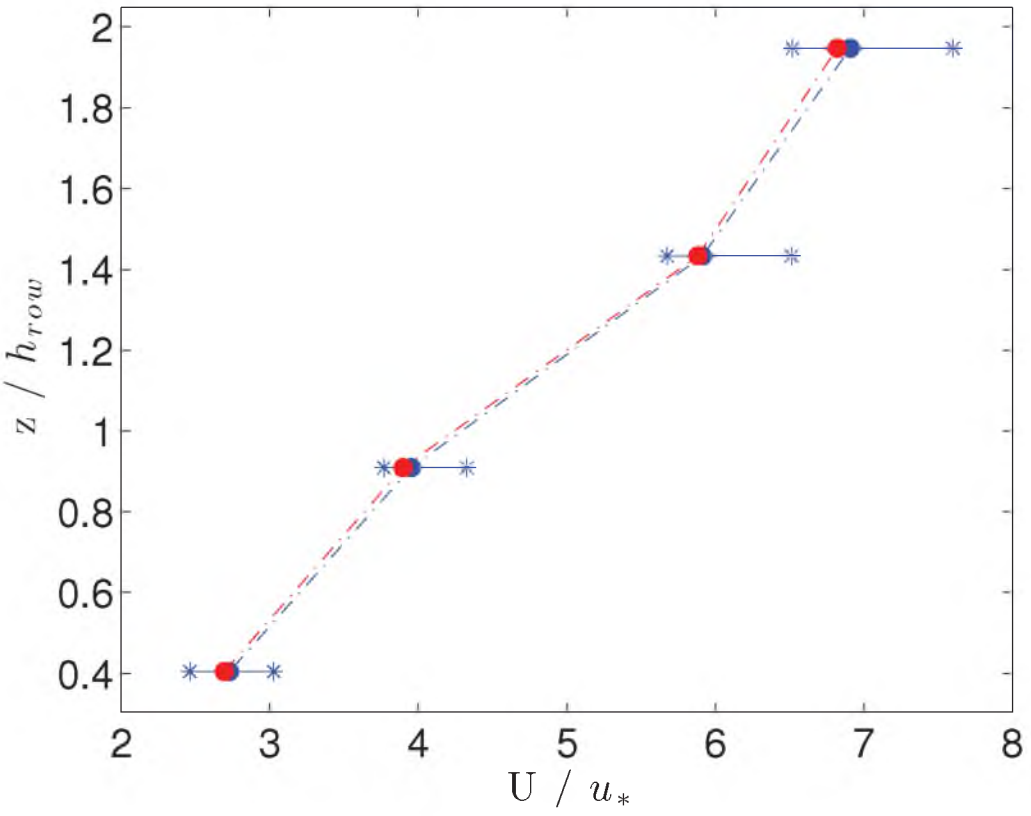

Figure 3.10. Wind magnitude, U, normalized by u_* vs. height of sonic, z, normalized by the height of the rows, h; (Along flow, $0 > \zeta > -1$). Red dots show mean of the data set, and the blue lines show the 25^{th}, 50^{th}, and 75^{th} percentiles.

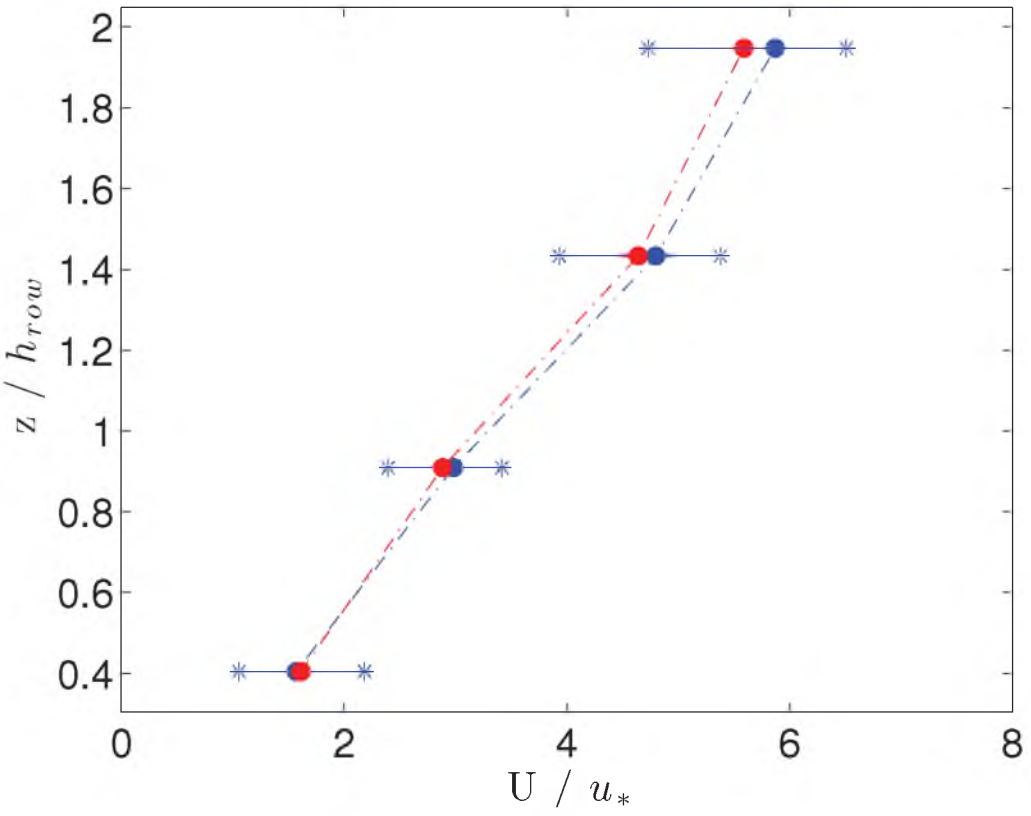

Figure 3.11. Wind magnitude, U, normalized by u_* vs. height of sonic, z, normalized by the height of the rows, h; (cross flow, $0 > \zeta > -1$). Red dots show mean of the data set, and the blue lines show the 25^{th}, 50^{th}, and 75^{th} percentiles.

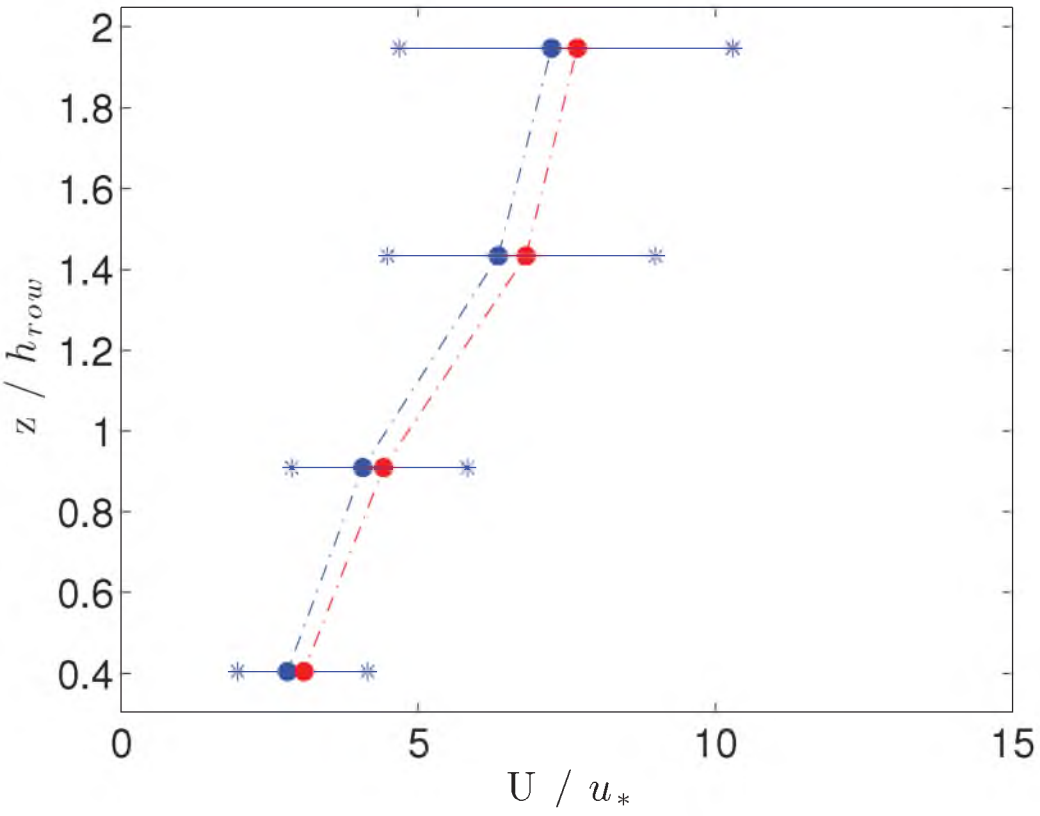

Figure 3.12. Wind magnitude, U, normalized by u_* vs. height of sonic, z, normalized by the height of the rows, h; (along flow, $-1 > \zeta$). Red dots show mean of the data set, and the blue lines show the 25^{th}, 50^{th}, and 75^{th} percentiles.

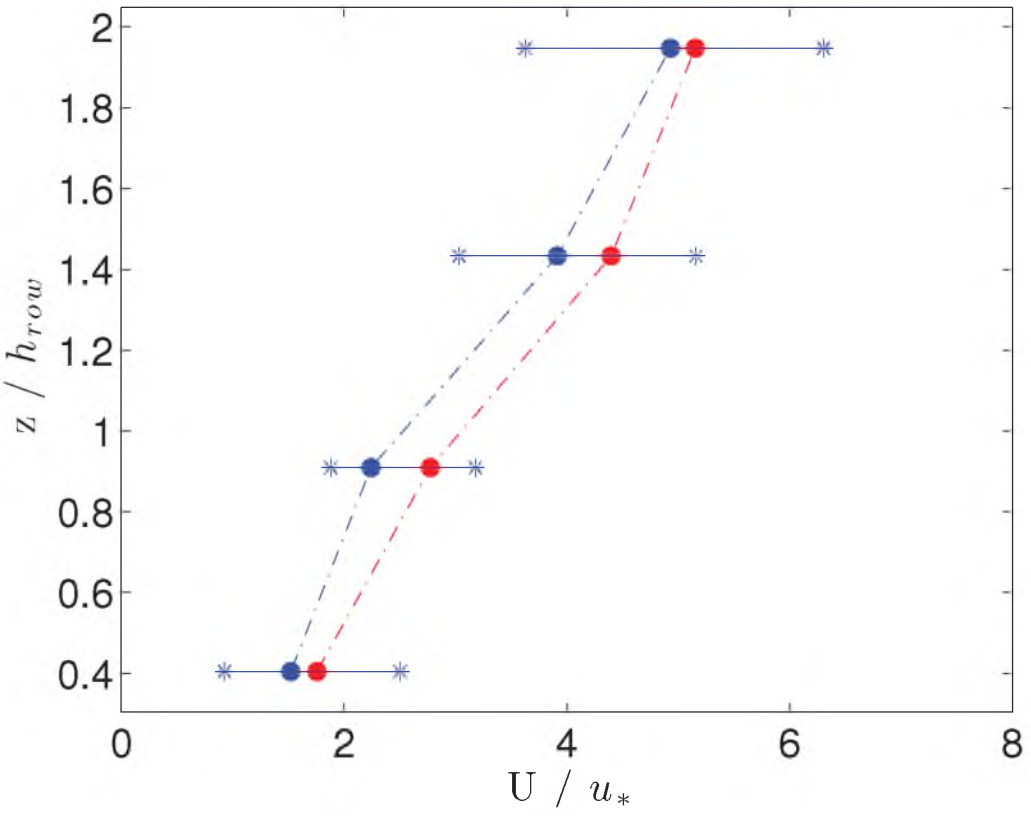

Figure 3.13. Wind magnitude, U, normalized by u_* vs. height of sonic, z, normalized by the height of the rows, h; (cross flow, $-1 > \zeta$). Red dots show mean of the data set, and the blue lines show the 25^{th}, 50^{th}, and 75^{th} percentiles.

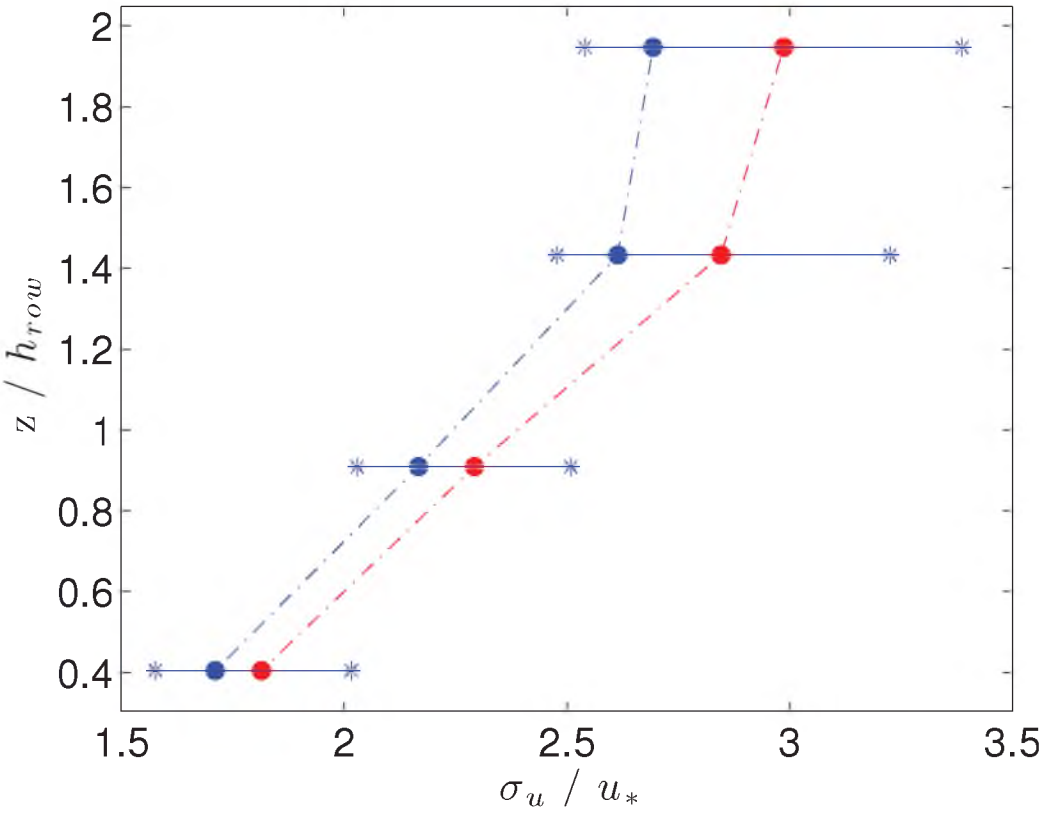

Figure 3.14. Deviation of u-component of wind, σ_u, normalized by u_* vs. height of sonic, z, normalized by the height of the rows, h; (Along flow, $0 > \zeta > -1$). Red dots show mean of the data set, and the blue lines show the 25^{th}, 50^{th}, and 75^{th} percentiles.

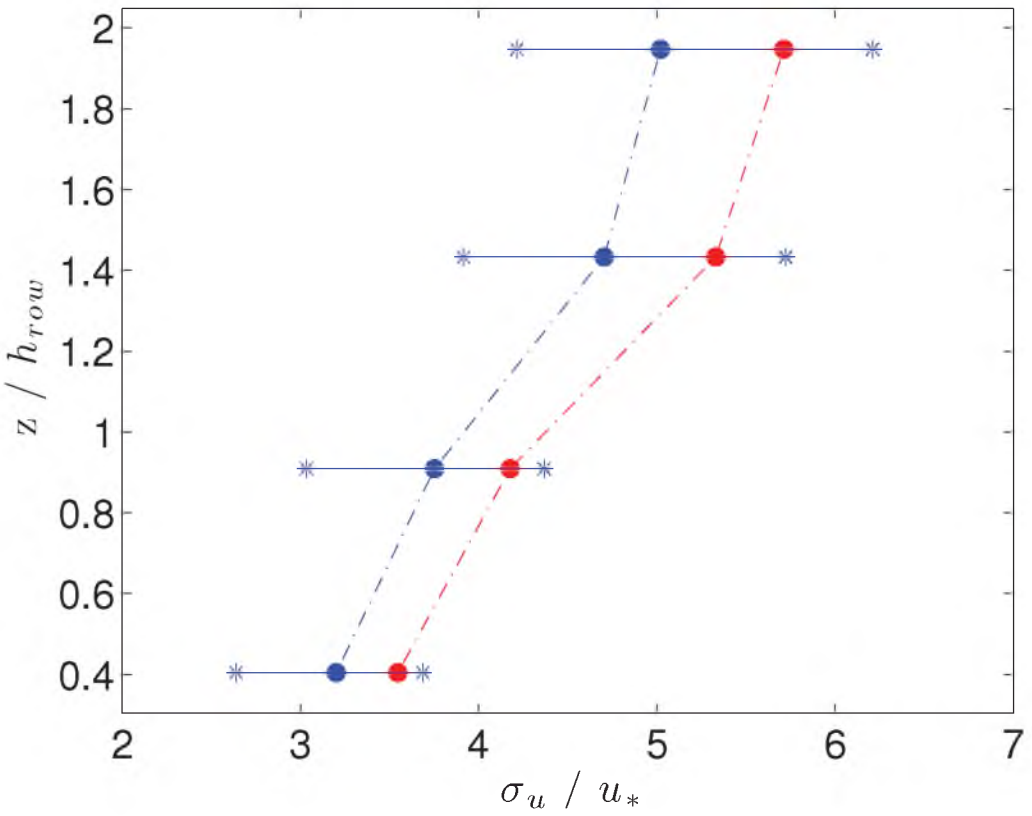

Figure 3.15. Deviation of u-component of wind, σ_u, normalized by u_* vs. height of sonic, z, normalized by the height of the rows, h; (cross flow, $0 > \zeta > -1$). Red dots show mean of the data set, and the blue lines show the 25^{th}, 50^{th}, and 75^{th} percentiles.

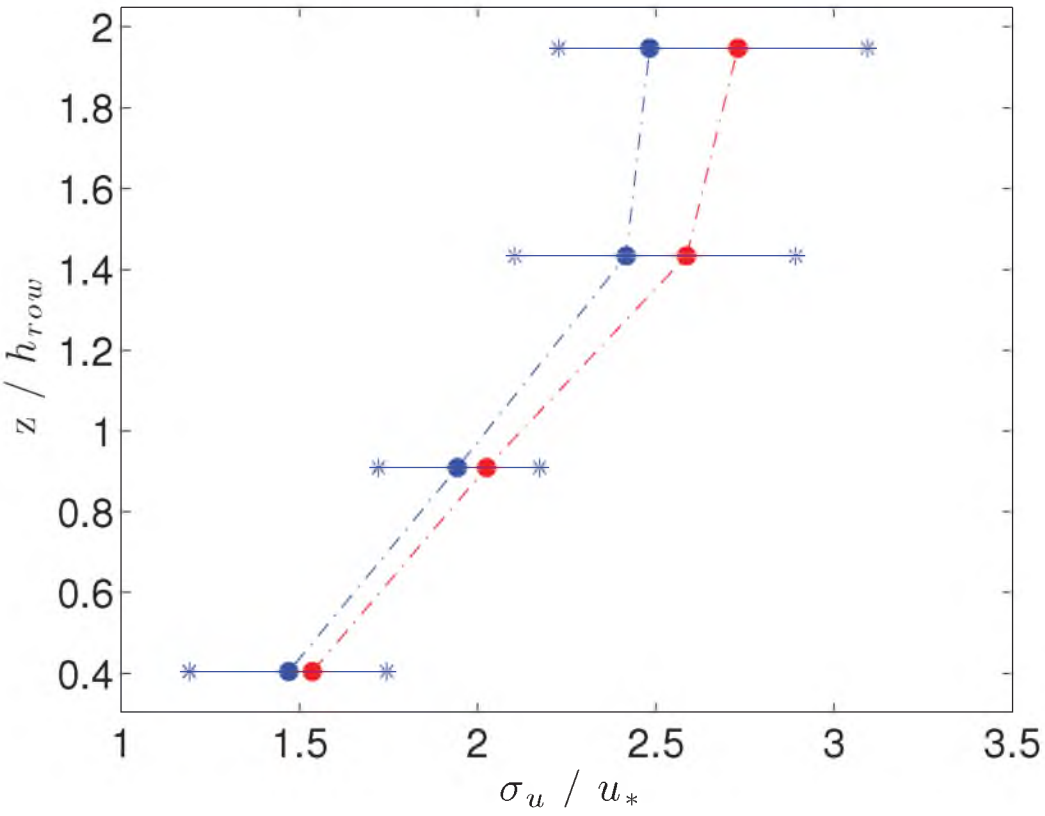

Figure 3.16. Deviation of u-component of wind, σ_u, normalized by u_* vs. height of sonic, z, normalized by the height of the rows, h; (along flow, $-1 > \zeta$). Red dots show mean of the data set, and the blue lines show the 25^{th}, 50^{th}, and 75^{th} percentiles.

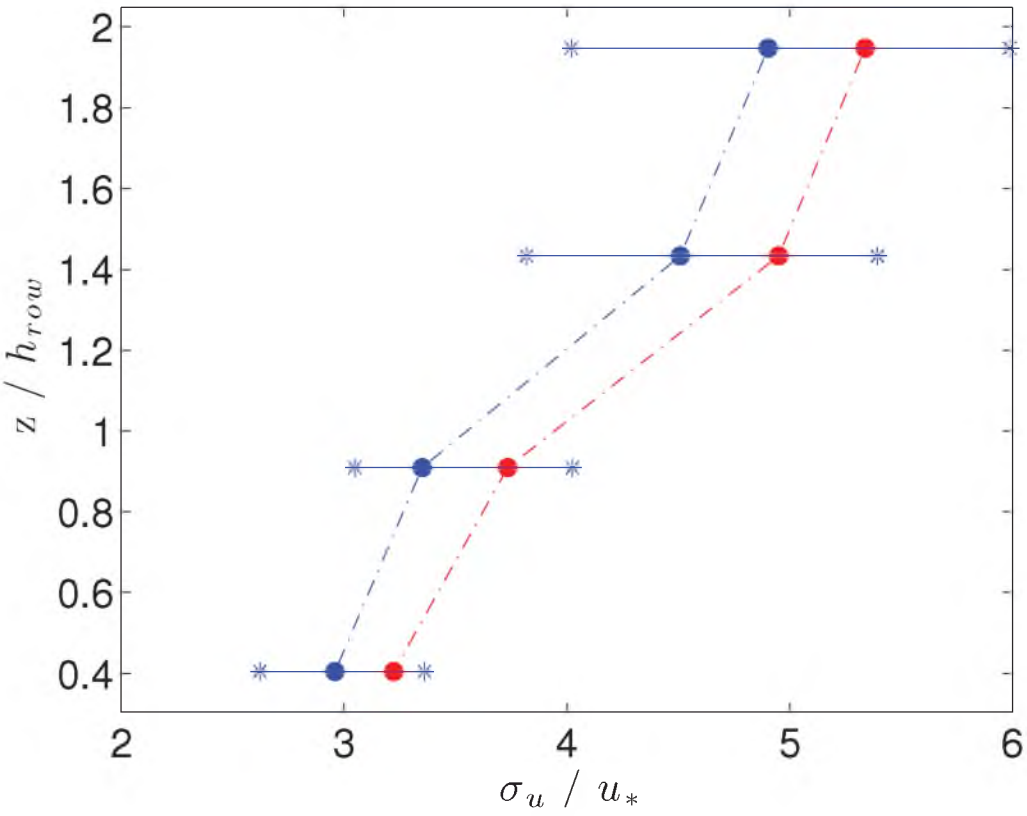

Figure 3.17. Deviation of u-component of wind, σ_u, normalized by u_* vs. height of sonic, z, normalized by the height of the rows, h; (cross flow, $-1 > \zeta$). Red dots show mean of the data set, and the blue lines show the 25^{th}, 50^{th}, and 75^{th} percentiles.

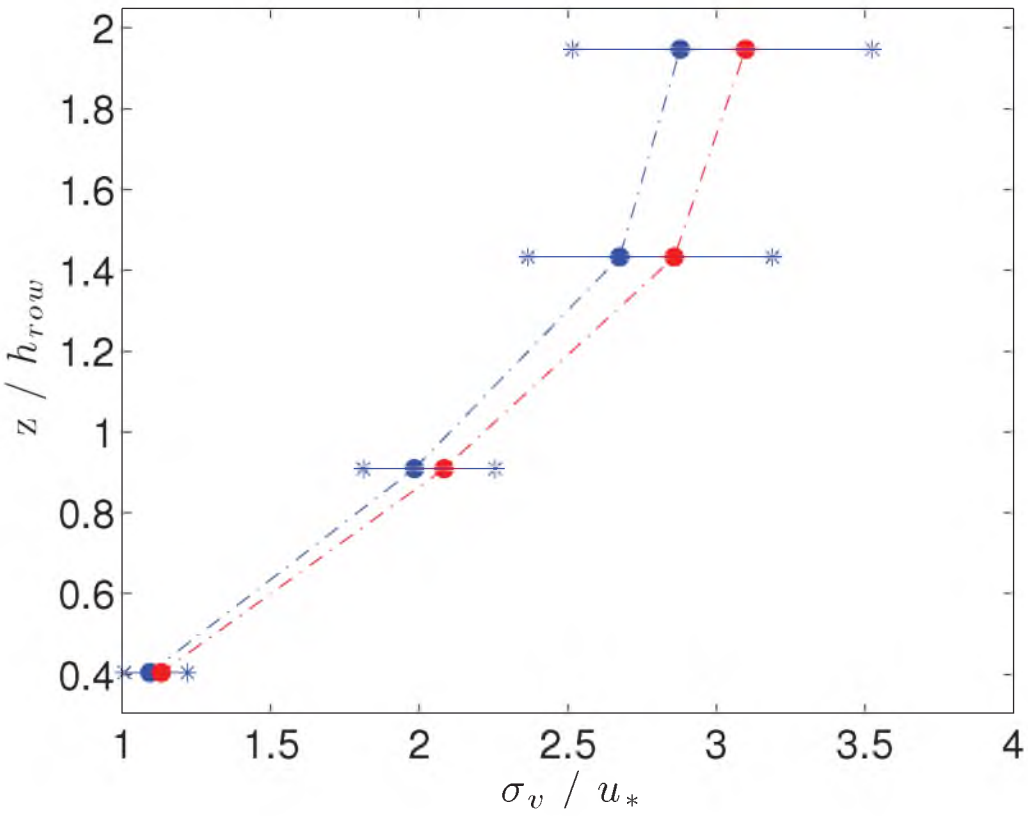

Figure 3.18. Deviation of v-component of wind, σ_v, normalized by u_* vs. height of sonic, z, normalized by the height of the rows, h; (Along flow, $0 > \zeta > -1$). Red dots show mean of the data set, and the blue lines show the 25^{th}, 50^{th}, and 75^{th} percentiles.

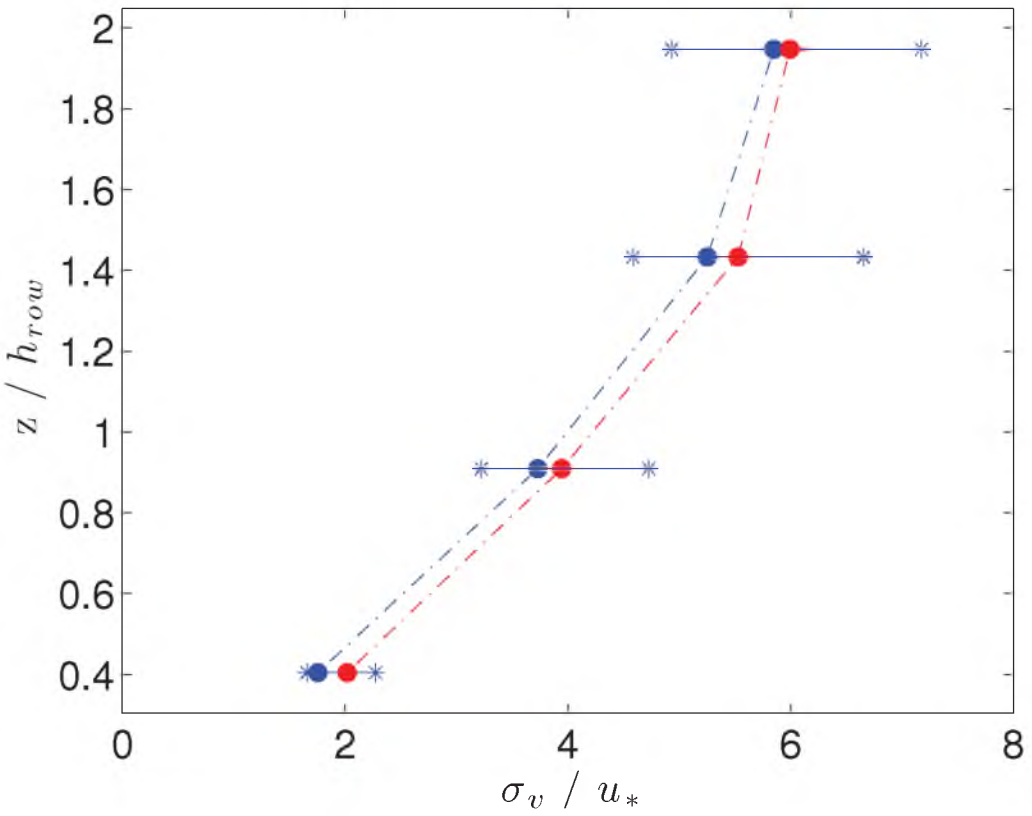

Figure 3.19. Deviation of v-component of wind, σ_v, normalized by u_* vs. height of sonic, z, normalized by the height of the rows, h; (cross flow, $0 > \zeta > -1$). Red dots show mean of the data set, and the blue lines show the 25^{th}, 50^{th}, and 75^{th} percentiles.

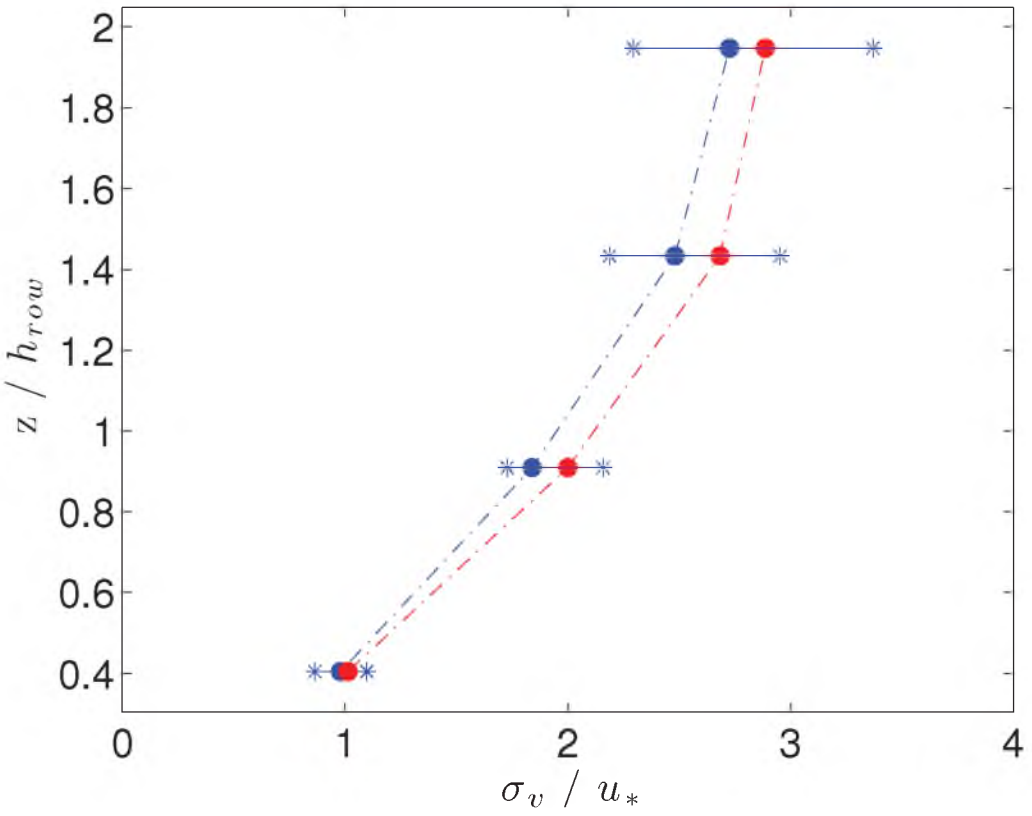

Figure 3.20. Deviation of v-component of wind, σ_v, normalized by u_* vs. height of sonic, z, normalized by the height of the rows, h; (along flow, $-1 > \zeta$). Red dots show mean of the data set, and the blue lines show the 25^{th}, 50^{th}, and 75^{th} percentiles.

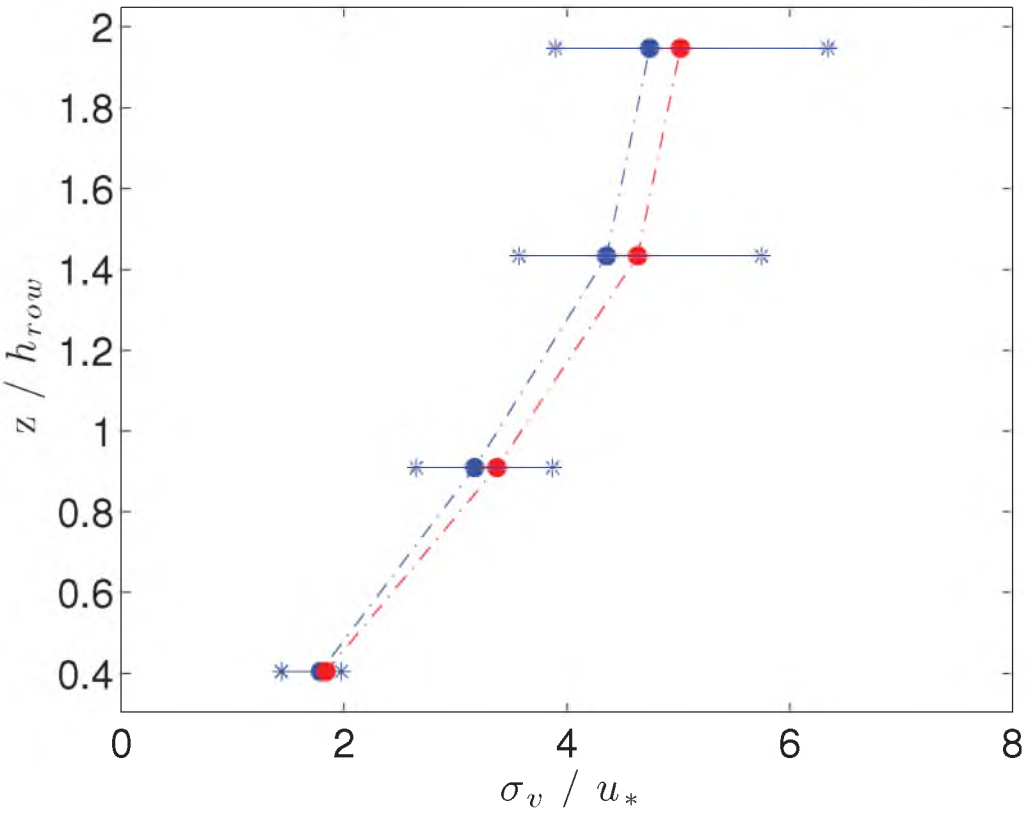

Figure 3.21. Deviation of v-component of wind, σ_v, normalized by u_* vs. height of sonic, z, normalized by the height of the rows, h; (cross flow, $-1 > \zeta$). Red dots show mean of the data set, and the blue lines show the 25^{th}, 50^{th}, and 75^{th} percentiles.

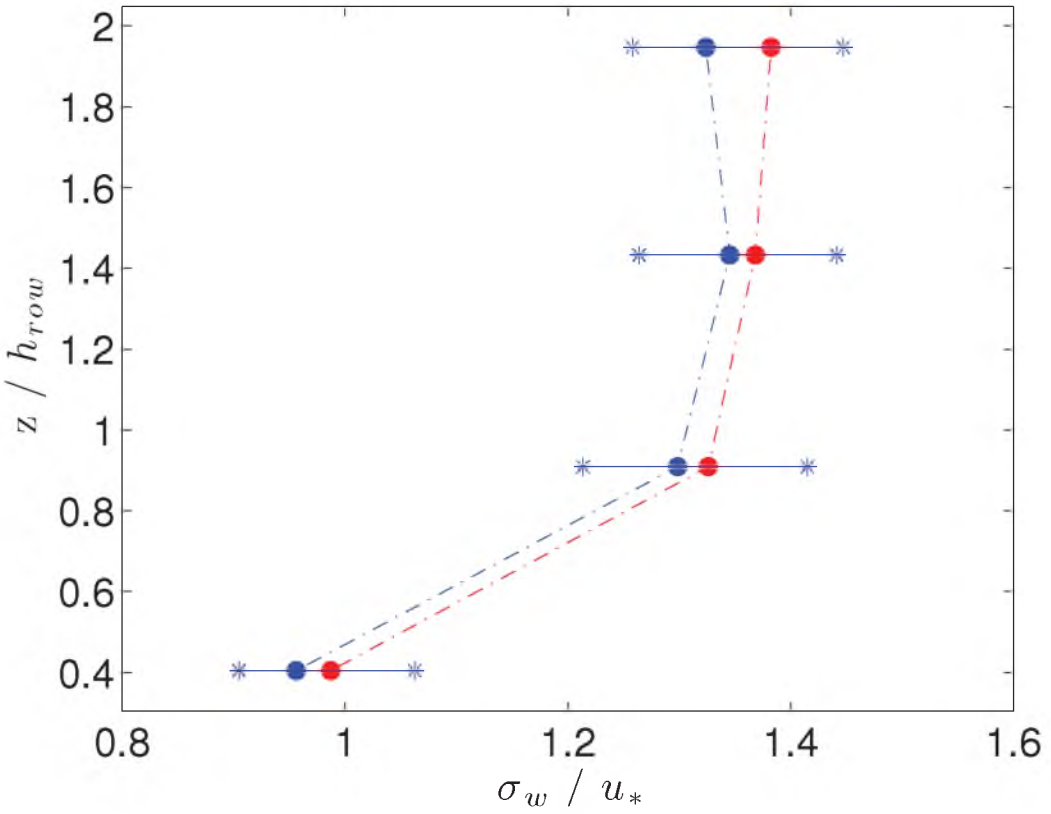

Figure 3.22. Deviation of w-component of wind, σ_w, normalized by u_* vs. height of sonic, z, normalized by the height of the rows, h; (Along flow, $0 > \zeta > -1$). Red dots show mean of the data set, and the blue lines show the 25^{th}, 50^{th}, and 75^{th} percentiles.

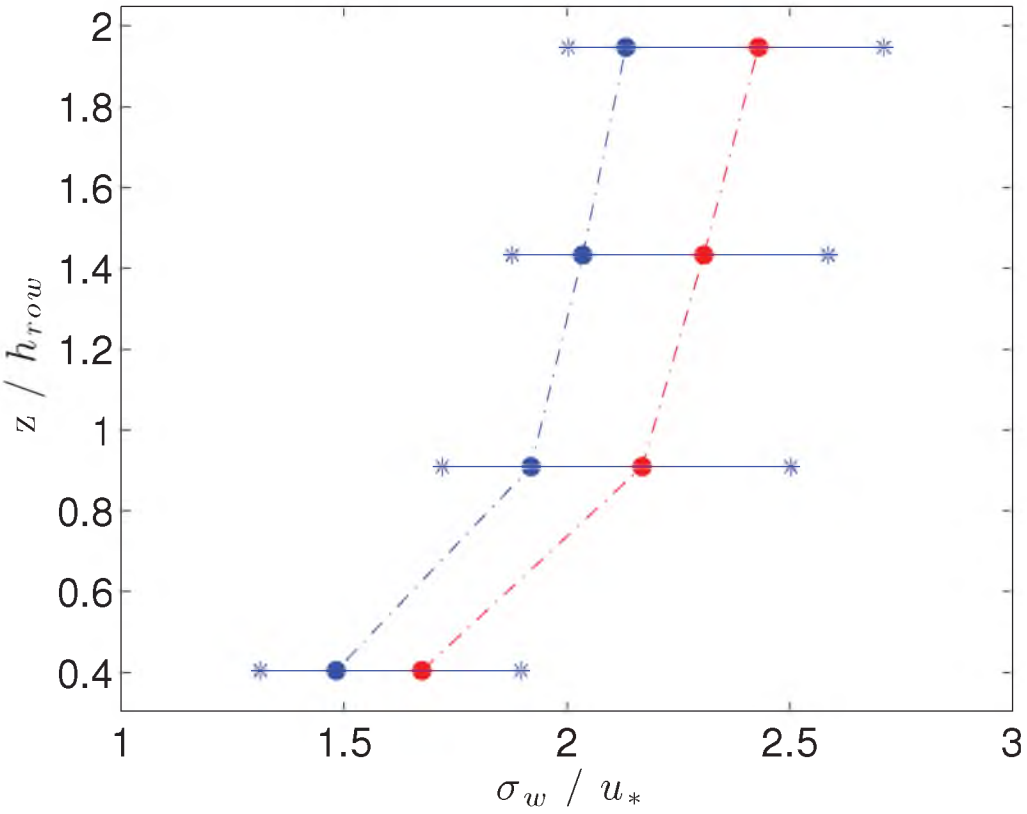

Figure 3.23. Deviation of w-component of wind, σ_w, normalized by u_* vs. height of sonic, z, normalized by the height of the rows, h; (cross flow, $0 > \zeta > -1$). Red dots show mean of the data set, and the blue lines show the 25^{th}, 50^{th}, and 75^{th} percentiles.

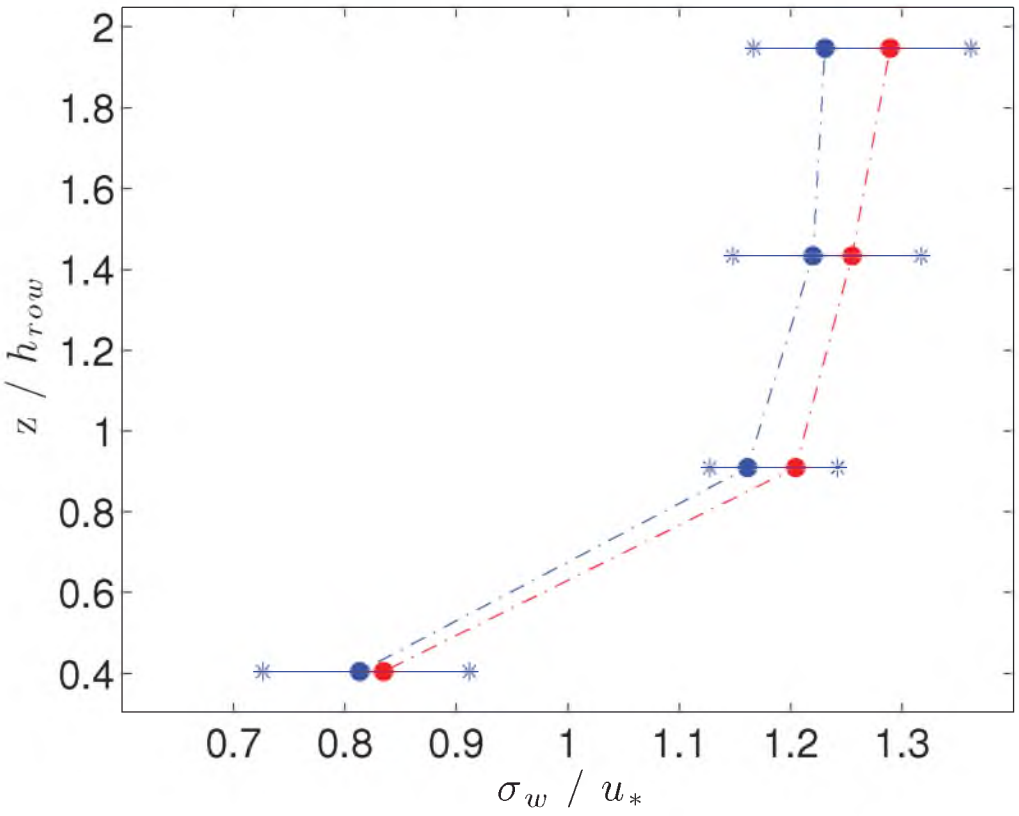

Figure 3.24. Deviation of w-component of wind, σ_w, normalized by u_* vs. height of sonic, z, normalized by the height of the rows, h; (along flow, $-1 > \zeta$). Red dots show mean of the data set, and the blue lines show the 25^{th}, 50^{th}, and 75^{th} percentiles.

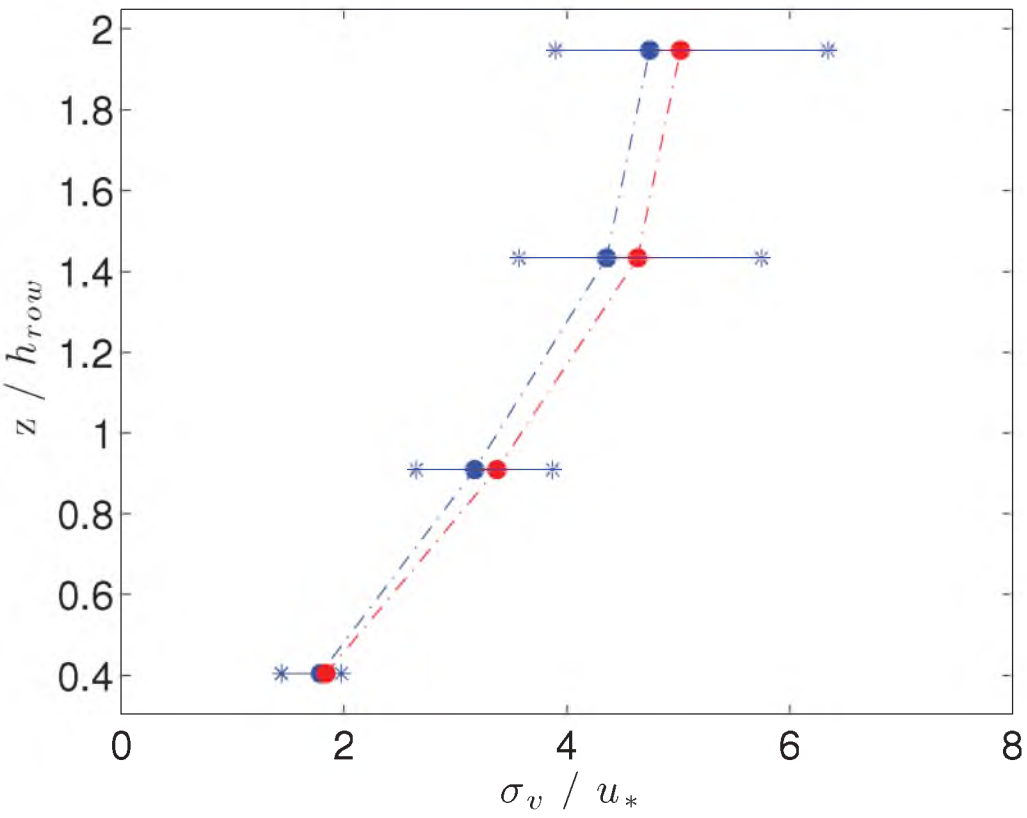

Figure 3.25. Deviation of v-component of wind, σ_v, normalized by u_* vs. height of sonic, z, normalized by the height of the rows, h; (cross flow, $-1 > \zeta$). Red dots show mean of the data set, and the blue lines show the 25^{th}, 50^{th}, and 75^{th} percentiles.

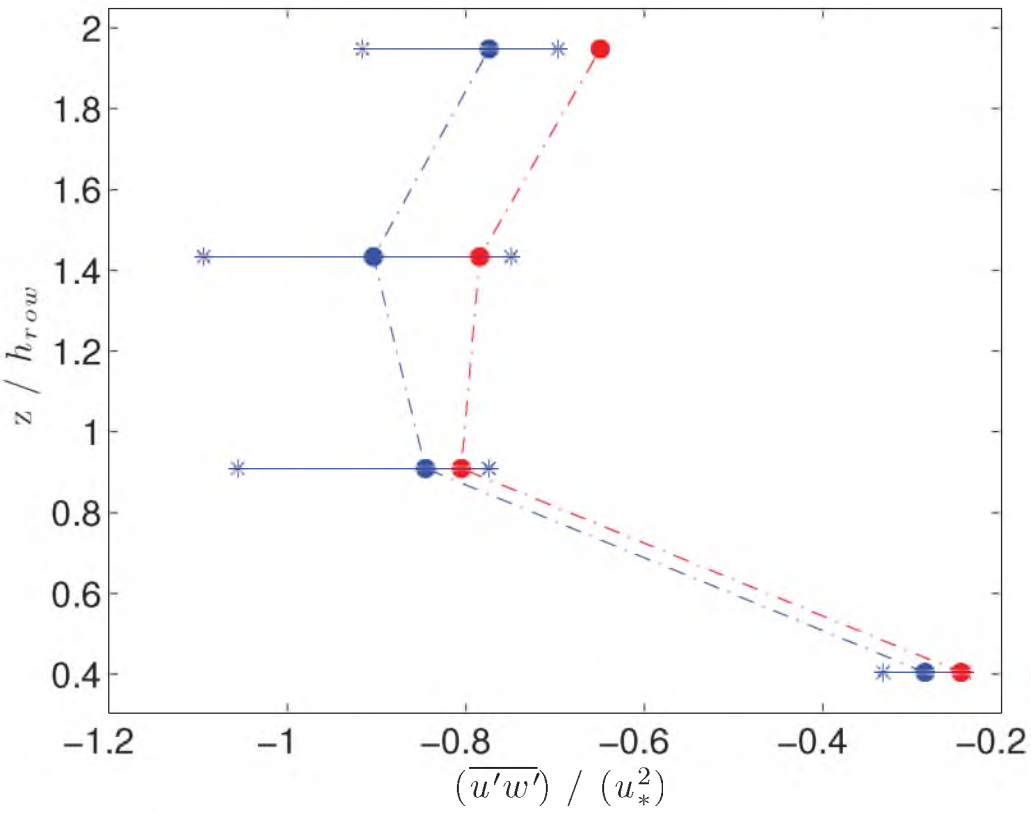

Figure 3.26. Vertical kinematic eddy flux of U-momentum, $\overline{u'w'}$, normalized by u_*^2 vs. height of sonic, z, normalized by the height of the rows, h; (Along flow, $0 > \zeta > -1$). Red dots show mean of the data set, and the blue lines show the 25^{th}, 50^{th}, and 75^{th} percentiles.

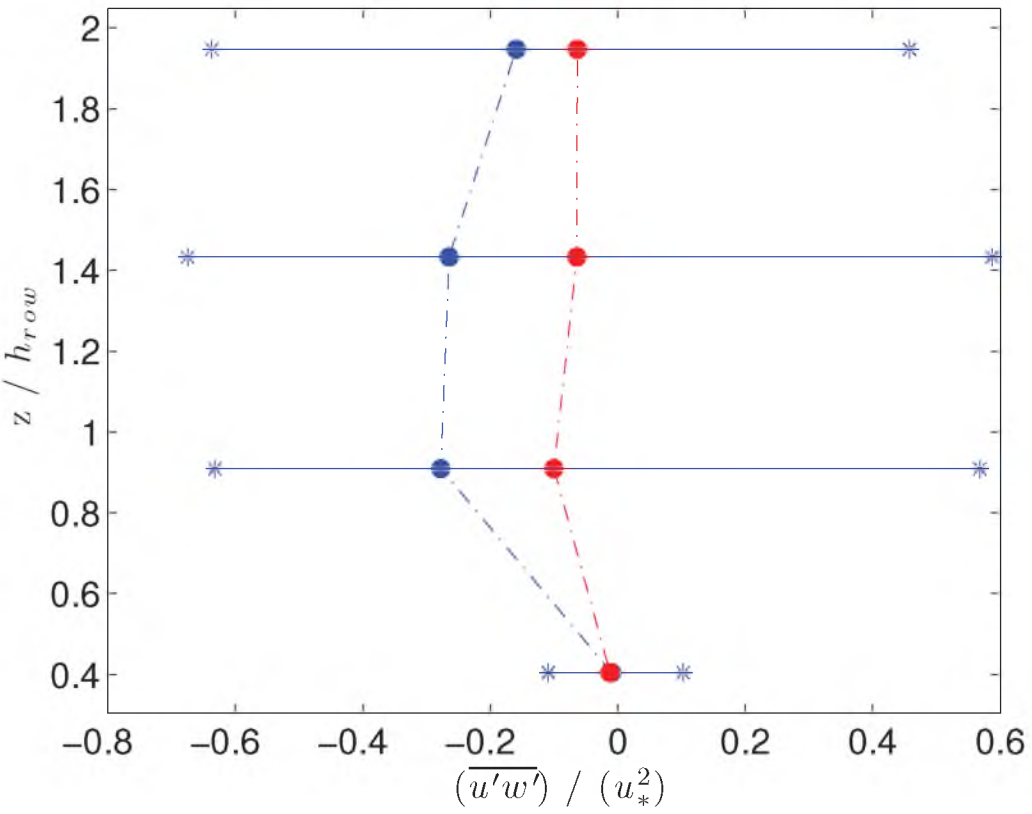

Figure 3.27. Vertical kinematic eddy flux of U-momentum, $\overline{u'w'}$, normalized by u_*^2 vs. height of sonic, z, normalized by the height of the rows, h; (cross flow, $0 > \zeta > -1$). Red dots show mean of the data set, and the blue lines show the 25^{th}, 50^{th}, and 75^{th} percentiles.

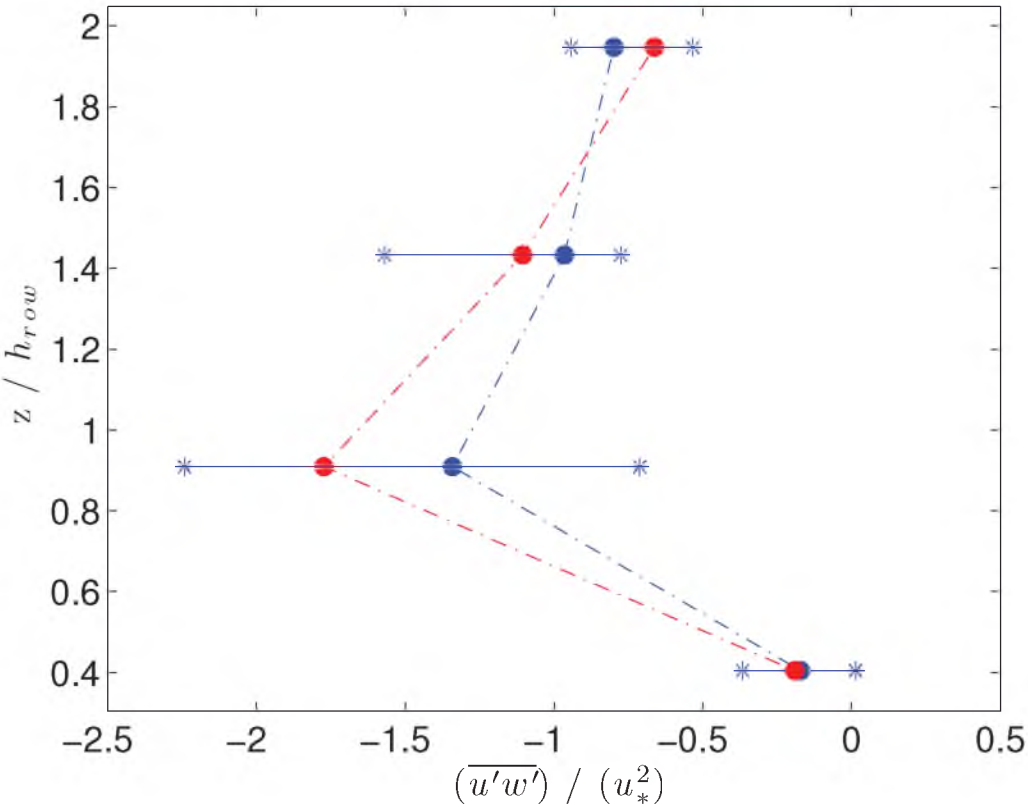

Figure 3.28. Vertical kinematic eddy flux of U-momentum, $\overline{u'w'}$, normalized by u_*^2 vs. height of sonic, z, normalized by the height of the rows, h; (along flow, $-1 > \zeta$). Red dots show mean of the data set, and the blue lines show the 25^{th}, 50^{th}, and 75^{th} percentiles.

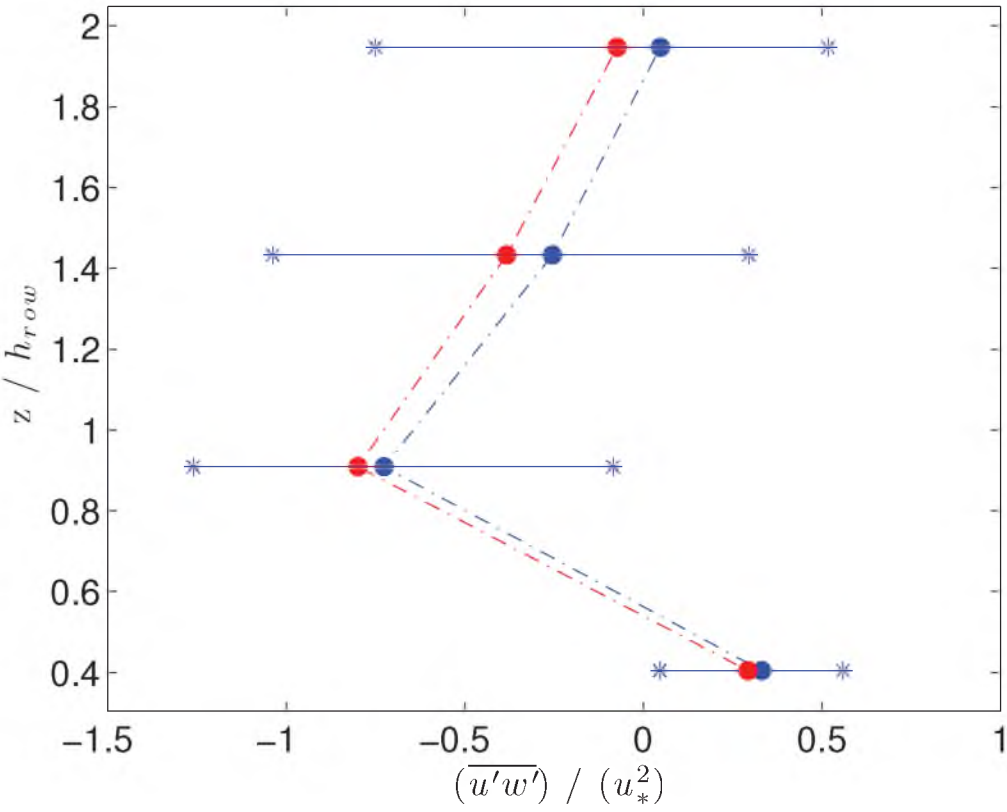

Figure 3.29. Vertical kinematic eddy flux of U-momentum, $\overline{u'\,w'}$, normalized by u_*^2 vs. height of sonic, z, normalized by the height of the rows, h; (cross flow, $-1 > \zeta$). Red dots show mean of the data set, and the blue lines show the 25^{th}, 50^{th}, and 75^{th} percentiles.

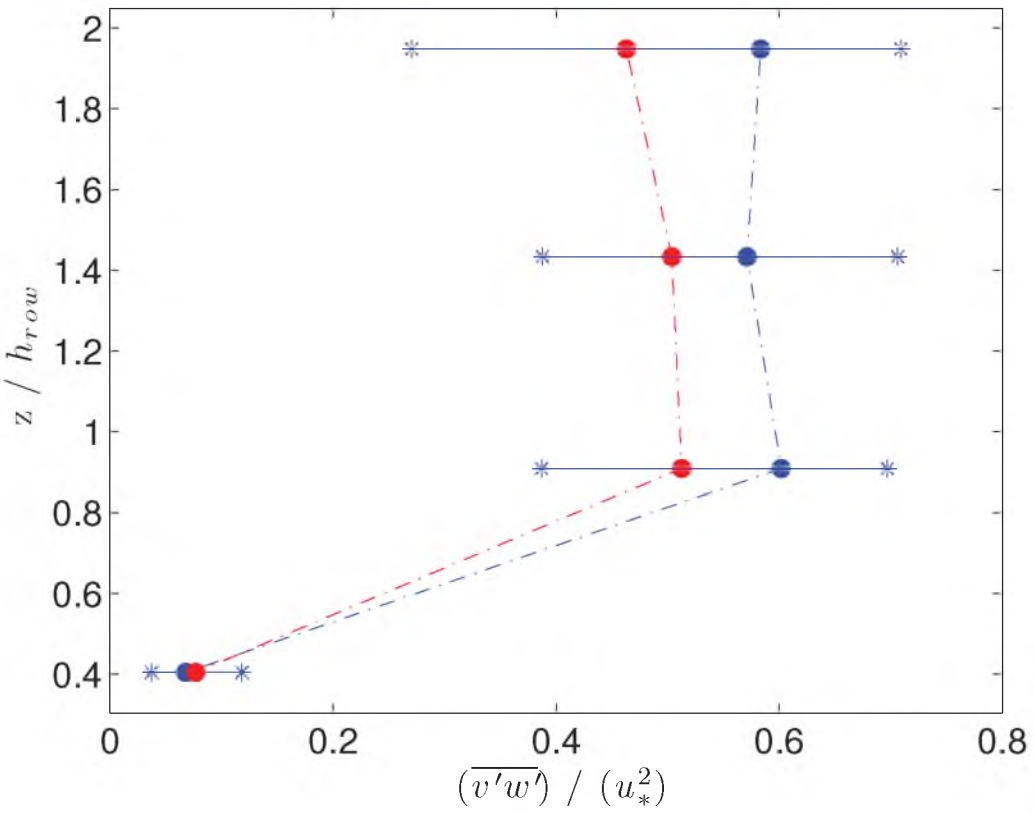

Figure 3.30. Vertical kinematic eddy flux of U-momentum, $\overline{v'w'}$, normalized by u_*^2 vs. height of sonic, z, normalized by the height of the rows, h; (Along flow, $0 > \zeta > -1$). Red dots show mean of the data set, and the blue lines show the 25^{th}, 50^{th}, and 75^{th} percentiles.

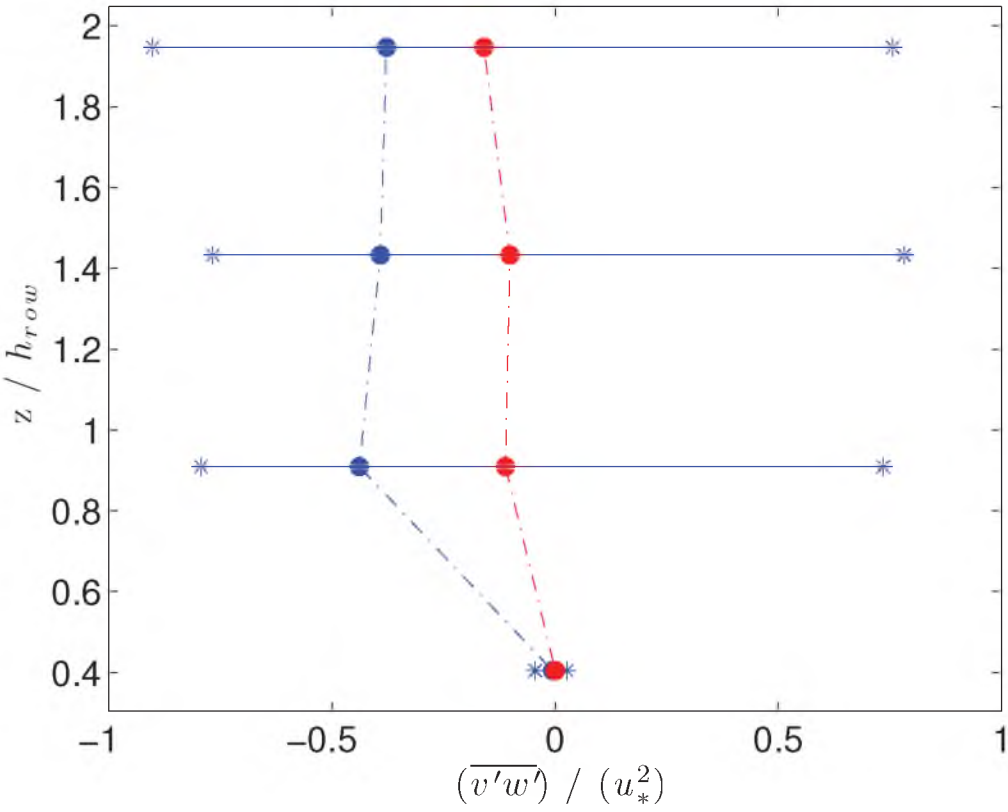

Figure 3.31. Vertical kinematic eddy flux of U-momentum, $\overline{v'w'}$, normalized by u_*^2 vs. height of sonic, z, normalized by the height of the rows, h; (cross flow, $0 > \zeta > -1$). Red dots show mean of the data set, and the blue lines show the 25^{th}, 50^{th}, and 75^{th} percentiles.

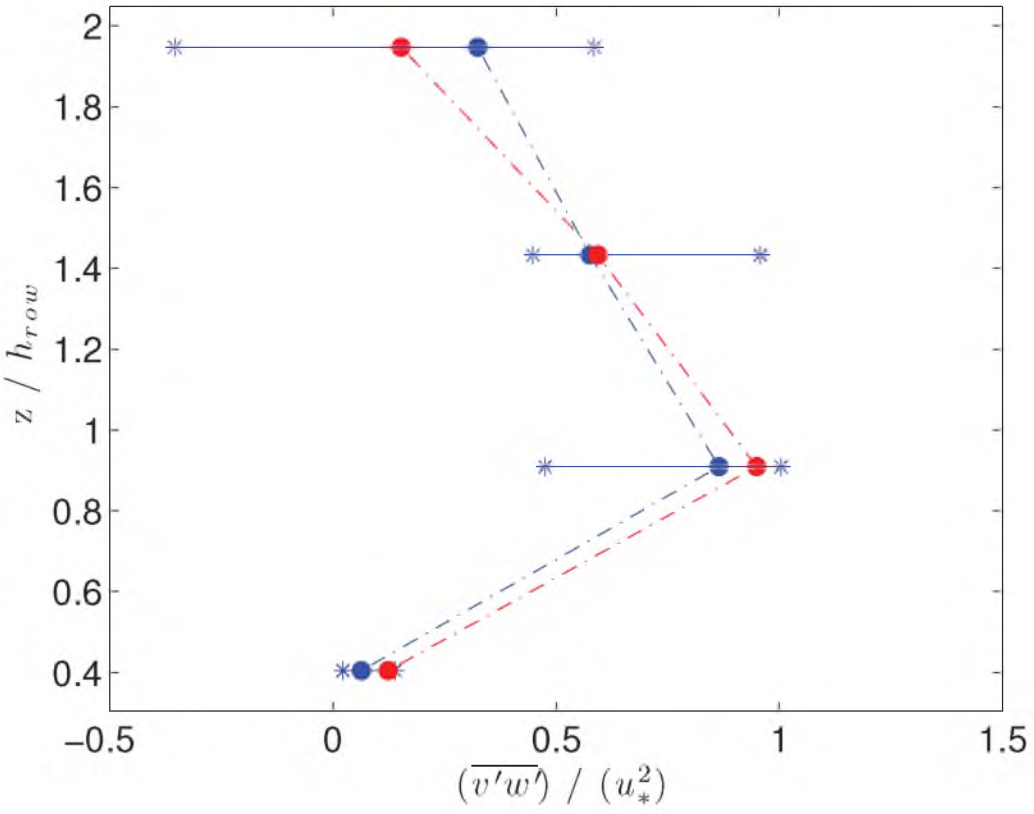

Figure 3.32. Vertical kinematic eddy flux of U-momentum, $\overline{v'\,w'}$, normalized by u_*^2 vs. height of sonic, z, normalized by the height of the rows, h; (along flow, $-1 > \zeta$). Red dots show mean of the data set, and the blue lines show the 25^{th}, 50^{th}, and 75^{th} percentiles.

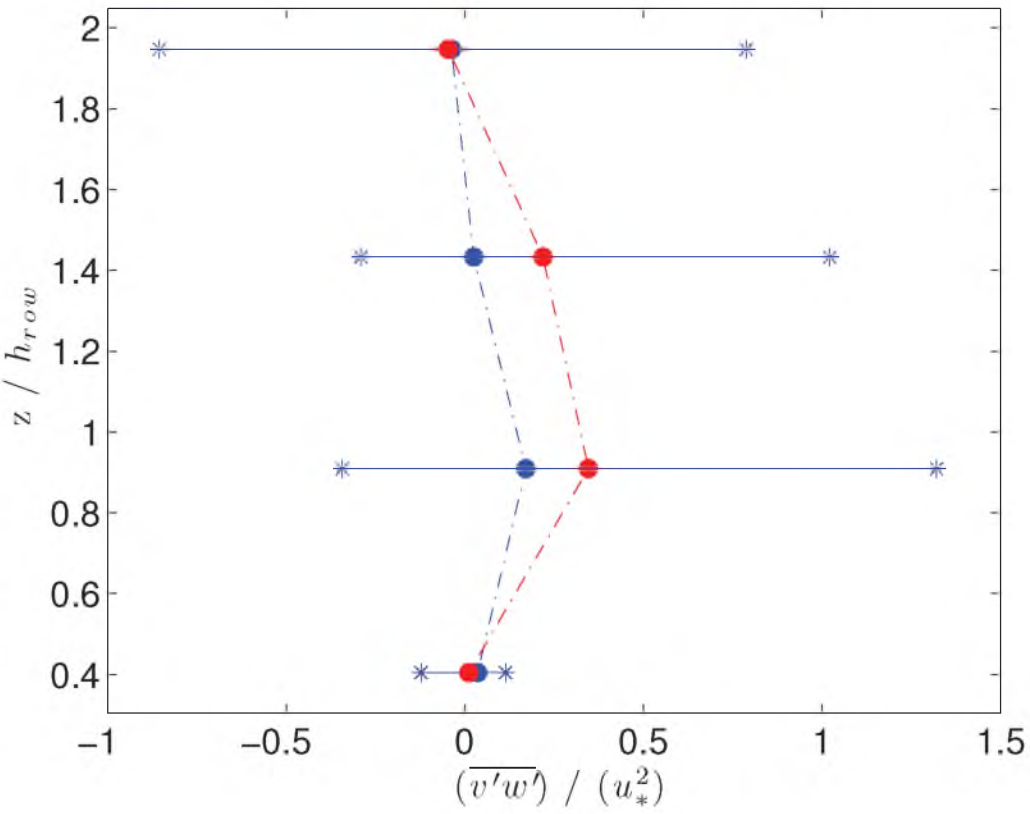

Figure 3.33. Vertical kinematic eddy flux of U-momentum, $\overline{v'\,w'}$, normalized by u_*^2 vs. height of sonic, z, normalized by the height of the rows, h; (cross flow, $-1 > \zeta$). Red dots show mean of the data set, and the blue lines show the 25^{th}, 50^{th}, and 75^{th} percentiles.

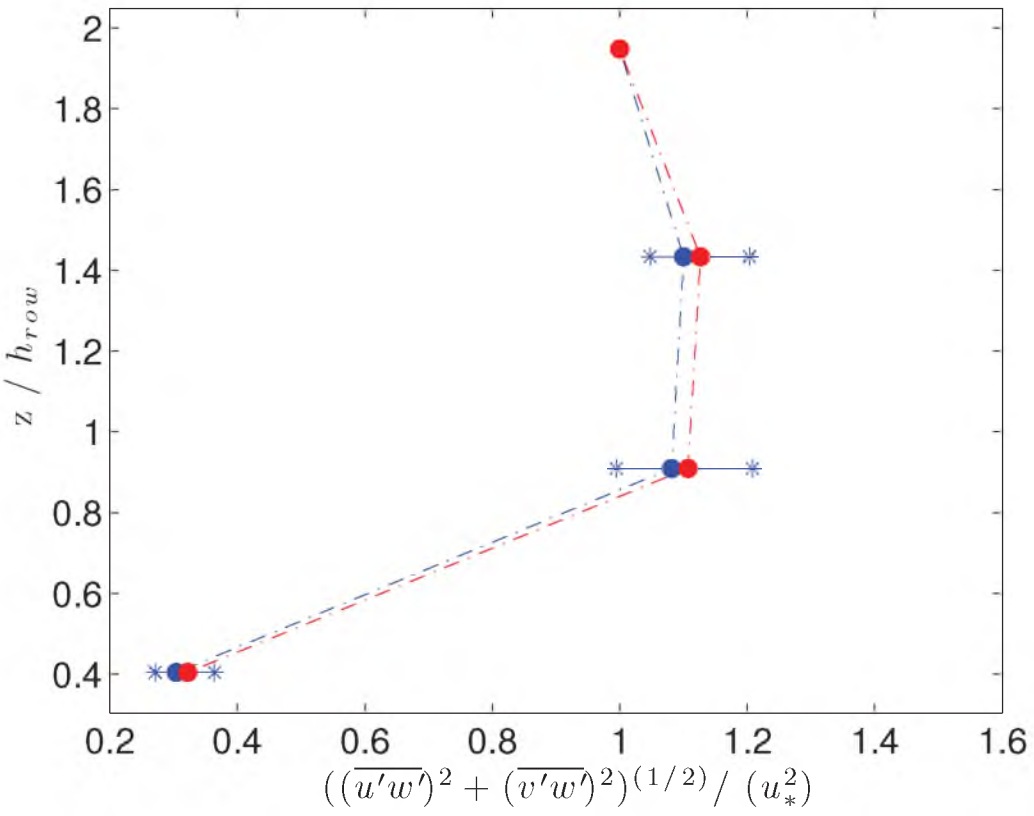

Figure 3.34. Vertical kinematic eddy flux of U-momentum, $\overline{u'\,w'}$ and $\overline{v'\,w'}$, normalized by u_*^2 vs. height of sonic, z, normalized by the height of the rows, h; (Along flow, $0 > \zeta > -1$). Red dots show mean of the data set, and the blue lines show the 25^{th}, 50^{th}, and 75^{th} percentiles.

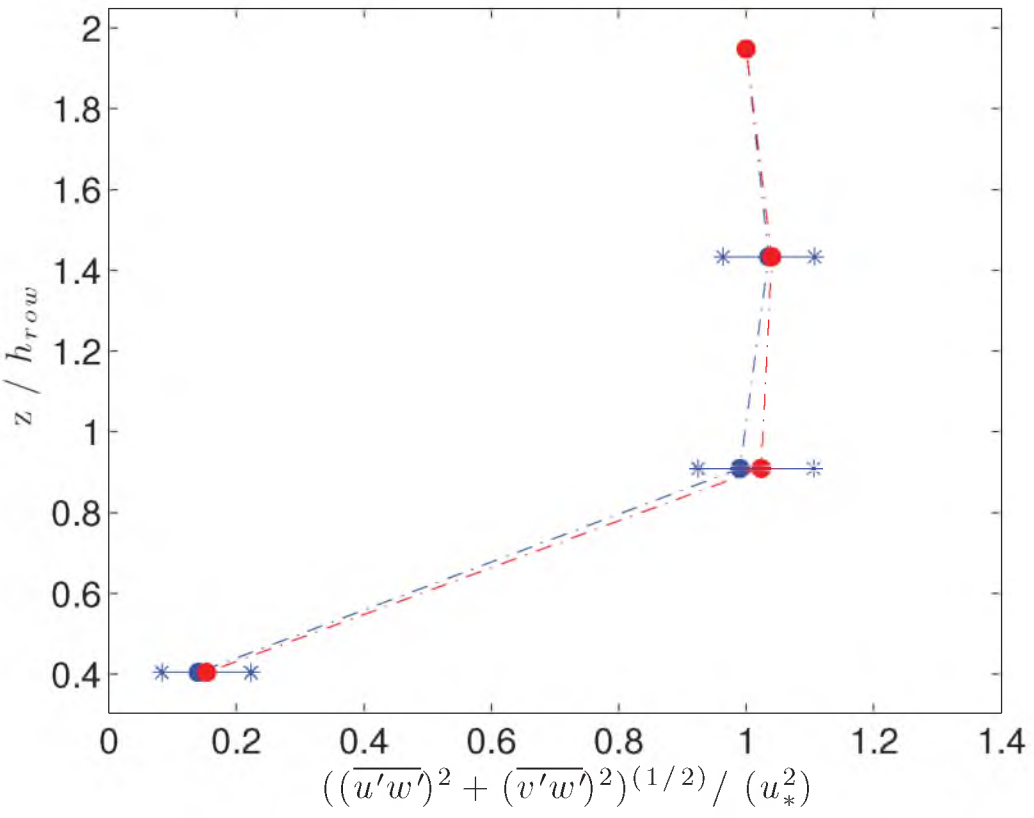

Figure 3.35. Vertical kinematic eddy flux of U-momentum, $\overline{u'\,w'}$ and $\overline{v'\,w'}$, normalized by u_*^2 vs. height of sonic, z, normalized by the height of the rows, h; (cross flow, $0 > \zeta > -1$). Red dots show mean of the data set, and the blue lines show the 25^{th}, 50^{th}, and 75^{th} percentiles.

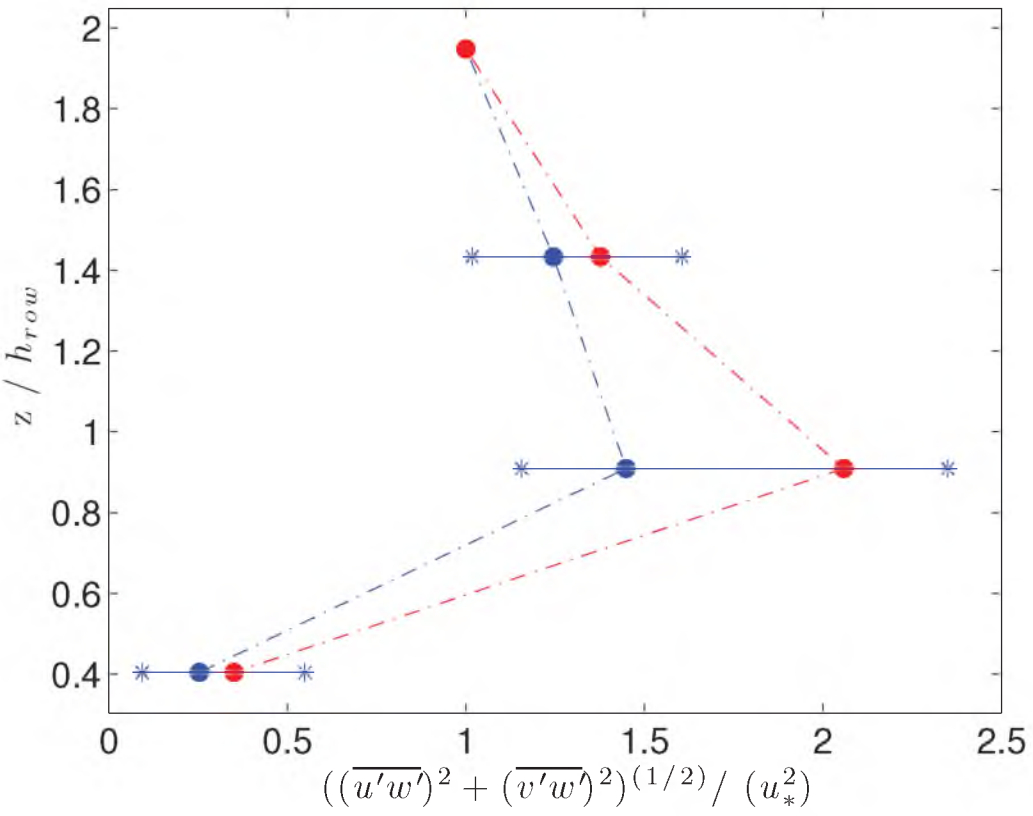

Figure 3.36. Vertical kinematic eddy flux of U-momentum, $\overline{u'\,w'}$ and $\overline{v'\,w'}$, normalized by u_*^2 vs. height of sonic, z, normalized by the height of the rows, h; (along flow, $-1 > \zeta$). Red dots show mean of the data set, and the blue lines show the 25^{th}, 50^{th}, and 75^{th} percentiles.

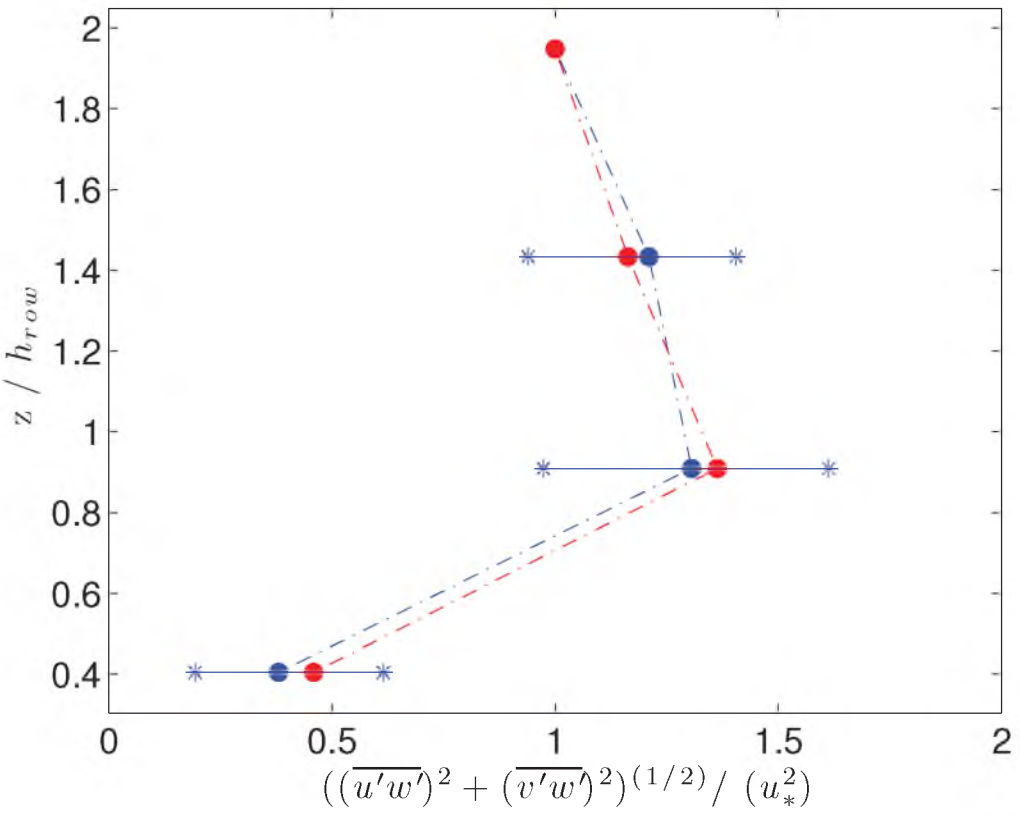

Figure 3.37. Vertical kinematic eddy flux of U-momentum, $\overline{u'\,w'}$ and $\overline{v'\,w'}$, normalized by u_*^2 vs. height of sonic, z, normalized by the height of the rows, h; (cross flow, $-1 > \zeta$). Red dots show mean of the data set, and the blue lines show the 25^{th}, 50^{th}, and 75^{th} percentiles.

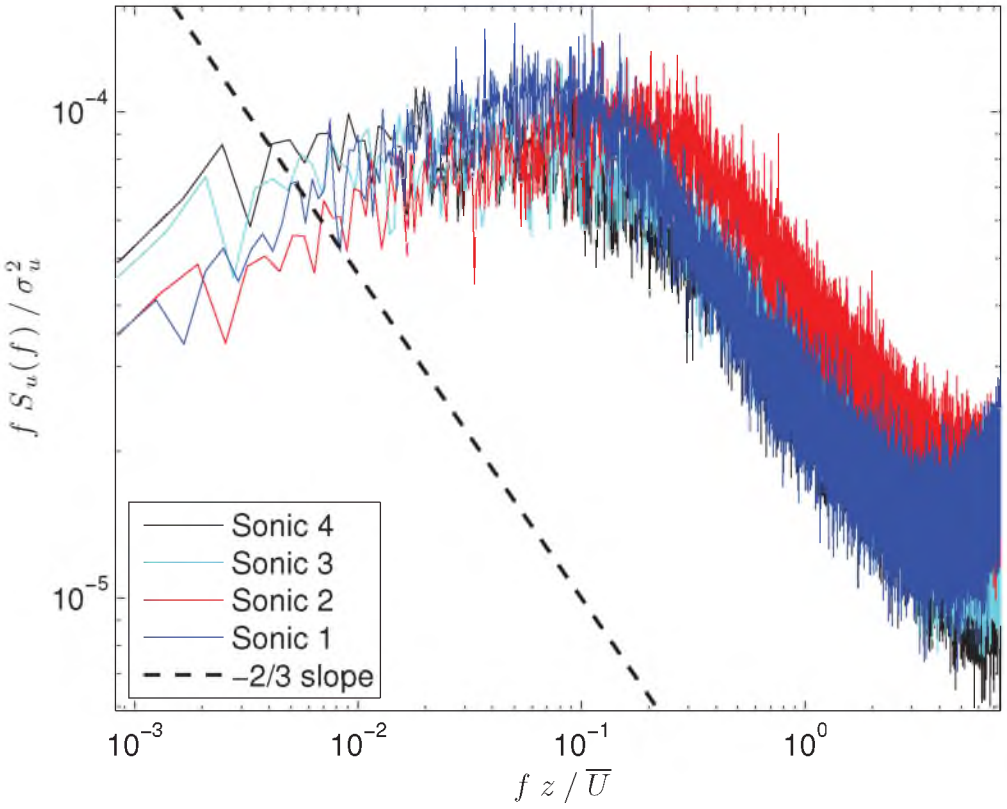

Figure 3.38. Spectra for u-component of wind. Sonic 1 was at a height of 0.8 m. Sonic 2 was at a height of 1.8 m. Sonic 3 was at a height of 2.9 m. Sonic 4 was at a height of 3.9 m; (Along flow, $0 > \zeta > -1$).

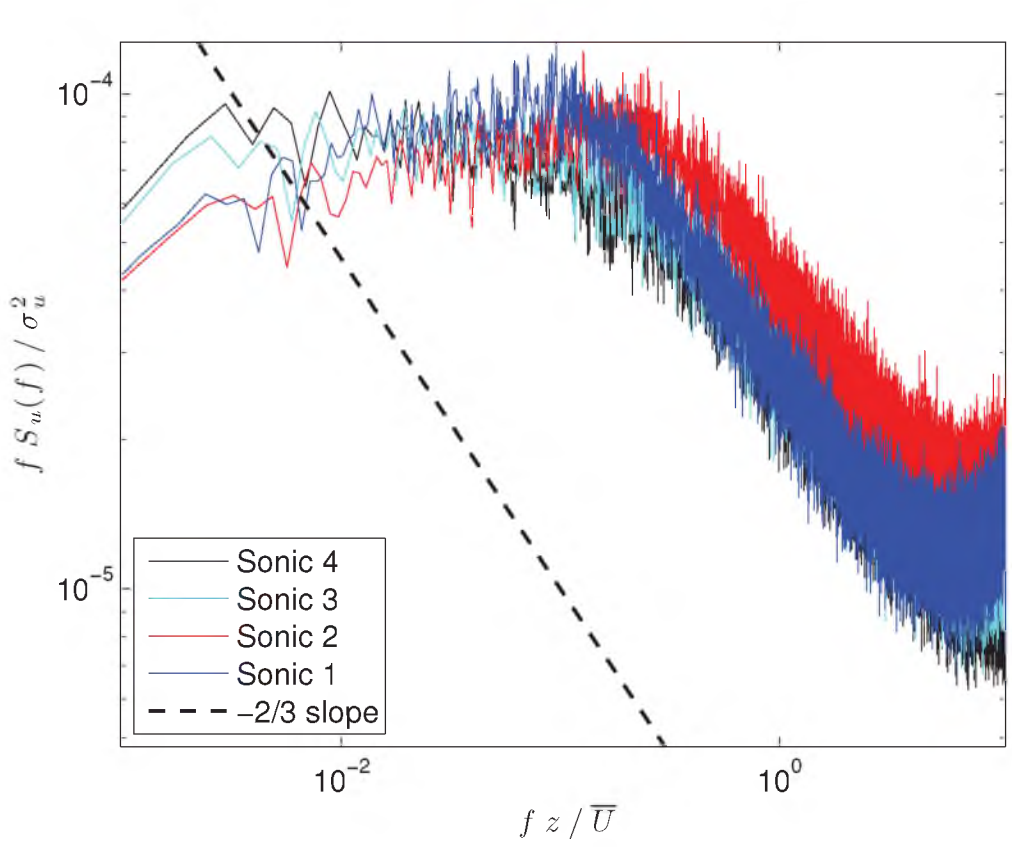

Figure 3.39. Spectra for u-component of wind. Sonic 1 was at a height of 0.8 m. Sonic 2 was at a height of 1.8 m. Sonic 3 was at a height of 2.9 m. Sonic 4 was at a height of 3.9 m; (cross flow, $0 > \zeta > -1$).

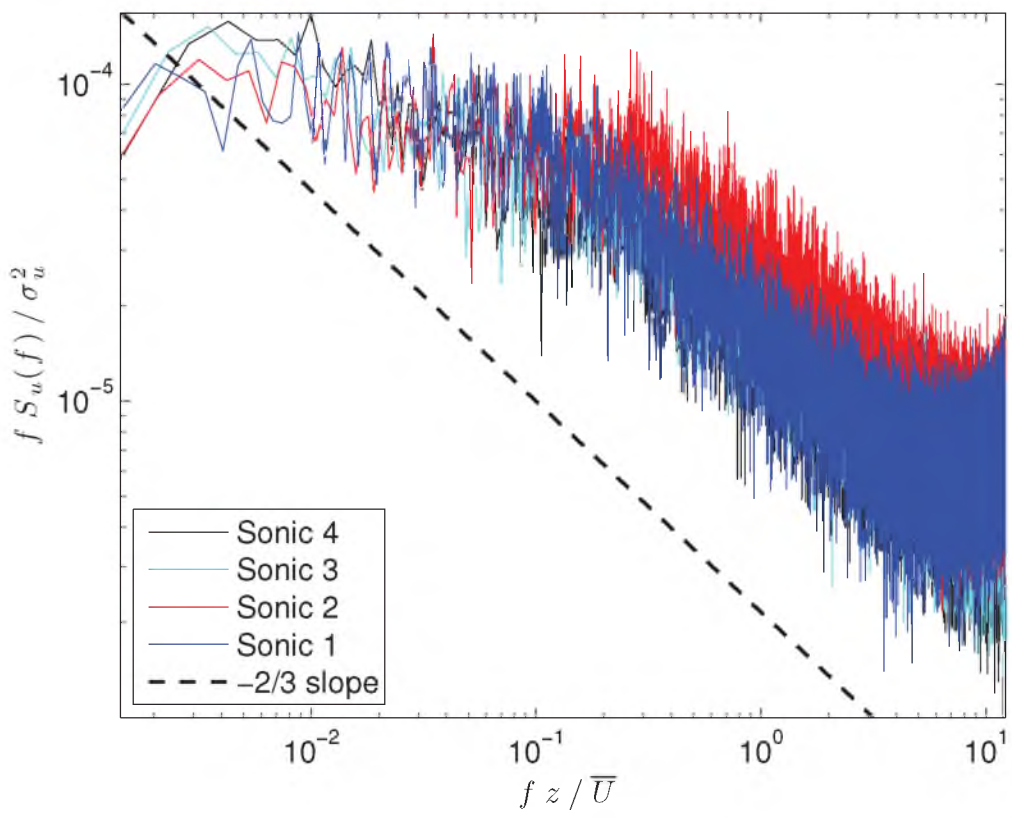

Figure 3.40. Spectra for u-component of wind. Sonic 1 was at a height of 0.8 m. Sonic 2 was at a height of 1.8 m. Sonic 3 was at a height of 2.9 m. Sonic 4 was at a height of 3.9 m; (along flow, $-1 > \zeta$).

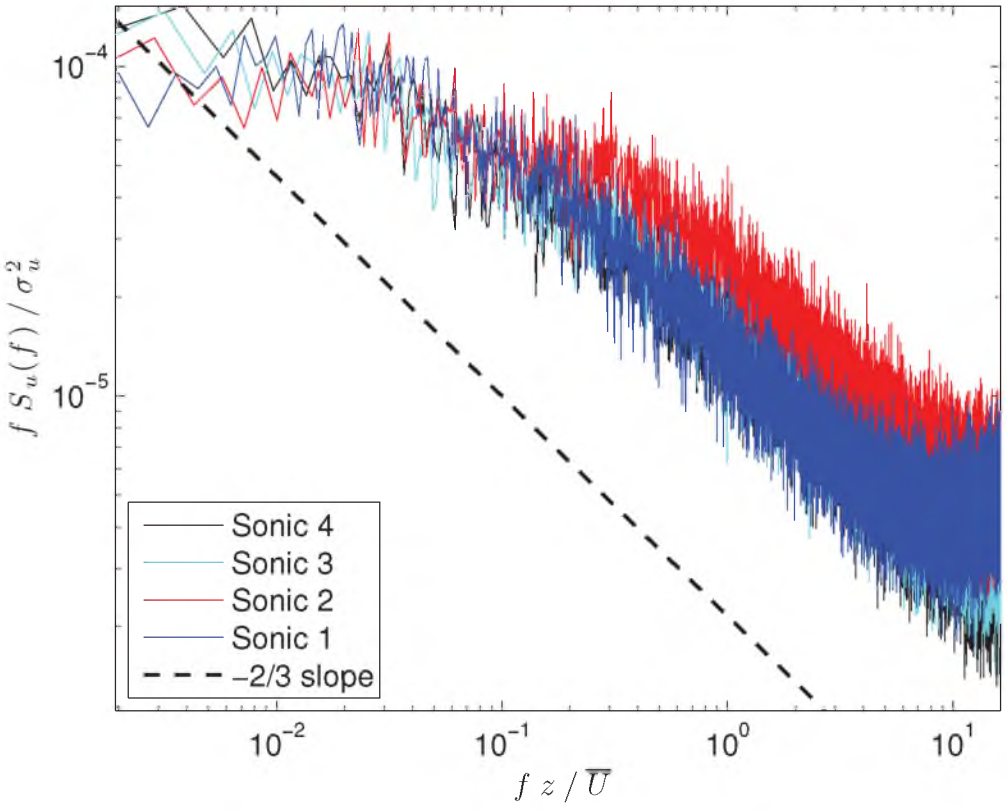

Figure 3.41. Spectra for u-component of wind. Sonic 1 was at a height of 0.8 m. Sonic 2 was at a height of 1.8 m. Sonic 3 was at a height of 2.9 m. Sonic 4 was at a height of 3.9 m; (cross flow, $-1 > \zeta$).

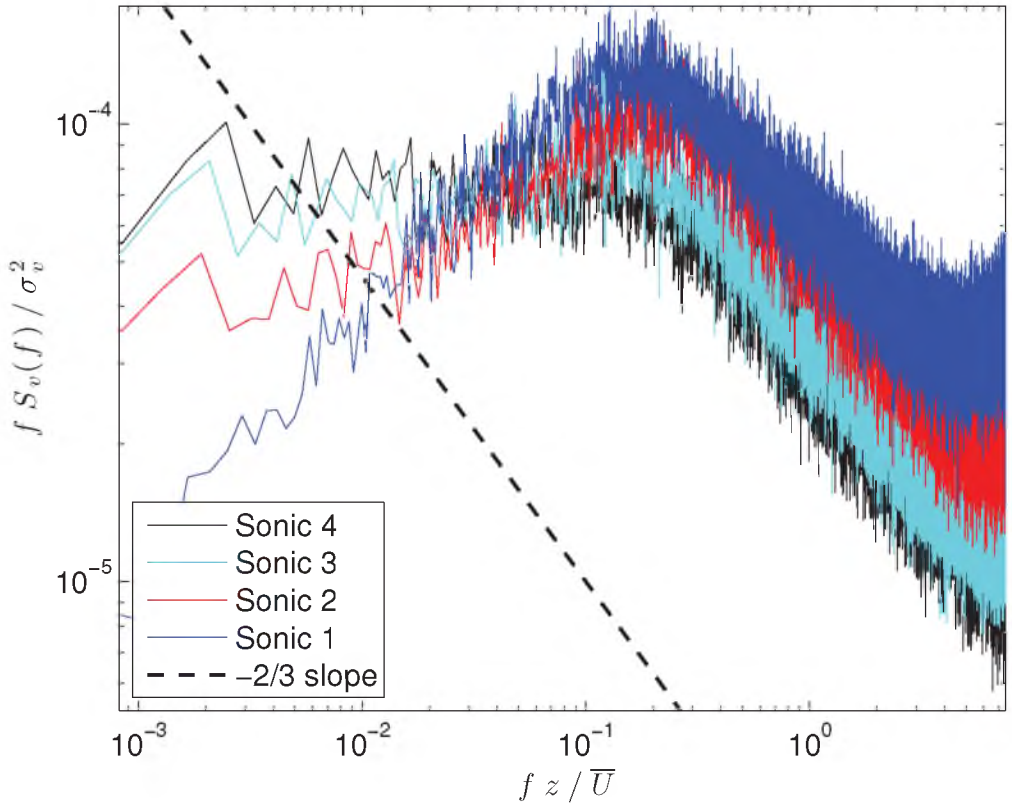

Figure 3.42. Spectra for v-component of wind. Sonic 1 was at a height of 0.8 m. Sonic 2 was at a height of 1.8 m. Sonic 3 was at a height of 2.9 m. Sonic 4 was at a height of 3.9 m; (Along flow, $0 > \zeta > -1$).

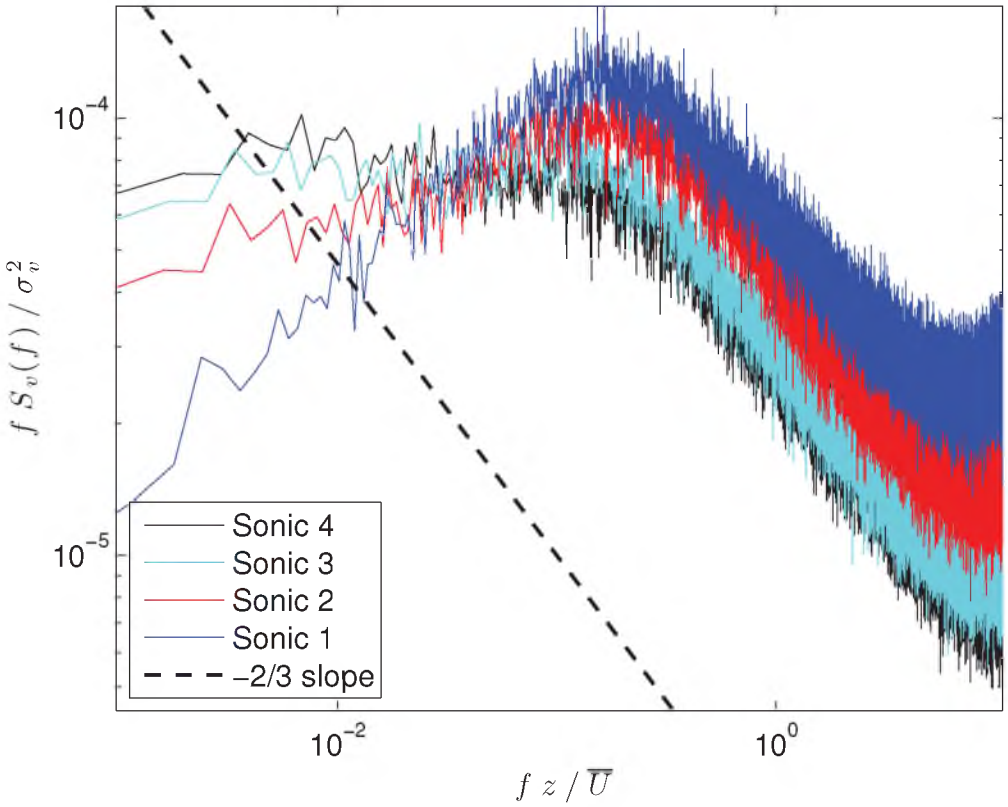

Figure 3.43. Spectra for v-component of wind. Sonic 1 was at a height of 0.8 m. Sonic 2 was at a height of 1.8 m. Sonic 3 was at a height of 2.9 m. Sonic 4 was at a height of 3.9 m; (cross flow, $0 > \zeta > -1$).

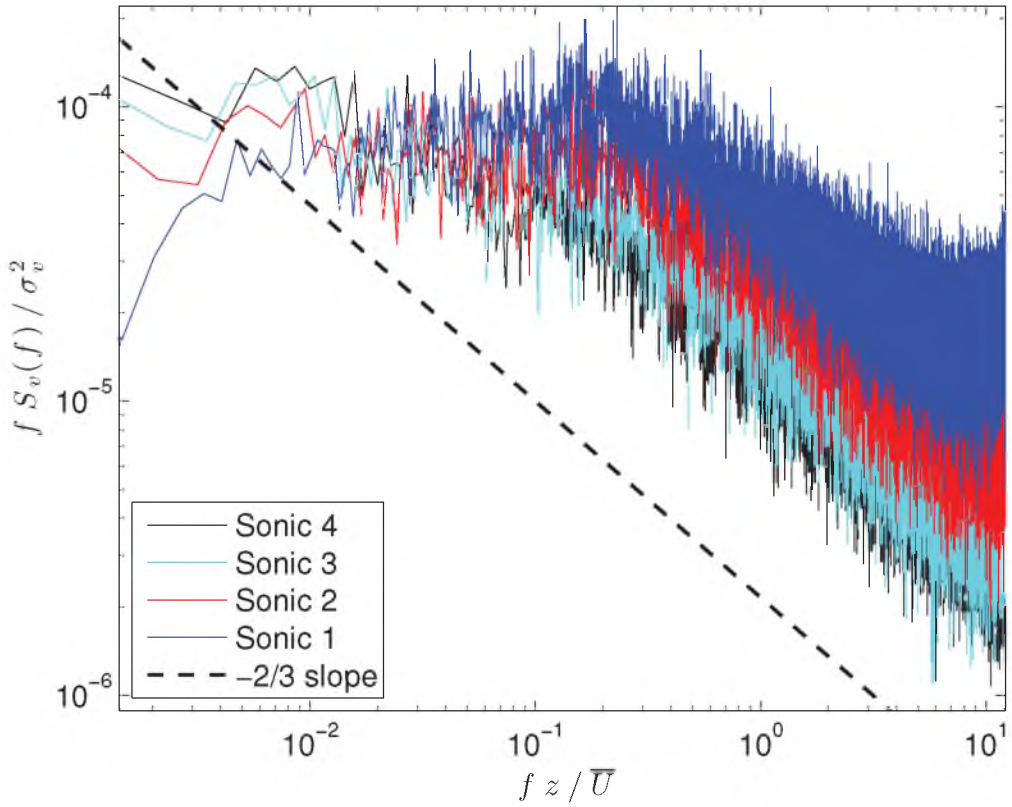

Figure 3.44. Spectra for v-component of wind. Sonic 1 was at a height of 0.8 m. Sonic 2 was at a height of 1.8 m. Sonic 3 was at a height of 2.9 m. Sonic 4 was at a height of 3.9 m; (along flow, $-1 > \zeta$).

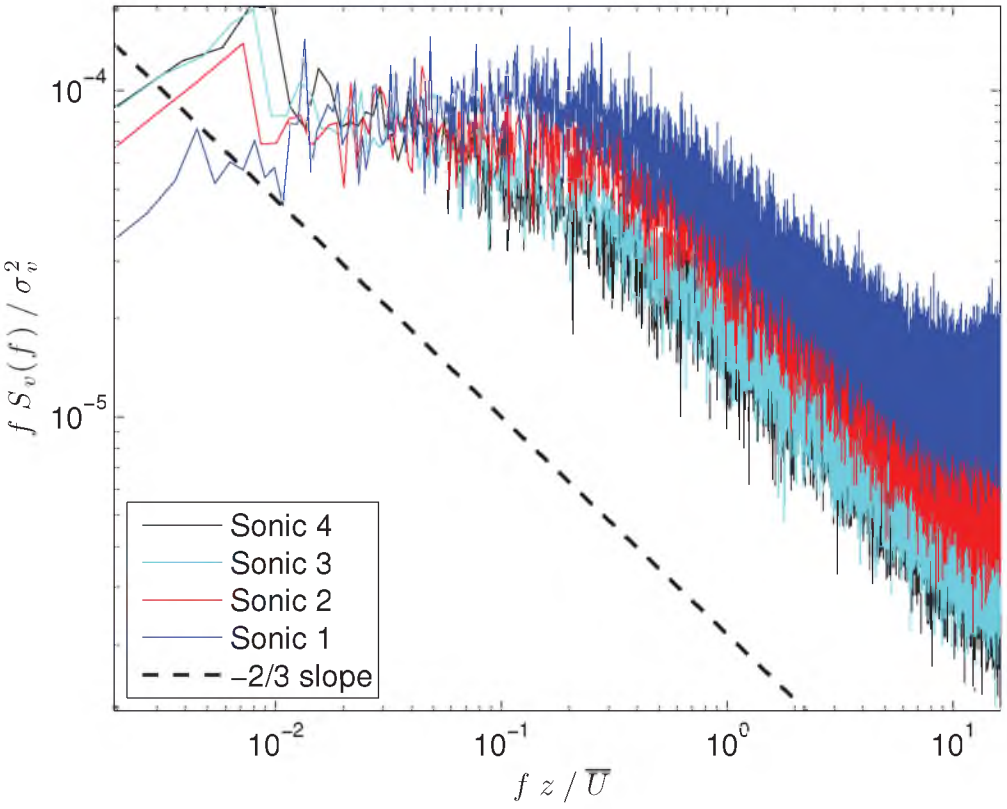

Figure 3.45. Spectra for v-component of wind. Sonic 1 was at a height of 0.8 m. Sonic 2 was at a height of 1.8 m. Sonic 3 was at a height of 2.9 m. Sonic 4 was at a height of 3.9 m; (cross flow, $-1 > \zeta$).

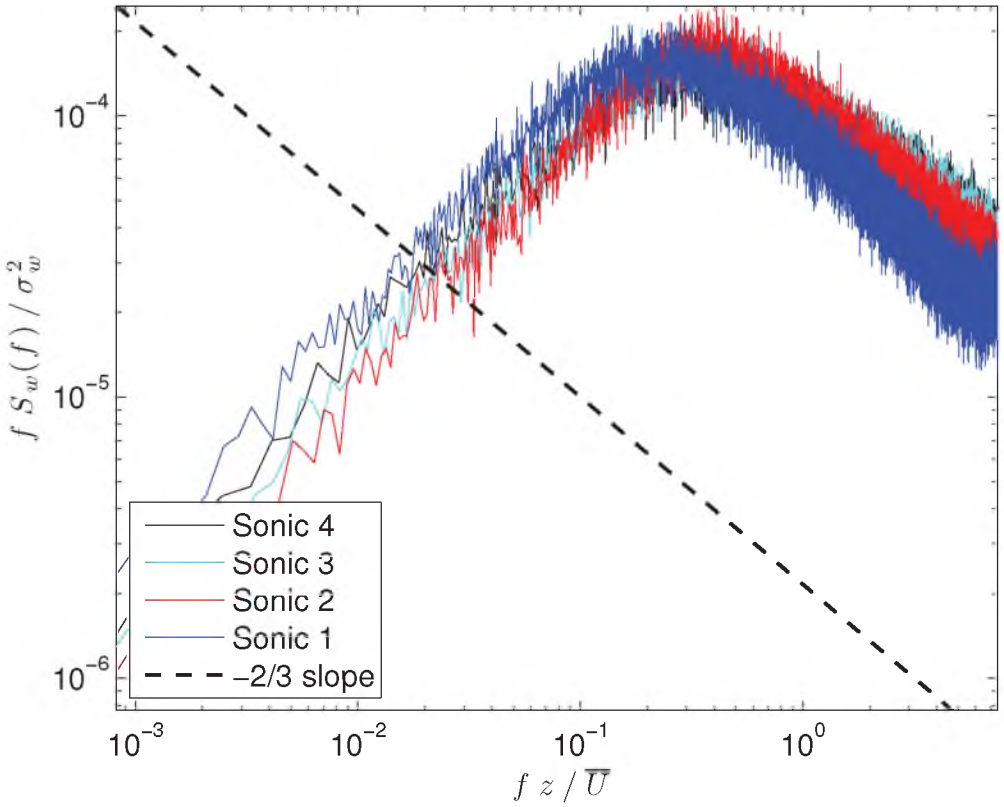

Figure 3.46. Spectra for w-component of wind. Sonic 1 was at a height of 0.8 m. Sonic 2 was at a height of 1.8 m. Sonic 3 was at a height of 2.9 m. Sonic 4 was at a height of 3.9 m; (Along flow, $0 > \zeta > -1$).

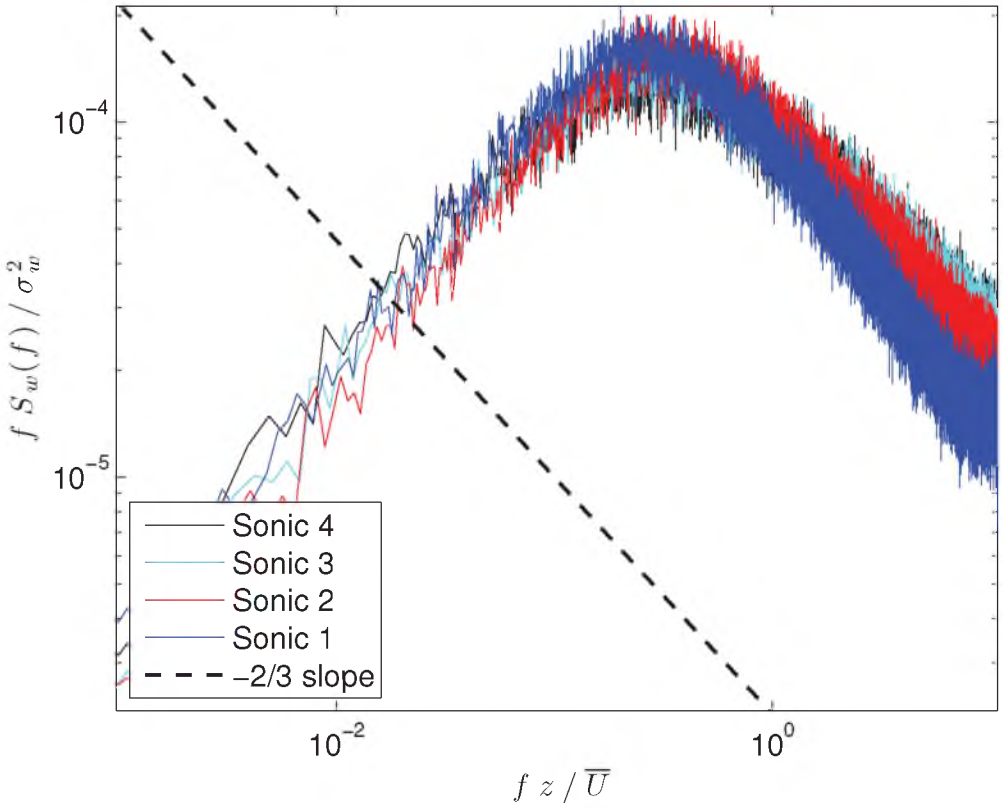

Figure 3.47. Spectra for w-component of wind. Sonic 1 was at a height of 0.8 m. Sonic 2 was at a height of 1.8 m. Sonic 3 was at a height of 2.9 m. Sonic 4 was at a height of 3.9 m; (cross flow, $0 > \zeta > -1$).

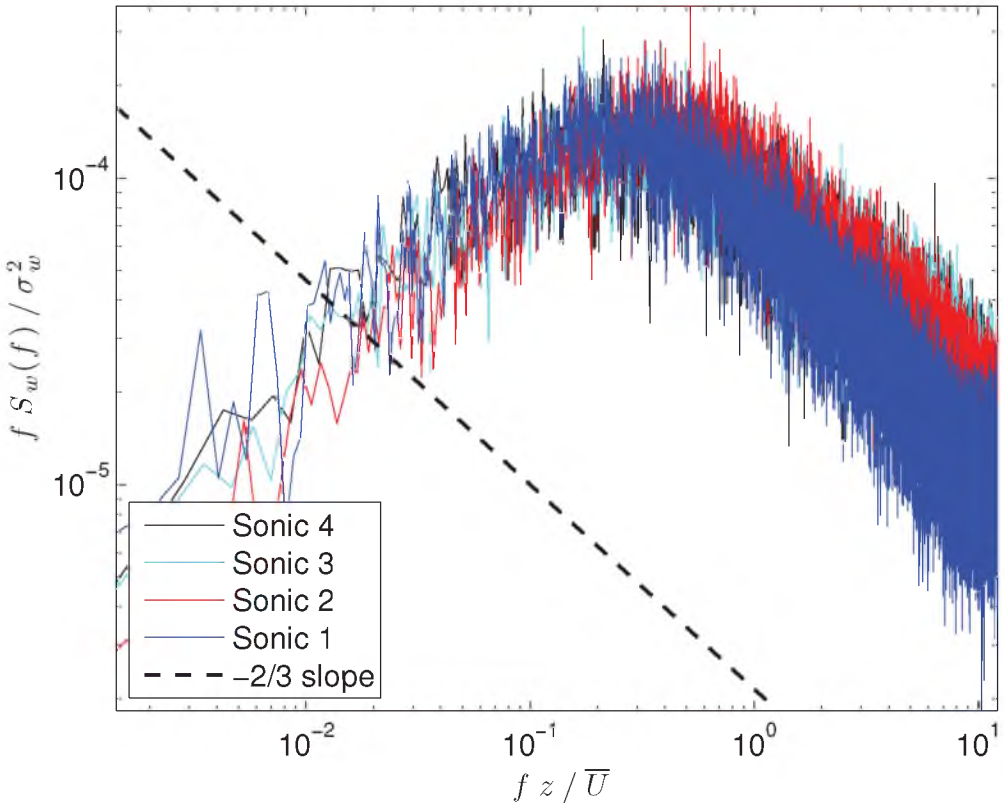

Figure 3.48. Spectra for w-component of wind. Sonic 1 was at a height of 0.8 m. Sonic 2 was at a height of 1.8 m. Sonic 3 was at a height of 2.9 m. Sonic 4 was at a height of 3.9 m; (along flow, $-1 > \zeta$).

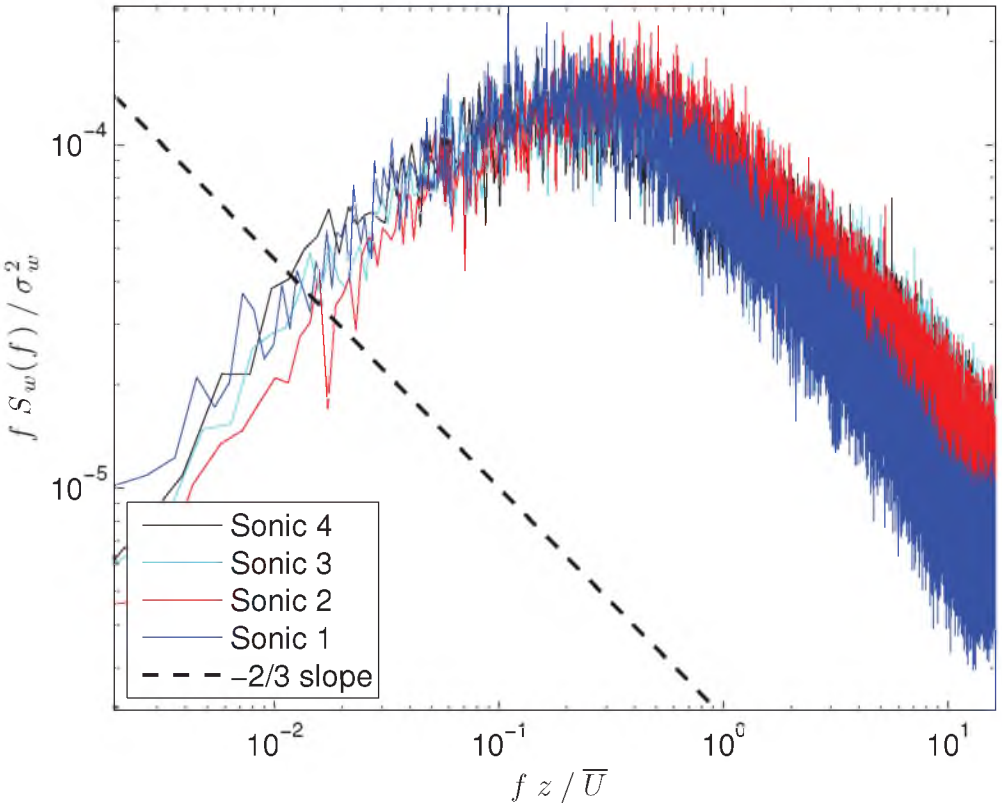

Figure 3.49. Spectra for w-component of wind. Sonic 1 was at a height of 0.8 m. Sonic 2 was at a height of 1.8 m. Sonic 3 was at a height of 2.9 m. Sonic 4 was at a height of 3.9 m; (cross flow, $-1 > \zeta$).

CHAPTER 4

PARTICLE SETUP

4.1 Particle Releases

In addition to the micrometeorological measurements collected during the field experiments, several particle release events were also performed. Two different types of particle release mechanisms were used to create sources within the grape vineyard. The first release mechanism was passive and injected particles at a single point using a gravity fed funnel system similar to [18], see Figures 4.1 and 4.2. The total mass of the particles was carefully measured before and after the release events to determine the amount of particles released. This release mechanism acted as a point source resulting in a three-dimensional dispersion plume. The three-dimensional nature of the plume makes this a challenging case for plume characterization. The second device sprayed a liquid particle mixture in a 2 m long line. The weight of the particles was carefully measured and then mixed with a specific volume of liquid to ensure a consistent amount of particles were released. The liquid quickly evaporated thus not effecting the particles path. The line source effectively results in a two-dimensional release due to the finite length of the spraying line. The advantage of this type of release is a wider initial plume increasing the likelihood that the roto-rod impaction trap arrays, will be correctly placed to capture the dispersion event. The disadvantage is a more complex dispersion plume. The release events lasted from 12 to 30 minutes depending on the amount of particles, which release device was used, and the prevailing winds.

4.2 Test Array

The impaction trap array was situated in the interior of the experimental site as to minimize edge effects. Five traps, placed vertically on top of each other, made an array. The traps were located at 3.7, 1.8, 1.3, 1.0 and 0.5 m above ground. See Figure 2.2. Particle dispersion was studied for two different flow fields: cross row

flow, and along row flow. The release and traps are all on the edge of the canopy to try to mimic both the release locations and how particles would be dispersed through the canopy structure. See Figures 4.2 and 4.3. Both release directions have 17 traps in the array (see Figures 4.4 and 4.5) at all five heights. The two release directions where chosen to illustrate the impact of the wind channeling observed in Figure 3.8 on the dispersion of heavy particles.

4.3 Particles

Powdery Mildew is a common occurrence in vineyards, so particles were chosen to have similar physical properties to the pathogen, but be inert as to not infect the crop. Both release devices utilized polyurethane particles, purchased from Cospheric, that had a mean diameter of 25 - 45 microns with a mean density of 1.04 g/cm^3. When the particles were lit with light that had a wavelength of 365 nm (black light) the particles fluoresced yellow. See Figure 4.6. This allowed the particles to be identified on the substrate of the roto-rod impaction traps without showing other particles that were collected on the substrate during the experiment.

4.4 Roto-Rod Impaction Traps

Particle concentration data were collected using roto-rod impaction traps placed in an array encompassing the expected near source particle distribution. See Figure 4.7. The roto-rod impaction trap consisted of a small direct current motor with an output shaft at approximately 2600 revolutions per minute. Connected to the shaft was a cross bar, roughly 7.5 cm long, that had a hole at each end. Substrates, roughly 3.5 cm long, were then inserted into the holes at the end of the cross bar. The cross bar was parallel to the ground of the vineyard, with the removable substrates vertical and above the cross bar and the motor vertical and below the cross bar. Each substrate had a thin coating of grease on the leading edge in order to improve impact efficiency of the particles as the motor spun the cross bar. The substrates were removed after each release event.

4.5 Particle Analysis

After the particles were release and captured on the roto-rod impaction traps, the substrates were removed and stored carefully, as not to affect the particles that were collected. In order to streamline the quantification of the particles captured on the traps, a program in MatLAB was written.

The rods were magnified and a picture was taken of them. See Figure 4.8. The pictures were then imported in MatLAB and transformed from color to black and white, as shown in Figure 4.9, to show better contrast to identify the particles. In addition Figure 4.10 the label for magnification was removed, so that the program would not count the label as particles as well.

Once the image was converted to black and white and the label removed, the particle count analysis was started. The black to white scale included various shades of grey. A built in function in MatLAB determined the threshold to determine at what level grey would be considered white or black. This allowed for every pixel to be converted into a binary form. See Figure 4.10. This binary form facilitated individual particle identification improving the particle count accuracy. See Figure 4.11. The problem with the image analysis is how to deduce what is a particle and what is a clumping of particles. This is where the "halo affect" spoke of earlier comes into play. As seen in the large grouping of particles were several particles were touching, the binary sees that clump as one particle. Whereas the smaller amount of particles can more accurately portray the individual particles. This means that the substrates with low amounts of particles are more accurately accounted for, and the traps with high number of particles under predicted the amount of particles actually on the substrate.

It was accepted that there would be errors associated with the ability of the program to read the rods correctly. A release event was counted manually and then compared to how the program performed. For low counts of particles the program was accurate, but for high counts of particles the program under predicted how many particles were present. This was due to how the particles fluoresced. When illuminated the particles produced an aura causing a "halo affect" on each particle. It made it hard for the program to differentiate between several particles in close proximity. Also, as the density of the particles increased it made it difficult for the

program to be able to tell where one particle ended and where the other particle began.

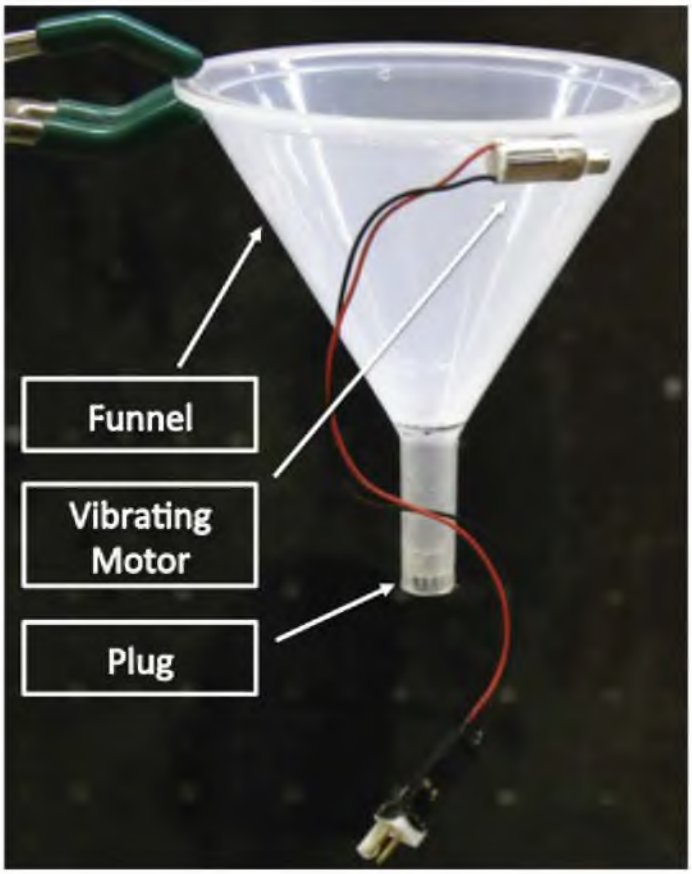

Figure 4.1. Particle point release device. The funnel holds a reservoir of particles. There is a plug at the end of the stem to control the amount of particles being released. At the top of the funnel is a vibrating motor that causes particles to be released.

Figure 4.2. The funnel release mechanism is in the center of the photo. It uses a vibrating motor to oscillate particles out of a small orifices in the bottom of the funnel.

Figure 4.3. Roto-rod impaction traps assembled into arrays throughout the vineyard. The traps are situated to be on the edge of the row.

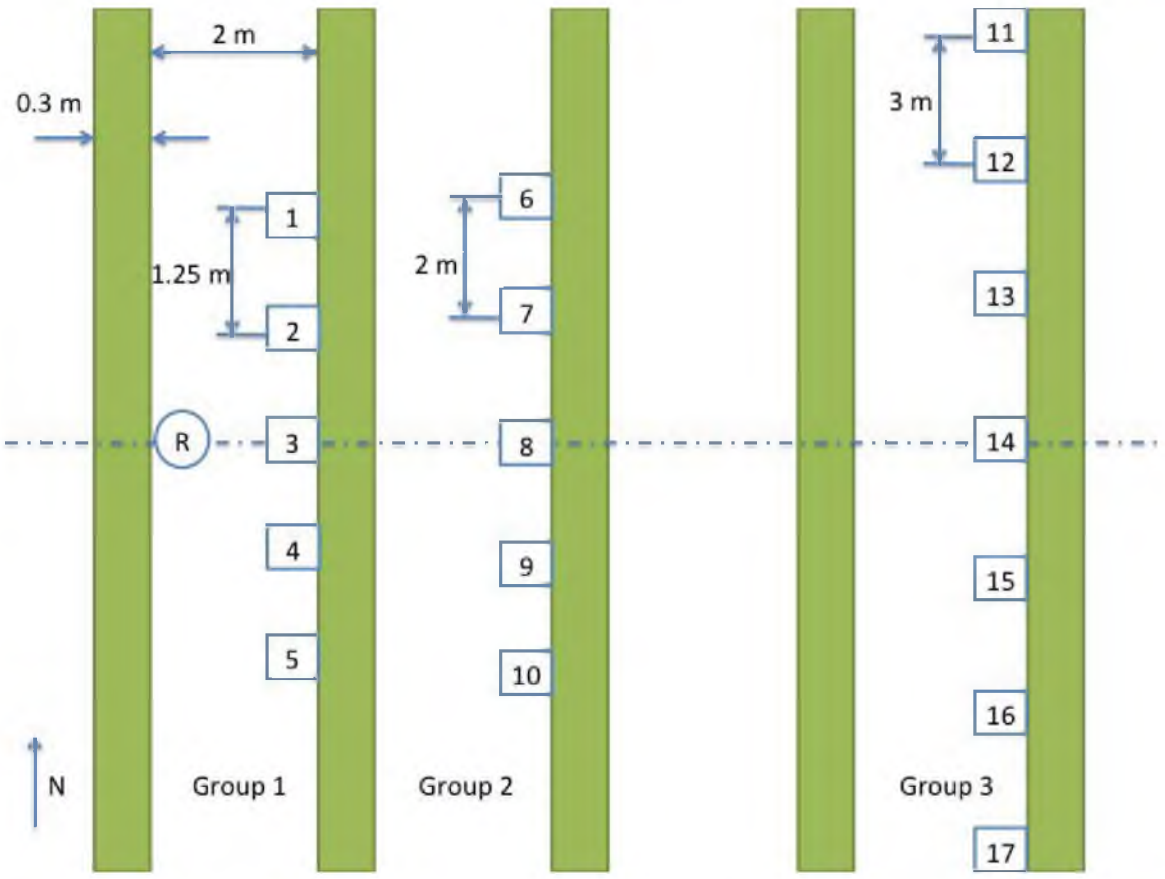

Figure 4.4. The setup for all cross flow experiments *(top view)*. The trap arrays were divided into three groups according to their distance downstream from the release point. The release point and the center trap array from each group are on the center line represented by the dashed line. Each group had different spacing in between the trap arrays in order to capture as many particles as possible from the release device. *(Not drawn to scale)*

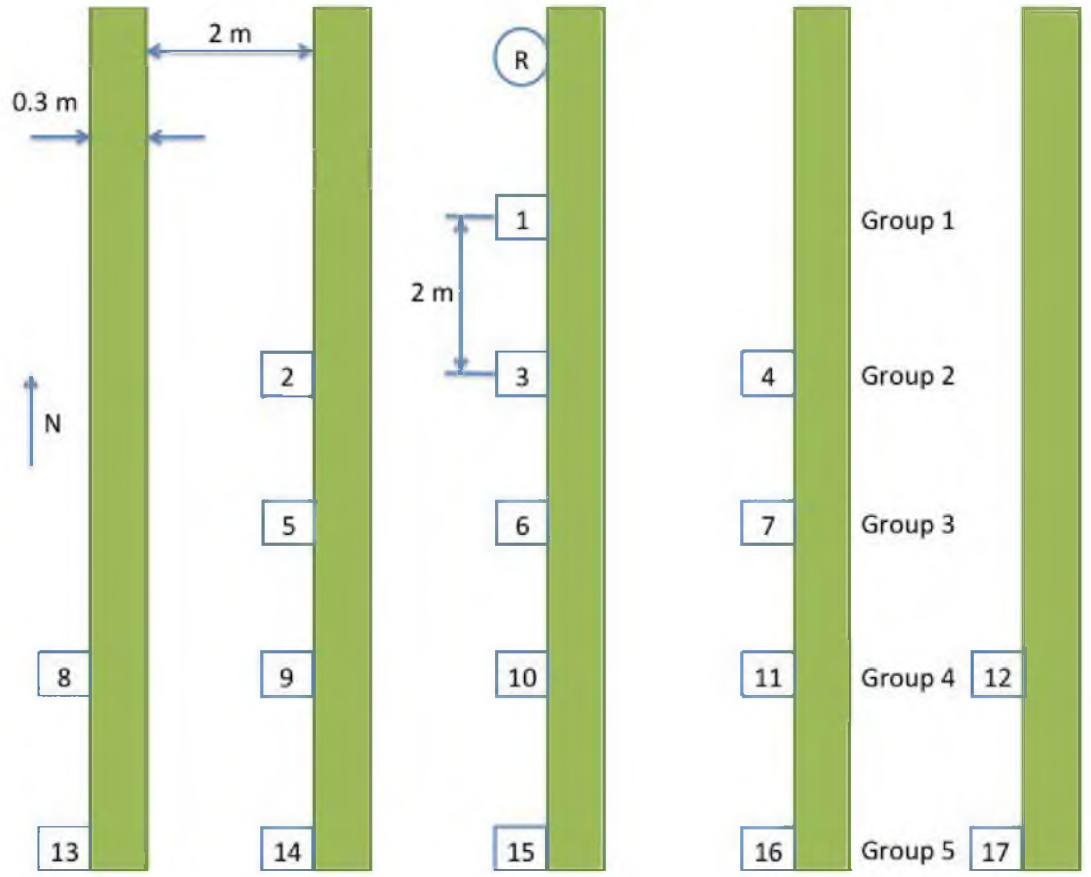

Figure 4.5. The setup for all along flow experiments *(top view)*. The trap array's were divided into five groups according to their distance downstream from the release point. The release point and center trap array from each group are aligned. All trap arrays are spaced by 2 m downstream and are spaced by each row distance, roughly 2.3 m, laterally. *(Not drawn to scale)*

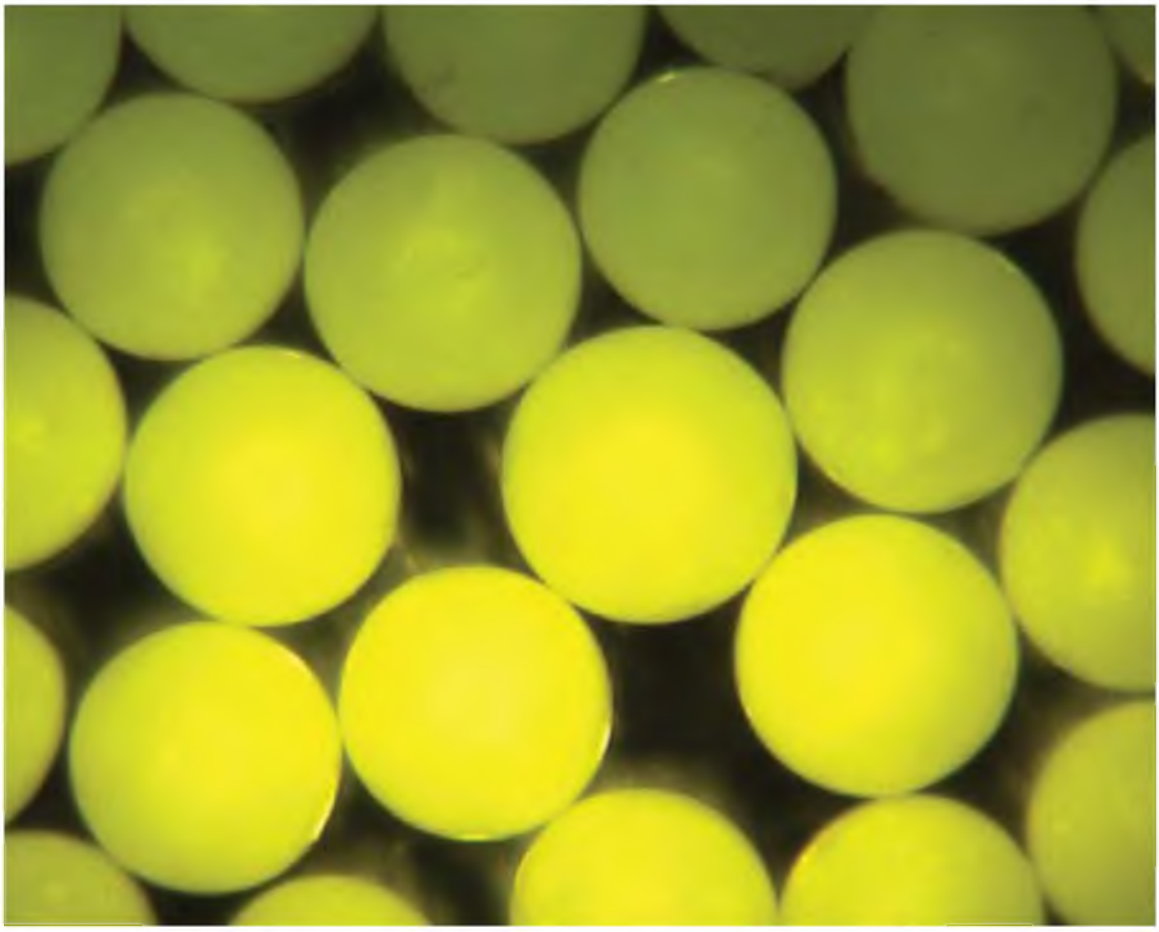

Figure 4.6. Magnified picture of the particles that were used in the release experiments. *Image taken from Cospheric's website*

Figure 4.7. A single roto-rod impaction trap in the canopy. The cross bar rotates on axis at high revolutions. The two vertical white polystyrene strips have been coated with a thin layer of grease, so that as the trap rotates particles are trapped.

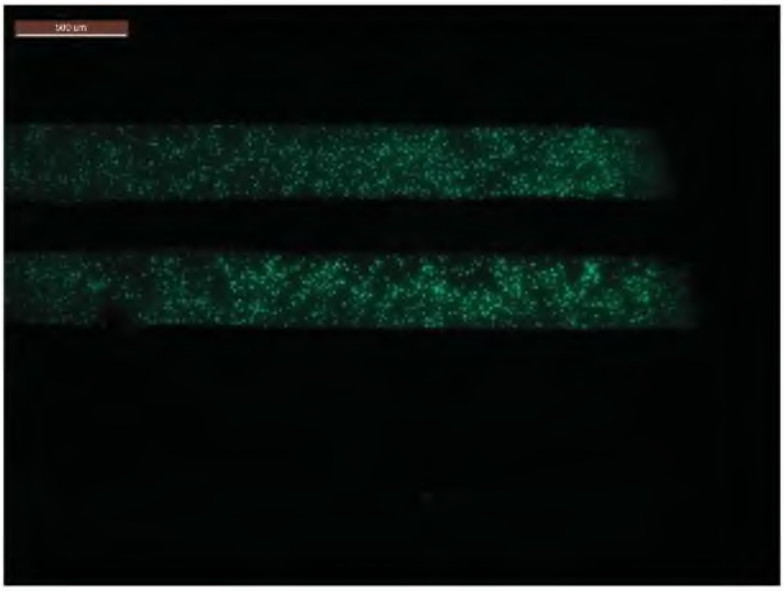

(A)

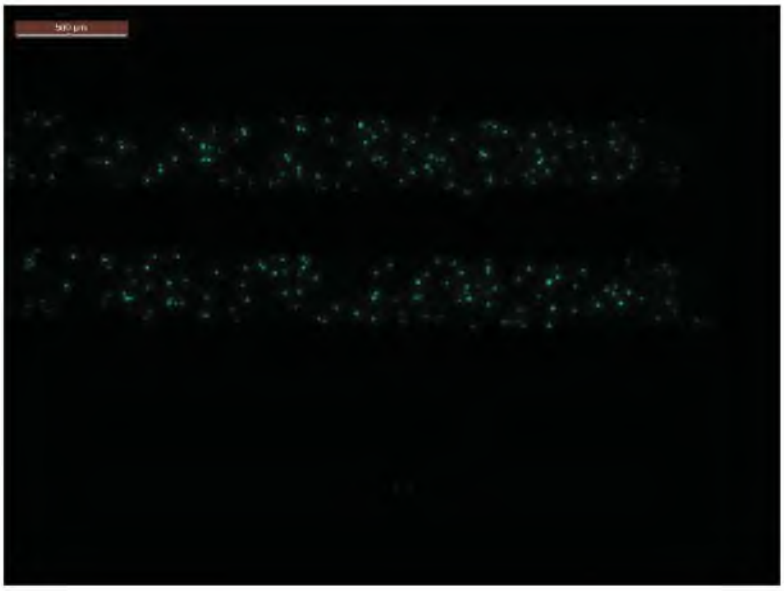

(B)

Figure 4.8. Original zoomed picture of the two removed substrates. Subplot *A* shows several thousand particles, subplot *B* shows a couple hundred particles.

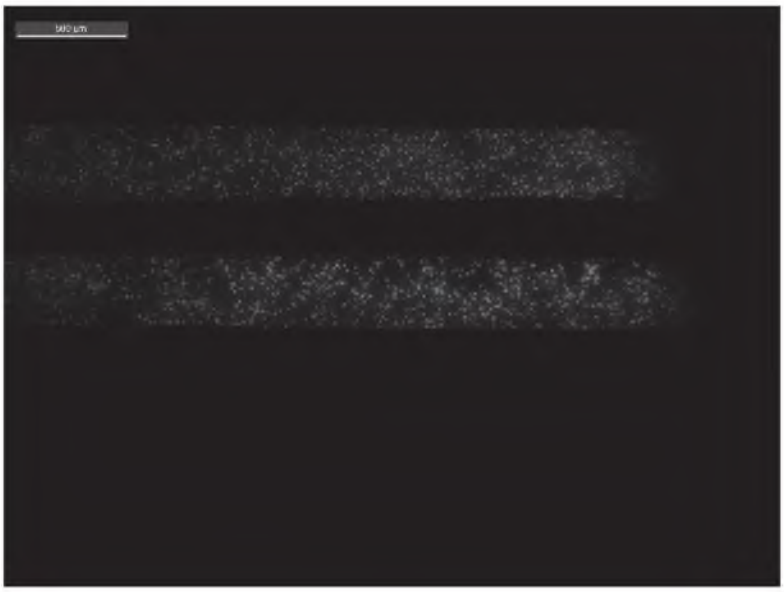

(A)

(B)

Figure 4.9. Black and white of zoomed picture of the two removed substrates. Subplot A shows several hundred particles, subplot B shows a couple of particles.

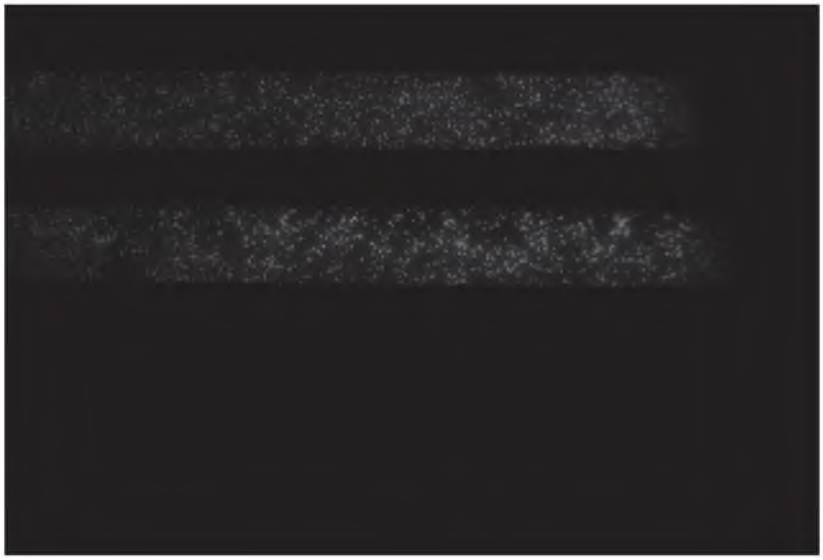

(A)

(B)

Figure 4.10. Cropped black and white zoomed picture of the two removed substrates. Subplot A shows several hundred particles, subplot B shows a couple of particles.

(A)

(B)

Figure 4.11. Binary version of zoomed picture of the two removed substrates. Subplot *A* shows several hundred particles, subplot *B* shows a couple of particles.

CHAPTER 5

PARTICLE TRANSPORT

The cross flow, Figure 4.4, was important to study because of the two predominant wind directions and its affect on particle transport. A total of six release events were conducted: three cross flow releases and three along flow releases. Table 5.1 shows the time of day the release started, the amount of particles released, and the release height for the six releases. Table 5.2 shows the trap setup, duration of release event, average wind speed for the release duration, average wind direction, the friction velocity, and atmospheric stability. All values were calculated using the highest sonic. Release 5 was during the early evening transition resulting in a positive Obukhov length. The other release events occurred during weakly convective ($-0.01 > \zeta > -1$) time periods.

5.1 Vertical Concentrations

The vertical concentrations for each trap array show where the particles were trapped. The concentrations of each trap were then calculated using equation 5.1

$$c_{trap} = \frac{\rho\, n\, \forall_{particle}}{\forall_{swept}\, \Omega\, t}. \tag{5.1}$$

The particle density (ρ), number of particles (n), volume of a single particle ($\forall_{particle}$), swept volume of the trap ($\forall_{swept}$), rotational rate of the motor (Ω), and the duration of the release (t) were used to form the concentration of particles that were trapped at that location during the entire release event. As the particles flow throughout the canopy the traps collect them. By counting the number of particles and knowing the density and volume of a single particle the mass was calculated. Then by looking at the swept volume of the trap times by the rotational velocity and time the traps were on the total volume of air trapped was determined. This then gave the concentration of particles in that specific location of the canopy. The rotation

rate of the traps were measured in a laboratory before the field experiment. The individual traps measured in the laboratory were not correlated with their location in the field experiment, thus an averaged rotational rate was used in equation 5.1. Error is associated with this number because of the change in rotational rate across each trap.

To compare vertical concentration profiles to various release events, equation 5.2 was used

$$\frac{u_* c}{q}. \tag{5.2}$$

The equation uses u_* (as defined in equation 2.5), c_{trap} (as defined in equation 5.1), and q (the amount of particles released over the experiment time length) were used 5.2 was used [11, 12, 34]

Figures 5.1 through 5.6 show the vertical concentrations for the cross flow releases. During the release the wind was predominantly out of the Southwest. As a result the general flow direction was identified by where the highest concentration profiles were located. Both releases have a wind out of the Southwest making the trap arrays towards the north have larger profiles. Figure 5.3, Traps 11 and 14 have a similar profile to the others that have been reported, but the other profiles in Figures 5.1 and 5.2 show an increase in concentration of roughly 40 % for traps in the middle of the plume from the top trap to bottom trap. In Figures 5.4 through 5.6 show different profiles. These profiles have concentrations that increase roughly 78%/m from above the release point till the top of the canopy, then decrease by almost 90%/m. The concentrations below the release point are much lower than above.

Figures 5.7 through 5.14 show the vertical concentrations for the along flow releases. The remaining vertical concentration plots are located in Appendix E. The concentrations show a decay from the bottom trap to the top trap for both releases. The wind is being channeled down the rows causing reduced turbulence and vertical flux. The magnitude decreases downstream and laterally.

5.2 Gaussian Plume

Gaussian plumes have been used in several particle transport studies as a model to describe concentrations at specific coordinates in a flow field [8, 23, 35, 37, 41]. The Gaussian Plume model was used to help describe the complex nature of the flow field. The model was derived from the equations found in Seinfeld and Pandis [49]. The Gaussian Plume model gives the concentration at its spatial location, equation 5.3

$$\langle c(x,y,z)\rangle = \frac{q}{2\pi\,\overline{U}\,\sigma^2}\exp\left(-\frac{y^2}{2\,\sigma^2}\right)\left[\exp\left(-\frac{(z-h)^2}{2\,\sigma^2}\right)-\exp\left(-\frac{(z+h)^2}{2\,\sigma^2}\right)\right]. \quad (5.3)$$

This equation identifies the source strength, and then how it disperses based off of atmospheric conditions. This model assumes that all particles that come into contact with the ground are totally absorbed, thus not being reflected back into the atmosphere. Also, it was assumed that the rate of vertical distribution of particle transport was equal to the horizontal distribution. The deviation was calculated by using equation 5.4

$$\sigma^2 = \frac{2\,K\,x}{\overline{U}}. \quad (5.4)$$

Equation 5.4 describes how the deviations expands the plumes in both the vertical and horizontal directions. In order to solve for σ^2 equation 5.5 is needed

$$K = \frac{\kappa\,u_*\,z}{\phi(\zeta)}. \quad (5.5)$$

This equation describes the rate at which the plume grows with distance. The von Karman constant ($\kappa = 0.40$) and the atmospheric conditions control this value. Equation 5.6 is an array of how the different classes of atmospheric stability will affect K, which affects σ^2, which determines the shape and concentration values of the Gaussian Plume

$$\phi(\zeta) = \begin{cases} 1+4.7\,\zeta & \zeta > 0 \text{ stable} \\ 1 & \zeta = 0 \text{ neutral} \\ (1-15\,\zeta)^{-1/2} & \zeta < 0 \text{ unstable.} \end{cases} \quad (5.6)$$

The value of $(\phi(\zeta))$ is determined by the atmospheric stability. The increasing instability will cause the plume to become wider with more dispersion of the plume.

The impaction trap (equation 5.1) and Gaussian Plume concentration (equation 5.3) can both be nondimensionalized using equation 5.7

$$\frac{c\,\overline{U}\,h^2}{q}. \tag{5.7}$$

This equation uses the mean magnitude of wind speed from the top sonic during the release event, release height, and amount of particles released to normalize the distance traveled and the source height between different release events as well as the calculated Gaussian Plume.

Figures 5.15 through 5.24 show the magnitudes of concentrations of both the fully developed steady state gaussian plume compared to the trap locations. The traps were compared to the Gaussian Plume at each trap level for release 1 and release 6. The traps locations are indicated by colored circles. The plume's and trap's color indicate the magnitude of the expected nondimensionalized concentration at that given location. Some traps malfunctioned during the release event. Those traps do not have a circle with a color associated with them. The remainder of the Gaussian Plume plots can be found in Appendix F.

5.3 Error of the Gaussian Plume

The plots depicting the error associated between the traps and the plume at each trap level are Figure 5.25 and Figure 5.26. The remainder of the Error of the Gaussian Plume plots can be found in Appendix G.

The model is based off of averaged statistics during the release period where as the traps provide information collected over the entire release period. The model does not adjust for wind speed or wind direction variation. The plume modeled on these figures represents only the average plume for the release period.

For release 1 and 2, the model over predicts for the trap locations inside of the plume and under predicts for the traps outside of the plume. The cross flow releases show how the particles are affected by the channeling in the rows causing the particles to be pushed down the rows. The along flow releases on average have a smaller percentage of error. This is due to the fact that the rows are not impacting the flow field as much as the cross flow situations. The Gaussian Plume is not a good model to

present accurate particle concentrations after a release event because of its inability to take into account the effect of the rows.

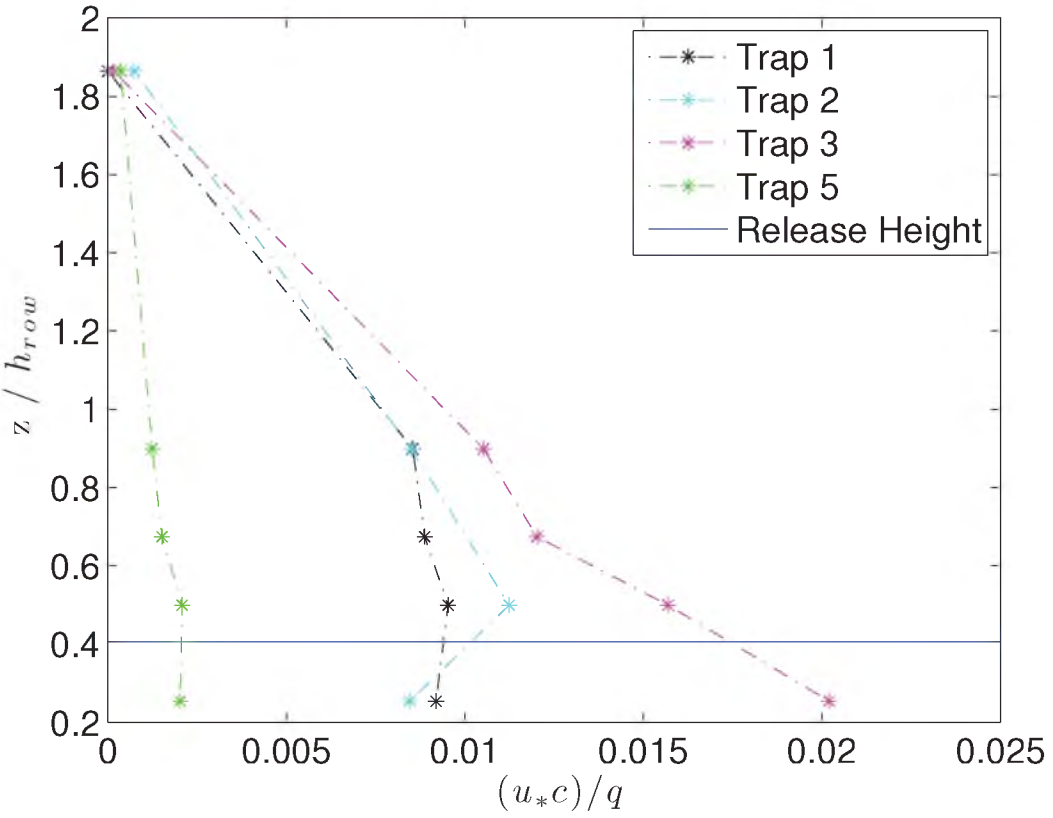

Figure 5.1. Values of concentration, $(u_* c) / q$, vs. height of sonic, z, normalized by the height of the rows, h, for Release 1 trap group 1. The blue line represents the release height normalized by row height.

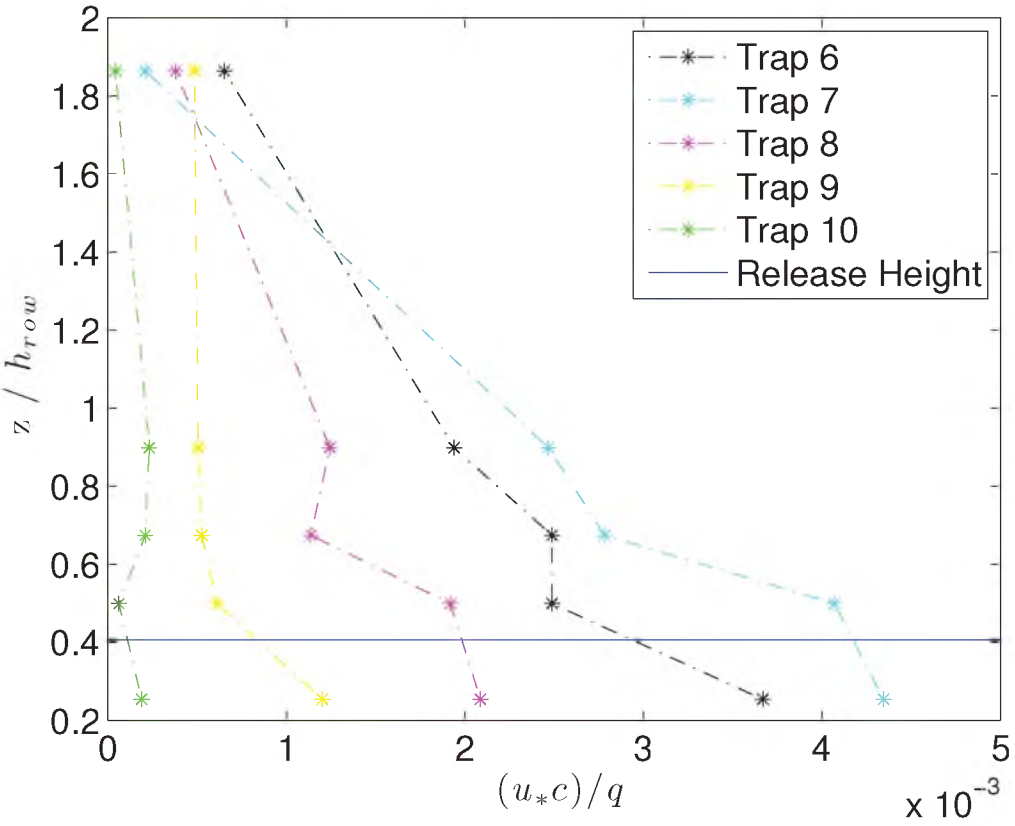

Figure 5.2. Values of concentration, $(u_* c) / q$, vs. height of sonic, z, normalized by the height of the rows, h, for Release 1 trap group 2. The blue line represents the release height normalized by row height.

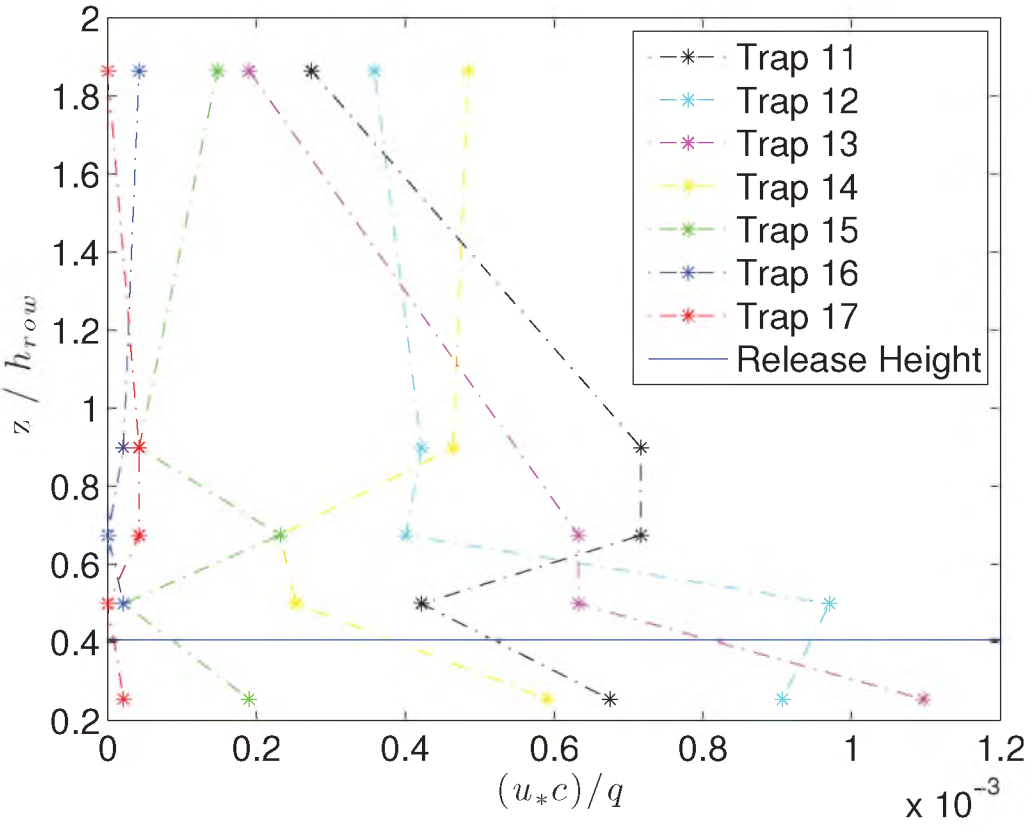

Figure 5.3. Values of concentration, $(u_* c) / q$, vs. height of sonic, z, normalized by the height of the rows, h, for Release 1 trap group 3. The blue line represents the release height normalized by row height.

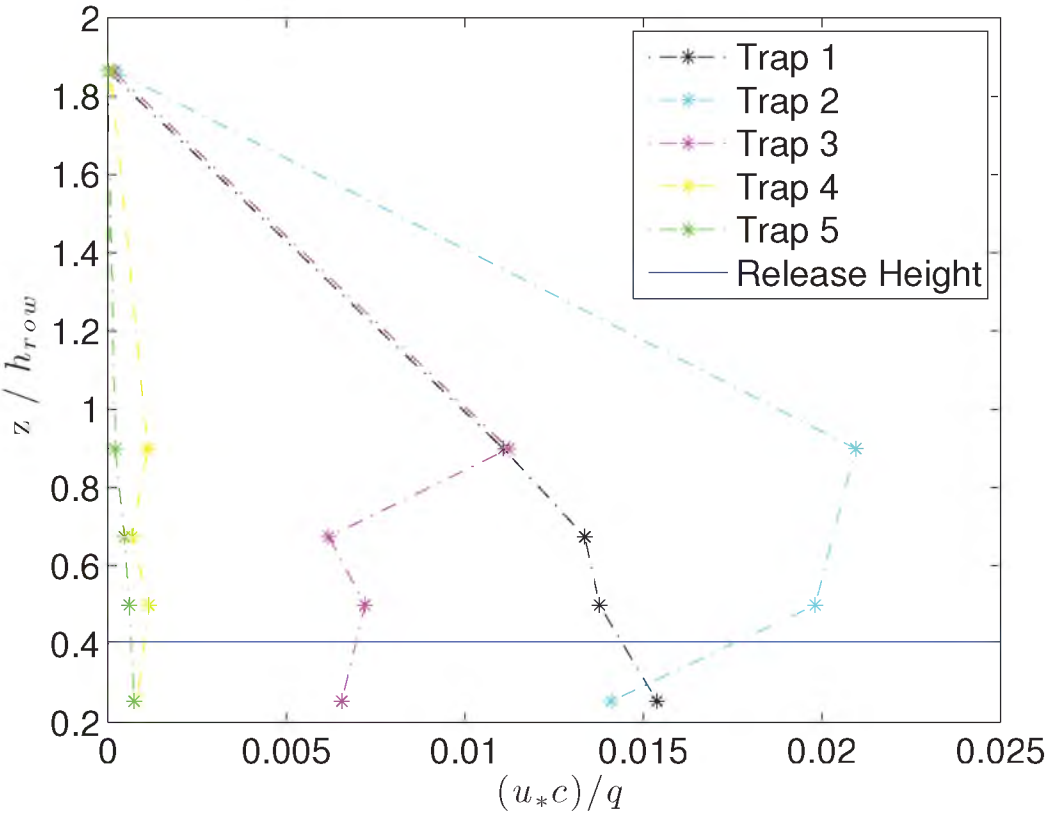

Figure 5.4. Values of concentration, $(u_* c) / q$, vs. height of sonic, z, normalized by the height of the rows, h, for Release 2 trap group 1. The blue line represents the release height normalized by row height.

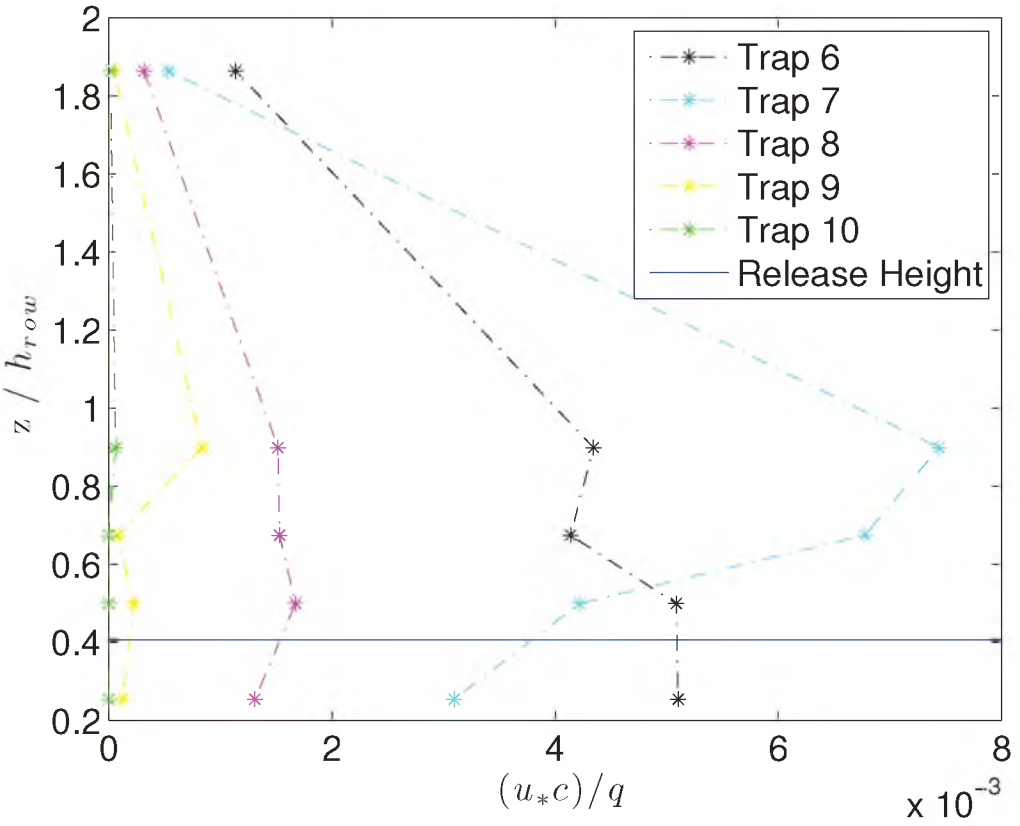

Figure 5.5. Values of concentration, $(u_* c) / q$, vs. height of sonic, z, normalized by the height of the rows, h, for Release 2 trap group 2. The blue line represents the release height normalized by row height.

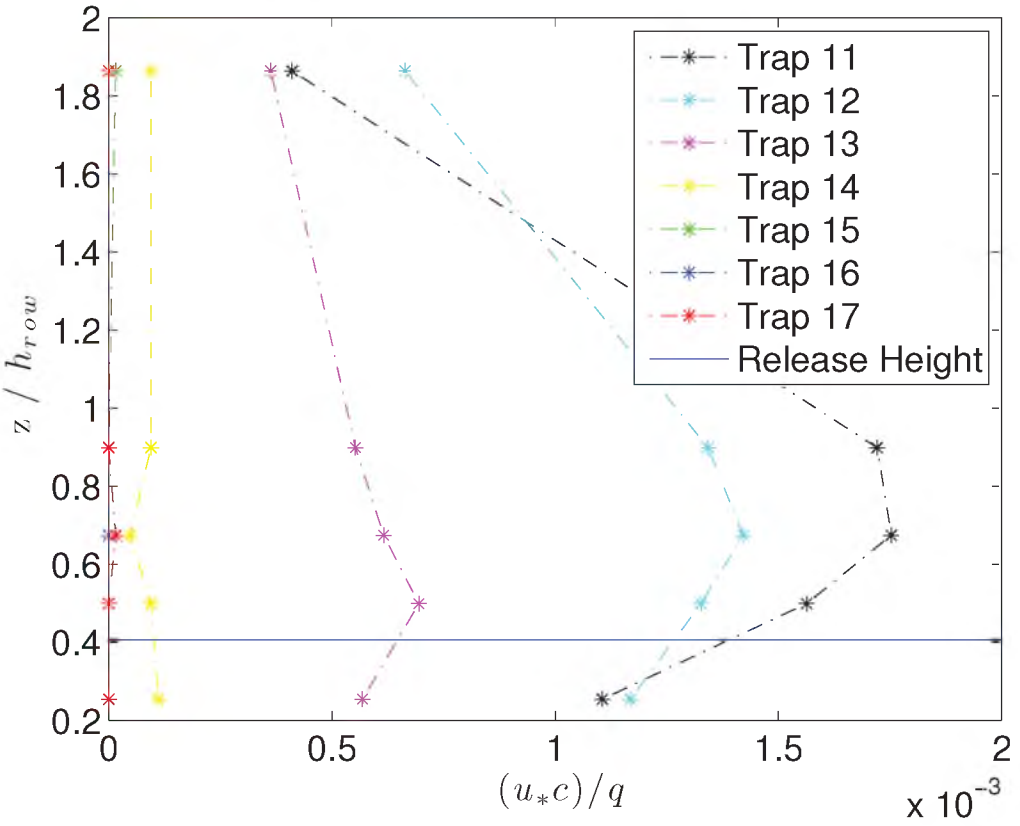

Figure 5.6. Values of concentration, $(u_* c) / q$, vs. height of sonic, z, normalized by the height of the rows, h, for Release 2 trap group 3. The blue line represents the release height normalized by row height.

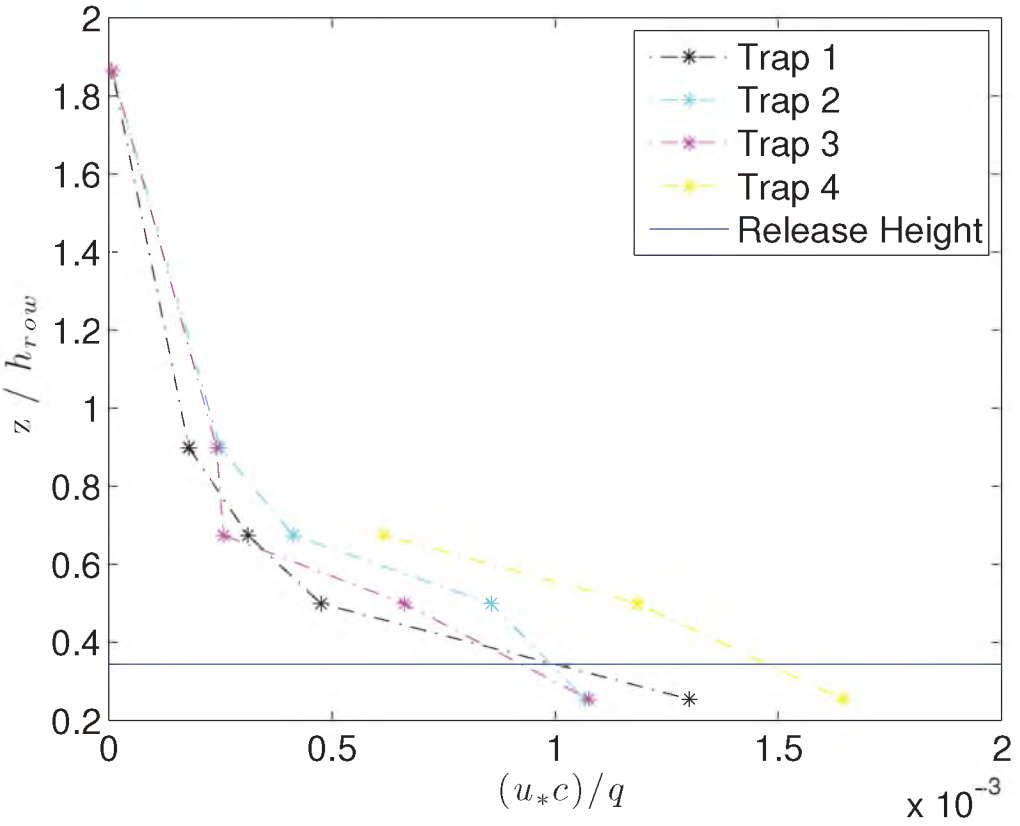

Figure 5.7. Values of concentration, $(u_* c) / q$, vs. height of sonic, z, normalized by the height of the rows, h, for Release 4 trap group 1. The blue line represents the release height normalized by row height.

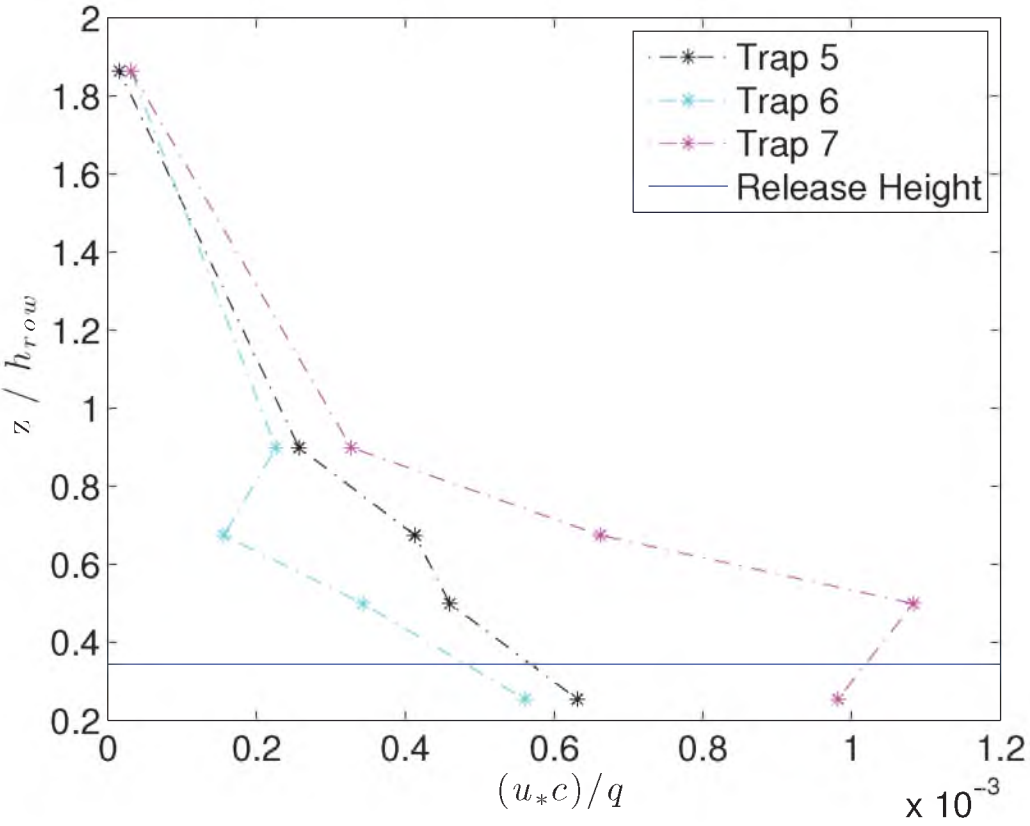

Figure 5.8. Values of concentration, $(u_* c) / q$, vs. height of sonic, z, normalized by the height of the rows, h, for Release 4 trap group 2. The blue line represents the release height normalized by row height.

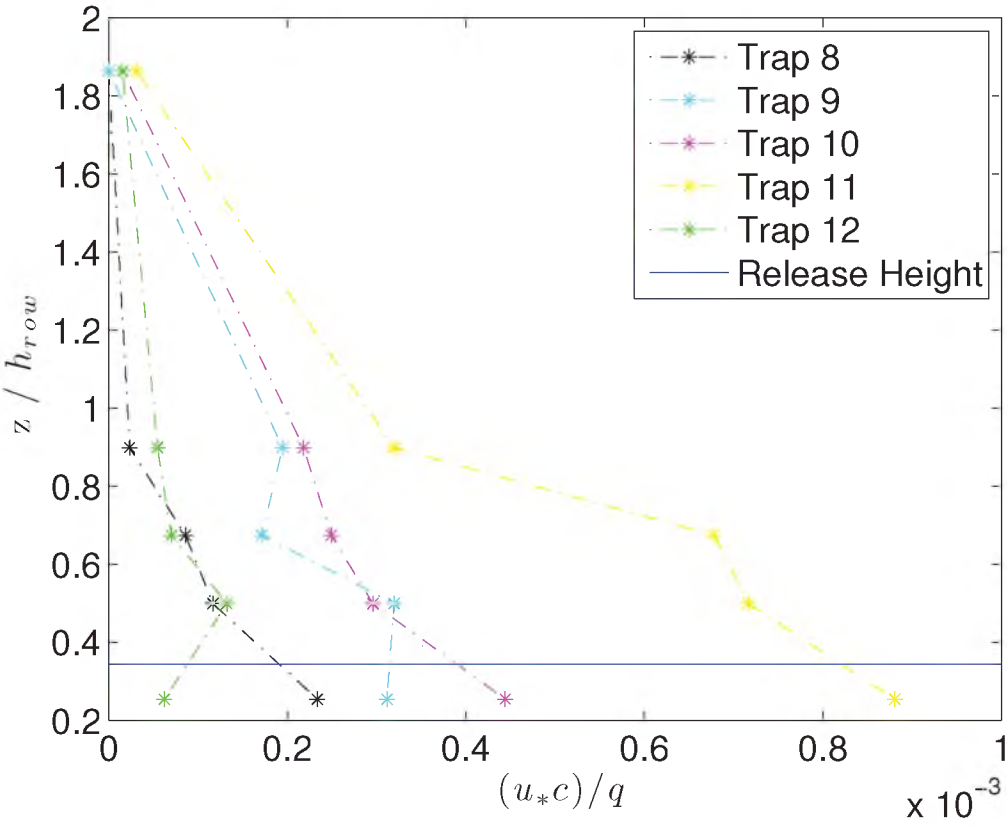

Figure 5.9. Values of concentration, $(u_* c) / q$, vs. height of sonic, z, normalized by the height of the rows, h, for Release 4 trap group 3. The blue line represents the release height normalized by row height.

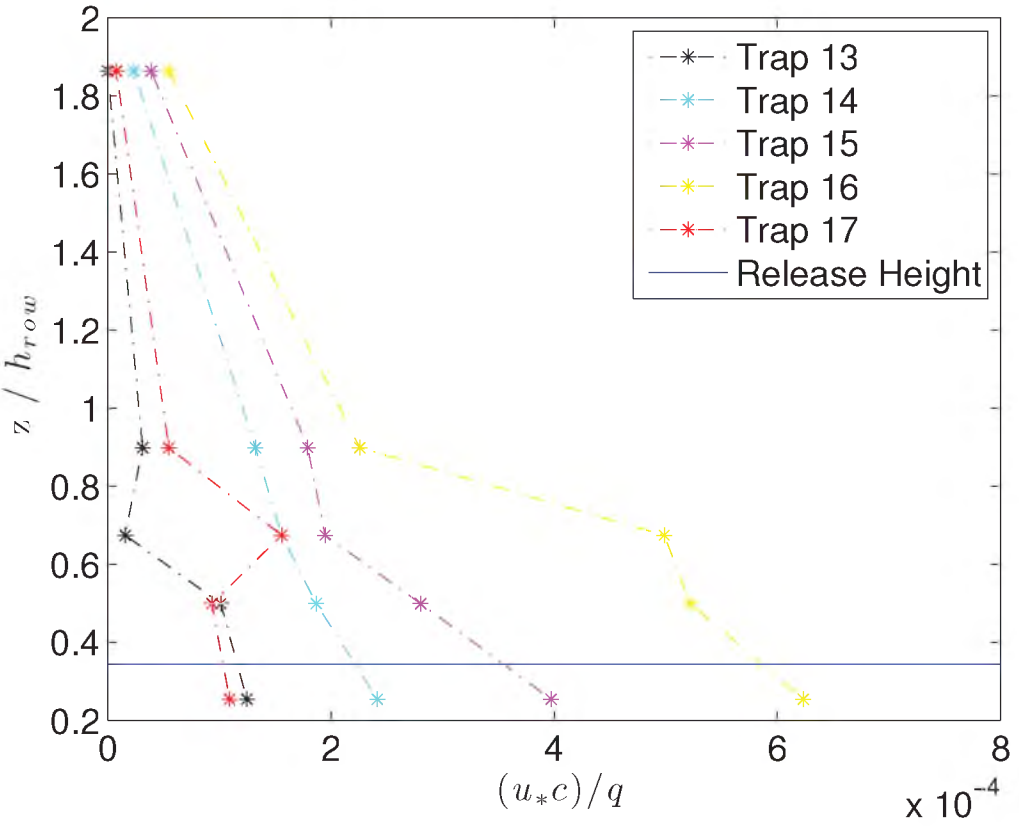

Figure 5.10. Values of concentration, $(u_* c) / q$, vs. height of sonic, z, normalized by the height of the rows, h, for Release 4 trap group 4. The blue line represents the release height normalized by row height.

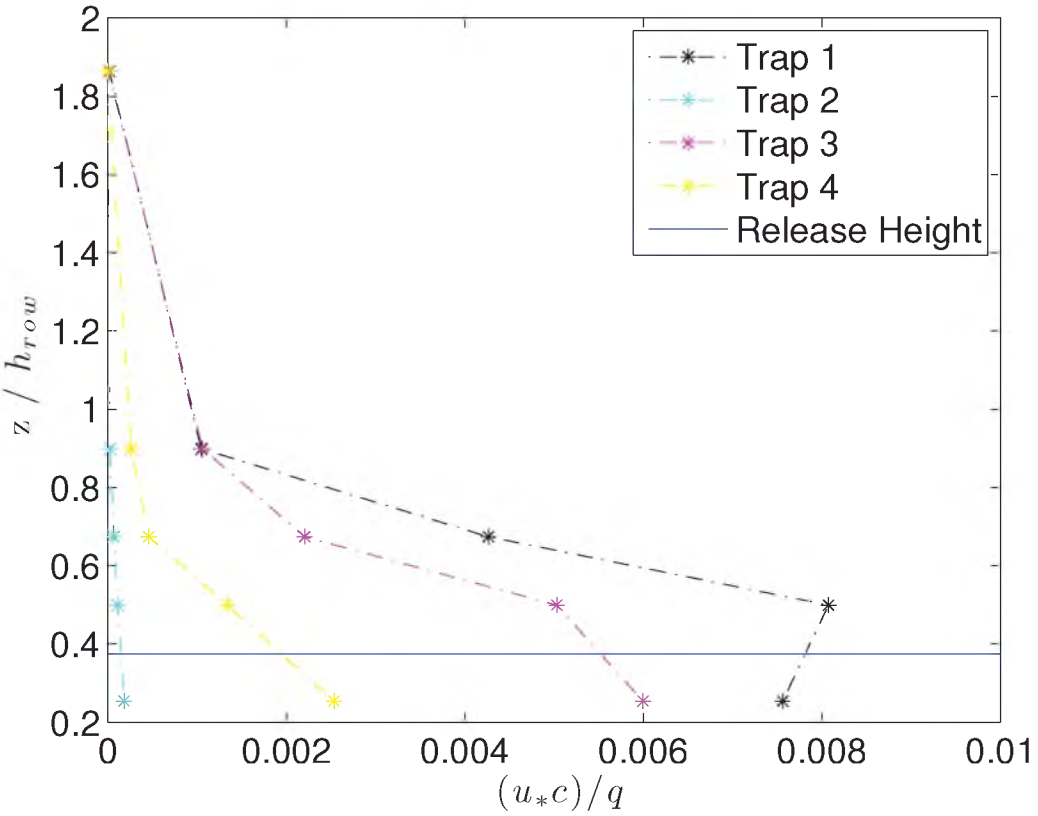

Figure 5.11. Values of concentration, $(u_* c) / q$, vs. height of sonic, z, normalized by the height of the rows, h, for Release 5 trap group 1. The blue line represents the release height normalized by row height.

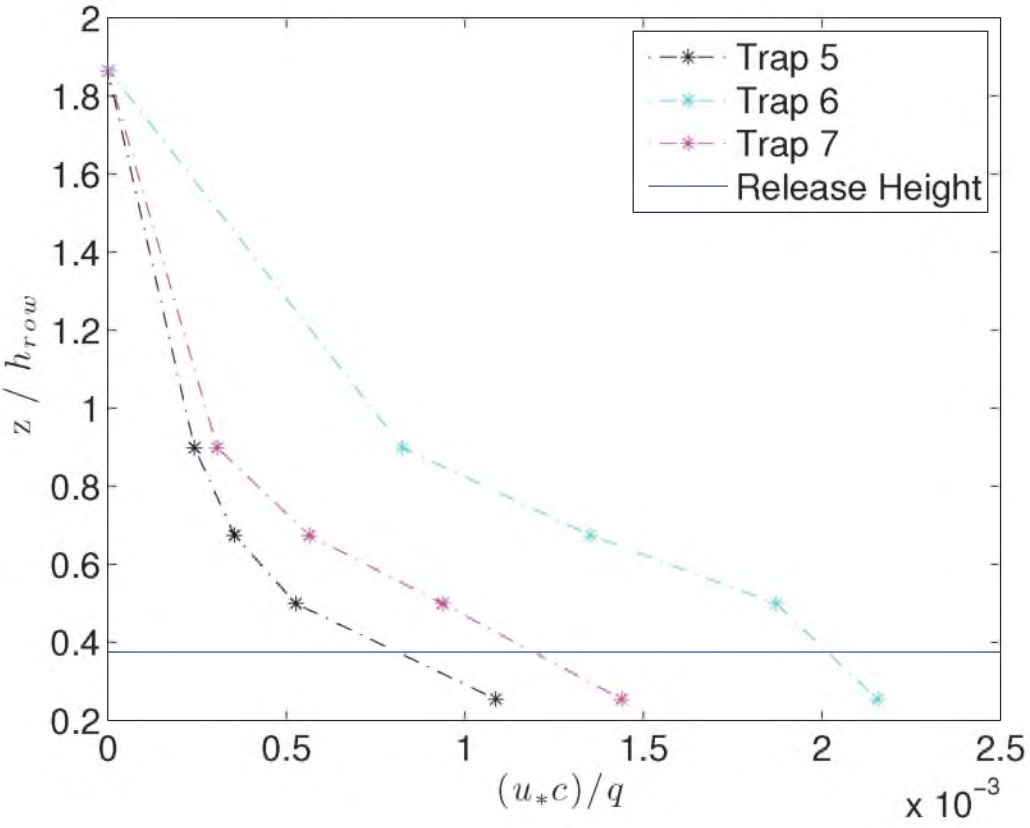

Figure 5.12. Values of concentration, $(u_* c) / q$, vs. height of sonic, z, normalized by the height of the rows, h, for Release 9 trap group 2. The blue line represents the release height normalized by row height.

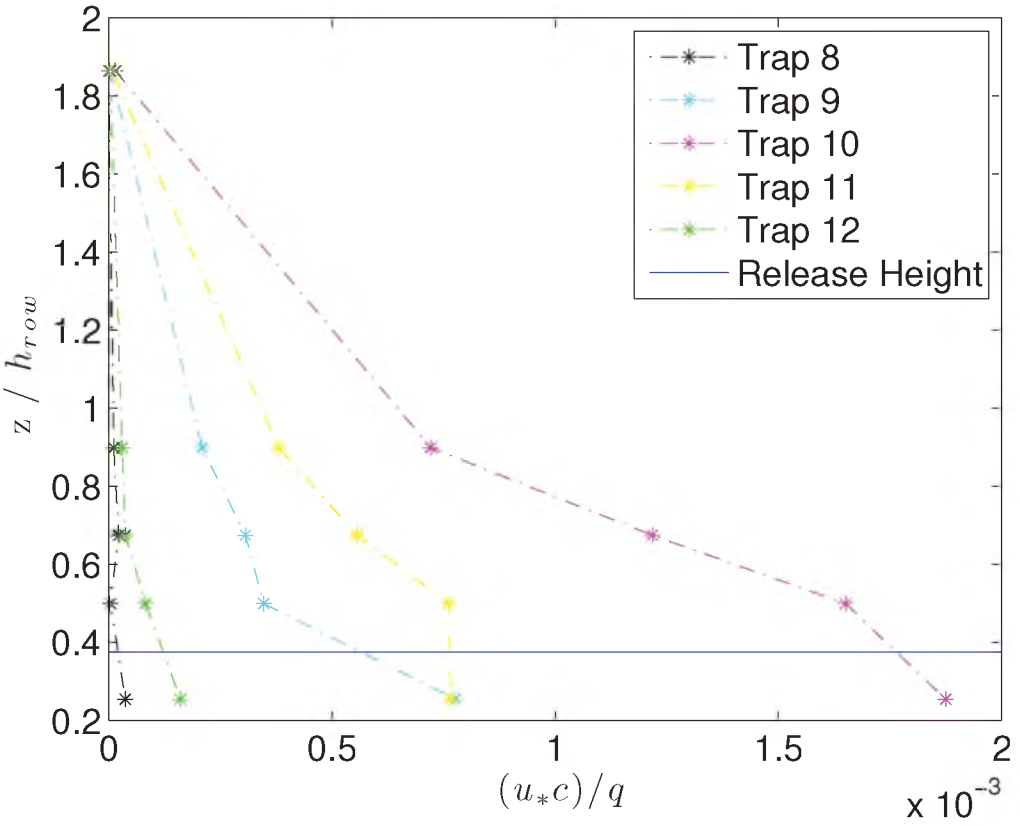

Figure 5.13. Values of concentration, $(u_* c) / q$, vs. height of sonic, z, normalized by the height of the rows, h, for Release 9 trap group 3. The blue line represents the release height normalized by row height.

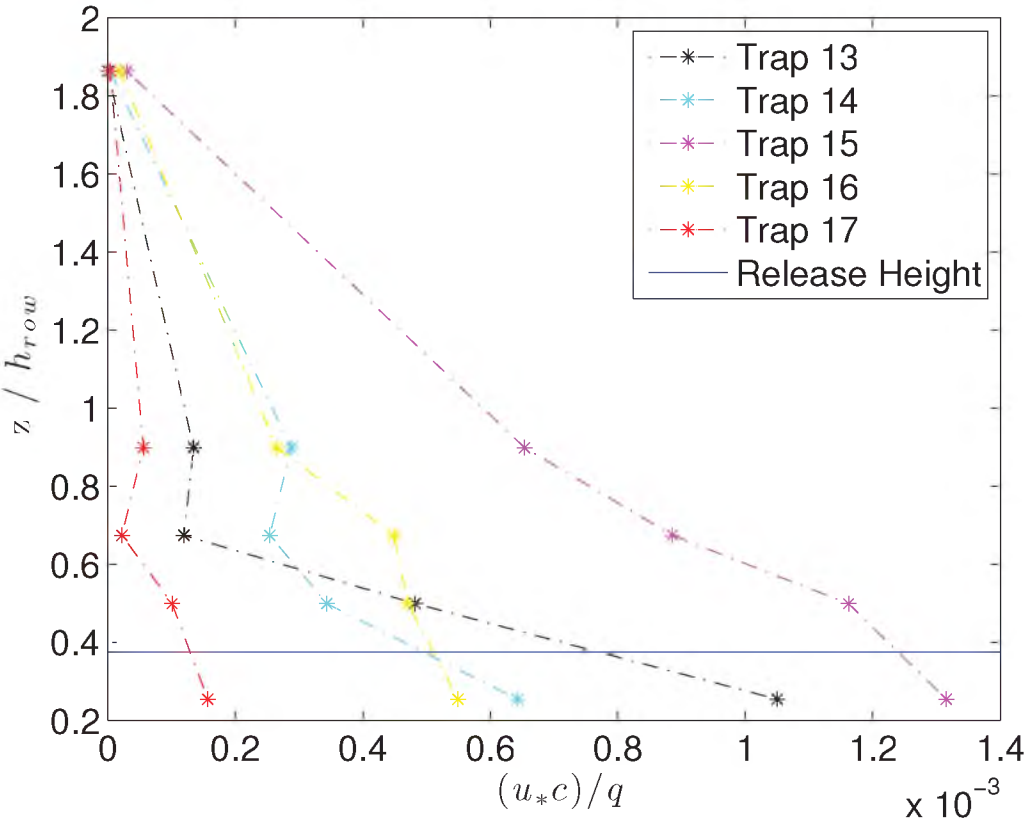

Figure 5.14. Values of concentration, $(u_* c) / q$, vs. height of sonic, z, normalized by the height of the rows, h, for Release 9 trap group 4. The blue line represents the release height normalized by row height.

Table 5.1. Release event parameters

Release	Start Time	Particles Released (g)	Release Height (m)
1	18:08	0.47	0.81
2	19:59	0.60	0.81
3	17:54	0.70	1.17
4	19:50	1.50	0.69
5	20:55	0.72	0.75
6	16:41	0.52	0.84

Table 5.2. Average meteorological data during release periods

Release	Trap Setup	Duration	Wind Speed	Wind Direction	u_*	ζ
1	Cross	20 min	1.81 m/s	242.21°	0.30	-0.17
2	Cross	20 min	1.77 m/s	245.48°	0.32	-0.02
3	Cross	20 min	1.56 m/s	353.26°	0.20	-0.27
4	Along	12 min	2.64 m/s	357.92°	0.33	-0.03
5	Along	20 min	1.39 m/s	350.96°	0.11	0.36
6	Along	20 min	2.86 m/s	7.61°	0.40	-0.11

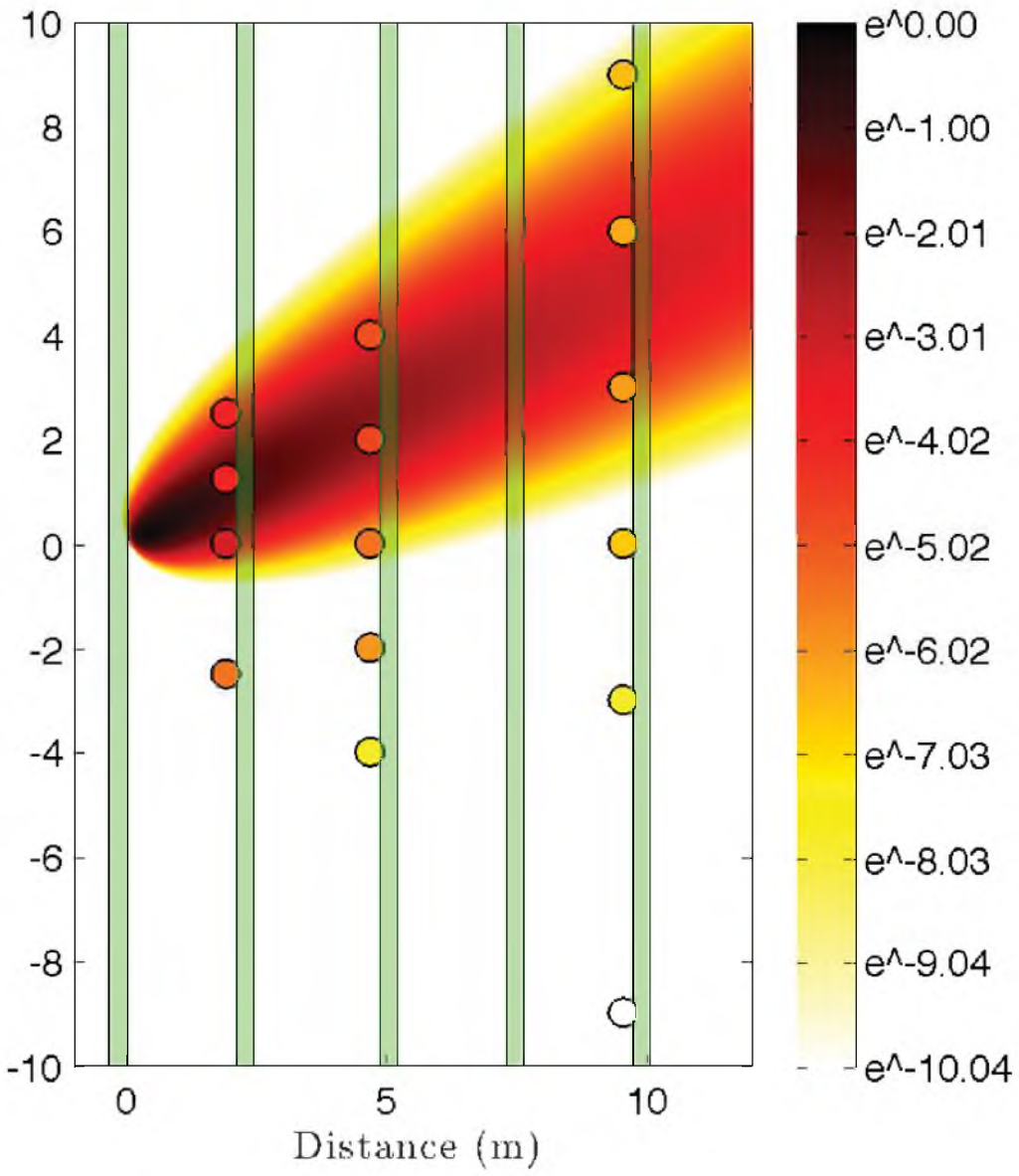

Figure 5.15. The normalized measured field data compared to the normalized Gaussian Plume model for release 1 at a height of 0.5 m or trap level 1. The measured field data were indicated by color filled circles. The release was located at (0.0m, 0.0m, 0.81m). Circles were omitted if data were not available at the trap location.

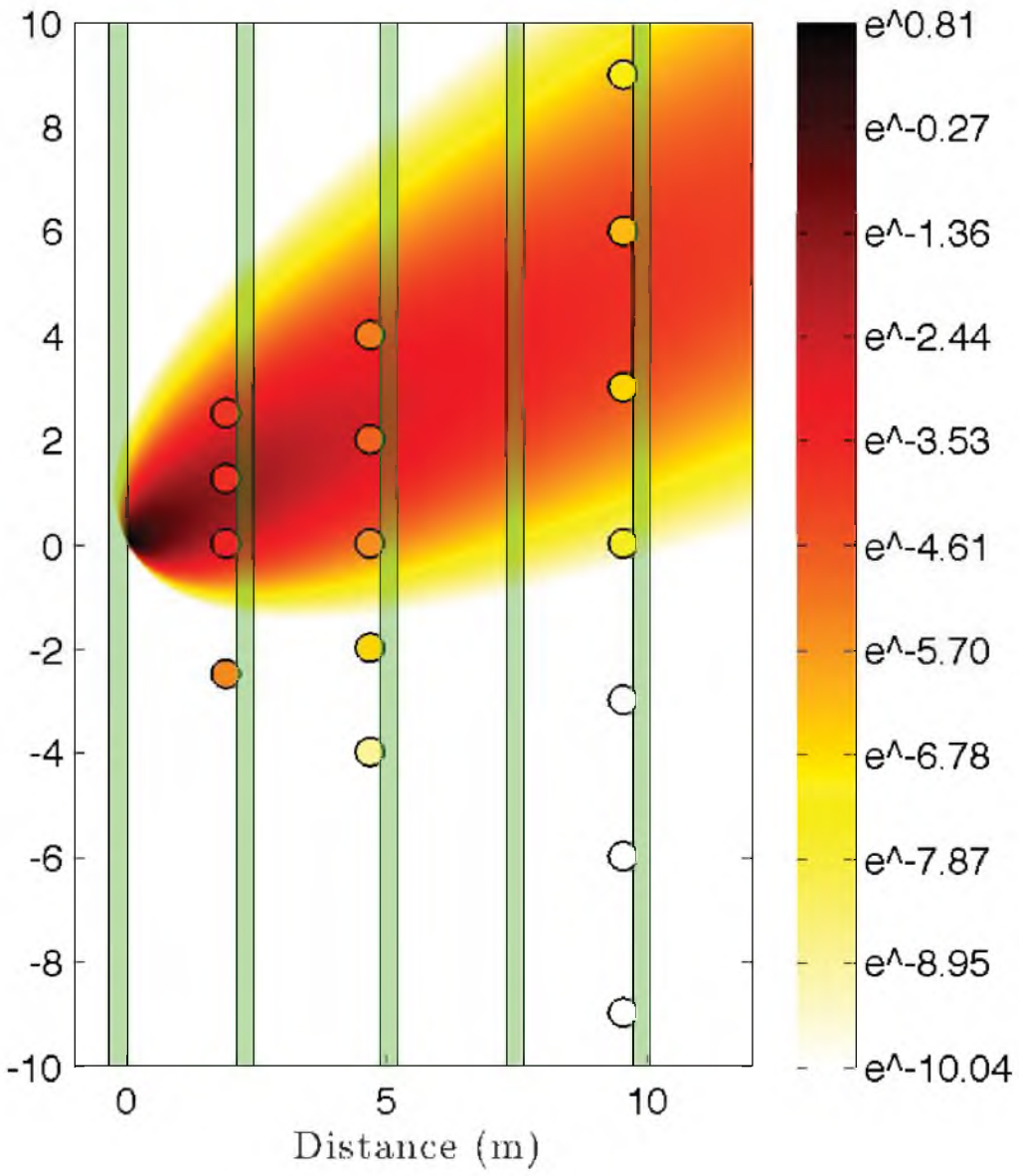

Figure 5.16. The normalized measured field data compared to the normalized Gaussian Plume model for release 1 at a height of 1.0 m or trap level 2. The measured field data were indicated by color filled circles. The release was located at (0.0m, 0.0m, 0.81m). Circles were omitted if data were not available at the trap location.

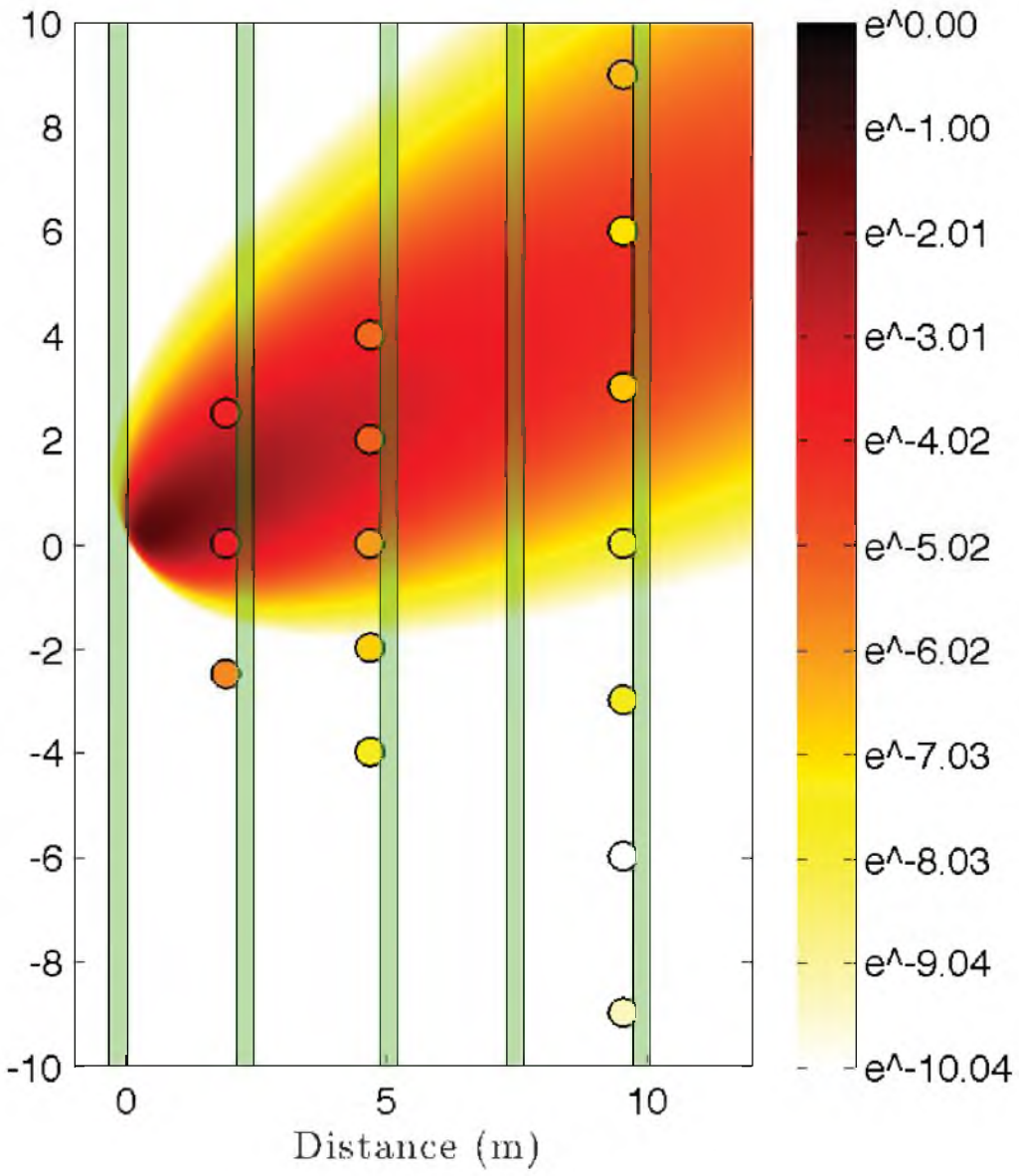

Figure 5.17. The normalized measured field data compared to the normalized Gaussian Plume model for release 1 at a height of 1.3 m or trap level 3. The measured field data were indicated by color filled circles. The release was located at (0.0m, 0.0m, 0.81m). Circles were omitted if data were not available at the trap location.

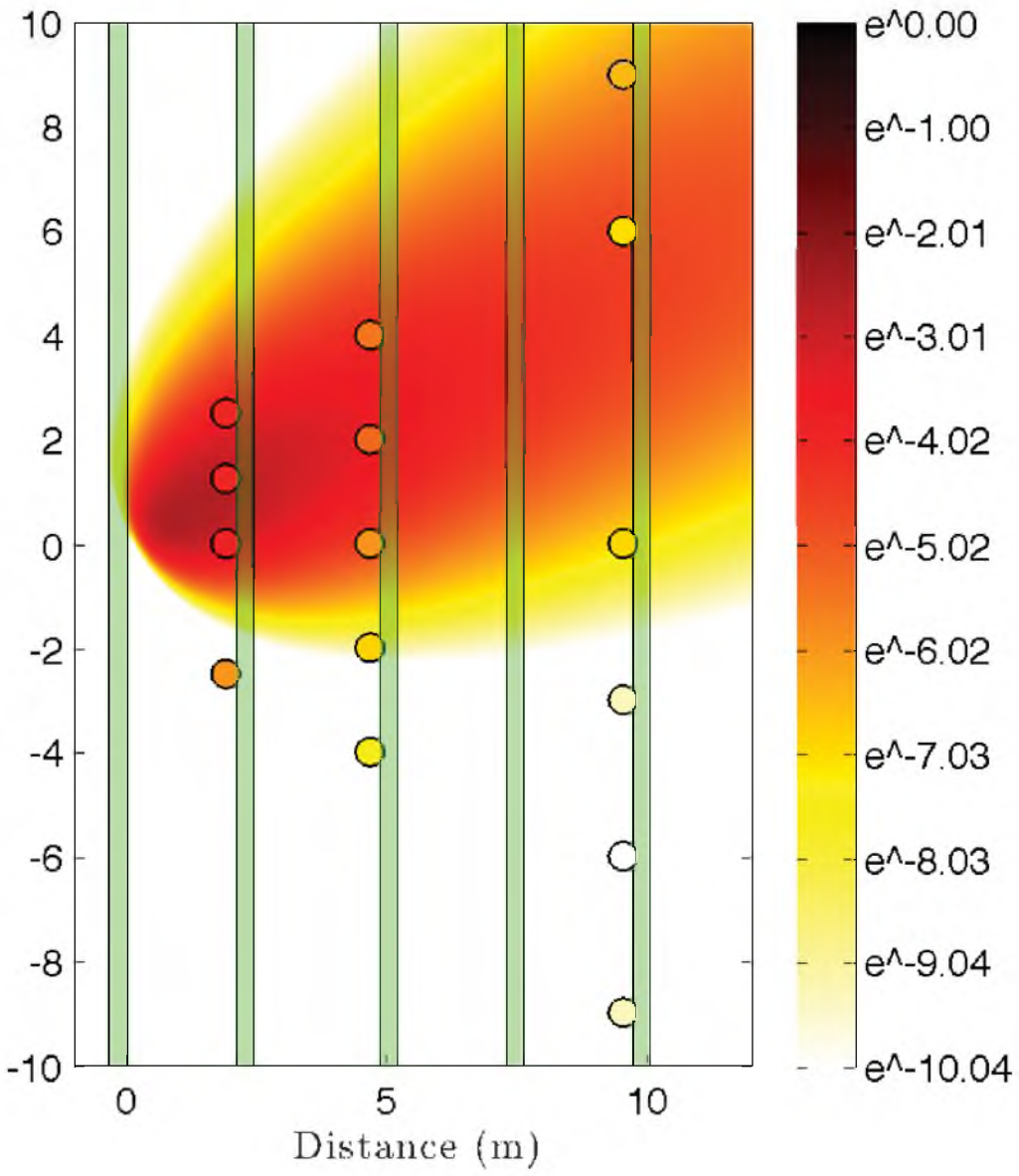

Figure 5.18. The normalized measured field data compared to the normalized Gaussian Plume model for release 1 at a height of 1.8 m or trap level 4. The measured field data were indicated by color filled circles. The release was located at (0.0m, 0.0m, 0.81m). Circles were omitted if data were not available at the trap location.

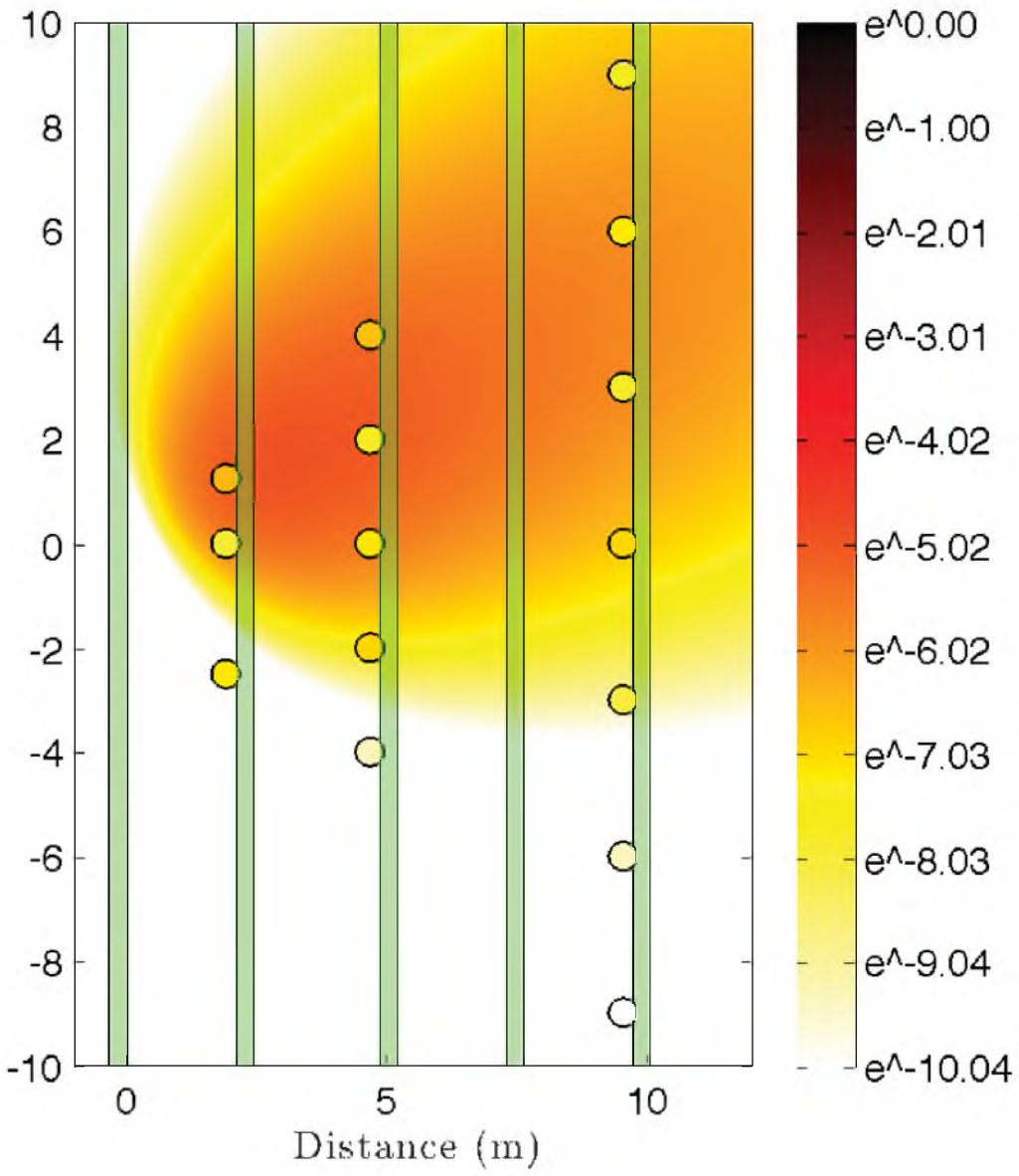

Figure 5.19. The normalized measured field data compared to the normalized Gaussian Plume model for release 1 at a height of 3.7 m or trap level 5. The measured field data were indicated by color filled circles. The release was located at (0.0m, 0.0m, 0.81m). Circles were omitted if data were not available at the trap location.

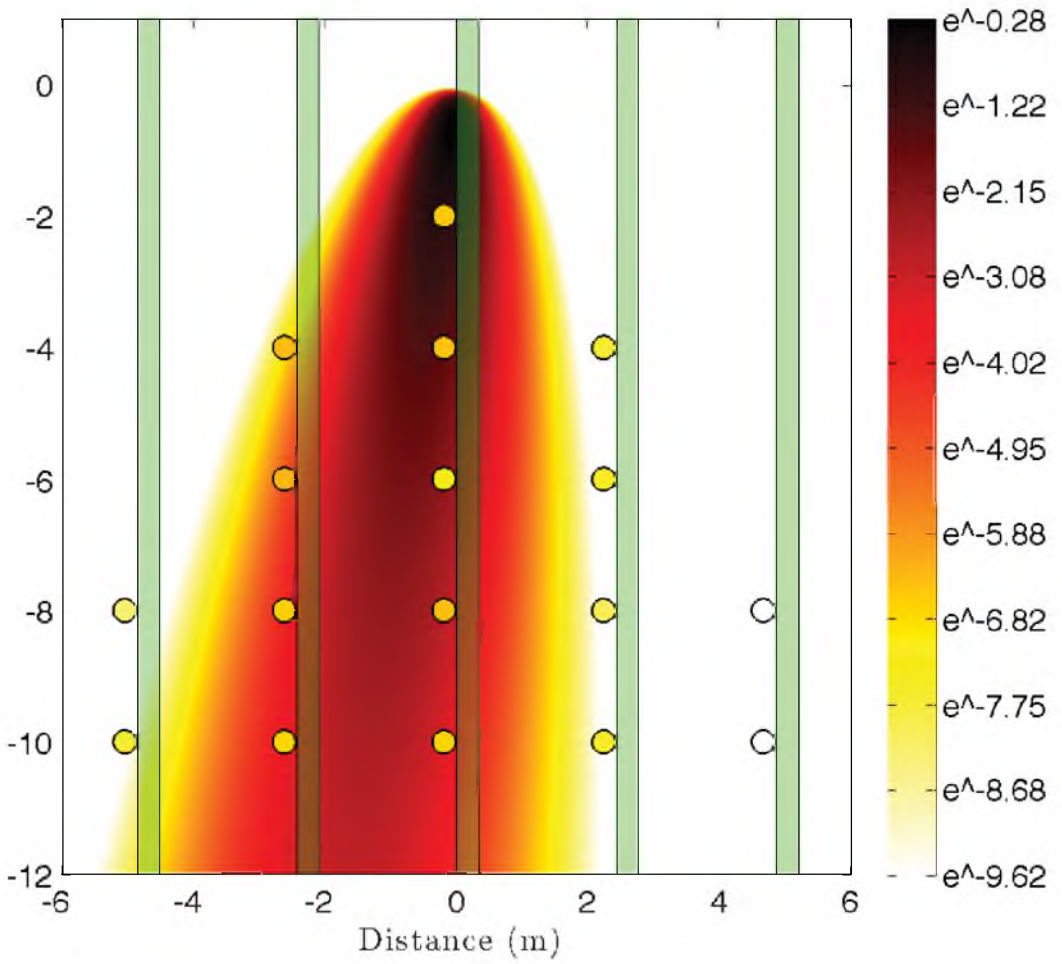

Figure 5.20. The normalized measured field data compared to the normalized Gaussian Plume model for release 6 at a height of 0.5 m or trap level 1. The measured field data were indicated by color filled circles. The release was located at (0.0m, 0.0m, 0.84m). Circles were omitted if data were not available at the trap location.

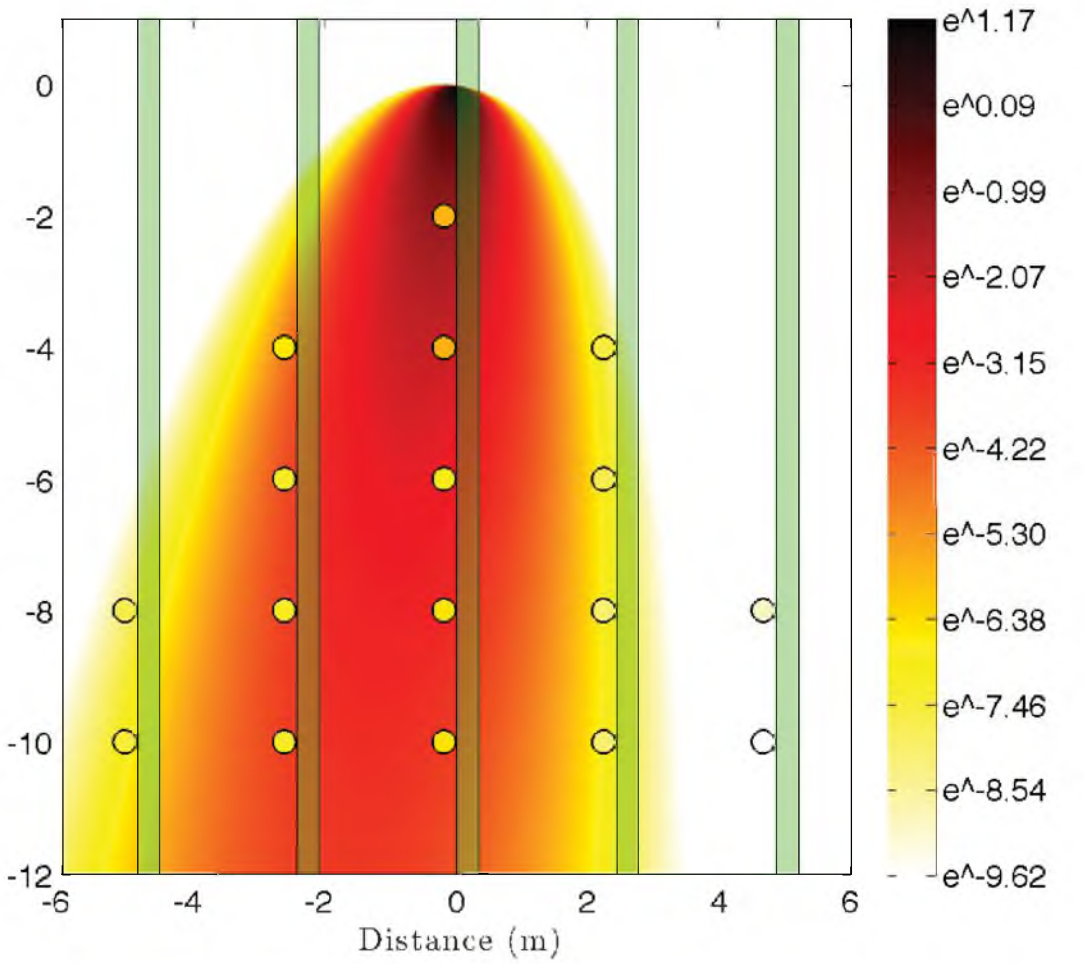

Figure 5.21. The normalized measured field data compared to the normalized Gaussian Plume model for release 6 at a height of 1.0 m or trap level 2. The measured field data were indicated by color filled circles. The release was located at (0.0m, 0.0m, 0.84m). Circles were omitted if data were not available at the trap location.

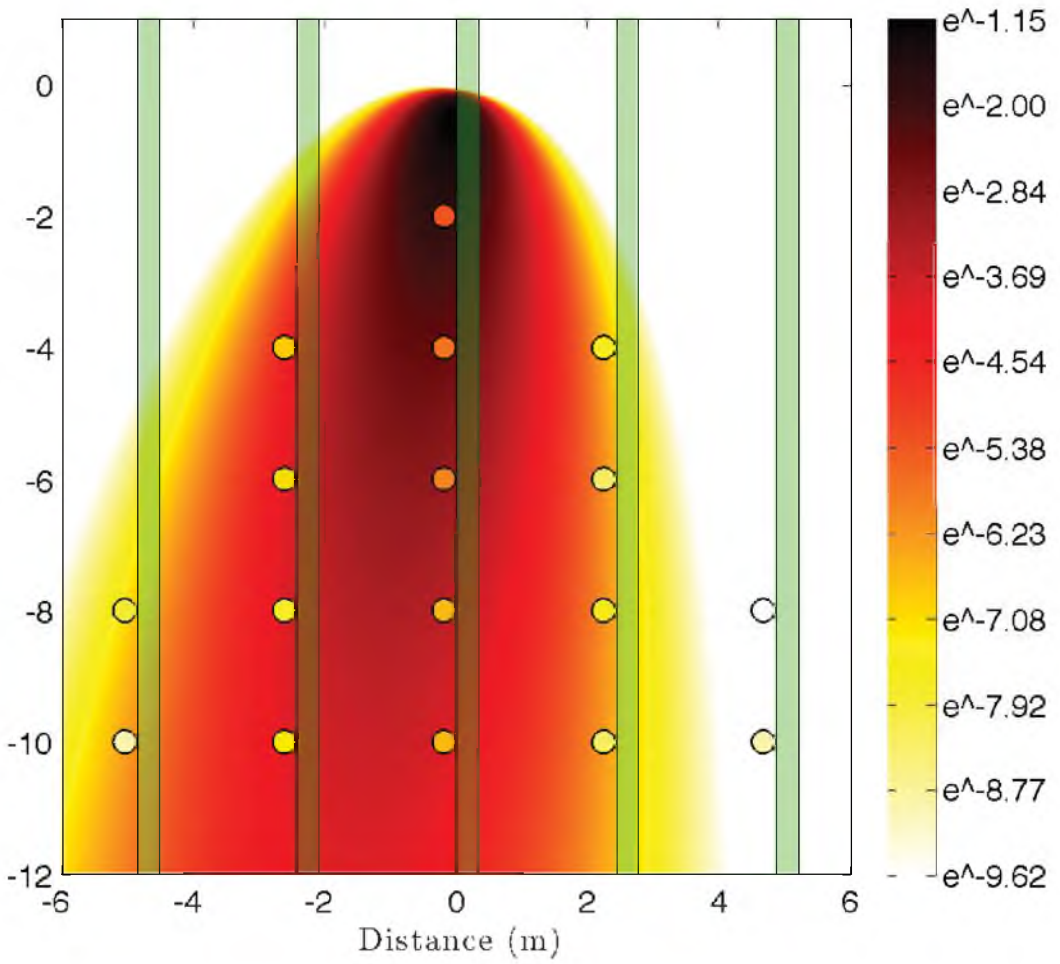

Figure 5.22. The normalized measured field data compared to the normalized Gaussian Plume model for release 6 at a height of 1.3 m or trap level 3. The measured field data were indicated by color filled circles. The release was located at (0.0m, 0.0m, 0.84m). Circles were omitted if data were not available at the trap location.

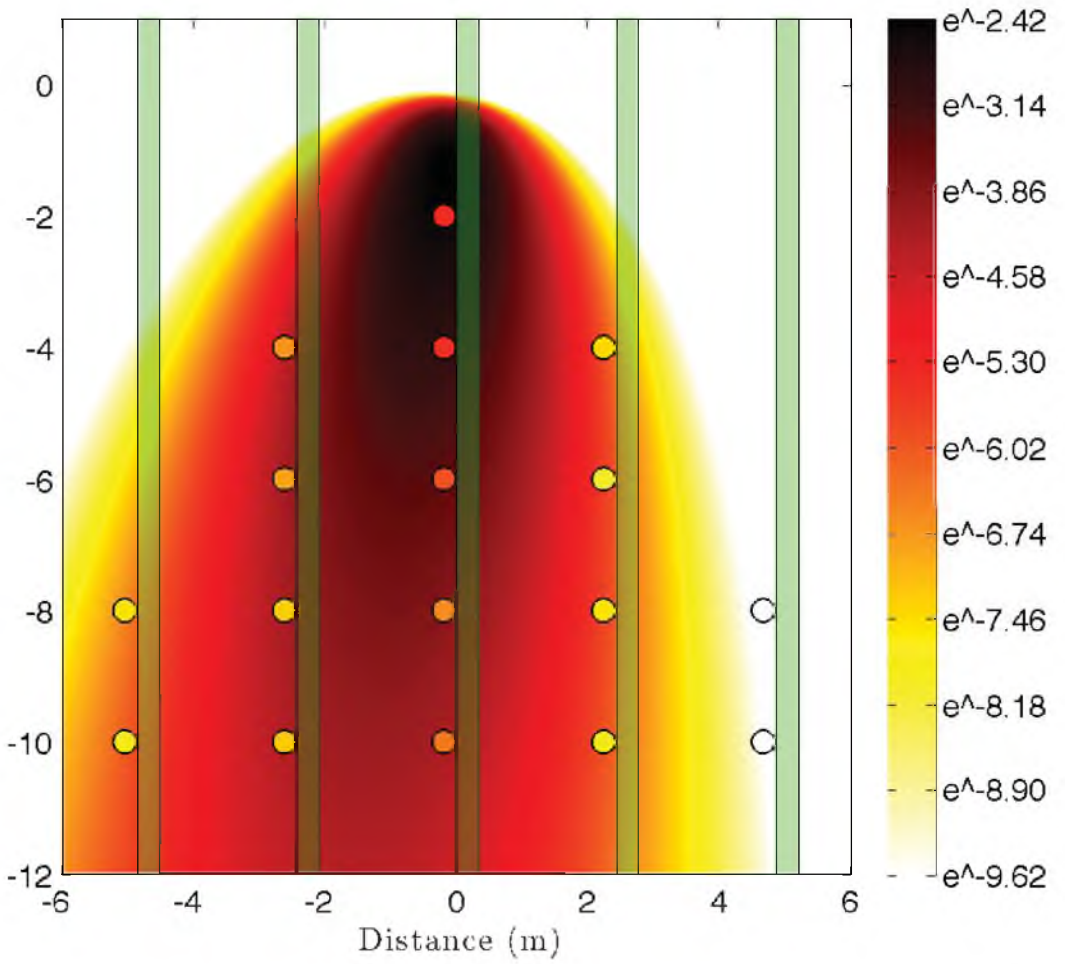

Figure 5.23. The normalized measured field data compared to the normalized Gaussian Plume model for release 6 at a height of 1.8 m or trap level 4. The measured field data were indicated by color filled circles. The release was located at (0.0m, 0.0m, 0.84m). Circles were omitted if data were not available at the trap location.

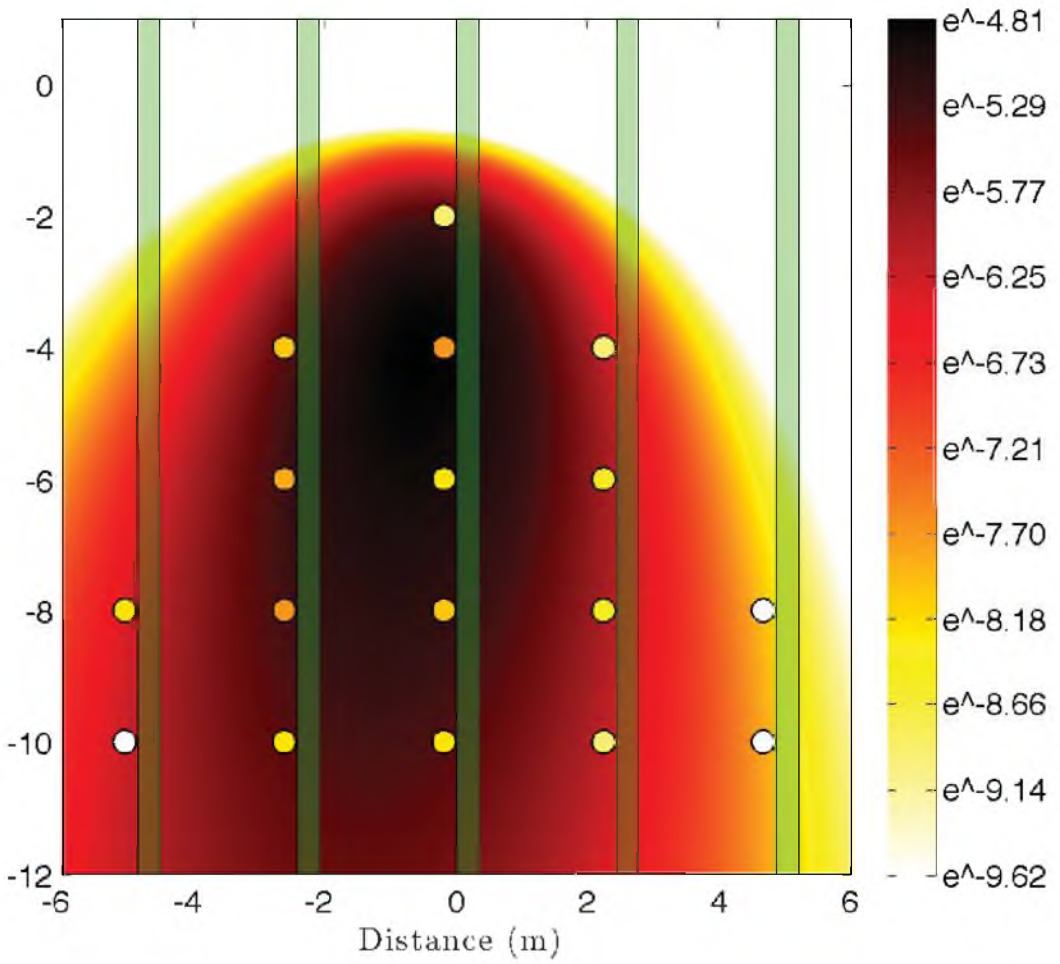

Figure 5.24. The normalized measured field data compared to the normalized Gaussian Plume model for release 6 at a height of 3.7 m or trap level 5. The measured field data were indicated by color filled circles. The release was located at (0.0m, 0.0m, 0.84m). Circles were omitted if data were not available at the trap location.

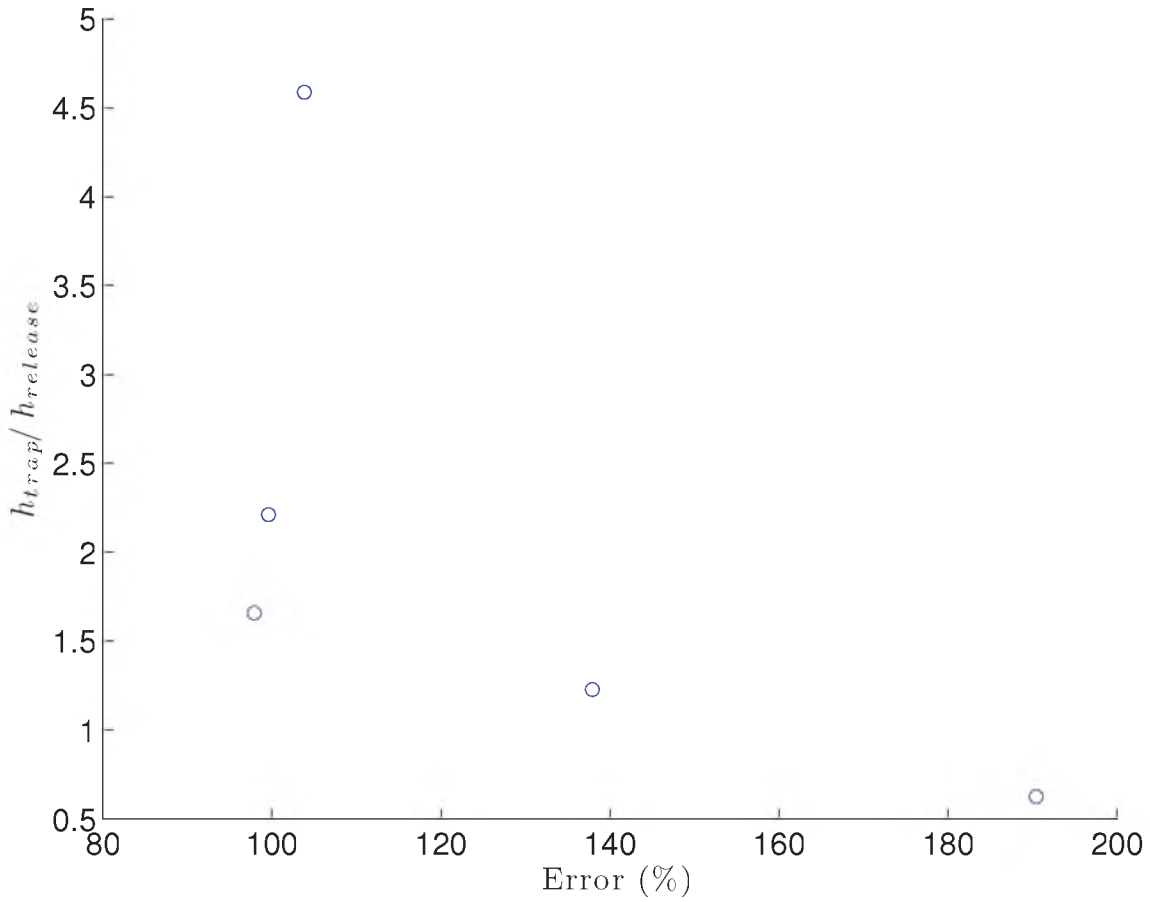

Figure 5.25. Depicts the amount of error between the measured data and the Gaussian Plume for the entire trap level at each trap height for release 1.

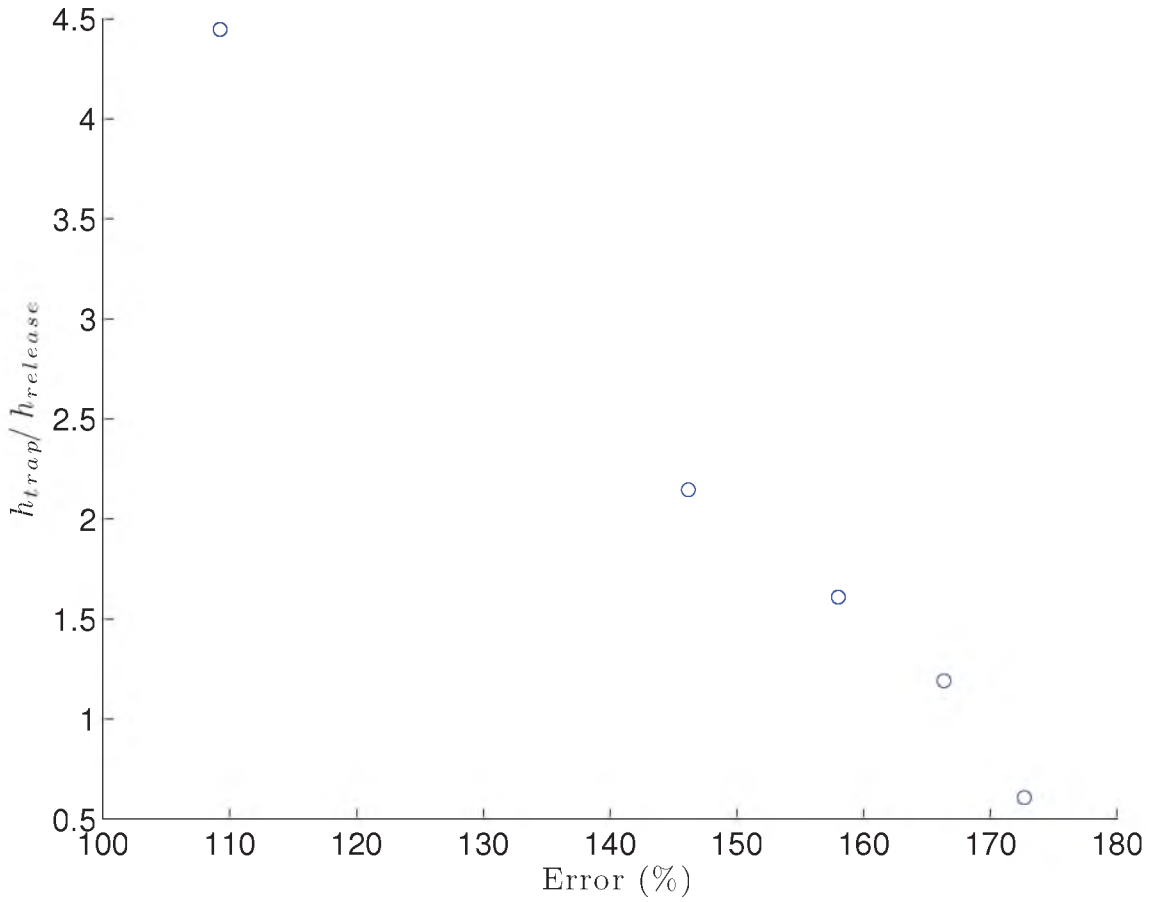

Figure 5.26. Depicts the amount of error between the measured data and the Gaussian Plume for the entire trap level at each trap height for release 6.

CHAPTER 6

CONCLUSION

The analysis of a field experiment was performed. The purpose of the experiment was to see how the momentum field affected particle transport in a canopy. Atmospheric measuring devices were deployed in the field to determine various momentum statistics. The momentum statistics show how the wind was channeled to be aligned with the row direction. With the wind rose showing a wide variety of wind directions at the top sonic being narrowed down to two major wind directions at the bottom sonic. These two wind directions became "along" flow meaning the wind travels down the row and "cross" flow because the wind travels against the rows. Magnitudes for cross flows could have as much as a 30% difference from the along flow. The profiles for σ_v and σ_w showed little difference, but had a magnitude increase of roughly 50% from weakly convective to strongly convective time periods. While σ_u showed different profiles for the different stability criteria with a rapid increase between sonic 2 and 3 of 23 %. The spectra remained unchanged with the production range being on the order of the canopy height, 2m. These statistics help show how particles could be dispersed throughout a canopy.

The inert particles, which represent powdery mildew, were released into the canopy and trap on roto-rod impaction traps. This, coupled with the atmospheric data, showed how particles flowed through the canopy. There were several different vertical concentration profiles exhibited based on the quality of the release event. These values were then compared to a gaussian plume model, which was a poor comparison of the actual results.

6.1 Future Work

In order to accurately model a path of a particle through a canopy several more studies along with higher resolution data needs to be performed. By increasing the

number of sonics within the canopy, profile trends would be better resolved and how they affect particle transport. Also, by having these sonics deployed for longer periods of time there would be a better chance of determining average statistics.

Several more release events would need to be accomplished to better identify concentration profiles throughout the vineyard. More release events would allow the removal of data sets where atmospheric conditions are not ideal. Larger trap arrays would also enable the use of data sets that would otherwise be unusable due to unplanned changes in atmospheric conditions. Many of the release events were inconclusive as to what would happen in future events with similar conditions.

By following the suggestions outlined above, particle transport within a canopy could be better understood.

APPENDIX A

WIND PROFILES FOR EACH 30-MINUTE PERIOD

Table A.1. Wind magnitude, U, normalized by u_* at sonic 1 (0.8m)

Wind Flow	Stability	25^{th}	50^{th}	75^{th}	Mean
Along	$0 > \zeta > -1$	2.46	2.73	3.03	2.69
Cross	$0 > \zeta > -1$	1.06	1.57	2.18	1.61
Along	$-1 > \zeta$	1.96	2.80	4.15	3.08
Cross	$-1 > \zeta$	0.93	1.52	2.50	1.76

Table A.2. Wind magnitude, U, normalized by u_* at sonic 2 (1.8m)

Wind Flow	Stability	25^{th}	50^{th}	75^{th}	Mean
Along	$0 > \zeta > -1$	3.77	3.95	4.33	3.90
Cross	$0 > \zeta > -1$	2.39	2.98	3.42	2.88
Along	$-1 > \zeta$	2.87	4.07	5.82	4.42
Cross	$-1 > \zeta$	1.88	2.24	3.18	2.77

Table A.3. Wind magnitude, U, normalized by u_* at sonic 3 (2.9m)

Wind Flow	Stability	25^{th}	50^{th}	75^{th}	Mean
Along	$0 > \zeta > -1$	5.68	5.91	6.51	5.88
Cross	$0 > \zeta > -1$	3.93	4.80	5.38	4.64
Along	$-1 > \zeta$	4.48	6.35	9.00	6.81
Cross	$-1 > \zeta$	3.03	3.92	5.16	4.40

Table A.4. Wind magnitude, U, normalized by u_* at sonic 4 (3.9m)

Wind Flow	Stability	25^{th}	50^{th}	75^{th}	Mean
Along	$0 > \zeta > -1$	6.52	6.91	7.60	6.82
Cross	$0 > \zeta > -1$	4.73	5.87	6.51	5.59
Along	$-1 > \zeta$	4.69	7.24	10.30	7.68
Cross	$-1 > \zeta$	3.63	4.93	6.31	5.15

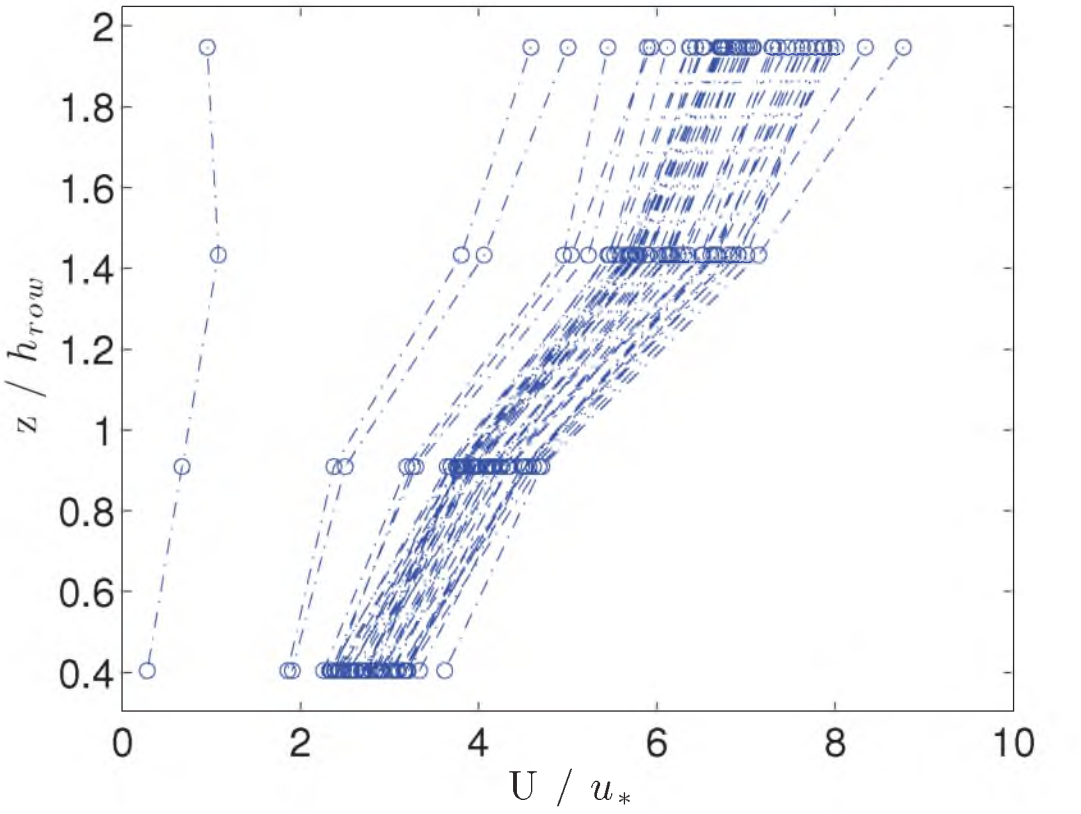

Figure A.1. Wind magnitude, U, normalized by u_* vs. height of sonic, z, normalized by the height of the rows, h; (Along flow, $0 > \zeta > -1$). Red dots show mean of the data set, and the blue lines show the 25^{th}, 50^{th}, and 75^{th} percentiles. All 30-minute period profiles.

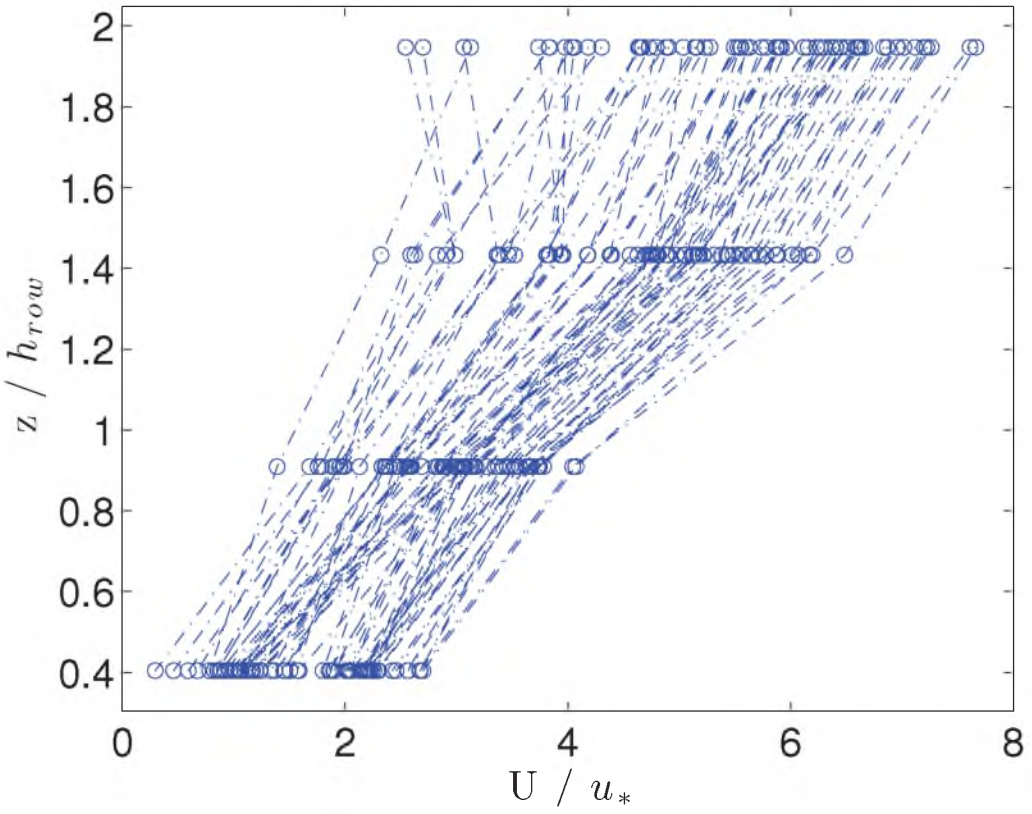

Figure A.2. Wind magnitude, U, normalized by u_* vs. height of sonic, z, normalized by the height of the rows, h; (cross flow, $0 > \zeta > -1$). Red dots show mean of the data set, and the blue lines show the 25^{th}, 50^{th}, and 75^{th} percentiles. All 30-minute period profiles.

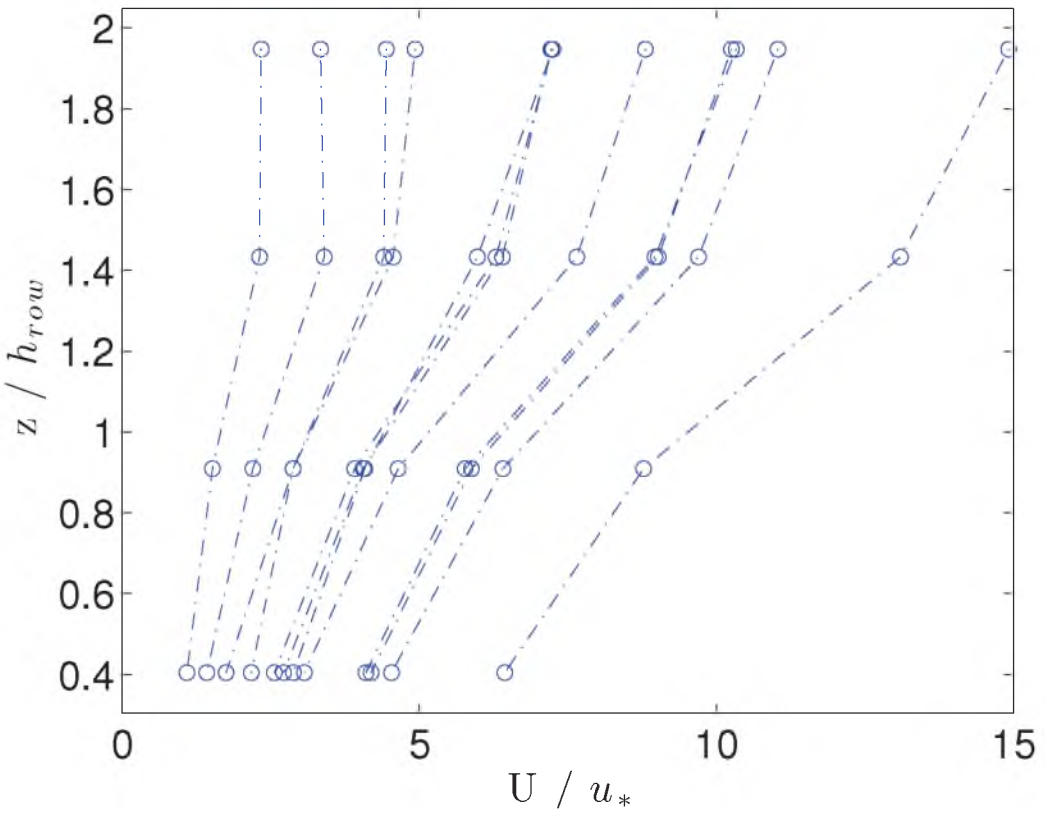

Figure A.3. Wind magnitude, U, normalized by u_* vs. height of sonic, z, normalized by the height of the rows, h; (along flow, $-1 > \zeta$). Red dots show mean of the data set, and the blue lines show the 25^{th}, 50^{th}, and 75^{th} percentiles. All 30-minute period profiles.

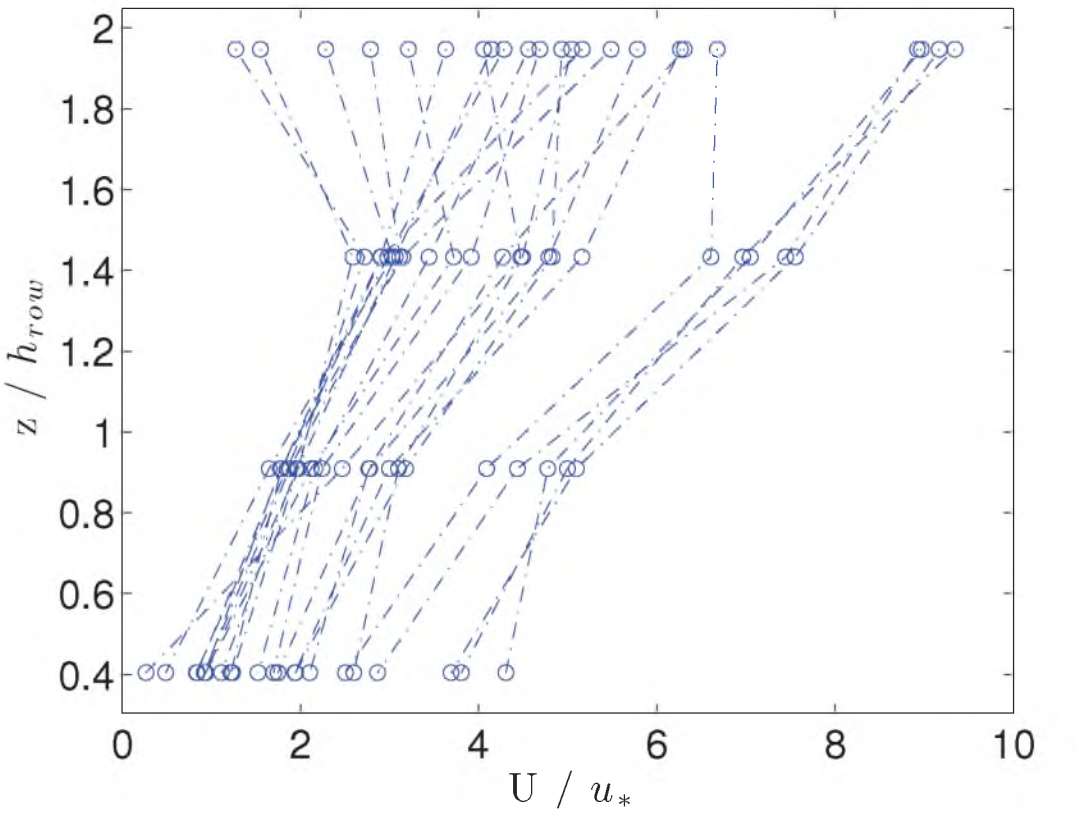

Figure A.4. Wind magnitude, U, normalized by u_* vs. height of sonic, z, normalized by the height of the rows, h; (cross flow, $-1 > \zeta$). Red dots show mean of the data set, and the blue lines show the 25^{th}, 50^{th}, and 75^{th} percentiles. All 30-minute period profiles.

APPENDIX B

PROFILES OF WIND COMPONENT DEVIATIONS

Table B.1. Deviation of u-component of wind, σ_u, normalized by u_* at sonic 1 (0.8m)

Wind Flow	Stability	25^{th}	50^{th}	75^{th}	Mean
Along	$0 > \zeta > -1$	1.58	1.71	2.02	1.81
Cross	$0 > \zeta > -1$	1.19	1.47	1.75	1.54
Along	$-1 > \zeta$	2.64	3.20	3.69	3.55
Cross	$-1 > \zeta$	2.62	2.96	3.36	3.22

Table B.2. Deviation of u-component of wind, σ_u, normalized by u_* at sonic 2 (1.8m)

Wind Flow	Stability	25^{th}	50^{th}	75^{th}	Mean
Along	$0 > \zeta > -1$	2.03	2.17	2.51	2.29
Cross	$0 > \zeta > -1$	1.72	1.94	2.17	2.03
Along	$-1 > \zeta$	3.03	3.75	4.37	4.18
Cross	$-1 > \zeta$	3.05	3.35	4.03	3.73

Table B.3. Deviation of u-component of wind, σ_u, normalized by u_* at sonic 3 (2.9m)

Wind Flow	Stability	25^{th}	50^{th}	75^{th}	Mean
Along	$0 > \zeta > -1$	2.48	2.61	3.23	2.85
Cross	$0 > \zeta > -1$	2.10	2.42	2.89	2.59
Along	$-1 > \zeta$	3.91	4.70	5.72	5.33
Cross	$-1 > \zeta$	3.82	4.51	5.40	4.95

Table B.4. Deviation of u-component of wind, σ_u, normalized by u_* at sonic 4 (3.9m)

Wind Flow	Stability	25^{th}	50^{th}	75^{th}	Mean
Along	$0 > \zeta > -1$	2.54	2.69	3.39	2.99
Cross	$0 > \zeta > -1$	2.23	2.48	3.09	2.73
Along	$-1 > \zeta$	4.21	5.02	6.21	5.71
Cross	$-1 > \zeta$	4.02	4.90	5.99	5.34

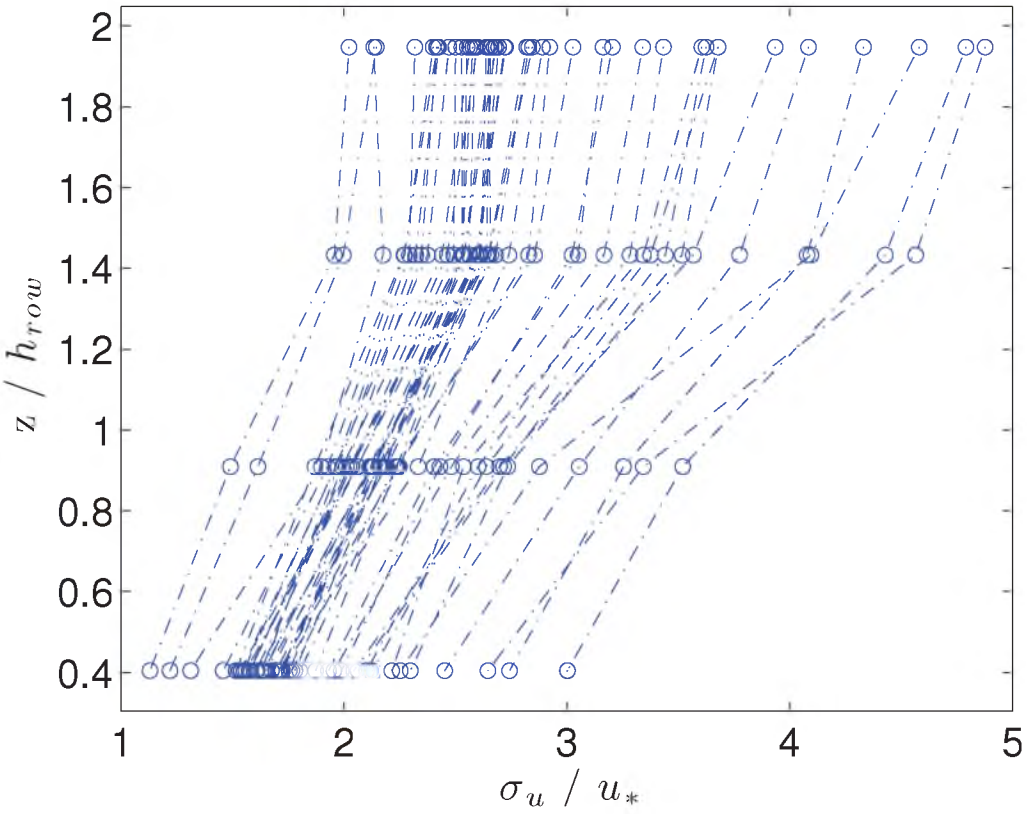

Figure B.1. Deviation of u-component of wind, σ_u, normalized by u_* vs. height of sonic, z, normalized by the height of the rows, h; (Along flow, $0 > \zeta > -1$). Red dots show mean of the data set, and the blue lines show the 25^{th}, 50^{th}, and 75^{th} percentiles. All 30-minute period.

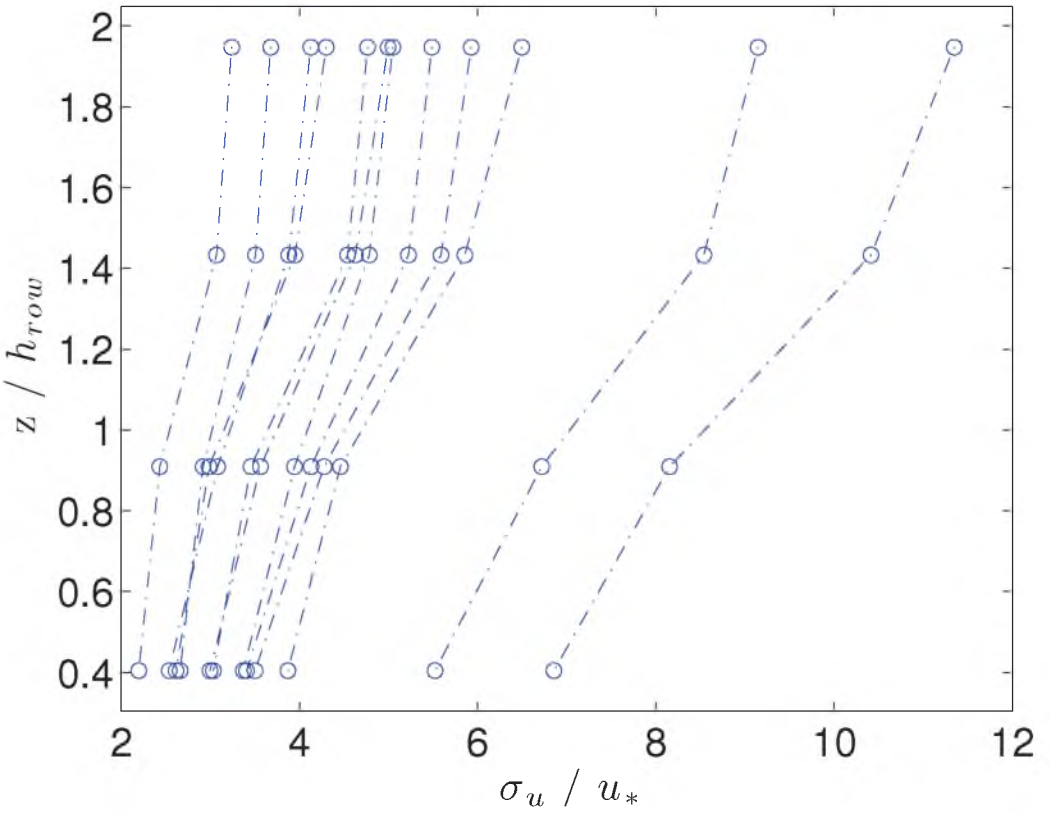

Figure B.2. Deviation of u-component of wind, σ_u, normalized by u_* vs. height of sonic, z, normalized by the height of the rows, h; (cross flow, $0 > \zeta > -1$). Red dots show mean of the data set, and the blue lines show the 25^{th}, 50^{th}, and 75^{th} percentiles. All 30-minute period.

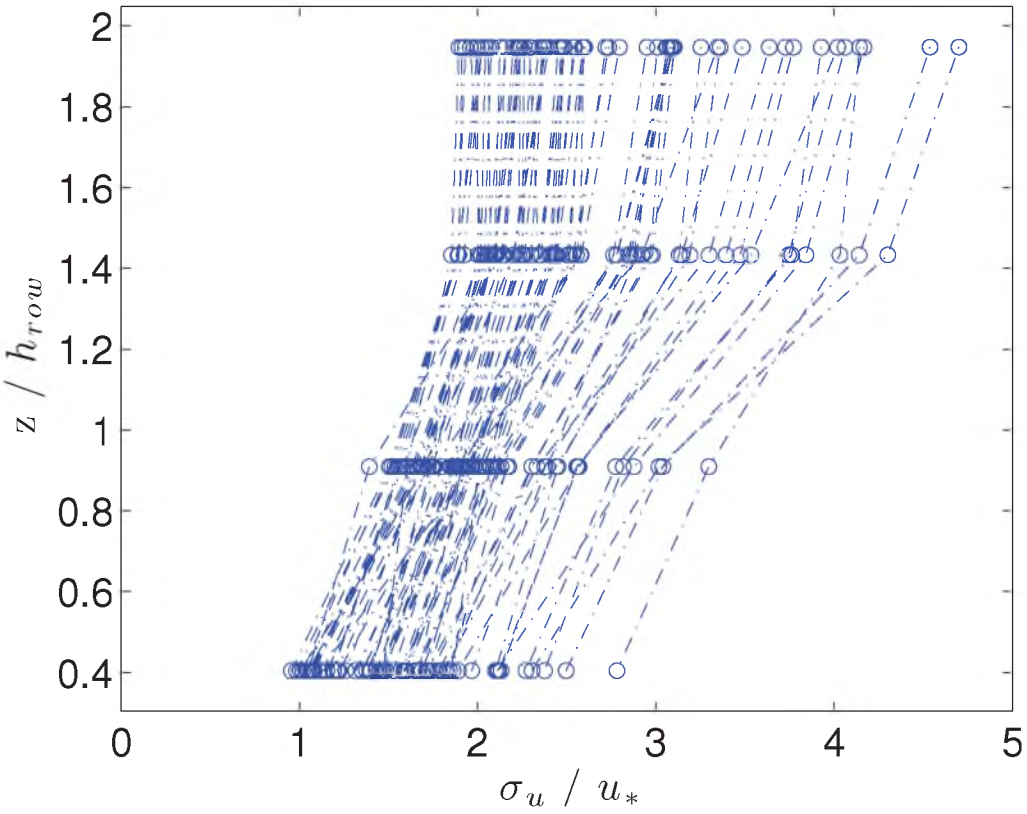

Figure B.3. Deviation of u-component of wind, σ_u, normalized by u_* vs. height of sonic, z, normalized by the height of the rows, h; (along flow, $-1 > \zeta$). Red dots show mean of the data set, and the blue lines show the 25^{th}, 50^{th}, and 75^{th} percentiles. All 30-minute period.

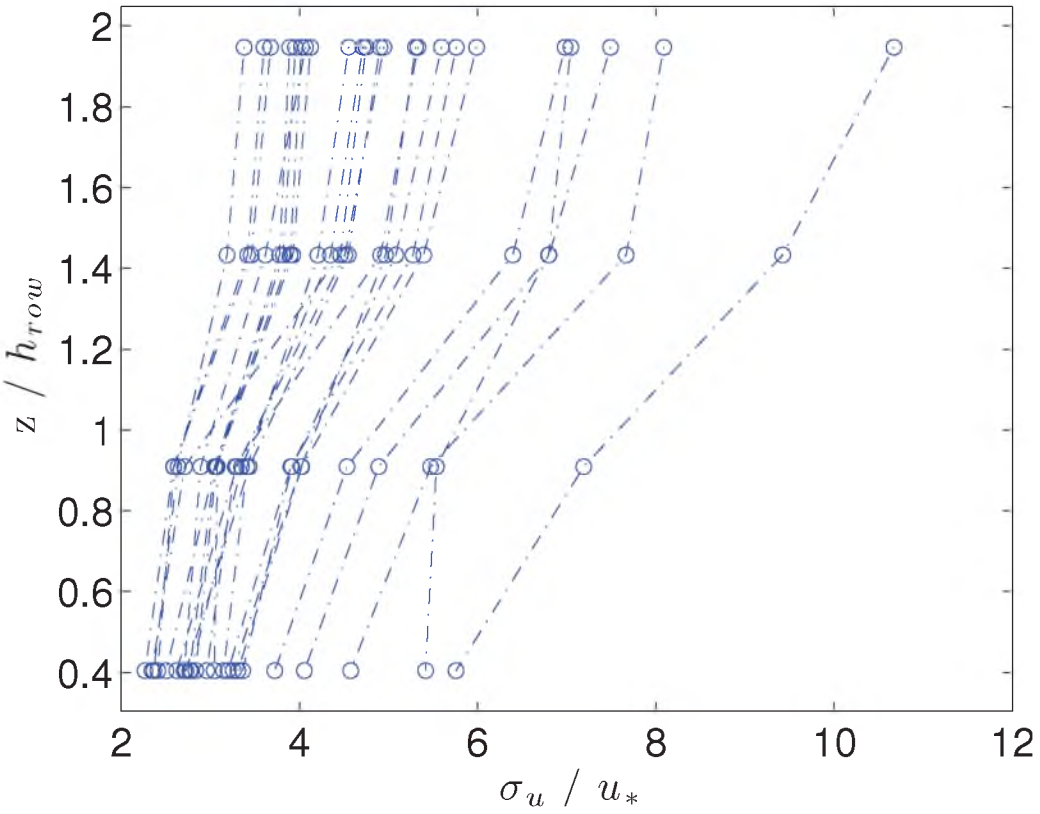

Figure B.4. Deviation of u-component of wind, σ_u, normalized by u_* vs. height of sonic, z, normalized by the height of the rows, h; (cross flow, $-1 > \zeta$). Red dots show mean of the data set, and the blue lines show the 25^{th}, 50^{th}, and 75^{th} percentiles. All 30-minute period.

Table B.5. Deviation of v-component of wind, σ_v, normalized by u_* at sonic 1 (0.8m)

Wind Flow	Stability	25^{th}	50^{th}	75^{th}	Mean
Along	$0 > \zeta > -1$	1.01	1.09	1.22	1.13
Cross	$0 > \zeta > -1$	0.86	0.98	1.10	1.01
Along	$-1 > \zeta$	1.66	1.76	2.27	2.02
Cross	$-1 > \zeta$	1.44	1.79	1.98	1.84

Table B.6. Deviation of v-component of wind, σ_v, normalized by u_* at sonic 2 (1.8m)

Wind Flow	Stability	25^{th}	50^{th}	75^{th}	Mean
Along	$0 > \zeta > -1$	1.81	1.98	2.23	2.08
Cross	$0 > \zeta > -1$	1.73	1.84	2.16	2.00
Along	$-1 > \zeta$	3.22	3.73	4.73	3.95
Cross	$-1 > \zeta$	2.65	3.17	3.87	3.37

Table B.7. Deviation of v-component of wind, σ_v, normalized by u_* at sonic 3 (2.9m)

Wind Flow	Stability	25^{th}	50^{th}	75^{th}	Mean
Along	$0 > \zeta > -1$	2.37	2.67	3.19	2.86
Cross	$0 > \zeta > -1$	2.19	2.48	2.95	2.68
Along	$-1 > \zeta$	4.59	5.25	6.66	5.53
Cross	$-1 > \zeta$	3.57	4.36	5.75	4.64

Table B.8. Deviation of v-component of wind, σ_v, normalized by u_* at sonic 4 (3.9m)

Wind Flow	Stability	25^{th}	50^{th}	75^{th}	Mean
Along	$0 > \zeta > -1$	2.52	2.88	3.52	3.10
Cross	$0 > \zeta > -1$	2.30	2.73	3.37	2.89
Along	$-1 > \zeta$	4.93	5.85	7.18	6.00
Cross	$-1 > \zeta$	3.90	4.74	6.35	5.02

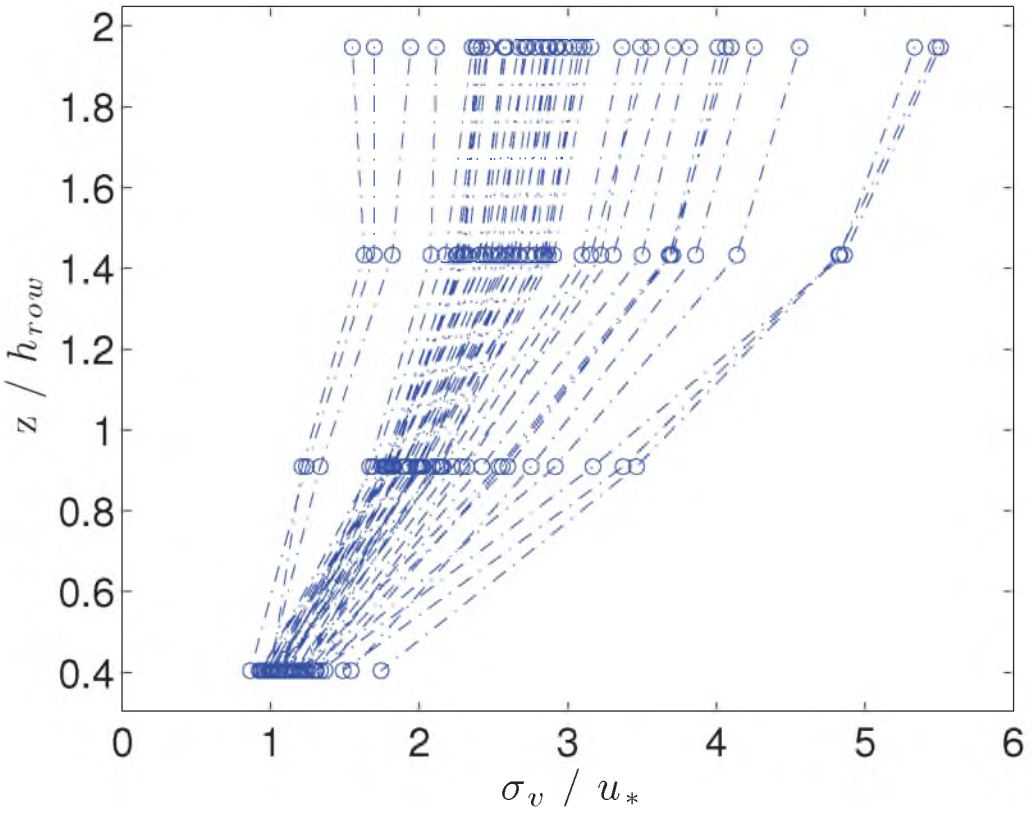

Figure B.5. Deviation of v-component of wind, σ_v, normalized by u_* vs. height of sonic, z, normalized by the height of the rows, h; (Along flow, $0 > \zeta > -1$). Red dots show mean of the data set, and the blue lines show the 25^{th}, 50^{th}, and 75^{th} percentiles. All 30-minute period profiles.

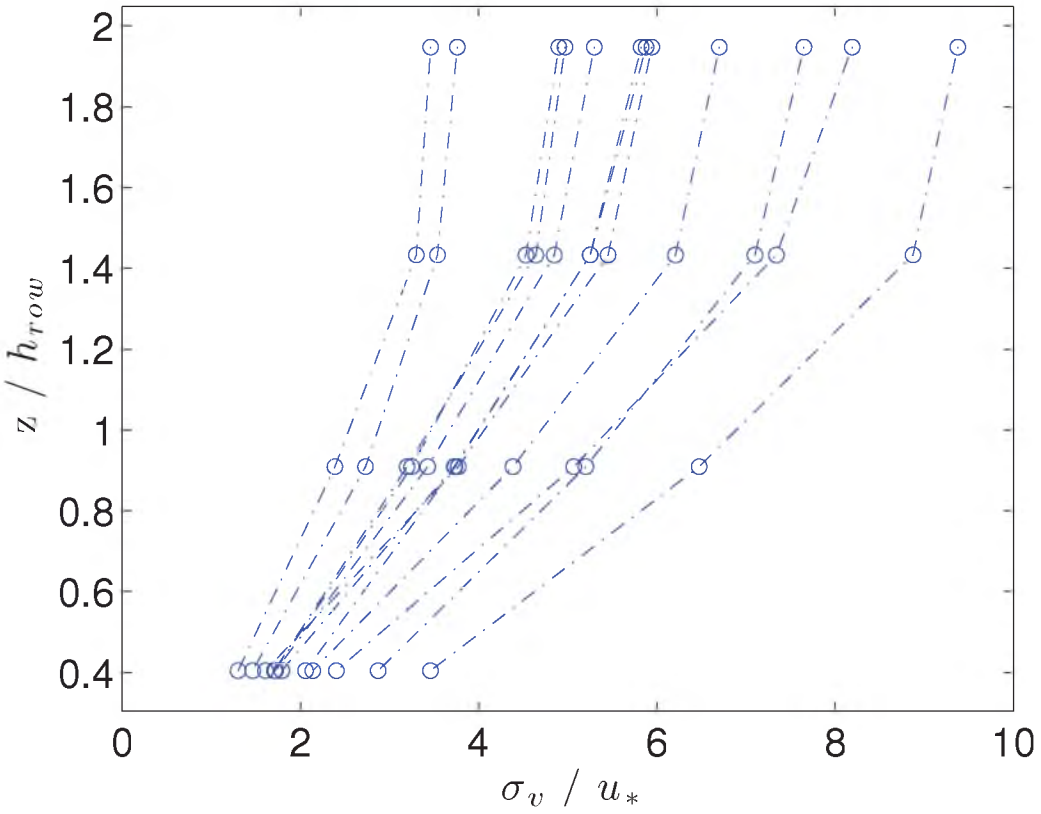

Figure B.6. Deviation of v-component of wind, σ_v, normalized by u_* vs. height of sonic, z, normalized by the height of the rows, h; (cross flow, $0 > \zeta > -1$). Red dots show mean of the data set, and the blue lines show the 25^{th}, 50^{th}, and 75^{th} percentiles. All 30-minute period profiles.

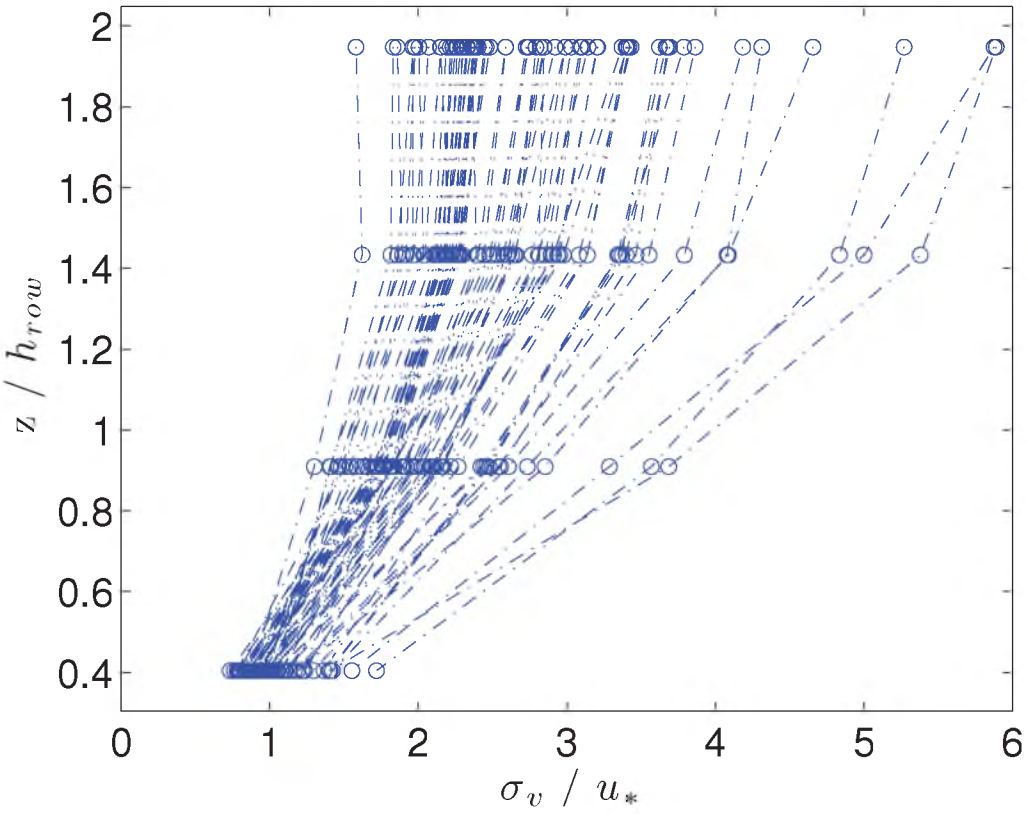

Figure B.7. Deviation of v-component of wind, σ_v, normalized by u_* vs. height of sonic, z, normalized by the height of the rows, h; (along flow, $-1 > \zeta$). Red dots show mean of the data set, and the blue lines show the 25^{th}, 50^{th}, and 75^{th} percentiles. All 30-minute period profiles.

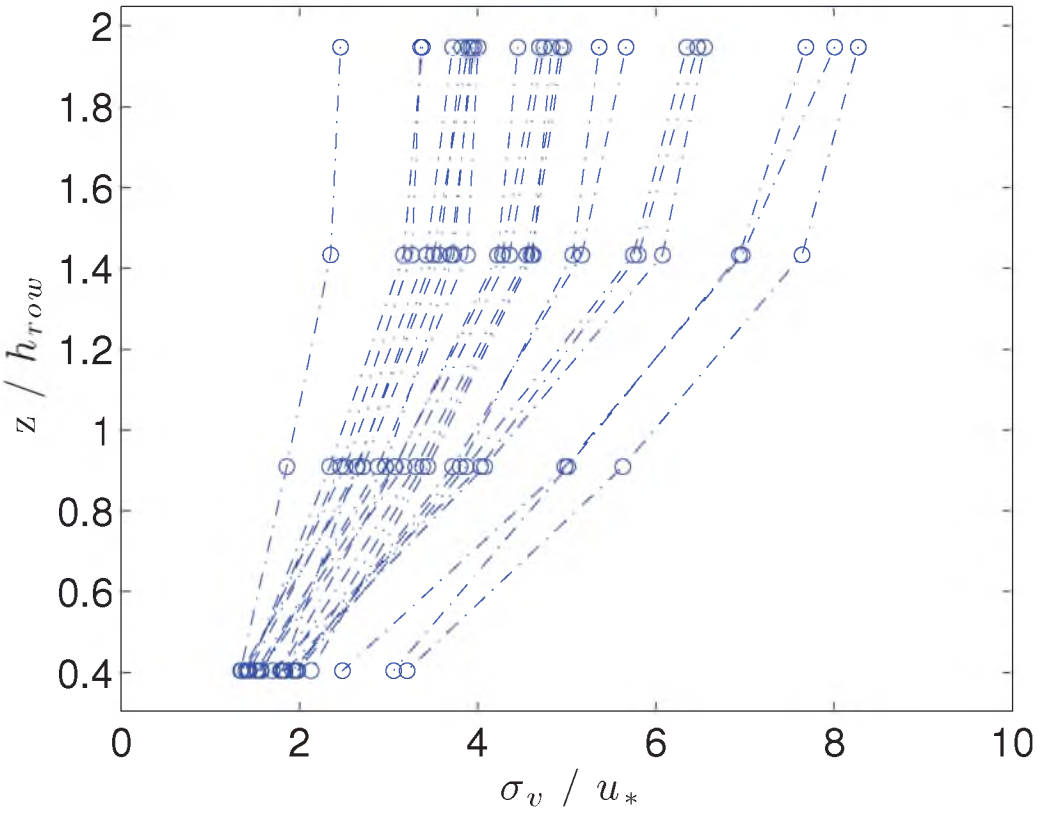

Figure B.8. Deviation of v-component of wind, σ_v, normalized by u_* vs. height of sonic, z, normalized by the height of the rows, h; (cross flow, $-1 > \zeta$). Red dots show mean of the data set, and the blue lines show the 25^{th}, 50^{th}, and 75^{th} percentiles. All 30-minute period profiles.

Table B.9. Deviation of w-component of wind, σ_w, normalized by u_* at sonic 1 (0.8m)

Wind Flow	Stability	25^{th}	50^{th}	75^{th}	Mean
Along	$0 > \zeta > -1$	0.90	0.96	1.06	0.99
Cross	$0 > \zeta > -1$	0.73	0.81	0.91	0.83
Along	$-1 > \zeta$	1.31	1.48	1.90	1.67
Cross	$-1 > \zeta$	1.25	1.40	1.50	1.47

Table B.10. Deviation of w-component of wind, σ_w, normalized by u_* at sonic 2 (1.8m)

Wind Flow	Stability	25^{th}	50^{th}	75^{th}	Mean
Along	$0 > \zeta > -1$	1.21	1.30	1.42	1.33
Cross	$0 > \zeta > -1$	1.13	1.16	1.24	1.20
Along	$-1 > \zeta$	1.72	1.92	2.50	2.17
Cross	$-1 > \zeta$	1.58	1.79	1.97	1.90

Table B.11. Deviation of w-component of wind, σ_w, normalized by u_* at sonic 3 (2.9m)

Wind Flow	Stability	25^{th}	50^{th}	75^{th}	Mean
Along	$0 > \zeta > -1$	1.26	1.35	1.44	1.37
Cross	$0 > \zeta > -1$	1.15	1.22	1.32	1.26
Along	$-1 > \zeta$	1.88	2.04	2.59	2.31
Cross	$-1 > \zeta$	1.70	1.95	2.20	2.08

Table B.12. Deviation of w-component of wind, σ_w, normalized by u_* at sonic 4 (3.9m)

Wind Flow	Stability	25^{th}	50^{th}	75^{th}	Mean
Along	$0 > \zeta > -1$	1.26	1.32	1.45	1.38
Cross	$0 > \zeta > -1$	1.17	1.23	1.36	1.29
Along	$-1 > \zeta$	2.00	2.13	2.71	2.43
Cross	$-1 > \zeta$	1.85	2.07	2.38	2.25

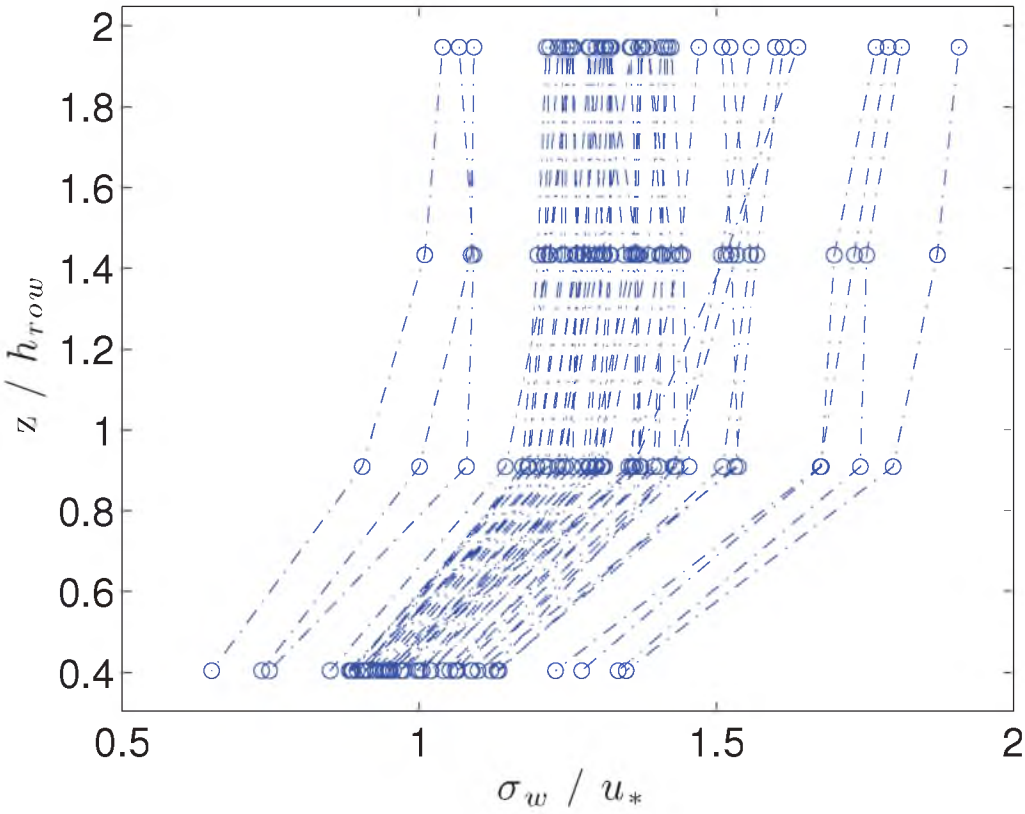

Figure B.9. Deviation of w-component of wind, σ_w, normalized by u_* vs. height of sonic, z, normalized by the height of the rows, h; (Along flow, $0 > \zeta > -1$). Red dots show mean of the data set, and the blue lines show the 25^{th}, 50^{th}, and 75^{th} percentiles. All 30-minute period.

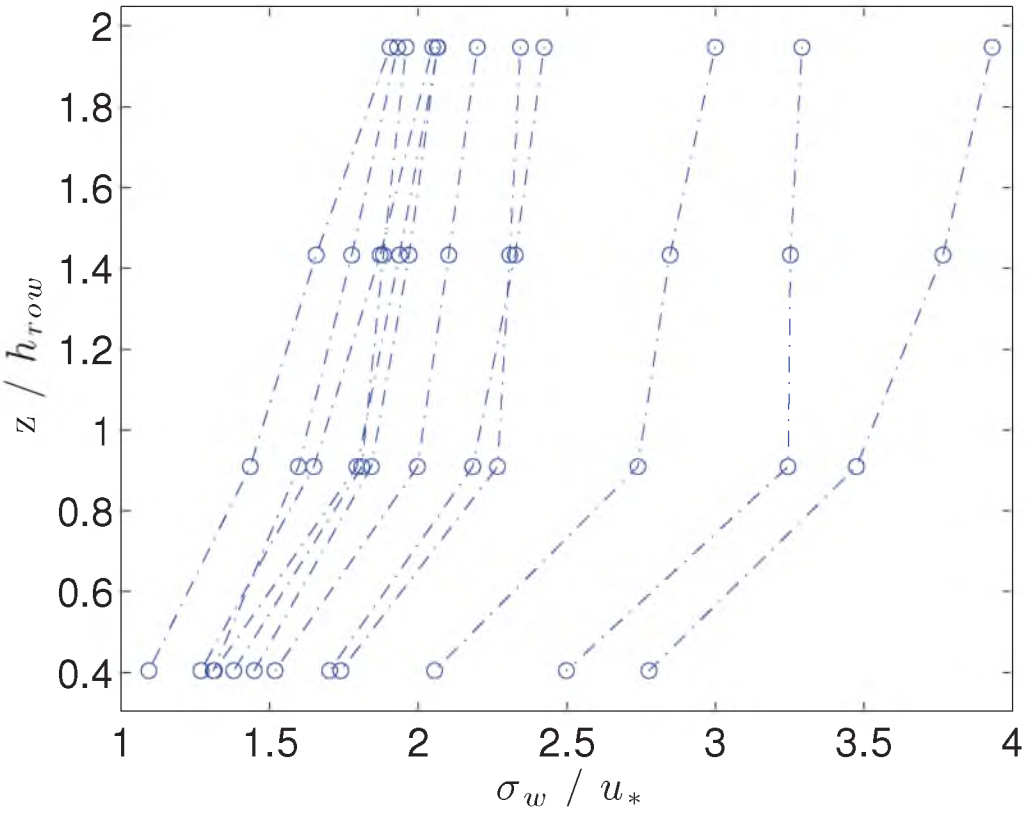

Figure B.10. Deviation of w-component of wind, σ_w, normalized by u_* vs. height of sonic, z, normalized by the height of the rows, h; (cross flow, $0 > \zeta > -1$). Red dots show mean of the data set, and the blue lines show the 25^{th}, 50^{th}, and 75^{th} percentiles. All 30-minute period.

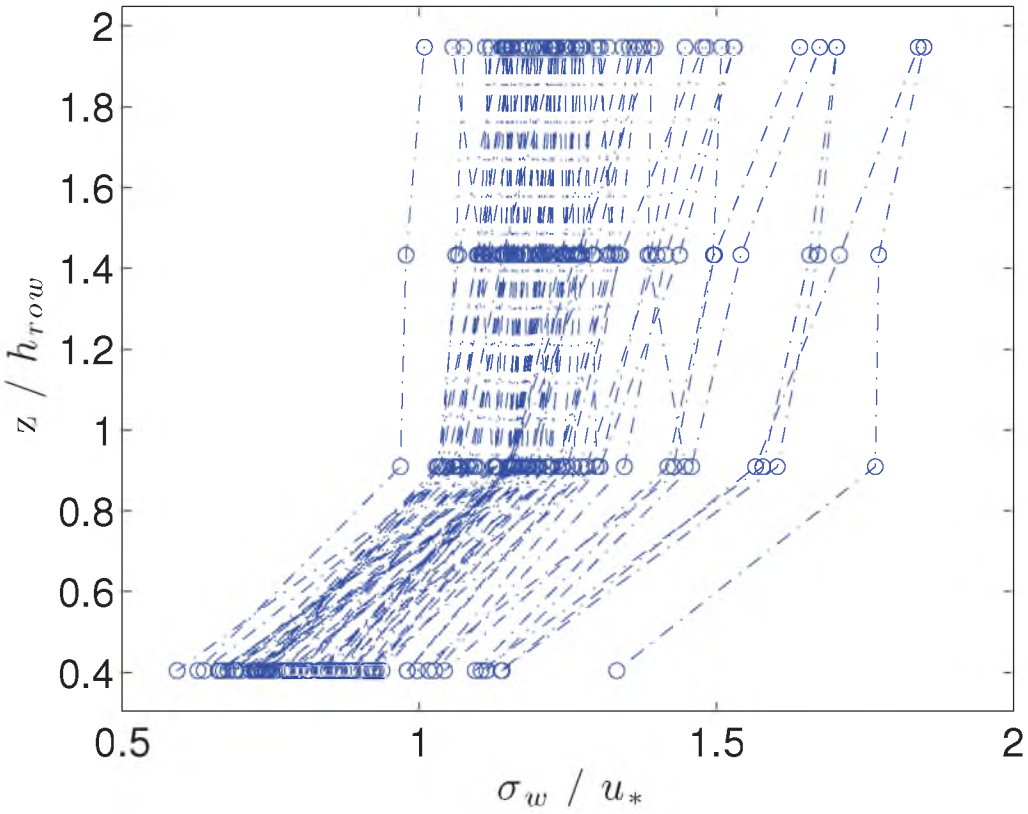

Figure B.11. Deviation of w-component of wind, σ_w, normalized by u_* vs. height of sonic, z, normalized by the height of the rows, h; (along flow, $-1 > \zeta$). Red dots show mean of the data set, and the blue lines show the 25^{th}, 50^{th}, and 75^{th} percentiles. All 30-minute period.

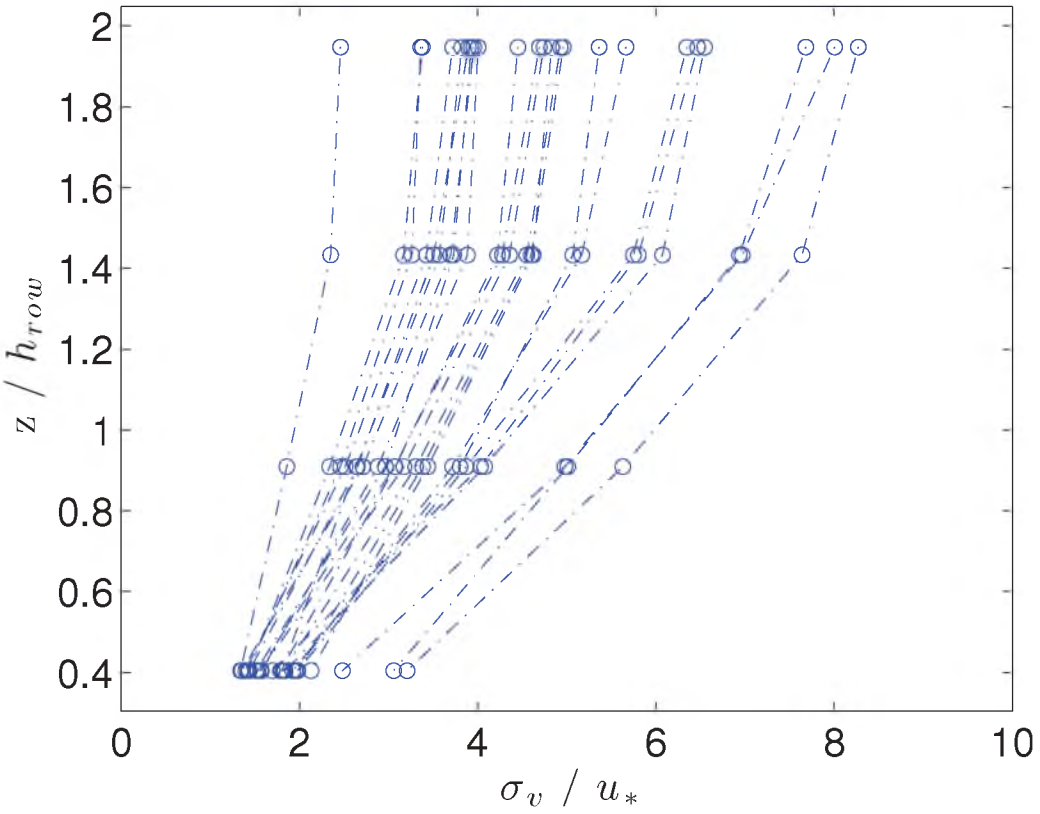

Figure B.12. Deviation of v-component of wind, σ_v, normalized by u_* vs. height of sonic, z, normalized by the height of the rows, h; (cross flow, $-1 > \zeta$). Red dots show mean of the data set, and the blue lines show the 25^{th}, 50^{th}, and 75^{th} percentiles. All 30-minute period.

APPENDIX C

PROFILES OF VERTICAL KINEMATIC FLUXES

Table C.1. Vertical kinematic eddy flux of U-momentum, $\overline{u'\,w'}$, normalized by u_*^2 at sonic 1 (0.8m)

Wind Flow	Stability	25^{th}	50^{th}	75^{th}	Mean
Along	$0 > \zeta > -1$	-0.33	-0.29	-0.24	-0.24
Cross	$0 > \zeta > -1$	-0.11	-0.01	0.10	-0.01
Along	$-1 > \zeta$	-0.37	-0.17	0.01	-0.19
Cross	$-1 > \zeta$	0.05	0.33	0.56	0.29

Table C.2. Vertical kinematic eddy flux of U-momentum, $\overline{u'\,w'}$, normalized by u_*^2 at sonic 2 (1.8m)

Wind Flow	Stability	25^{th}	50^{th}	75^{th}	Mean
Along	$0 > \zeta > -1$	-1.06	-0.85	-0.77	-0.81
Cross	$0 > \zeta > -1$	-0.63	-0.28	0.57	-0.10
Along	$-1 > \zeta$	-2.24	-1.34	-0.71	-1.77
Cross	$-1 > \zeta$	-1.26	-0.73	-0.08	-0.80

Table C.3. Vertical kinematic eddy flux of U-momentum, $\overline{u'\,w'}$, normalized by u_*^2 at sonic 3 (2.9m)

Wind Flow	Stability	25^{th}	50^{th}	75^{th}	Mean
Along	$0 > \zeta > -1$	-1.09	-0.90	-0.75	-0.78
Cross	$0 > \zeta > -1$	-0.67	-0.26	0.59	-0.06
Along	$-1 > \zeta$	-1.57	-0.97	-0.78	-1.11
Cross	$-1 > \zeta$	-1.04	-0.25	0.30	-0.38

Table C.4. Vertical kinematic eddy flux of U-momentum, $\overline{u'\,w'}$, normalized by u_*^2 at sonic 4 (3.9m)

Wind Flow	Stability	25^{th}	50^{th}	75^{th}	Mean
Along	$0 > \zeta > -1$	-0.92	-0.77	-0.70	-0.65
Cross	$0 > \zeta > -1$	-0.64	-0.16	0.59	-0.06
Along	$-1 > \zeta$	-0.94	-0.80	-0.53	-0.66
Cross	$-1 > \zeta$	-0.75	0.05	0.52	-0.07

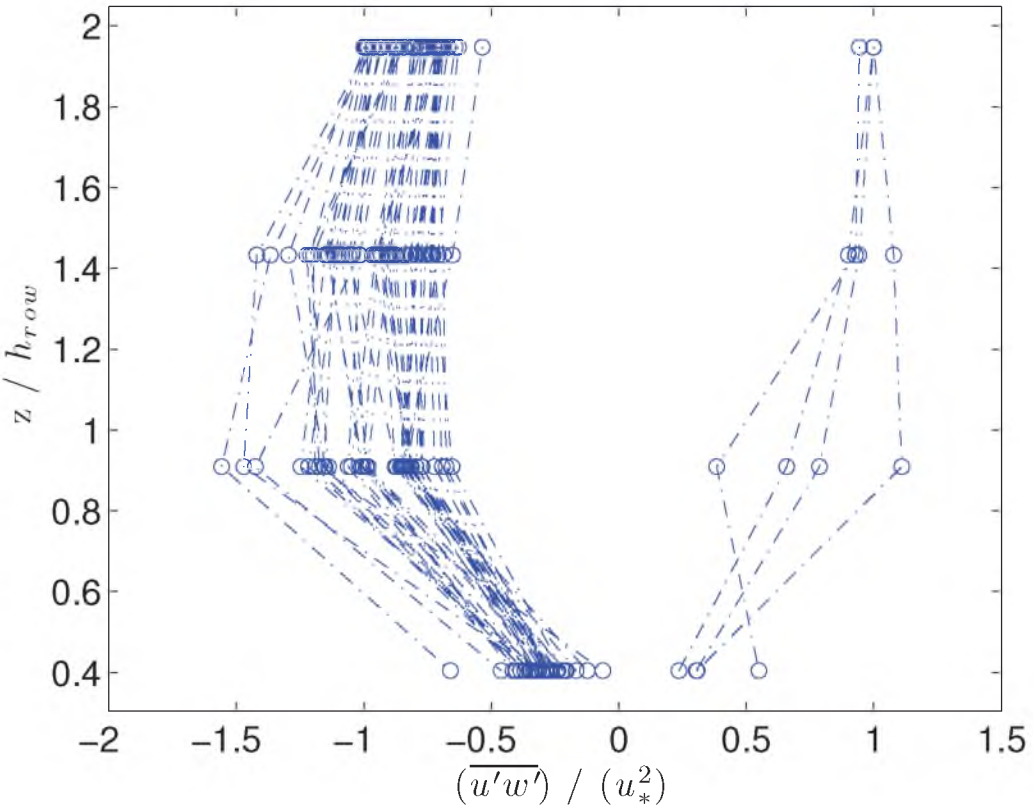

Figure C.1. Vertical kinematic eddy flux of U-momentum, $\overline{u'\,w'}$, normalized by u_*^2 vs. height of sonic, z, normalized by the height of the rows, h; (Along flow, $0 > \zeta > -1$). Red dots show mean of the data set, and the blue lines show the 25^{th}, 50^{th}, and 75^{th} percentiles. All 30-minute period profiles.

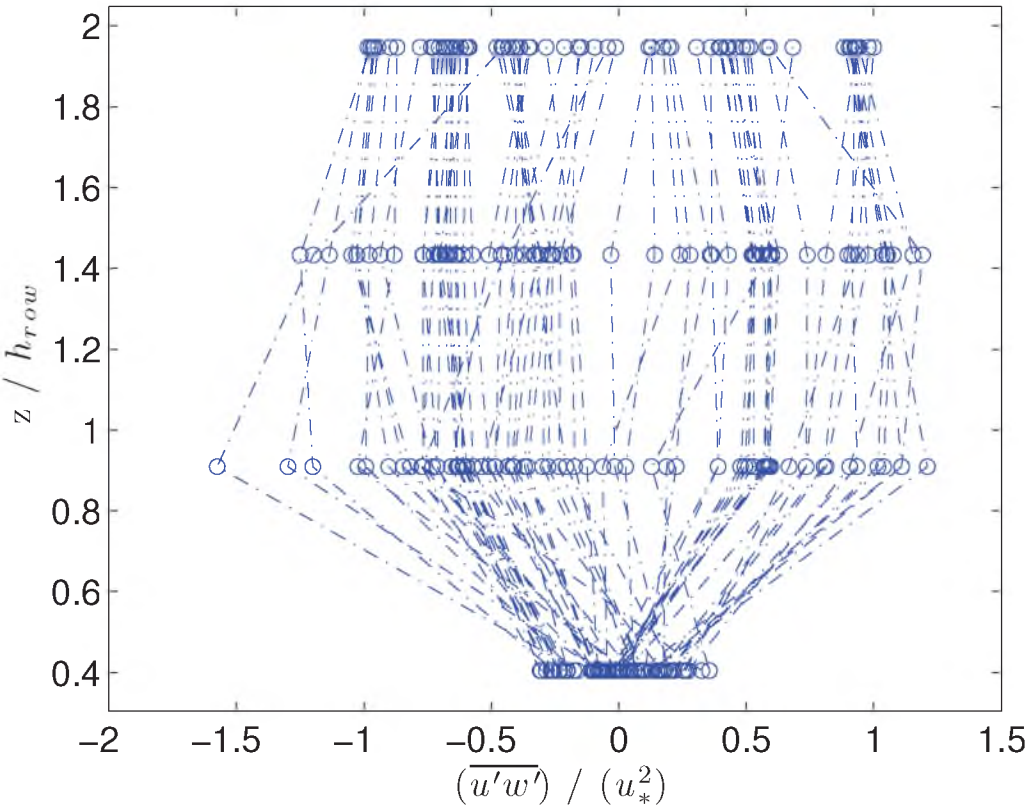

Figure C.2. Vertical kinematic eddy flux of U-momentum, $\overline{u'\,w'}$, normalized by u_*^2 vs. height of sonic, z, normalized by the height of the rows, h; (cross flow, $0 > \zeta > -1$). Red dots show mean of the data set, and the blue lines show the 25^{th}, 50^{th}, and 75^{th} percentiles. All 30-minute period profiles.

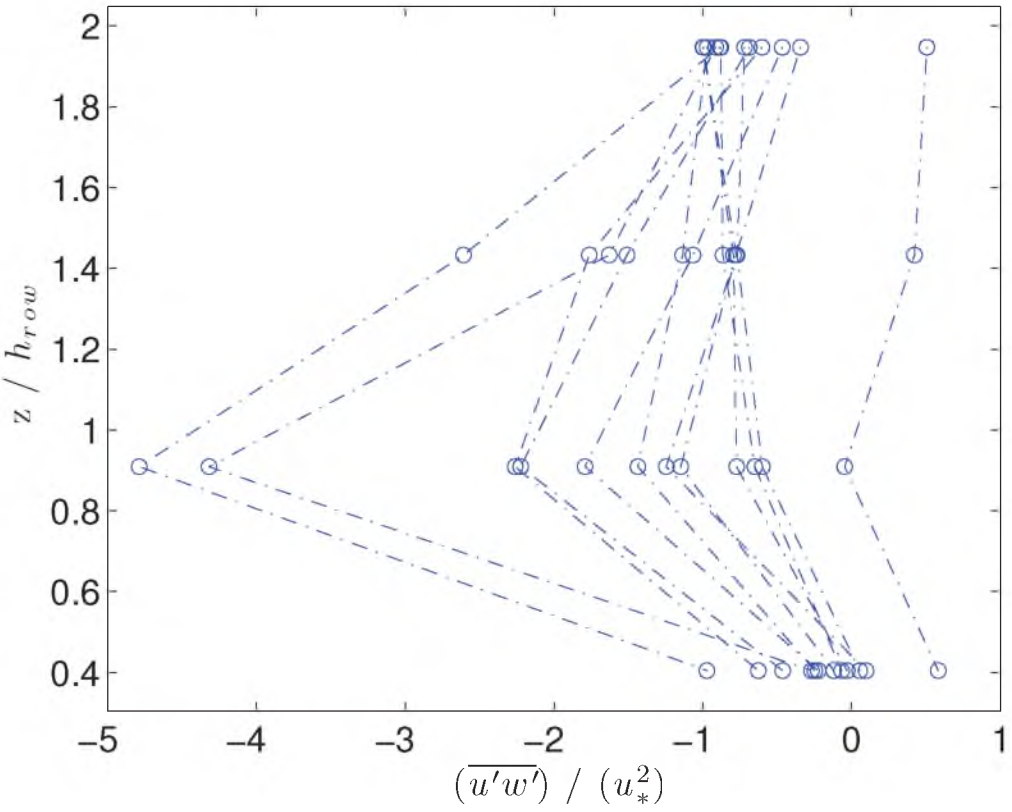

Figure C.3. Vertical kinematic eddy flux of U-momentum, $\overline{u'\,w'}$, normalized by u_*^2 vs. height of sonic, z, normalized by the height of the rows, h; (along flow, $-1 > \zeta$). Red dots show mean of the data set, and the blue lines show the 25^{th}, 50^{th}, and 75^{th} percentiles. All 30-minute period profiles.

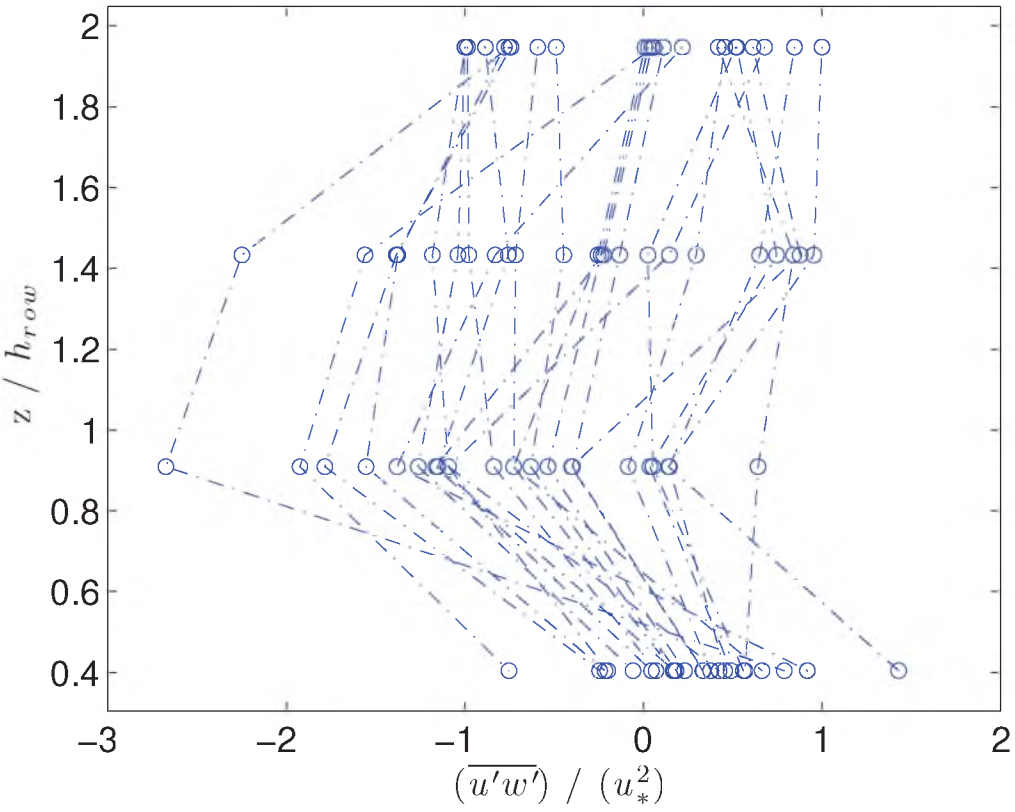

Figure C.4. Vertical kinematic eddy flux of U-momentum, $\overline{u'\,w'}$, normalized by u_*^2 vs. height of sonic, z, normalized by the height of the rows, h; (cross flow, $-1 > \zeta$). Red dots show mean of the data set, and the blue lines show the 25^{th}, 50^{th}, and 75^{th} percentiles. All 30-minute period profiles.

Table C.5. Vertical kinematic eddy flux of U-momentum, $\overline{v'\,w'}$, normalized by u_*^2 at sonic 1 (0.8m)

Wind Flow	Stability	25^{th}	50^{th}	75^{th}	Mean
Along	$0 > \zeta > -1$	0.04	0.07	0.12	0.08
Cross	$0 > \zeta > -1$	-0.04	-0.01	0.03	0.00
Along	$-1 > \zeta$	0.02	0.06	0.14	0.12
Cross	$-1 > \zeta$	-0.12	0.04	0.11	0.01

Table C.6. Vertical kinematic eddy flux of U-momentum, $\overline{v'\,w'}$, normalized by u_*^2 at sonic 2 (1.8m)

Wind Flow	Stability	25^{th}	50^{th}	75^{th}	Mean
Along	$0 > \zeta > -1$	0.39	0.60	0.70	0.51
Cross	$0 > \zeta > -1$	-0.79	-0.44	0.74	-0.11
Along	$-1 > \zeta$	0.48	0.87	1.00	0.95
Cross	$-1 > \zeta$	-0.34	0.17	1.32	0.35

Table C.7. Vertical kinematic eddy flux of U-momentum, $\overline{v'\,w'}$, normalized by u_*^2 at sonic 3 (2.9m)

Wind Flow	Stability	25^{th}	50^{th}	75^{th}	Mean
Along	$0 > \zeta > -1$	0.39	0.57	0.71	0.50
Cross	$0 > \zeta > -1$	-0.77	-0.39	0.78	-0.10
Along	$-1 > \zeta$	0.45	0.58	0.96	0.59
Cross	$-1 > \zeta$	-0.29	0.03	1.02	0.22

Table C.8. Vertical kinematic eddy flux of U-momentum, $\overline{v'\,w'}$, normalized by u_*^2 at sonic 4 (3.9m)

Wind Flow	Stability	25^{th}	50^{th}	75^{th}	Mean
Along	$0 > \zeta > -1$	0.27	0.58	0.71	0.46
Cross	$0 > \zeta > -1$	-0.90	-0.38	0.76	-0.16
Along	$-1 > \zeta$	-0.35	0.32	0.59	0.15
Cross	$-1 > \zeta$	-0.86	-0.04	0.79	-0.05

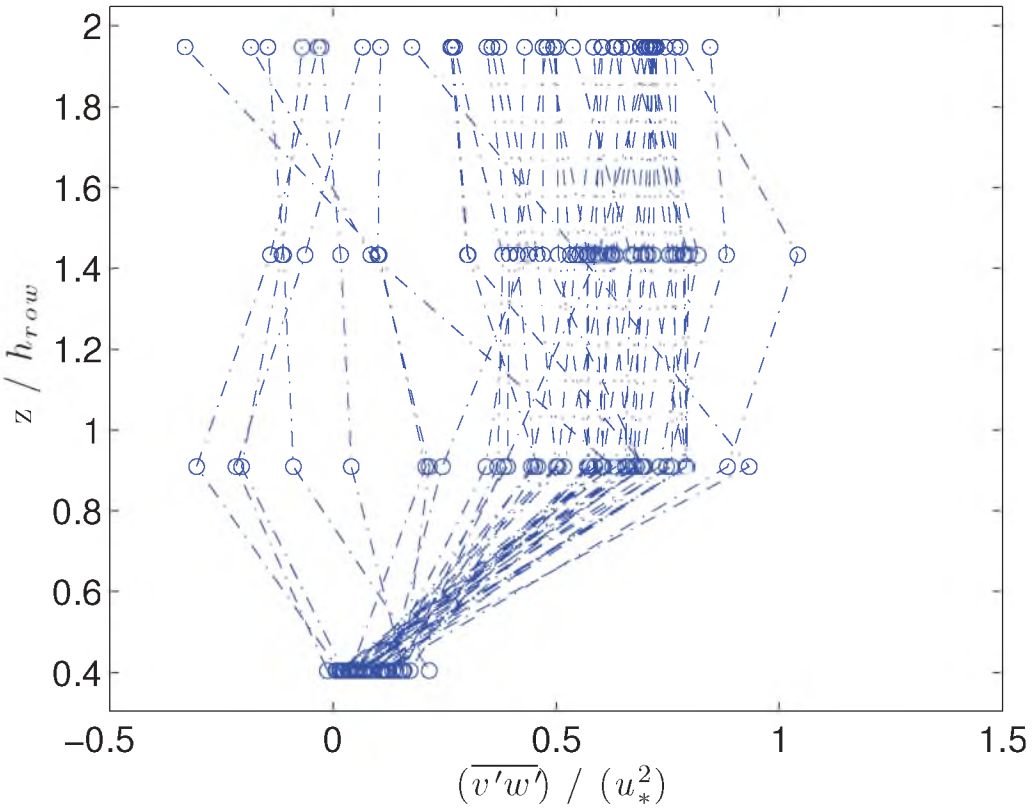

Figure C.5. Vertical kinematic eddy flux of U-momentum, $\overline{v'\,w'}$, normalized by u_*^2 vs. height of sonic, z, normalized by the height of the rows, h; (Along flow, $0 > \zeta > -1$). Red dots show mean of the data set, and the blue lines show the 25^{th}, 50^{th}, and 75^{th} percentiles. All 30-minute period profiles.

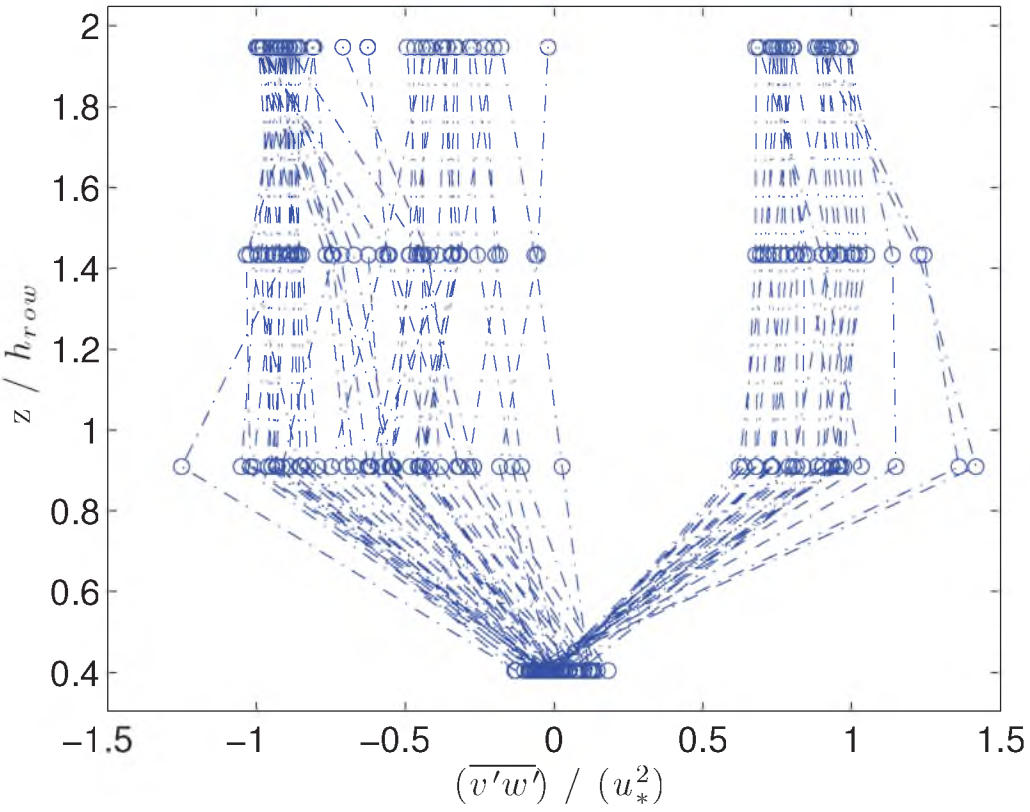

Figure C.6. Vertical kinematic eddy flux of U-momentum, $\overline{v'\,w'}$, normalized by u_*^2 vs. height of sonic, z, normalized by the height of the rows, h; (cross flow, $0 > \zeta > -1$). Red dots show mean of the data set, and the blue lines show the 25^{th}, 50^{th}, and 75^{th} percentiles. All 30-minute period profiles.

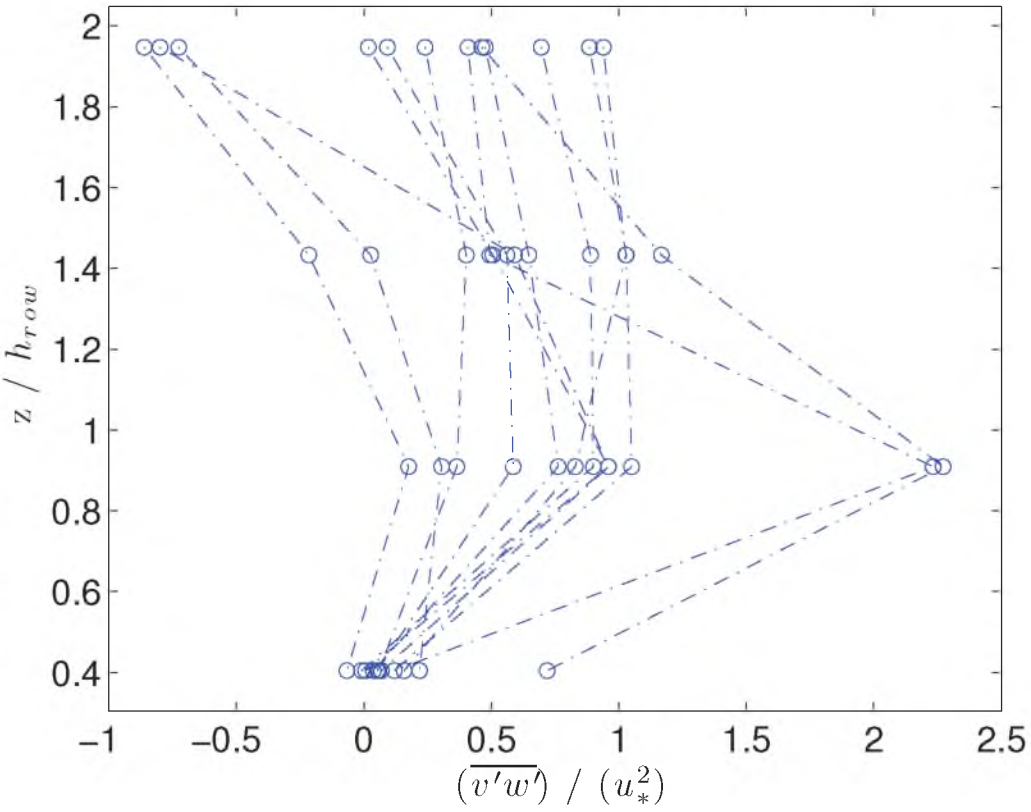

Figure C.7. Vertical kinematic eddy flux of U-momentum, $\overline{v'w'}$, normalized by u_*^2 vs. height of sonic, z, normalized by the height of the rows, h; (along flow, $-1 > \zeta$). Red dots show mean of the data set, and the blue lines show the 25^{th}, 50^{th}, and 75^{th} percentiles. All 30-minute period profiles.

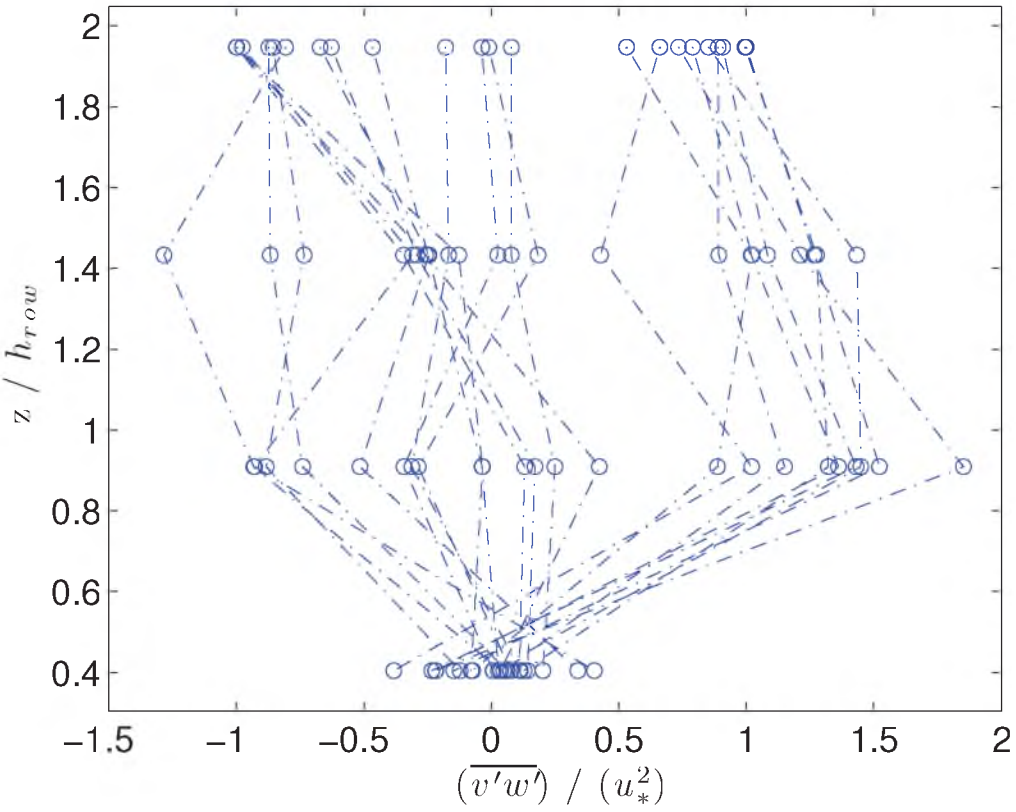

Figure C.8. Vertical kinematic eddy flux of U-momentum, $\overline{v'\,w'}$, normalized by u_*^2 vs. height of sonic, z, normalized by the height of the rows, h; (cross flow, $-1 > \zeta$). Red dots show mean of the data set, and the blue lines show the 25^{th}, 50^{th}, and 75^{th} percentiles. All 30-minute period profiles.

Table C.9. Vertical kinematic eddy flux of U-momentum, $\overline{u'\,w'}$ and $\overline{v'\,w'}$, normalized by u_*^2 at sonic 1 (0.8m)

Wind Flow	Stability	25^{th}	50^{th}	75^{th}	Mean
Along	$0 > \zeta > -1$	0.27	0.30	0.36	0.32
Cross	$0 > \zeta > -1$	0.08	0.14	0.22	0.15
Along	$-1 > \zeta$	0.09	0.25	0.55	0.35
Cross	$-1 > \zeta$	0.19	0.38	0.62	0.46

Table C.10. Vertical kinematic eddy flux of U-momentum, $\overline{u'\,w'}$ and $\overline{v'\,w'}$, normalized by u_*^2 at sonic 2 (1.8m)

Wind Flow	Stability	25^{th}	50^{th}	75^{th}	Mean
Along	$0 > \zeta > -1$	0.99	1.08	1.21	1.11
Cross	$0 > \zeta > -1$	0.92	0.99	1.11	1.02
Along	$-1 > \zeta$	1.16	1.45	2.35	2.06
Cross	$-1 > \zeta$	0.97	1.31	1.61	1.36

Table C.11. Vertical kinematic eddy flux of U-momentum, $\overline{u'\,w'}$ and $\overline{v'\,w'}$, normalized by u_*^2 at sonic 3 (2.9m)

Wind Flow	Stability	25^{th}	50^{th}	75^{th}	Mean
Along	$0 > \zeta > -1$	1.05	1.10	1.20	1.13
Cross	$0 > \zeta > -1$	0.96	1.04	1.11	1.04
Along	$-1 > \zeta$	1.02	1.25	1.61	1.38
Cross	$-1 > \zeta$	0.94	1.21	1.41	1.16

Table C.12. Vertical kinematic eddy flux of U-momentum, $\overline{u'\,w'}$ and $\overline{v'\,w'}$, normalized by u_*^2 at sonic 4 (3.9m)

Wind Flow	Stability	25^{th}	50^{th}	75^{th}	Mean
Along	$0 > \zeta > -1$	1.00	1.00	1.00	1.00
Cross	$0 > \zeta > -1$	1.00	1.00	1.00	1.00
Along	$-1 > \zeta$	1.00	1.00	1.00	1.00
Cross	$-1 > \zeta$	1.00	1.00	1.00	1.00

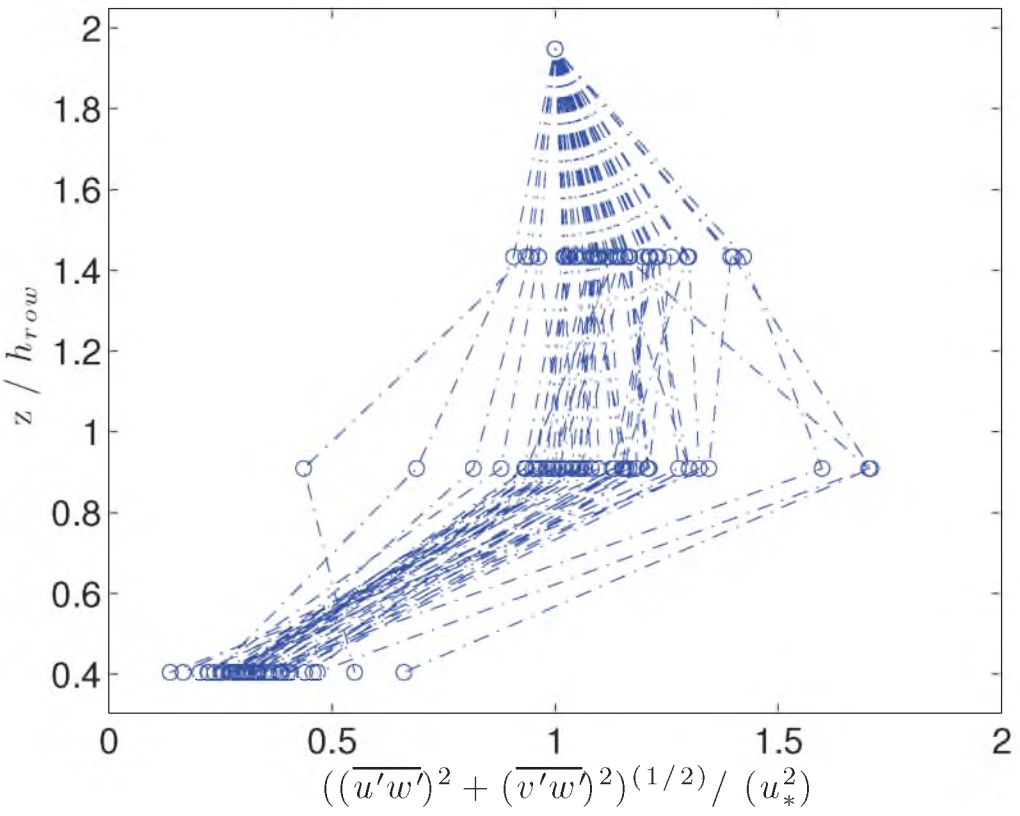

Figure C.9. Vertical kinematic eddy flux of U-momentum, $\overline{u'\,w'}$ and $\overline{v'\,w'}$, normalized by u_*^2 vs. height of sonic, z, normalized by the height of the rows, h; (Along flow, $0 > \zeta > -1$). Red dots show mean of the data set, and the blue lines show the 25^{th}, 50^{th}, and 75^{th} percentiles. All 30-minute period profiles.

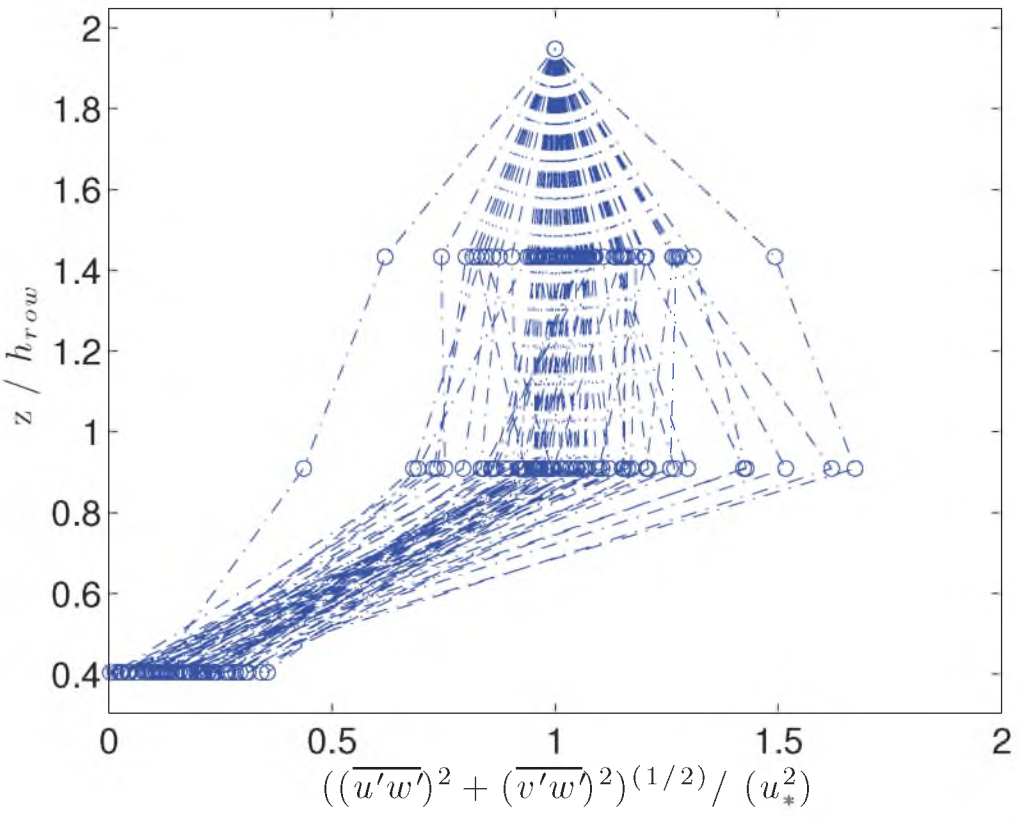

Figure C.10. Vertical kinematic eddy flux of U-momentum, $\overline{u'\,w'}$ and $\overline{v'\,w'}$, normalized by u_*^2 vs. height of sonic, z, normalized by the height of the rows, h; (cross flow, $0 > \zeta > -1$). Red dots show mean of the data set, and the blue lines show the 25^{th}, 50^{th}, and 75^{th} percentiles. All 30-minute period profiles.

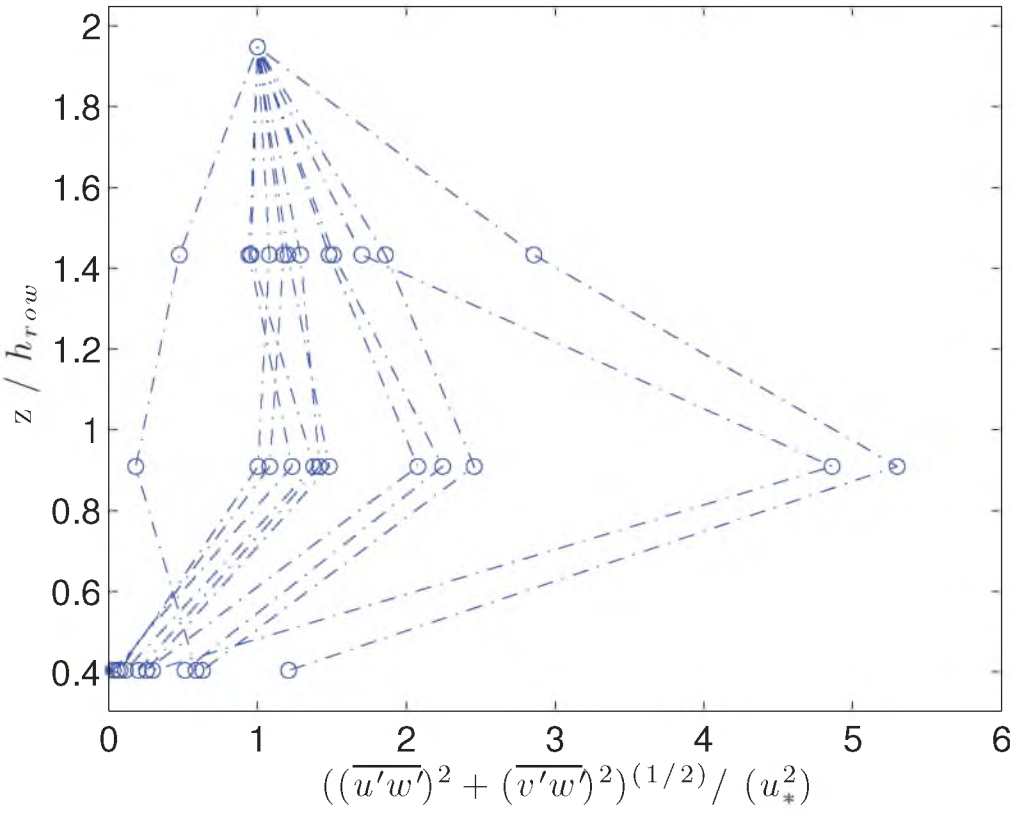

Figure C.11. Vertical kinematic eddy flux of U-momentum, $\overline{u'\,w'}$ and $\overline{v'\,w'}$, normalized by u_*^2 vs. height of sonic, z, normalized by the height of the rows, h; (along flow, $-1 > \zeta$). Red dots show mean of the data set, and the blue lines show the 25^{th}, 50^{th}, and 75^{th} percentiles. All 30-minute period profiles.

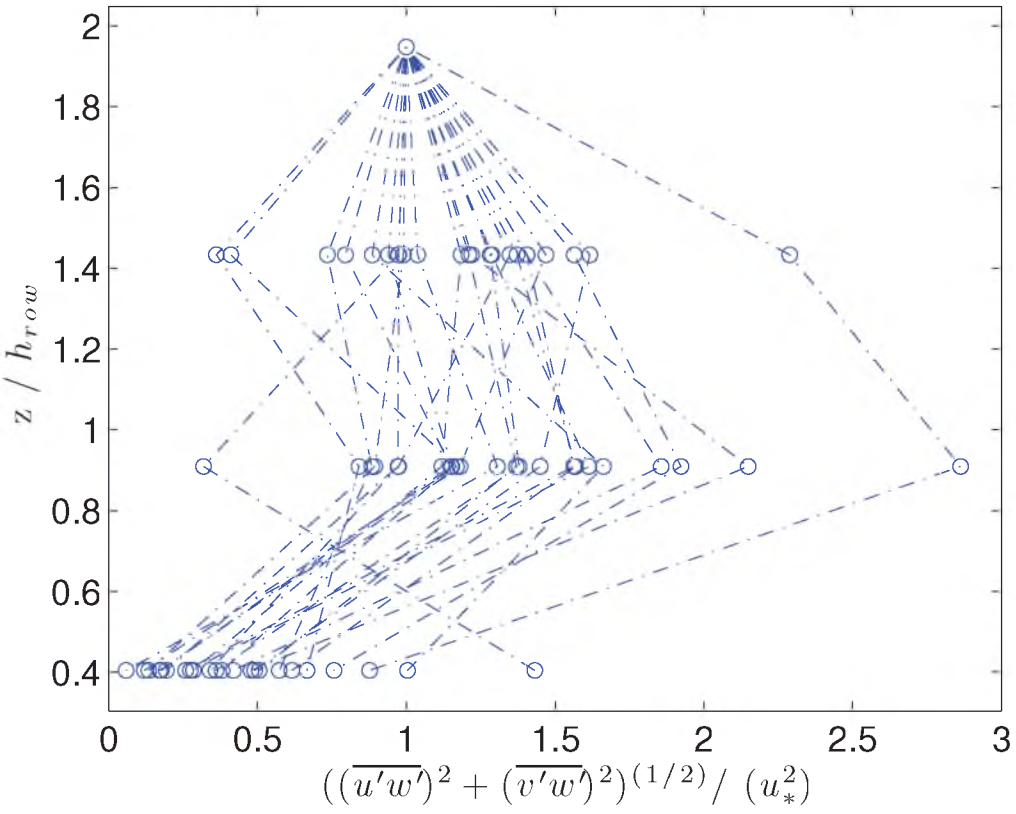

Figure C.12. Vertical kinematic eddy flux of U-momentum, $\overline{u'\,w'}$ and $\overline{v'\,w'}$, normalized by u_*^2 vs. height of sonic, z, normalized by the height of the rows, h; (cross flow, $-1 > \zeta$). Red dots show mean of the data set, and the blue lines show the 25^{th}, 50^{th}, and 75^{th} percentiles. All 30-minute period profiles.

APPENDIX D

RELEASE AND TRAP DESIGN

D.1 Point Release

The first release utilized a simplistic funnel design. A funnel that had an exit opening of 1.016 mm was suspended on a stake in the canopy. A small vibrating motor was attached to the rim of the release. As the motor vibrated particles would be sifted out of the funnel and released into the canopy. When the motor was not running the particles would stay in the funnel. This method allowed for very little energy being added to the particle through means of ejection. This release device was considered a point source since particles were being released from one point. This is ideal because it will give a three-dimensional view of how the particles are being transported throughout the canopy.

D.2 Line Release

The second release was designed as a line source. A measured amount of particles were mixed in a large reservoir of ethanol. To ensure the particles stayed suspended in the solution an agitator was used. The solution was then pumped from the reservoir into a manifold with four outlets. Each outlet had spray nozzles that sprayed a flat mist. The spray was oriented upwards in the cross flow of the wind. This source was ideal because it increased the changes of particles being trapped regardless on how much the wind shifted during the experiment.

D.3 Impaction Traps

The root-rod traps were used to trap the particles. A small motor had a cross bar mounted to the output shaft. At either end of the cross bar small holes were drilled in order to place polystyrene strips in the ends while still being removable. The leading edge of the strips were coated with a grease in order to trap the particles as they

entered the swept volume of the traps. The traps rotated at such a rate as to have a very high stokes number, meaning that the particles would not divert their path due to the spinning of the rods. The traps were setup in vertical arrays and at various distances away from the source. After a release event all the polystyrene strips would be removed and stored. The strips were then magnified and photographed to be used in image analysis suite provided by MatLAB.

APPENDIX E

VERTICAL CONCENTRATION PLOTS

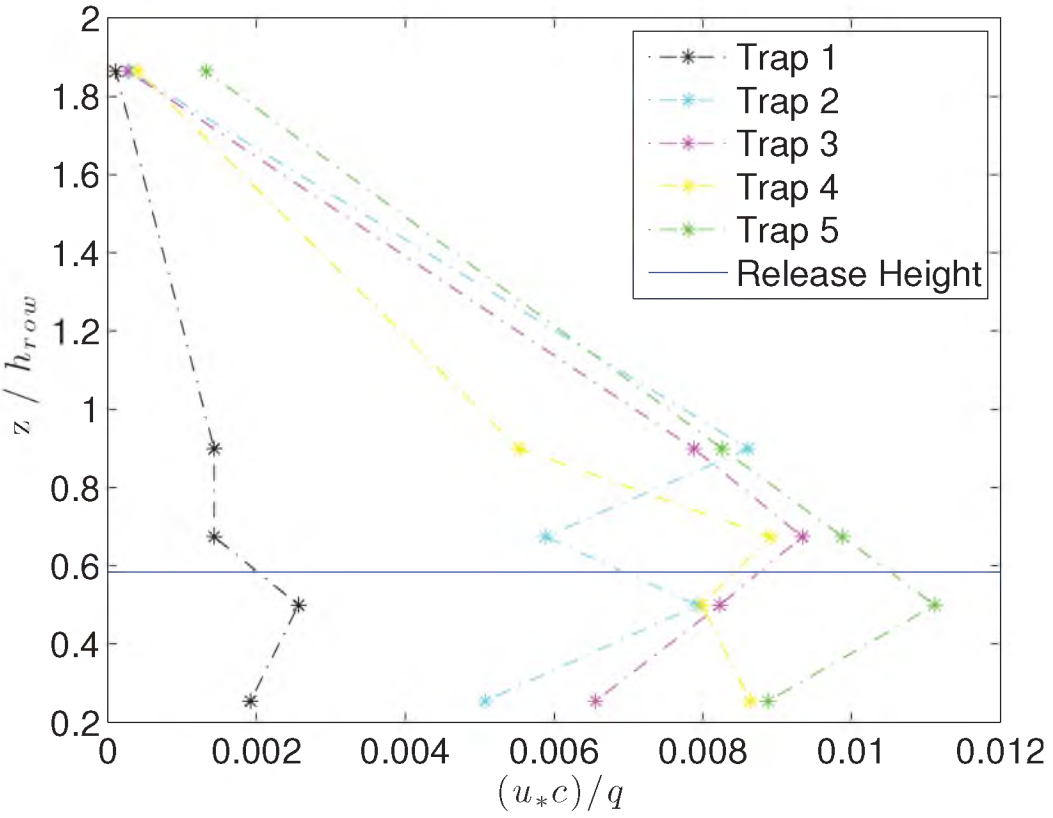

Figure E.1. Values of concentration, $(u_* c) / q$, vs. height of sonic, z, normalized by the height of the rows, h, for Release 3 trap group 1. The blue line represents the release height normalized by row height.

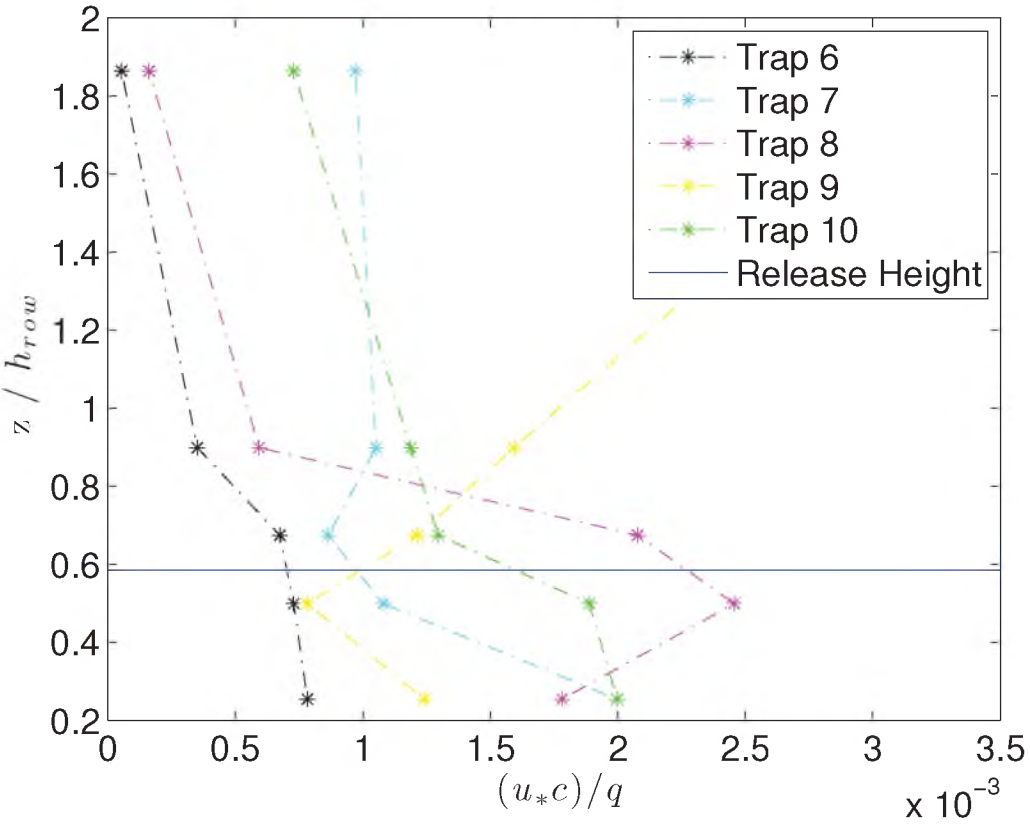

Figure E.2. Values of concentration, $(u_* c) / q$, vs. height of sonic, z, normalized by the height of the rows, h, for Release 3 trap group 2. The blue line represents the release height normalized by row height.

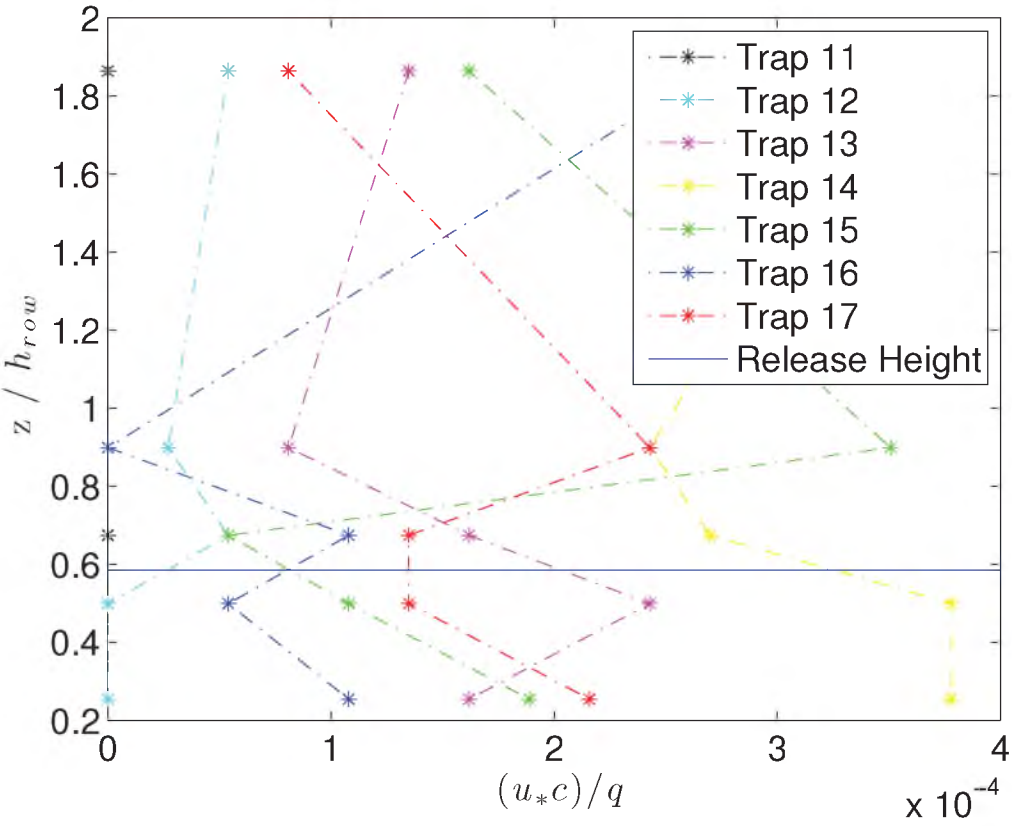

Figure E.3. Values of concentration, $(u_* c) / q$, vs. height of sonic, z, normalized by the height of the rows, h, for Release 3 trap group 3. The blue line represents the release height normalized by row height.

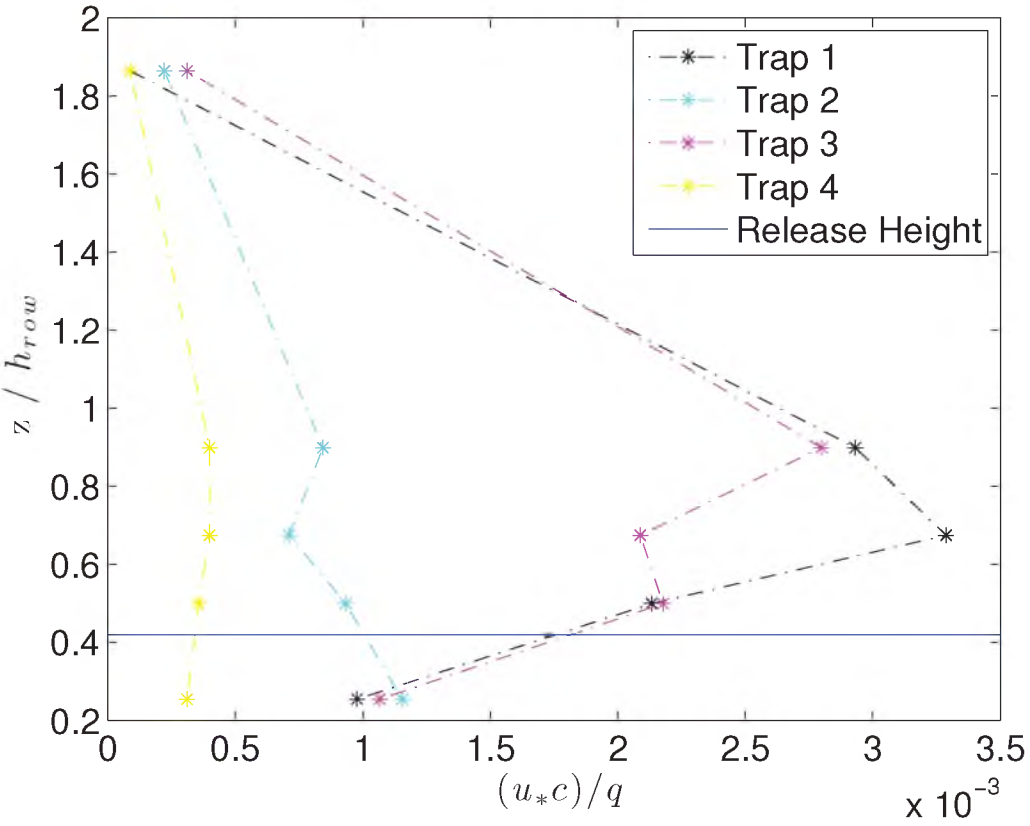

Figure E.4. Values of concentration, $(u_* c) / q$, vs. height of sonic, z, normalized by the height of the rows, h, for Release 6 trap group 1. The blue line represents the release height normalized by row height.

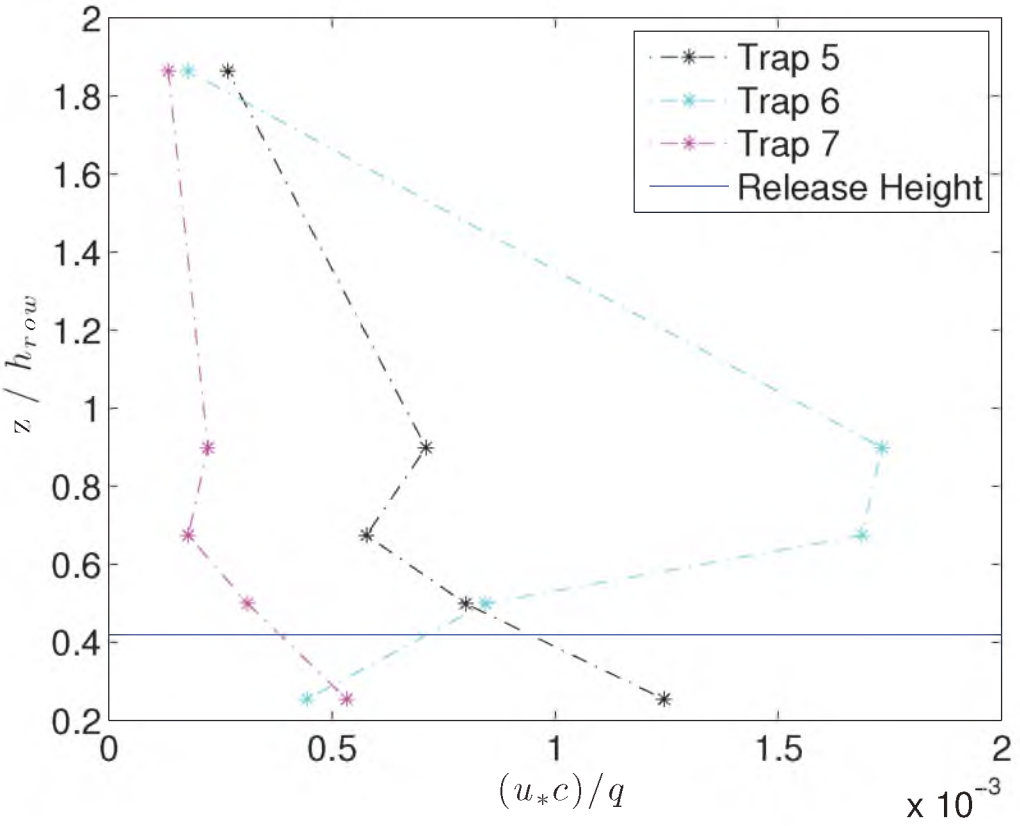

Figure E.5. Values of concentration, $(u_* c) / q$, vs. height of sonic, z, normalized by the height of the rows, h, for Release 6 trap group 2. The blue line represents the release height normalized by row height.

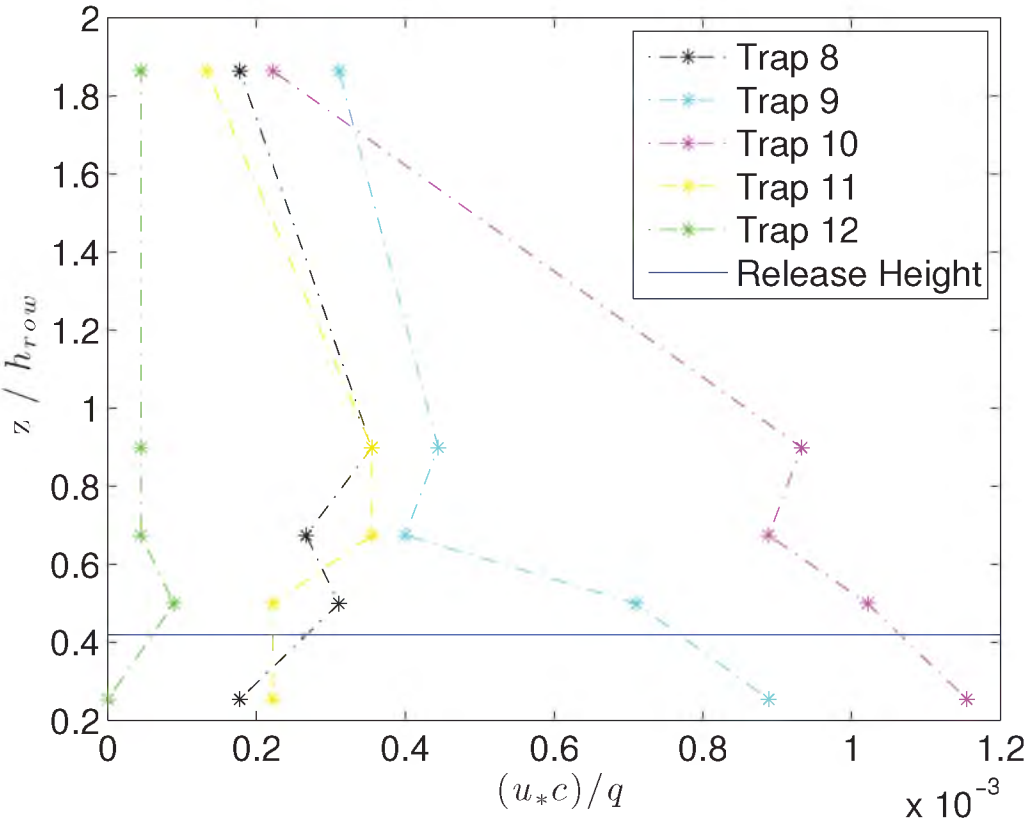

Figure E.6. Values of concentration, $(u_* c) / q$, vs. height of sonic, z, normalized by the height of the rows, h, for Release 6 trap group 3. The blue line represents the release height normalized by row height.

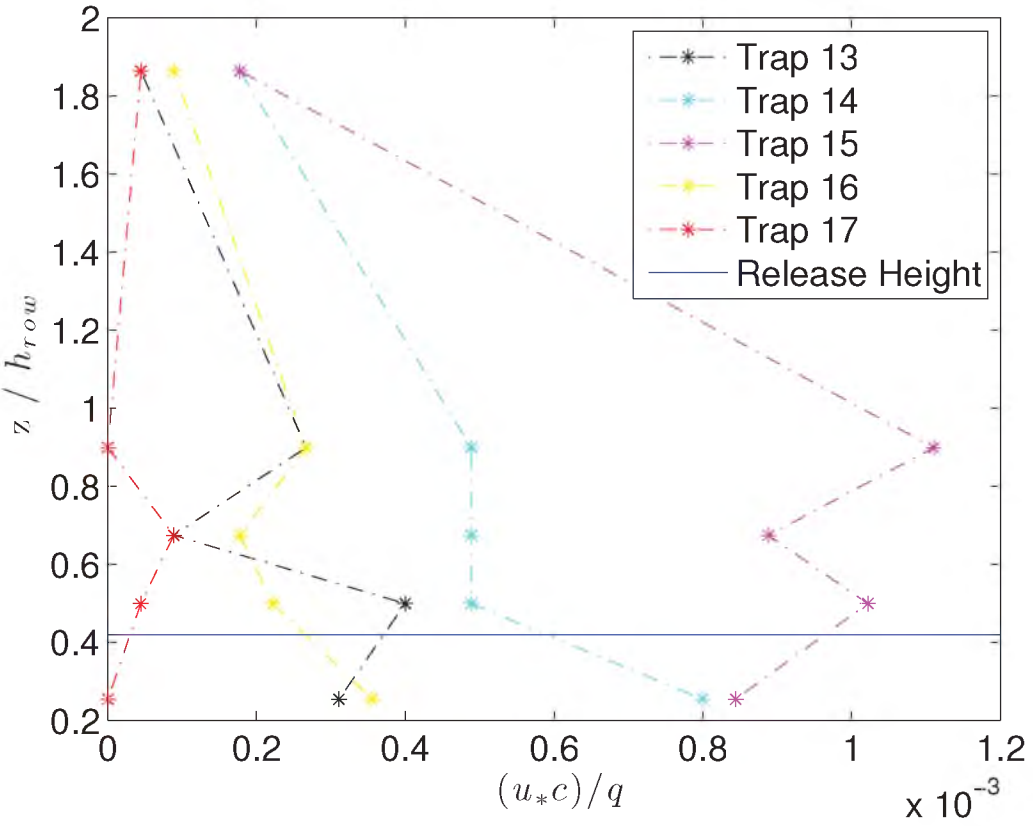

Figure E.7. Values of concentration, $(u_* c) / q$, vs. height of sonic, z, normalized by the height of the rows, h, for Release 6 trap group 4. The blue line represents the release height normalized by row height.

APPENDIX F

GAUSSIAN PLUME PLOTS

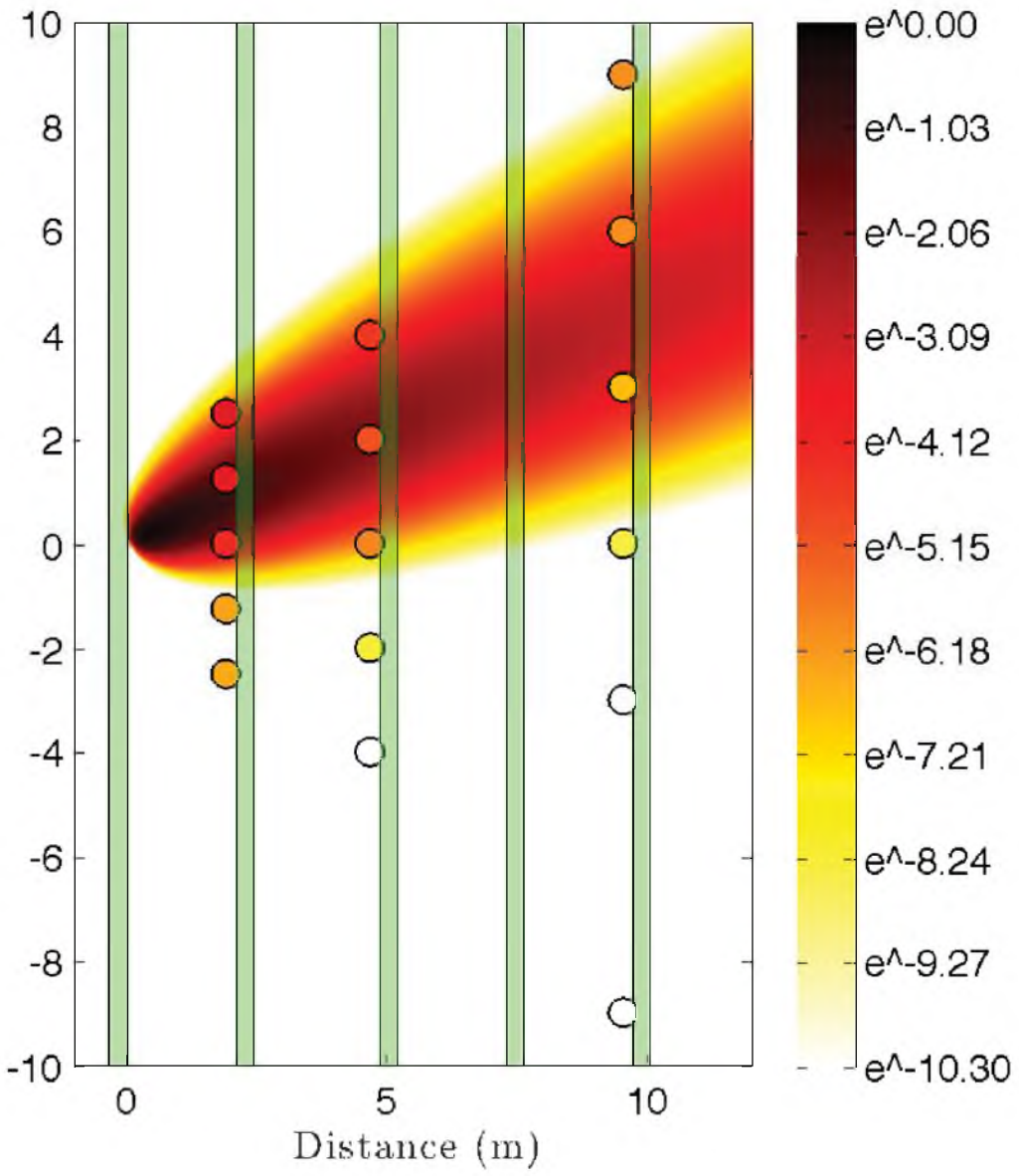

Figure F.1. The normalized measured field data compared to the normalized Gaussian Plume model for release 2 at a height of 0.5 m or trap level 1. The measured field data were indicated by color filled circles. The release was located at (0.0m, 0.0m, 0.81m). Circles were omitted if data were not available at the trap location.

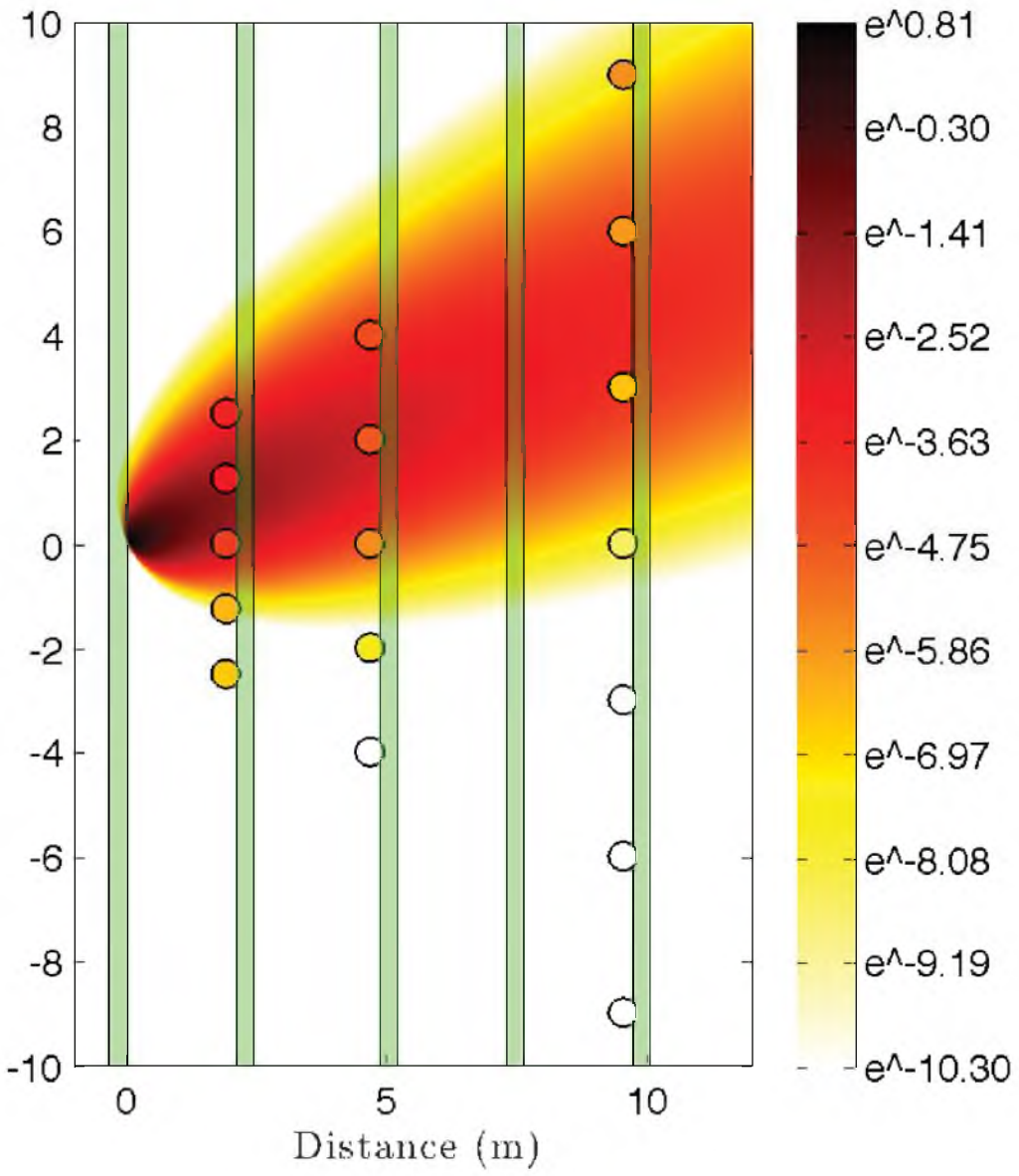

Figure F.2. The normalized measured field data compared to the normalized Gaussian Plume model for release 2 at a height of 1.0 m or trap level 2. The measured field data were indicated by color filled circles. The release was located at (0.0m, 0.0m, 0.81m). Circles were omitted if data were not available at the trap location.

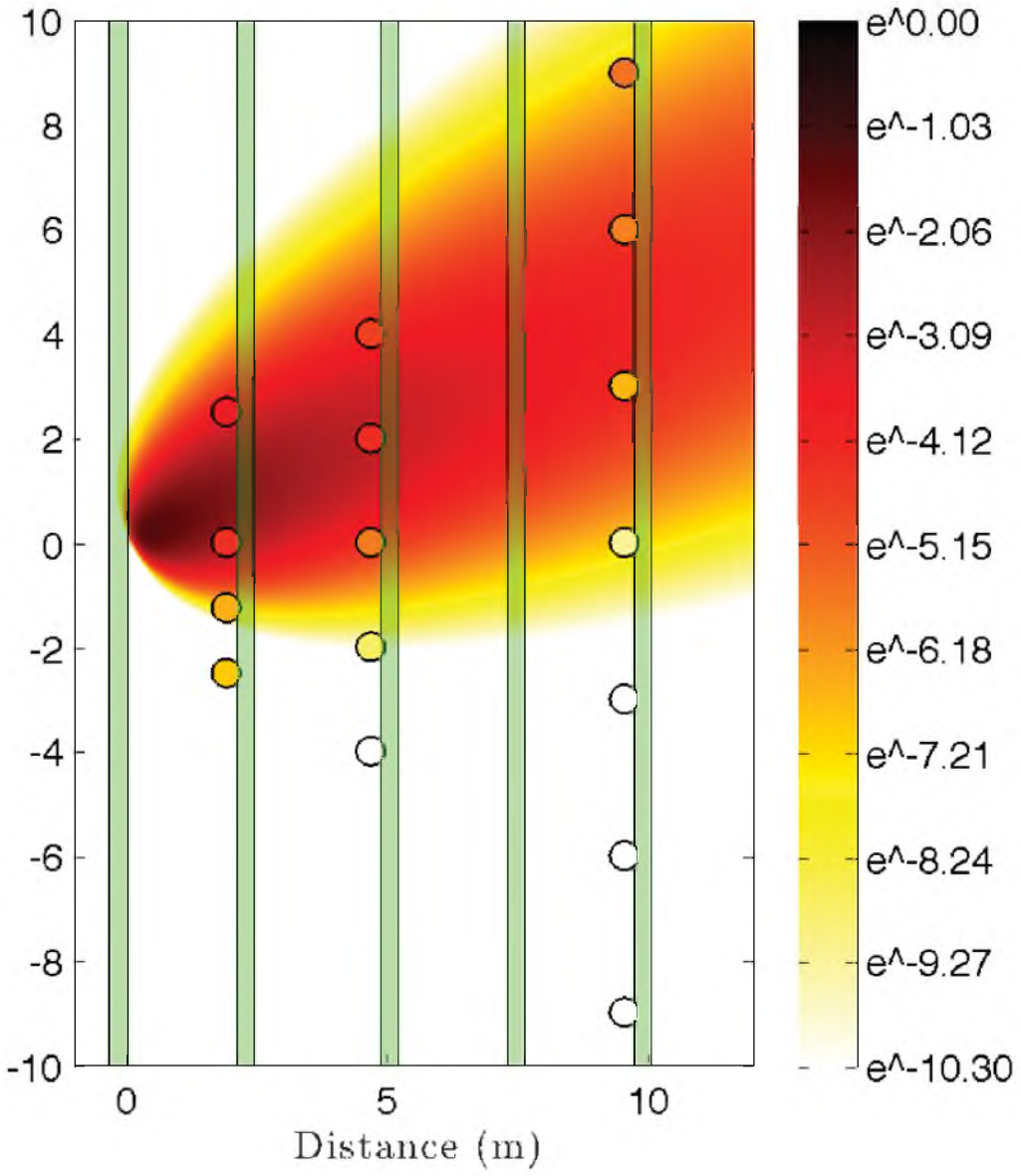

Figure F.3. The normalized measured field data compared to the normalized Gaussian Plume model for release 2 at a height of 1.3 m or trap level 3. The measured field data were indicated by color filled circles. The release was located at (0.0m, 0.0m, 0.81m). Circles were omitted if data were not available at the trap location.

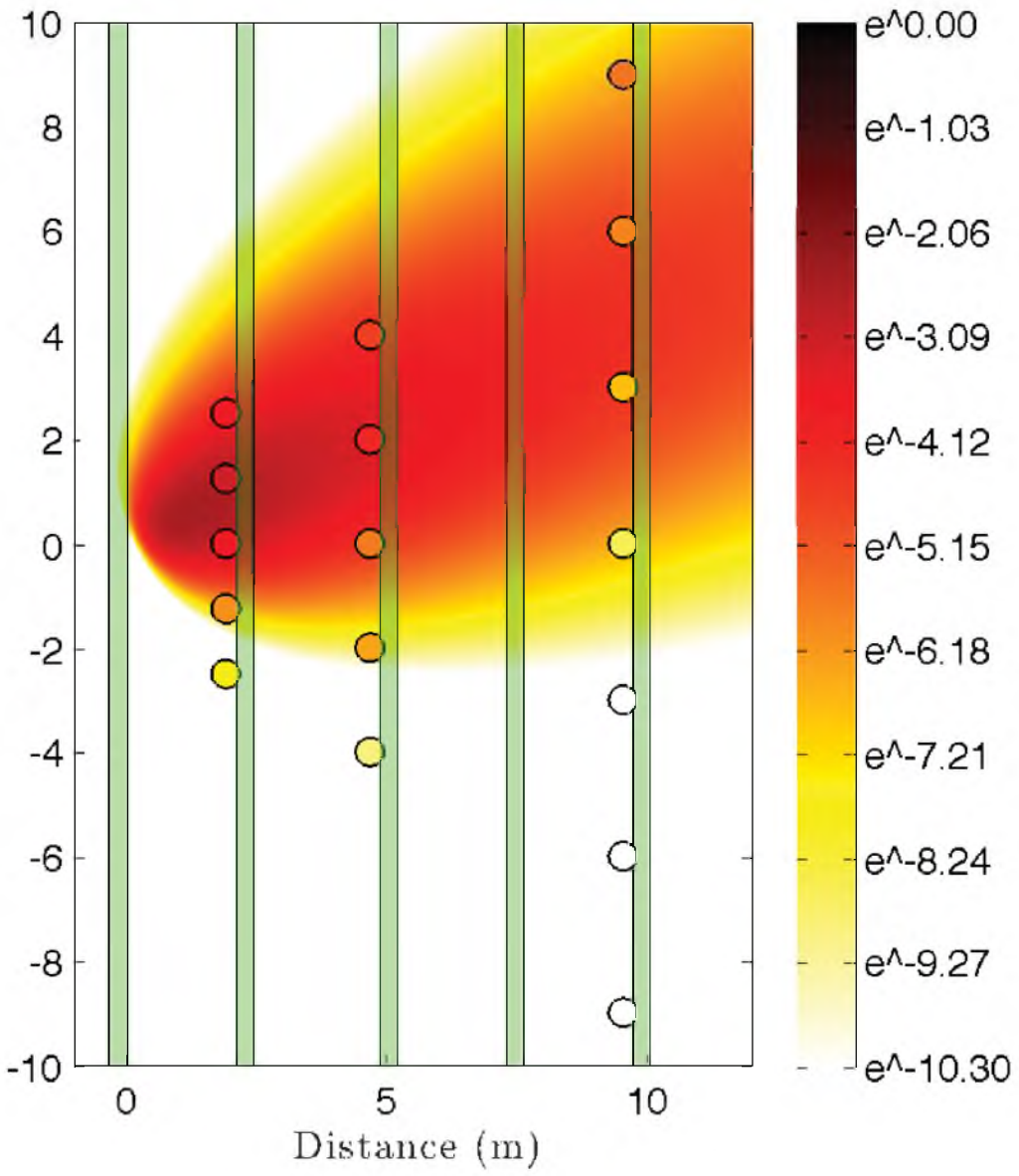

Figure F.4. The normalized measured field data compared to the normalized Gaussian Plume model for release 2 at a height of 1.8 m or trap level 4. The measured field data were indicated by color filled circles. The release was located at (0.0m, 0.0m, 0.81m). Circles were omitted if data were not available at the trap location.

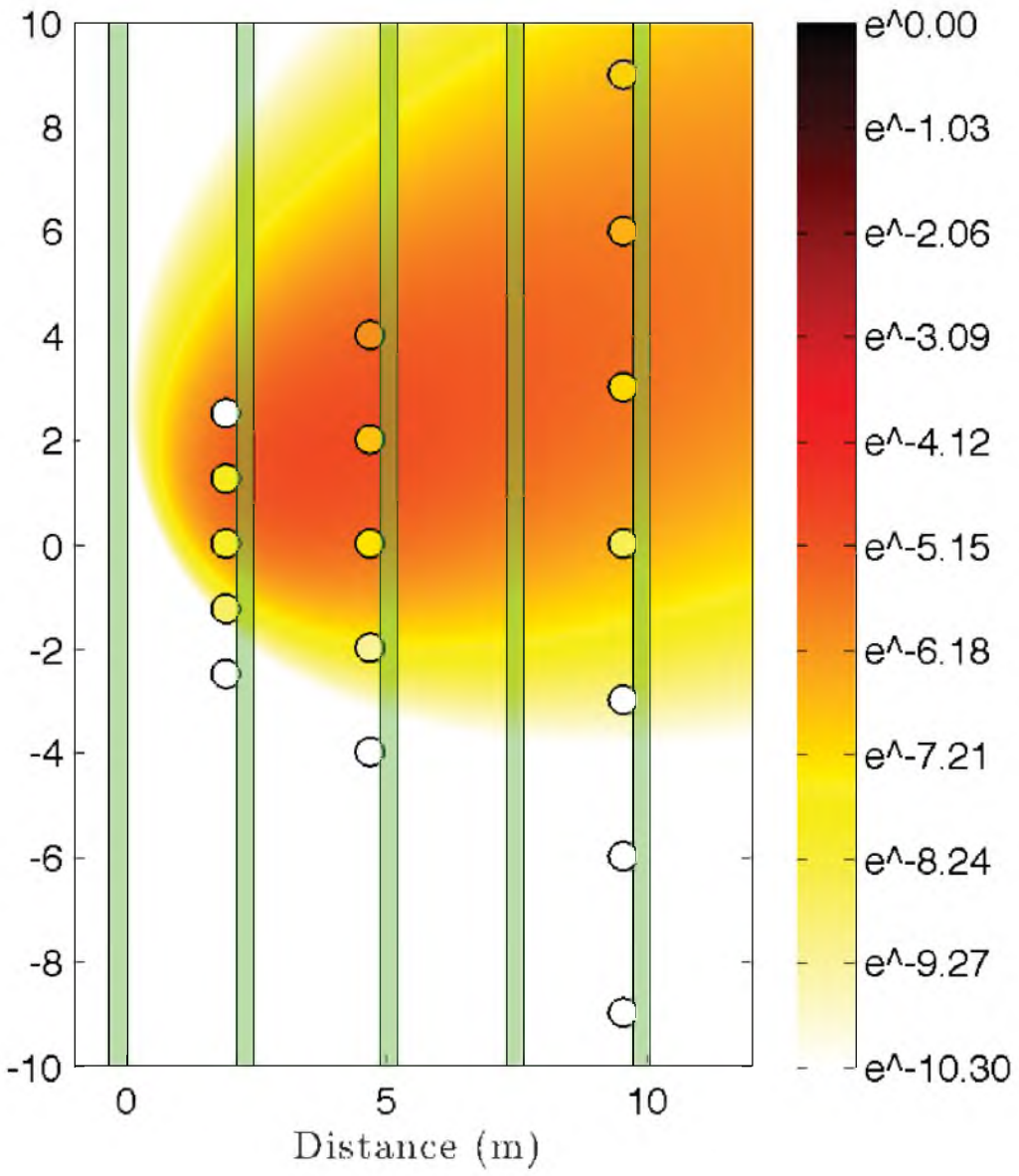

Figure F.5. The normalized measured field data compared to the normalized Gaussian Plume model for release 2 at a height of 3.7 m or trap level 5. The measured field data were indicated by color filled circles. The release was located at (0.0m, 0.0m, 0.81m). Circles were omitted if data were not available at the trap location.

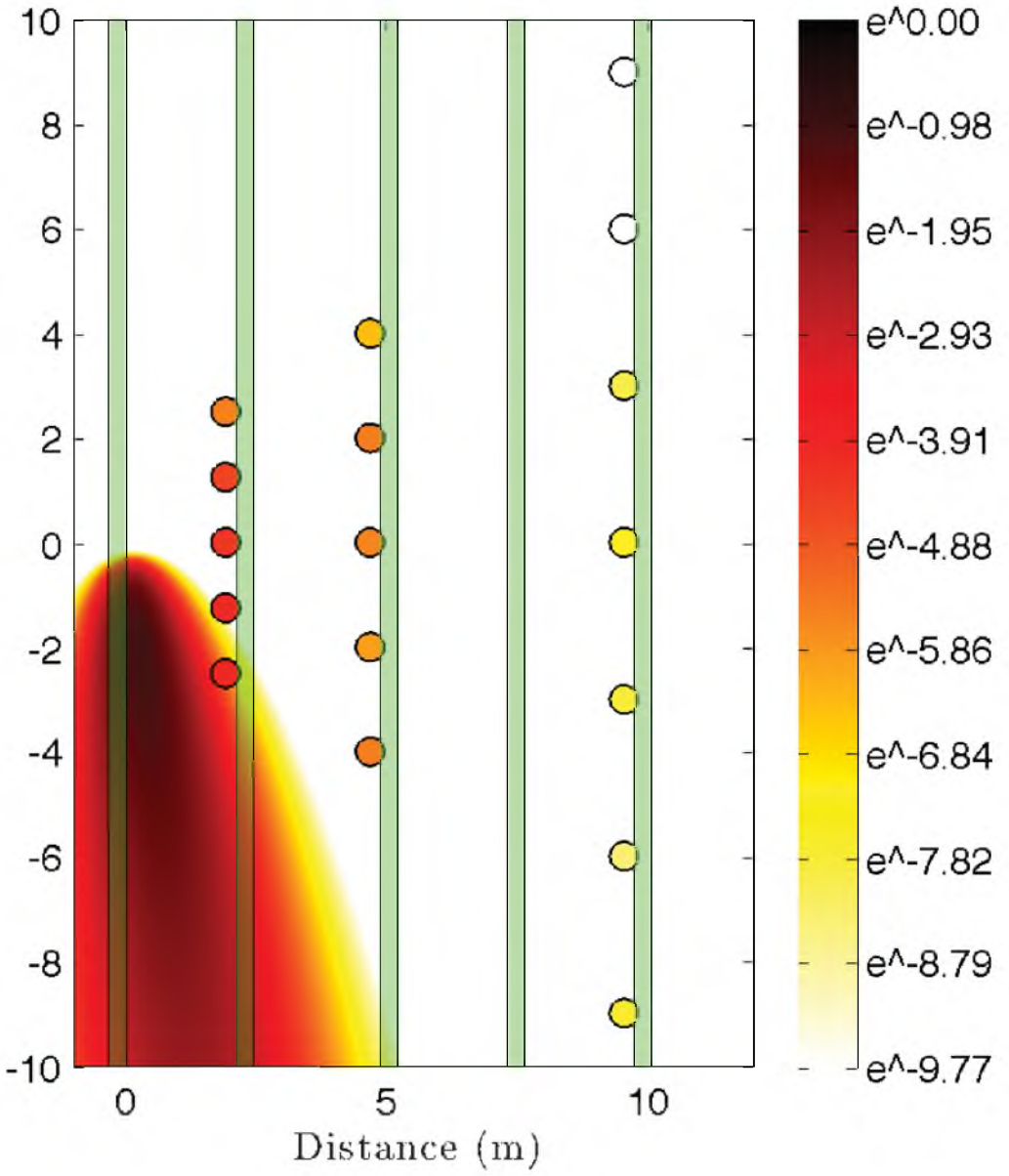

Figure F.6. The normalized measured field data compared to the normalized Gaussian Plume model for release 3 at a height of 0.5 m or trap level 1. The measured field data were indicated by color filled circles. The release was located at (0.0m, 0.0m, 1.17m). Circles were omitted if data were not available at the trap location.

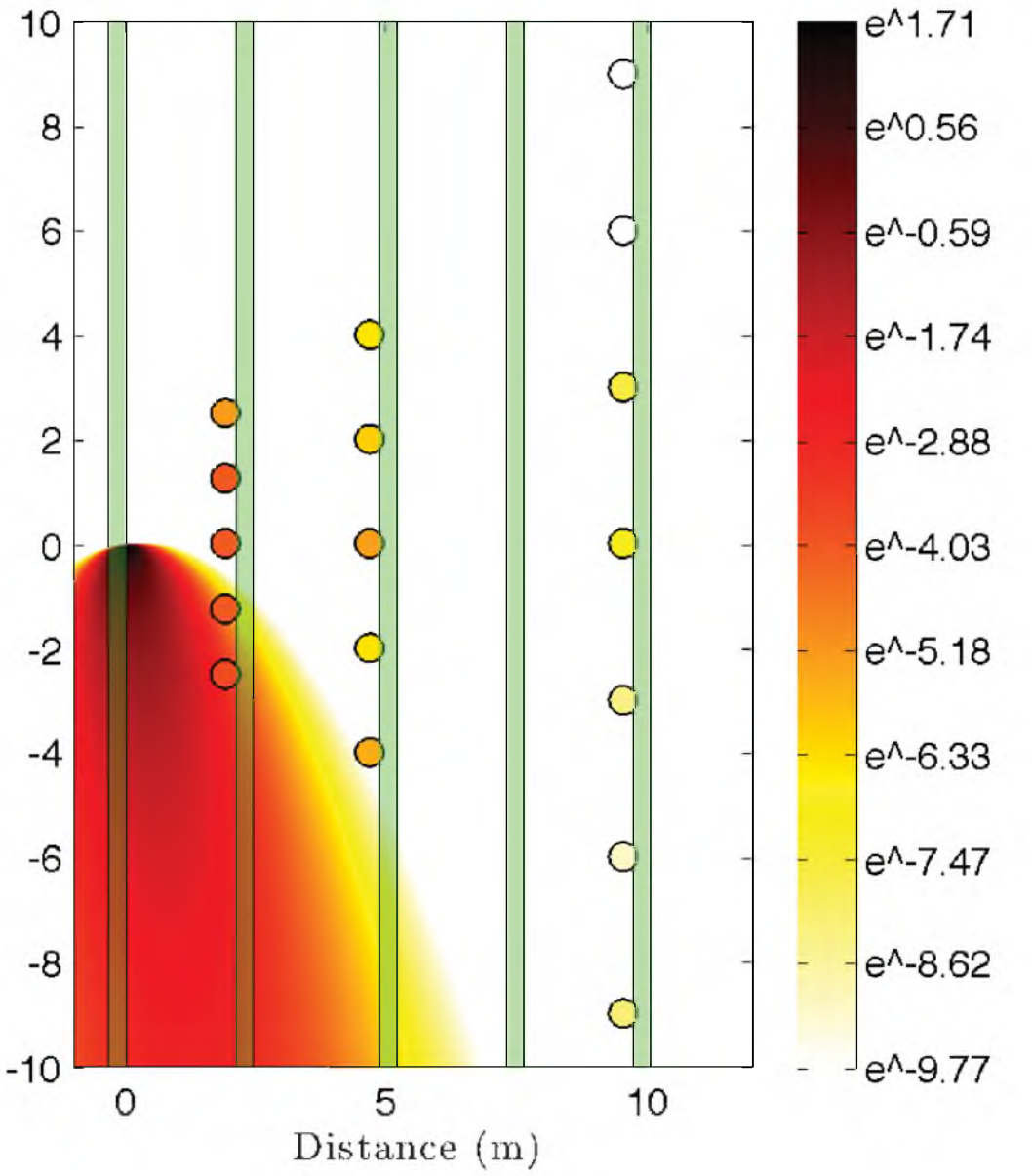

Figure F.7. The normalized measured field data compared to the normalized Gaussian Plume model for release 3 at a height of 1.0 m or trap level 2. The measured field data were indicated by color filled circles. The release was located at (0.0m, 0.0m, 1.17m). Circles were omitted if data were not available at the trap location.

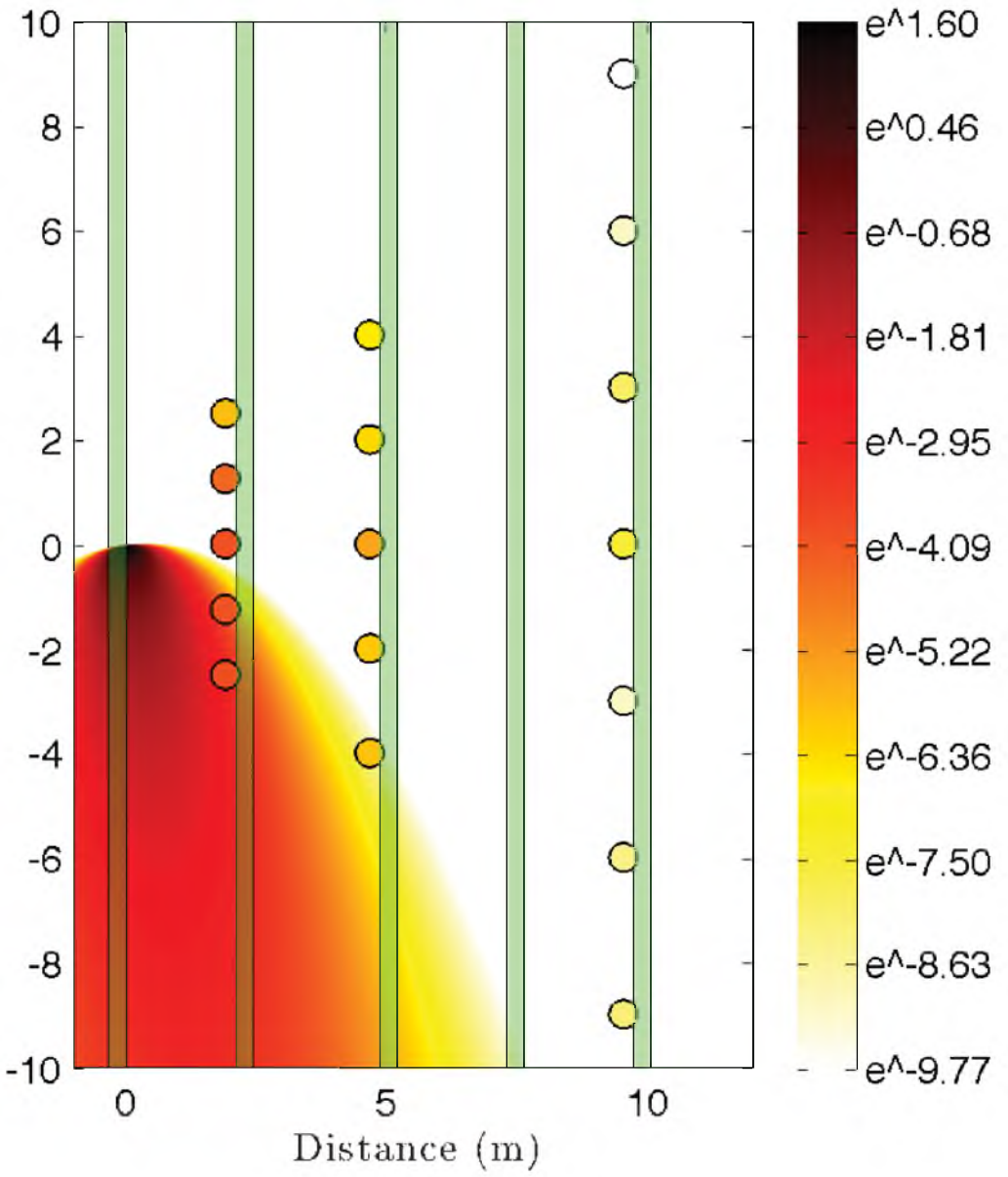

Figure F.8. The normalized measured field data compared to the normalized Gaussian Plume model for release 3 at a height of 1.3 m or trap level 3. The measured field data were indicated by color filled circles. The release was located at (0.0m, 0.0m, 1.17m). Circles were omitted if data were not available at the trap location.

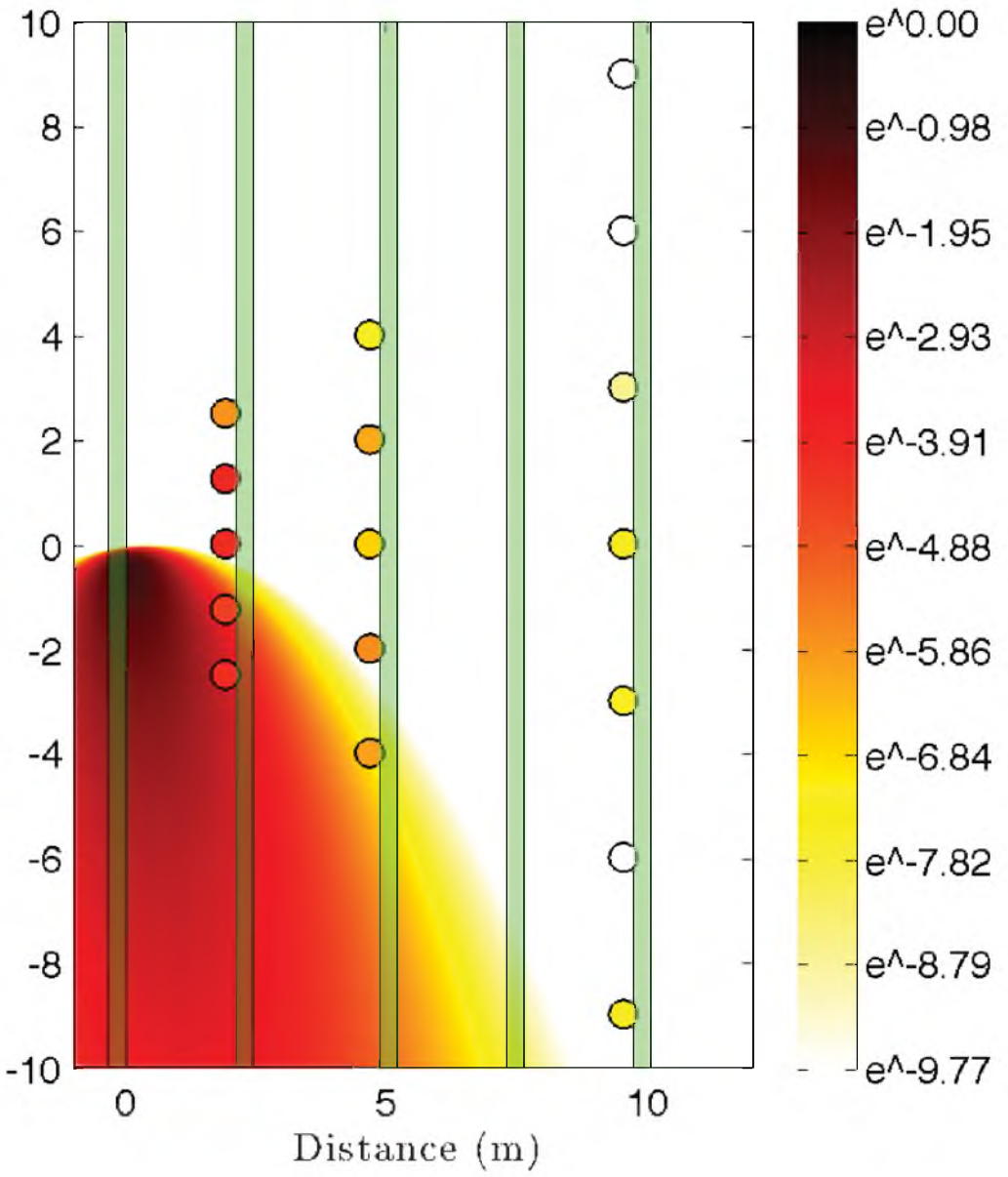

Figure F.9. The normalized measured field data compared to the normalized Gaussian Plume model for release 3 at a height of 1.8 m or trap level 4. The measured field data were indicated by color filled circles. The release was located at (0.0m, 0.0m, 1.17m). Circles were omitted if data were not available at the trap location.

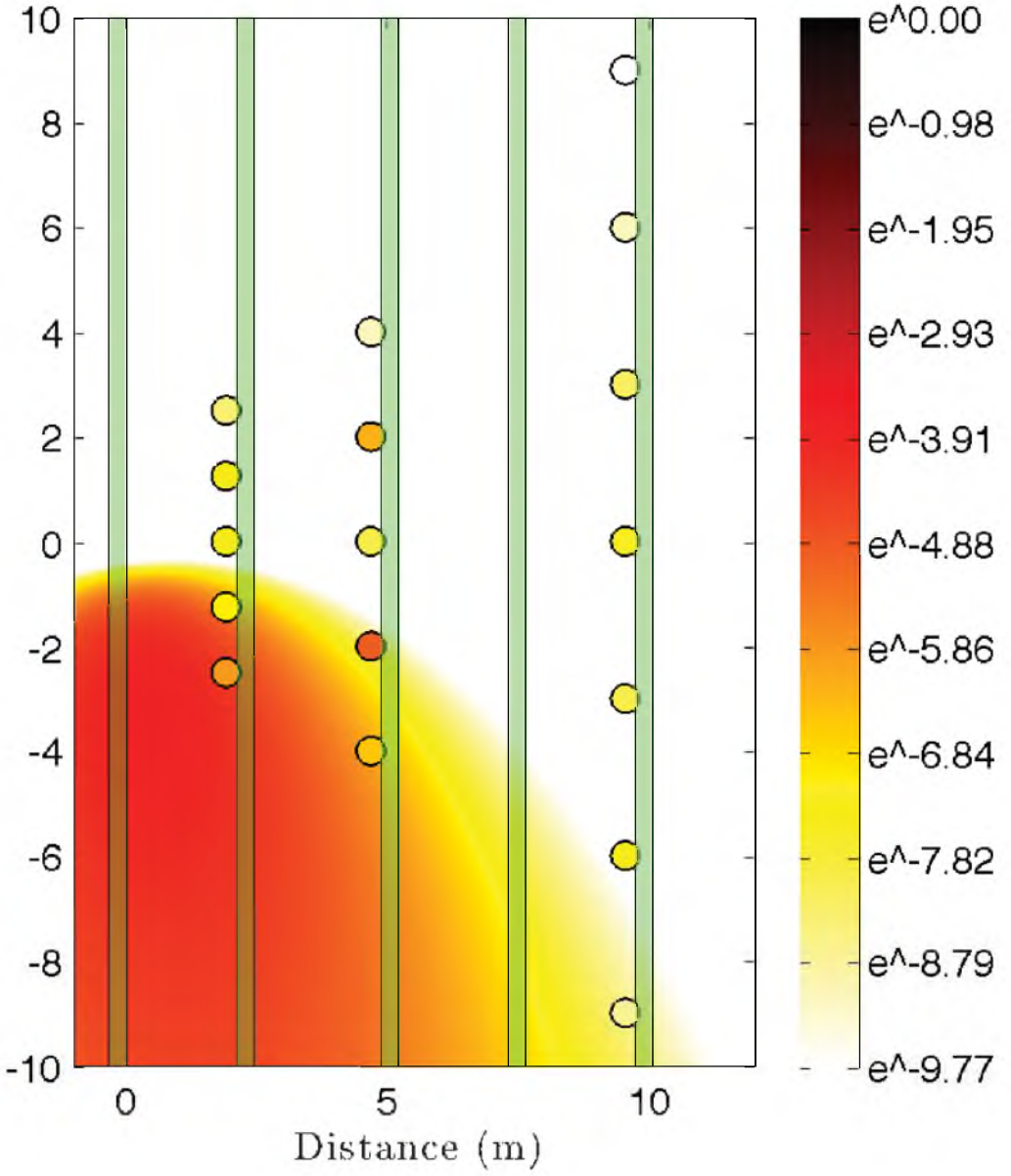

Figure F.10. The normalized measured field data compared to the normalized Gaussian Plume model for release 3 at a height of 3.7 m or trap level 5. The measured field data were indicated by color filled circles. The release was located at (0.0m, 0.0m, 1.17m). Circles were omitted if data were not available at the trap location.

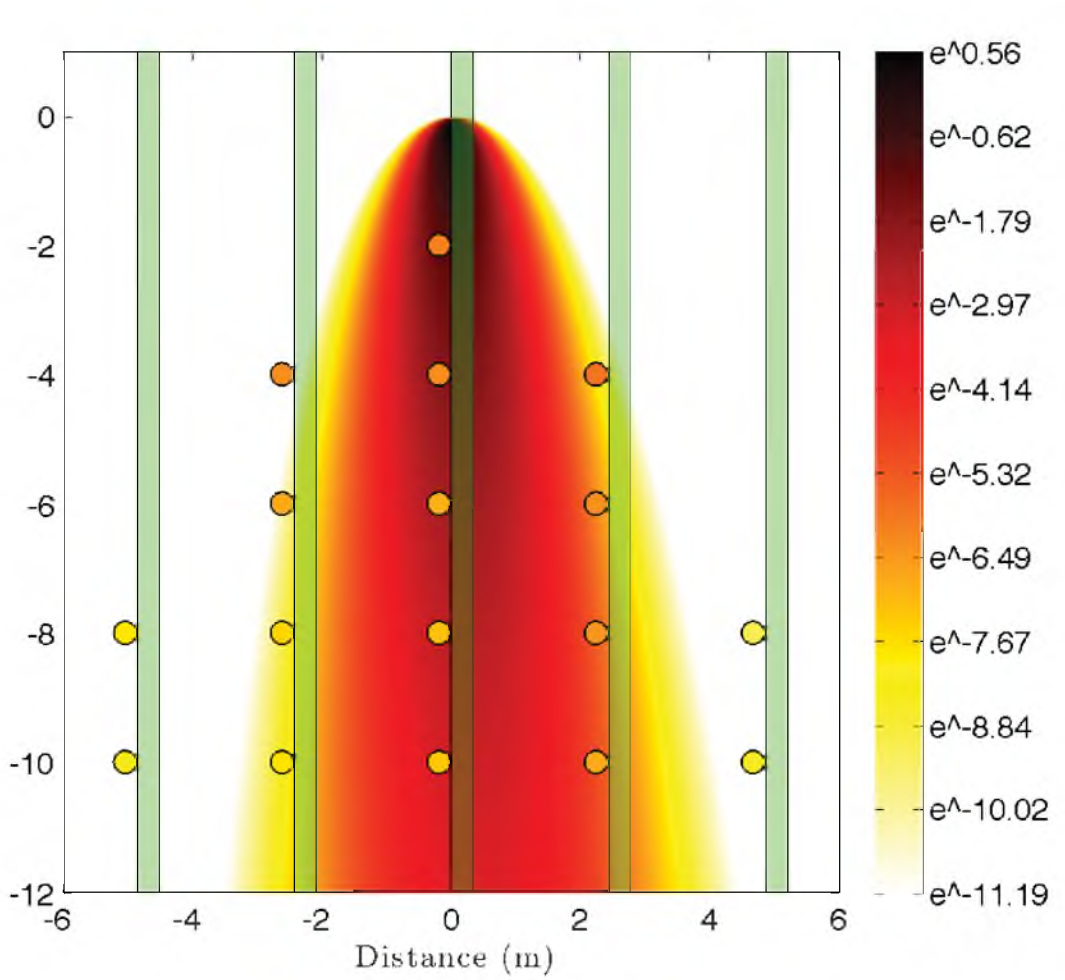

Figure F.11. The normalized measured field data compared to the normalized Gaussian Plume model for release 4 at a height of 0.5 m or trap level 1. The measured field data were indicated by color filled circles. The release was located at (0.0m, 0.0m, 0.69m). Circles were omitted if data were not available at the trap location.

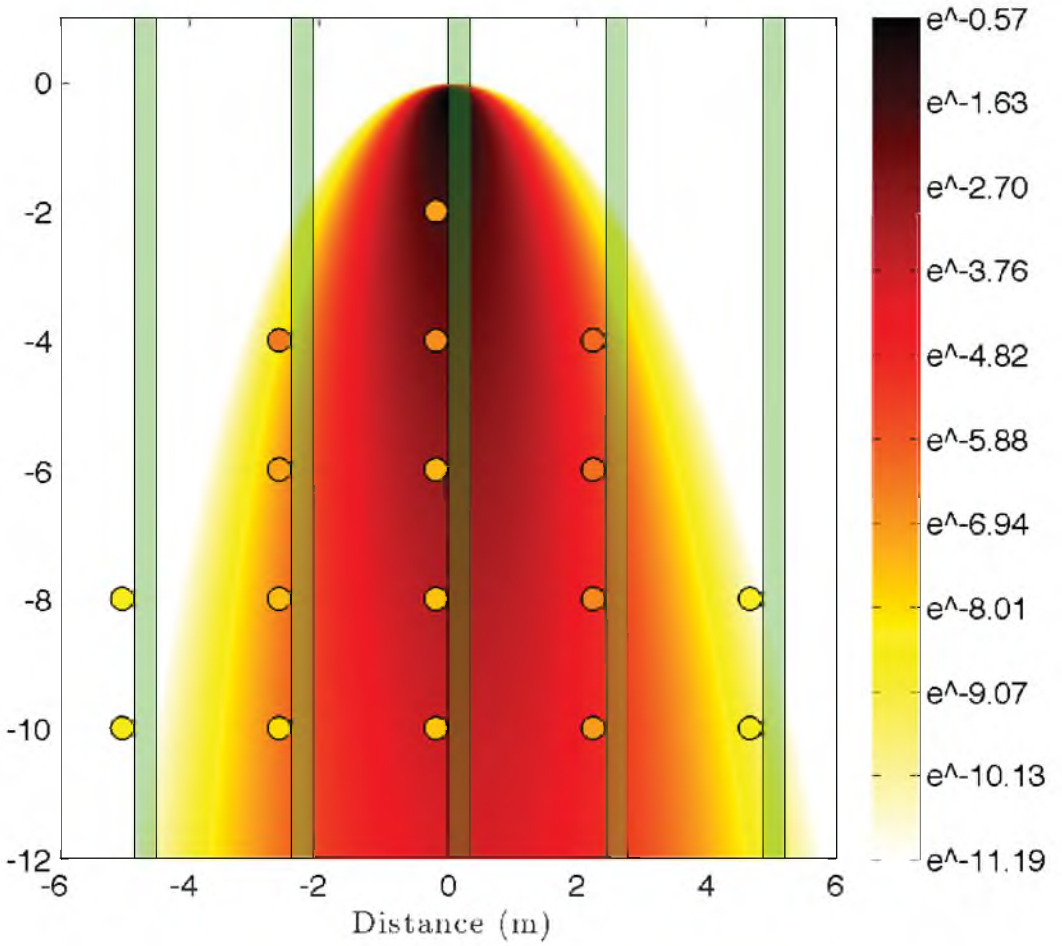

Figure F.12. The normalized measured field data compared to the normalized Gaussian Plume model for release 4 at a height of 1.0 m or trap level 2. The measured field data were indicated by color filled circles. The release was located at (0.0m, 0.0m, 0.69m). Circles were omitted if data were not available at the trap location.

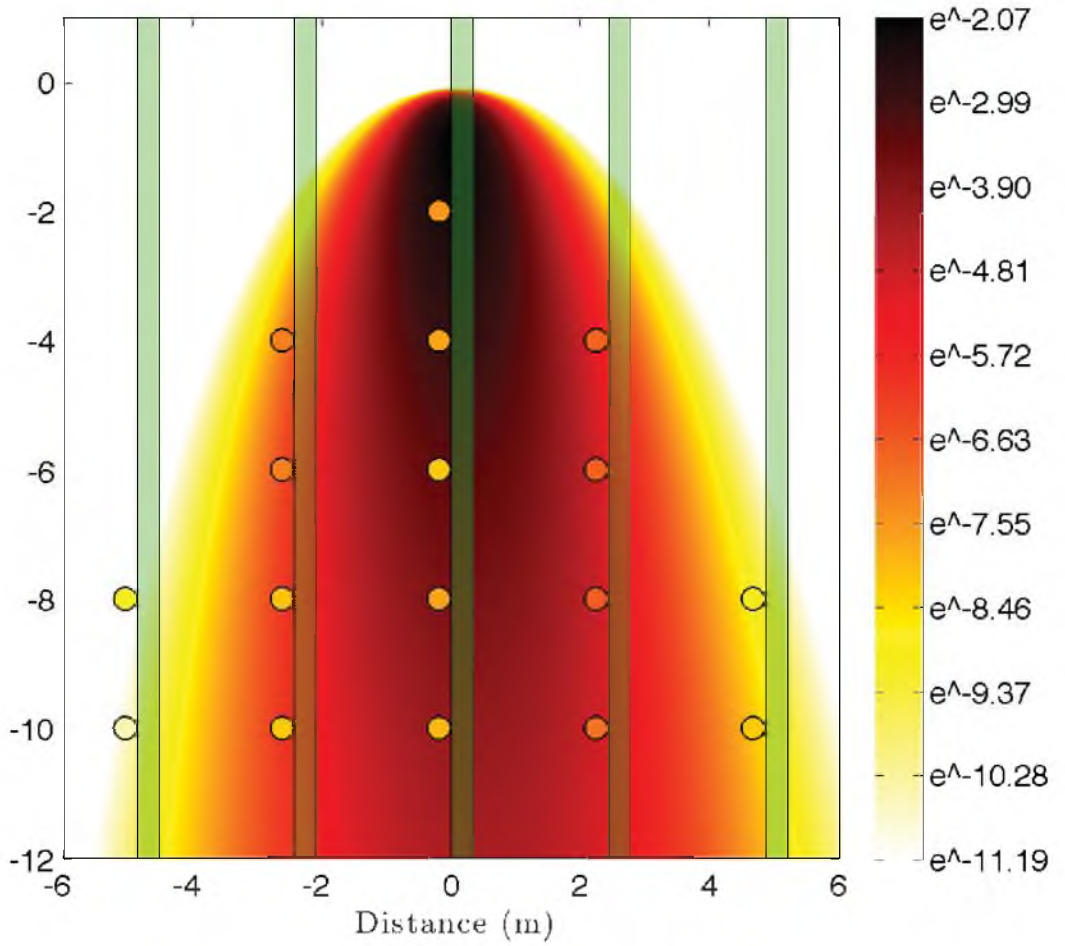

Figure F.13. The normalized measured field data compared to the normalized Gaussian Plume model for release 4 at a height of 1.3 m or trap level 3. The measured field data were indicated by color filled circles. The release was located at (0.0m, 0.0m, 0.69m). Circles were omitted if data were not available at the trap location.

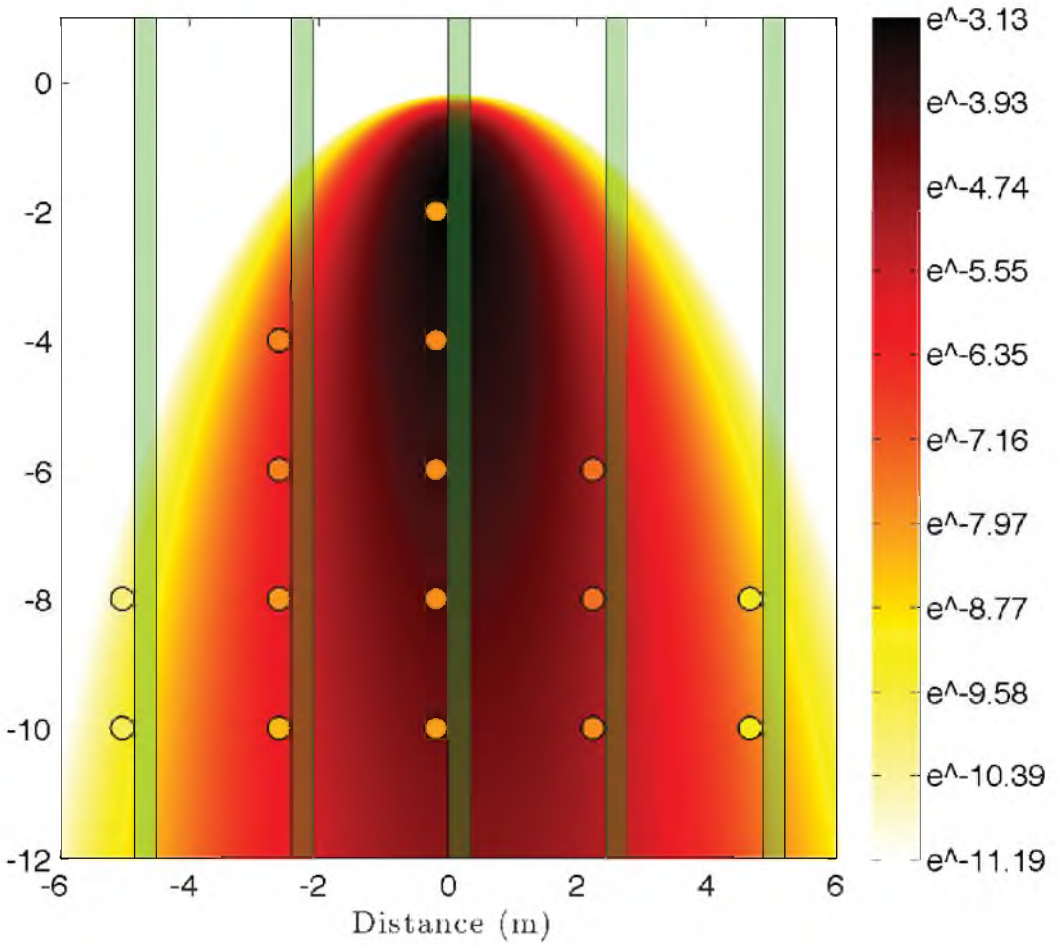

Figure F.14. The normalized measured field data compared to the normalized Gaussian Plume model for release 4 at a height of 1.8 m or trap level 4. The measured field data were indicated by color filled circles. The release was located at (0.0m, 0.0m, 0.69m). Circles were omitted if data were not available at the trap location.

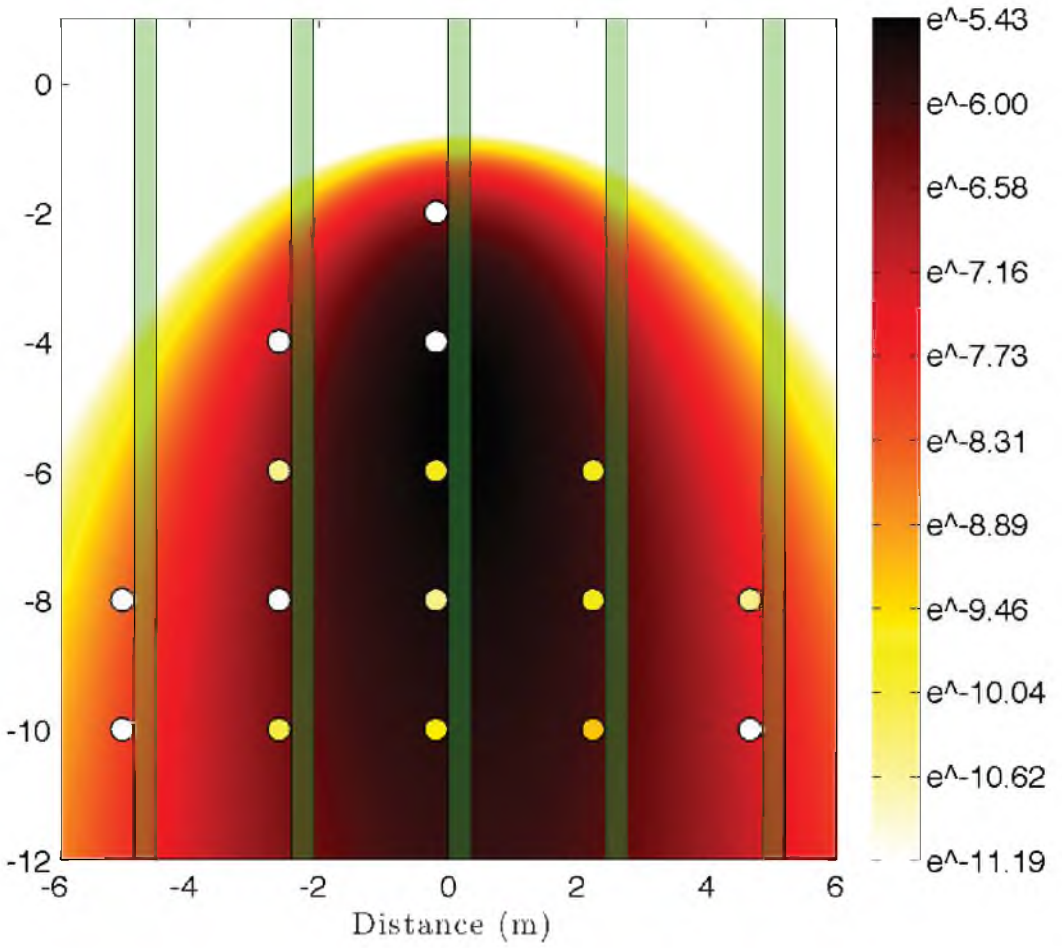

Figure F.15. The normalized measured field data compared to the normalized Gaussian Plume model for release 4 at a height of 3.7 m or trap level 5. The measured field data were indicated by color filled circles. The release was located at (0.0m, 0.0m, 0.69m). Circles were omitted if data were not available at the trap location.

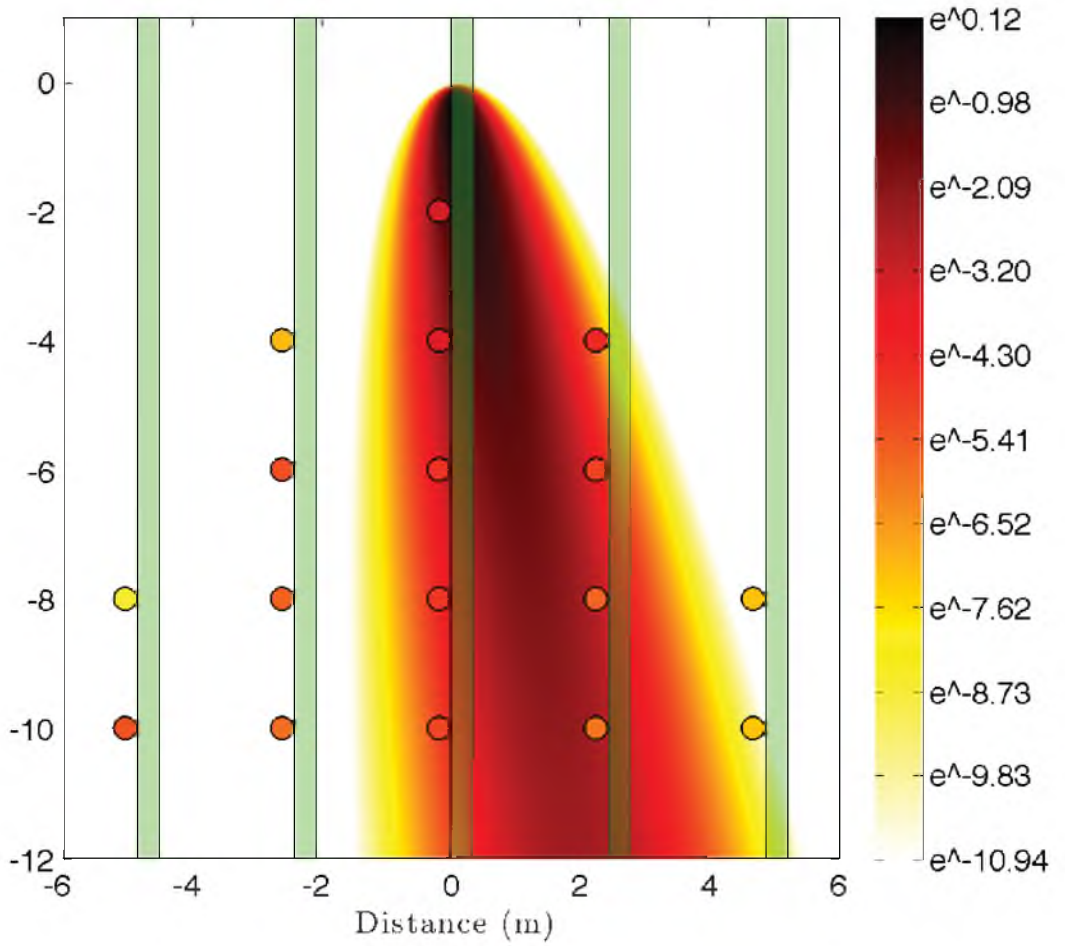

Figure F.16. The normalized measured field data compared to the normalized Gaussian Plume model for release 5 at a height of 0.5 m or trap level 1. The measured field data were indicated by color filled circles. The release was located at (0.0m, 0.0m, 0.75m). Circles were omitted if data were not available at the trap location.

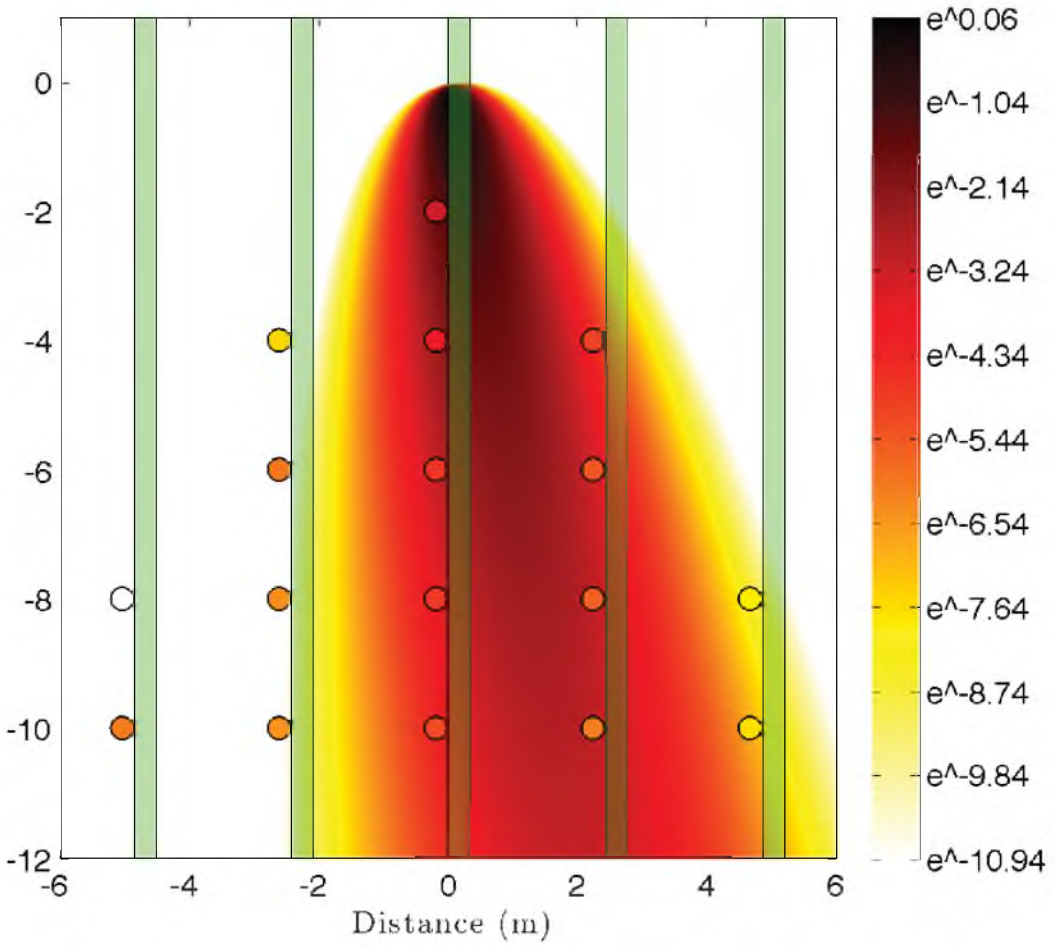

Figure F.17. The normalized measured field data compared to the normalized Gaussian Plume model for release 5 at a height of 1.0 m or trap level 2. The measured field data were indicated by color filled circles. The release was located at (0.0m, 0.0m, 0.75m). Circles were omitted if data were not available at the trap location.

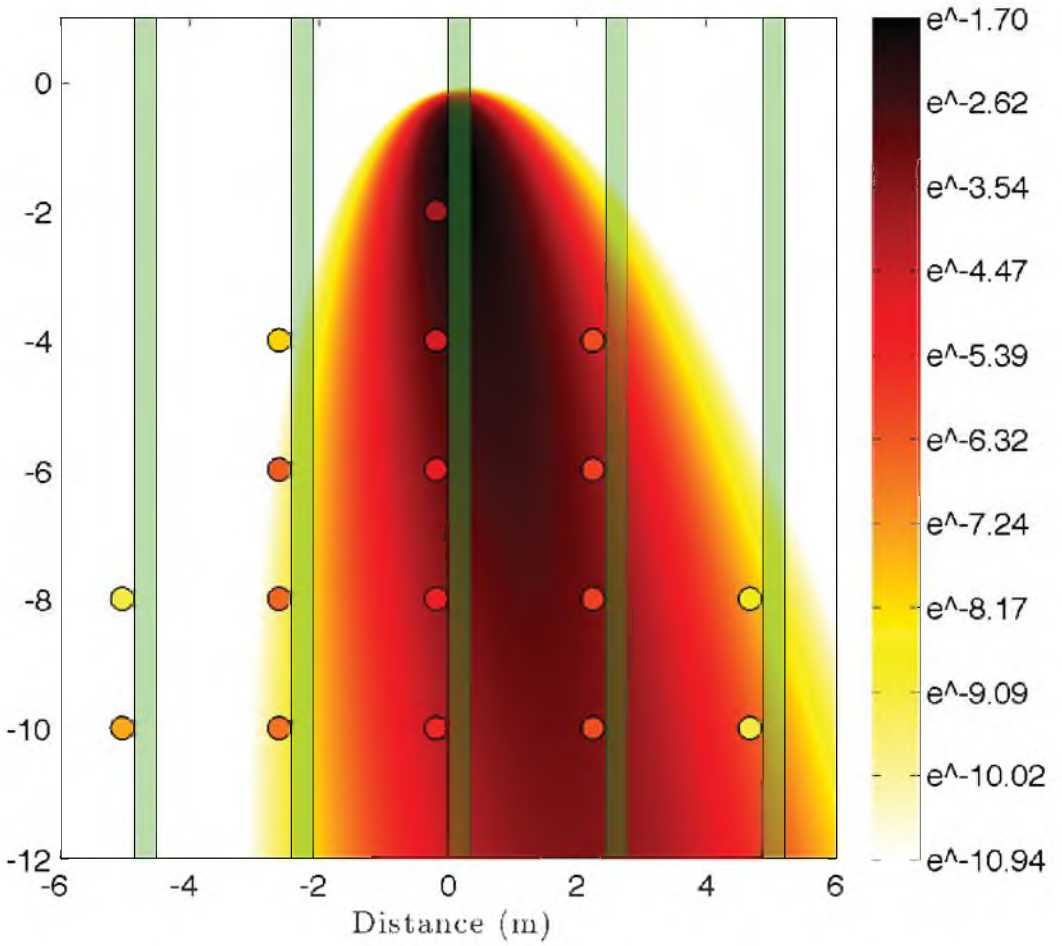

Figure F.18. The normalized measured field data compared to the normalized Gaussian Plume model for release 5 at a height of 1.3 m or trap level 3. The measured field data were indicated by color filled circles. The release was located at (0.0m, 0.0m, 0.75m). Circles were omitted if data were not available at the trap location.

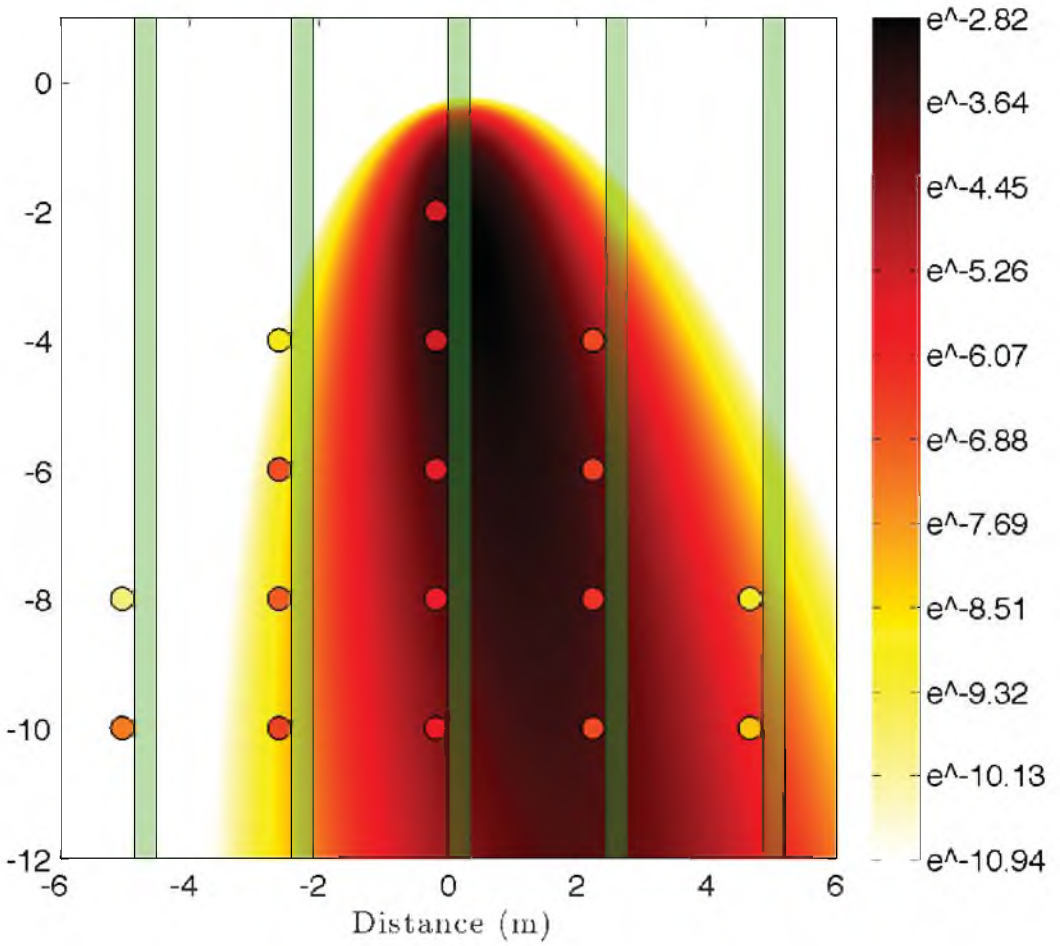

Figure F.19. The normalized measured field data compared to the normalized Gaussian Plume model for release 5 at a height of 1.8 m or trap level 4. The measured field data were indicated by color filled circles. The release was located at (0.0m, 0.0m, 0.75m). Circles were omitted if data were not available at the trap location.

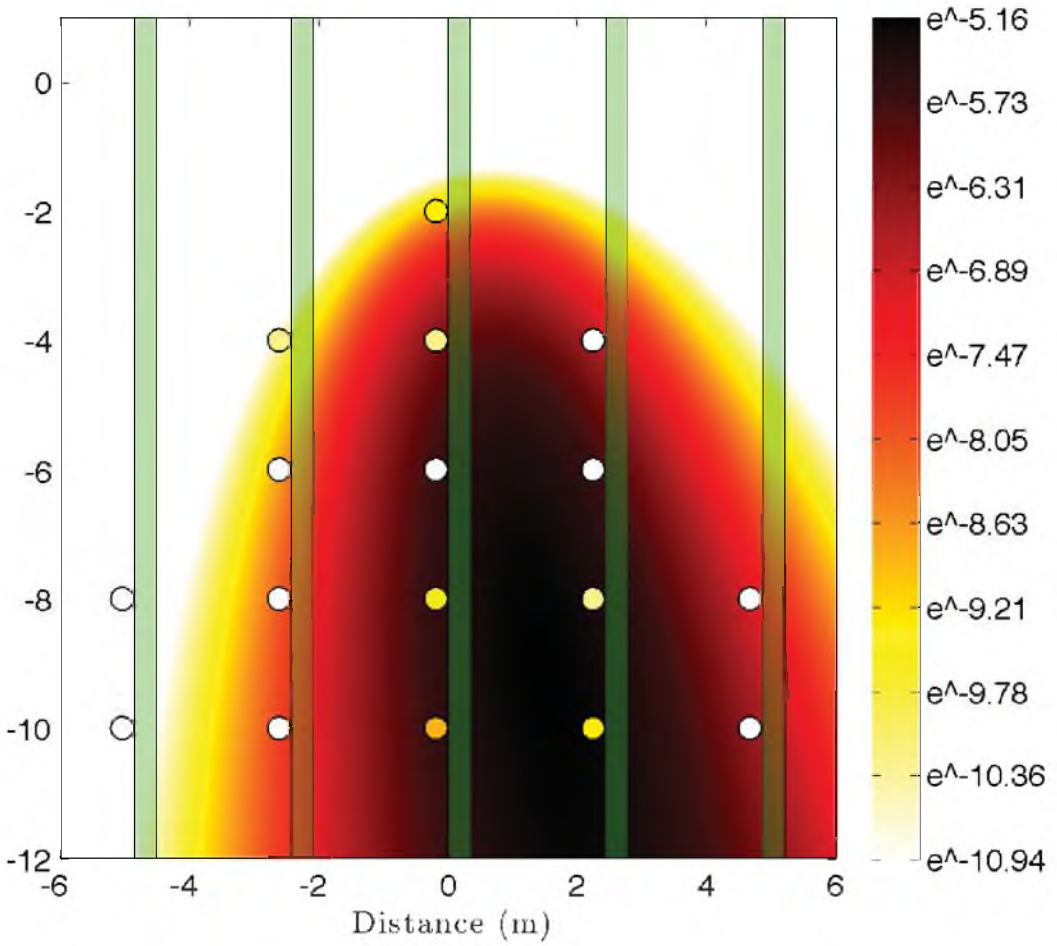

Figure F.20. The normalized measured field data compared to the normalized Gaussian Plume model for release 5 at a height of 3.7 m or trap level 5. The measured field data were indicated by color filled circles. The release was located at (0.0m, 0.0m, 0.75m). Circles were omitted if data were not available at the trap location.

APPENDIX G

ERROR PLOTS OF THE GAUSSIAN PLUME

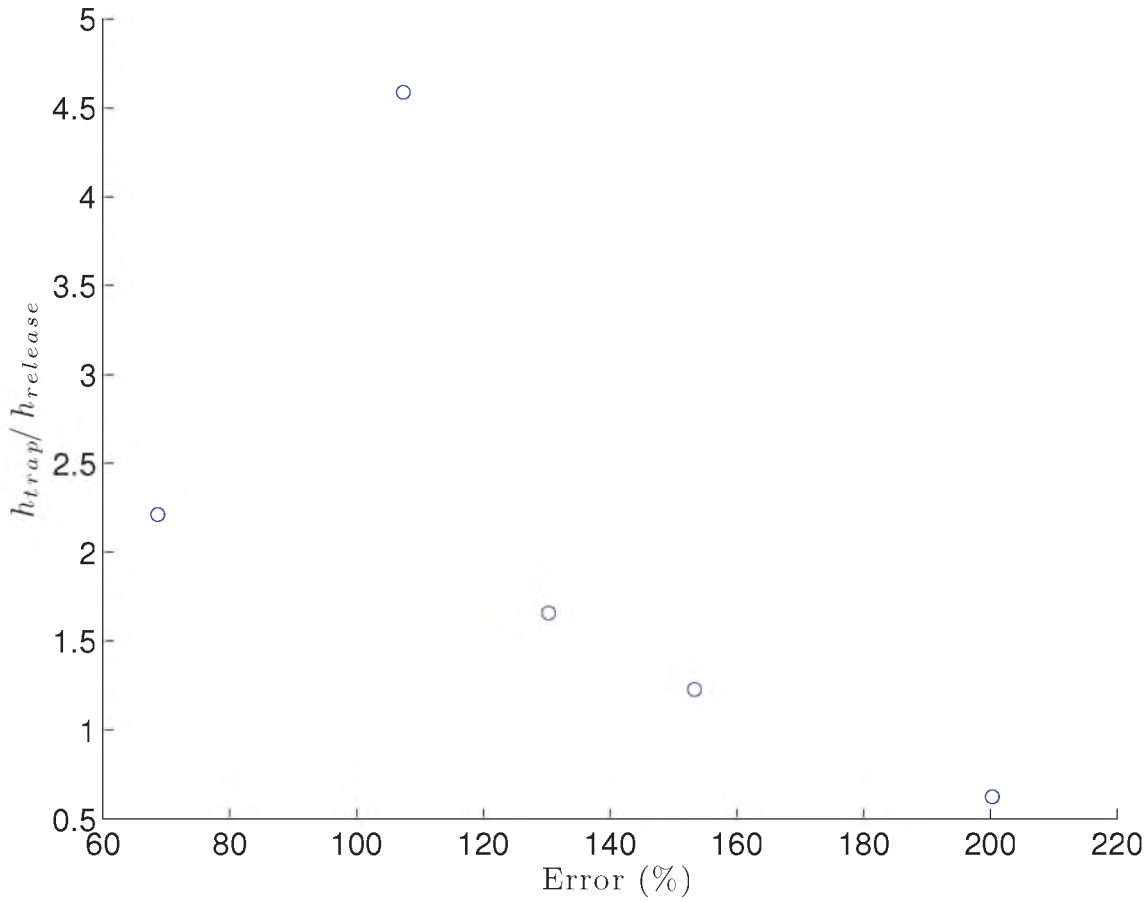

Figure G.1. Depicts the amount of error between the measured data and the Gaussian Plume for the entire trap level at each trap height for release 2.

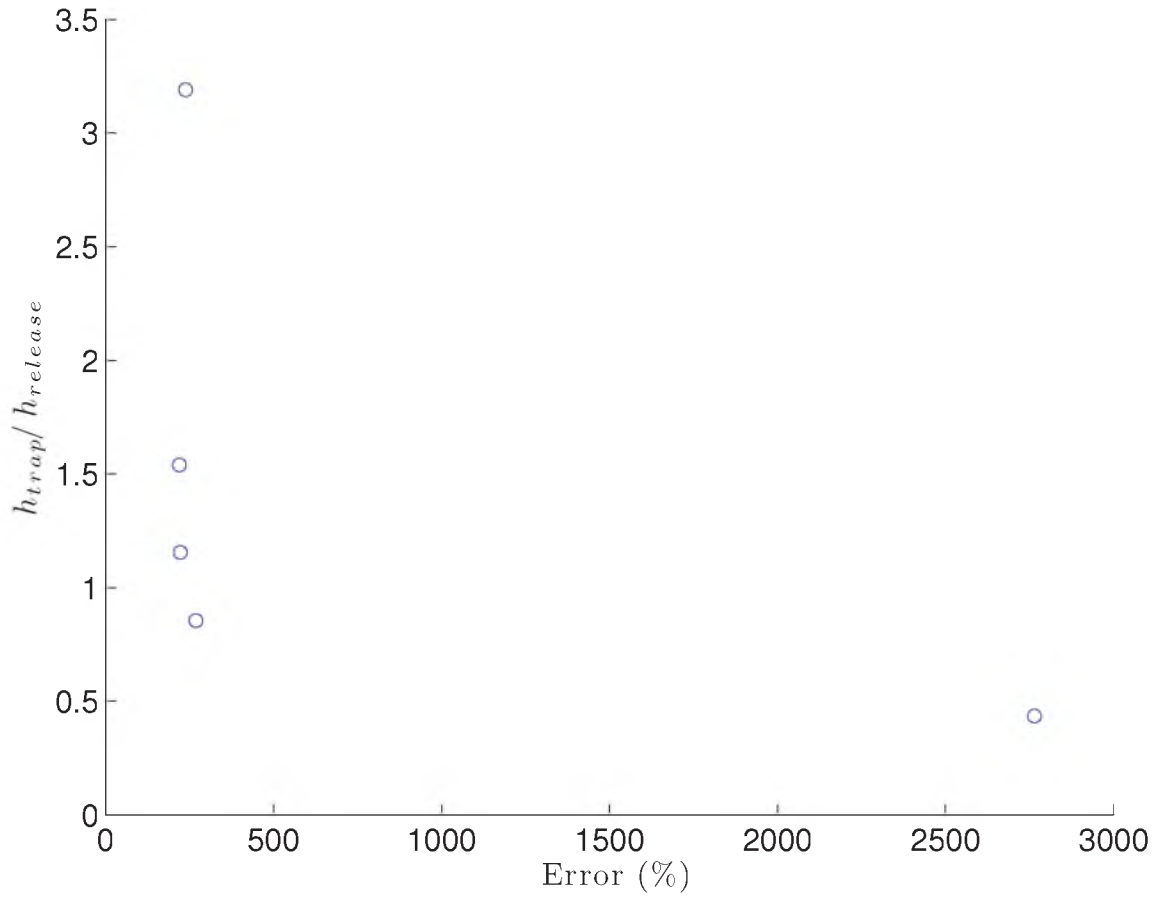

Figure G.2. Depicts the amount of error between the measured data and the Gaussian Plume for the entire trap level at each trap height for release 3.

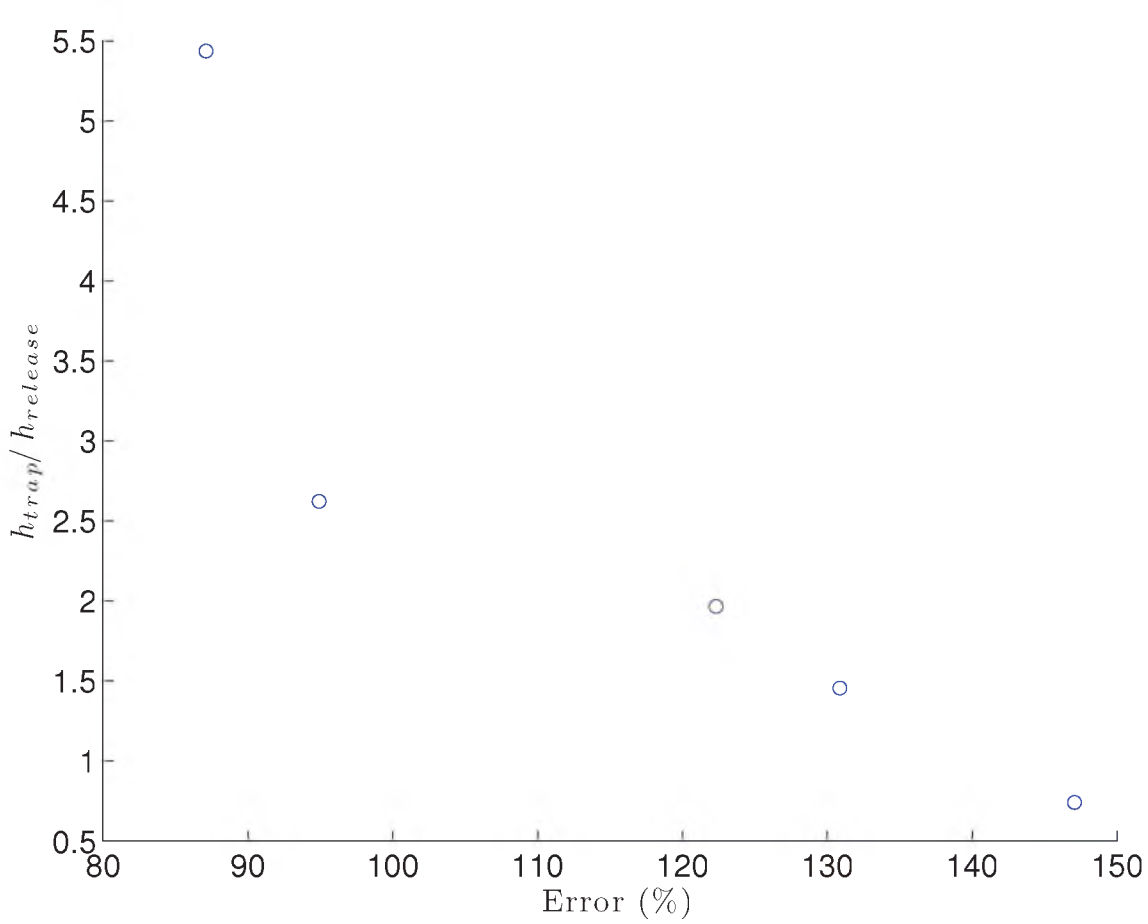

Figure G.3. Depicts the amount of error between the measured data and the Gaussian Plume for the entire trap level at each trap height for release 4.

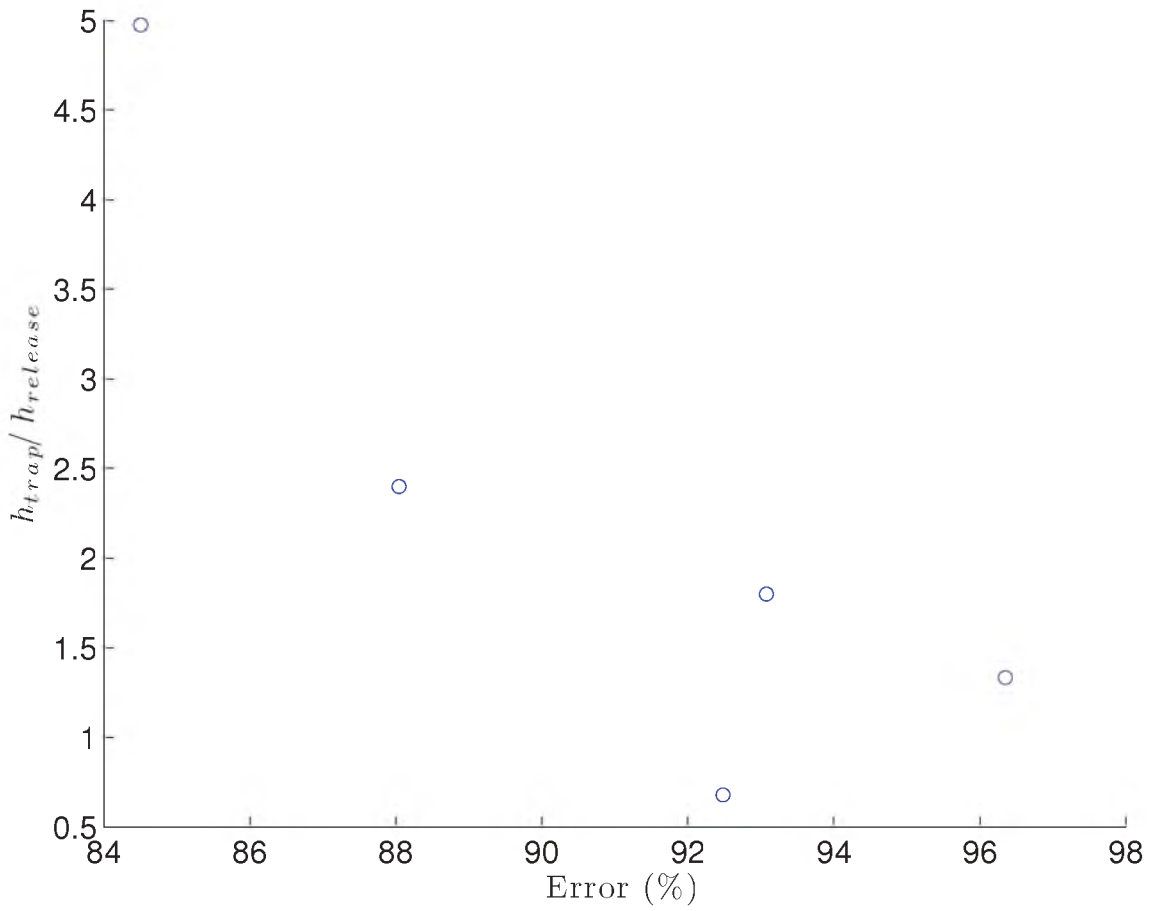

Figure G.4. Depicts the amount of error between the measured data and the Gaussian Plume for the entire trap level at each trap height for release 5.

REFERENCES

[1] Abbott, M. L., and et al. Atmospheric mercury near salmon falls creek reservoir in southern idaho. *Applied Geochemistry 23* (2008), 438–453.

[2] Andrade, D., Pan, Z., and Dannevik, W. Modeling soybean rust spore escape from infected canopies: Model description and preliminary results. *Journal of Applied Meteorology and Climatology 49* (2009), 789–803.

[3] Aylor, D. Dispersal in time and space: aerial pathogens. *Plant Disease: an Advanced Treatise 2* (1978), 159–180.

[4] Aylor, D. E. Deposition of particles in a plant canopy. *Journal of Applied Meteorology 14* (1974), 52–57.

[5] Aylor, D. E. Aerial spore dispersal close to a focus of disease. *Agricultural and Forest Meteorology 47* (1989), 109–122.

[6] Aylor, D. E. The role of intermittent wind in the dispersal of fungal pathogens. *Annu. Rev. Phytopathol. 28* (1990), 73–92.

[7] Aylor, D. E. Vertical variation of aerial concentration of venturia inaequalis ascospores in an apple orchard. *The American Phytopathological Society 85* (1995), 175–181.

[8] Aylor, D. E. Biophysical scaling and the passive dispersal of fungus spores: relationship to integrated pest management strategies. *Agricultural and Forest Meteorology 97* (1999), 275–292.

[9] Aylor, D. E. Settling speed of corn (zeo mays) pollen. *Journal of Aerosol Science 33* (2002), 1601–1607.

[10] Aylor, D. E. Spread of plant disease on a continental scale: Role of aerial dispersal of pathogens. *Ecology 84* (2003), 1989–1997.

[11] Aylor, D. E., and Ferrandino, F. J. Dispersion of spores released from an elevated line source within a wheat canopy. *Boundary-Layer Meteorology 46* (1989), 251–273.

[12] Aylor, D. E., and Flesch, T. K. Estimating spore release rates using a lagrangian stochastic simulation model. *Journal of Applied Meteorology and Climatology 40* (2001), 1196–1208.

[13] Aylor, D. E., and Lukens, R. J. Liberation of helminthosporium maydis spores by wind in the field. *Phytopathology 64* (1974), 146–151.

[14] Aylor, D. E., and Qiu, J. Micrometeorological determination of release rate of venturia inaequalis ascospores from a ground-level source during rain. *Agricultural and Forest Meteorology 81* (1996), 157–178.

[15] Aylor, D. E., Wang, Y., and Miller, D. R. Intermittent wind close to the ground within a grass canopy. *Boundary-Layer Meteorology 66* (1993), 427–448.

[16] Bailey, B. N., and Stoll, R. Turbulence in sparse, organized vegetative canopies: A large-eddy simulation study. *Boundary-Layer Meteorology* (2012).

[17] Bohrer, G., and et al. Effects of canopy heterogeneity, seed abscission and inertia on wind-driven dispersal kernels of tree seeds. *Journal of Ecology 96* (2008), 569–580.

[18] Bouvet, T., Wilson, J. D., and Tuzet, A. Observations and modeling of heavy particle deposition in a windbreak flow. *American Meteorological Society 45* (2006), 1332–1349.

[19] Caughey, S. J., and Palmer, S. G. Some aspects of turbulence structure through the depth of the convective boundary layer. *Quarterly Journal of the Royal Meteorological Society 105* (1979), 811–827.

[20] Cava, D., and Katul, G. G. Spectral short-circuiting and wake production within the canopy trunk space of an alpine hardwood forest. *Boundary-Layer Meteorology 126* (2008), 415–431.

[21] Chamecki, M., and et al. Concentration profiles of particles settling in the neutral and stratified atmospheric boundary layer. *Boundary-Layer Meteorology 125* (2007), 25–38.

[22] Chamecki, M., Meneveau, C., and Parlagne, M. B. Large eddy simulation of pollen transport in the atmospheric boundary layer. *Aerosol Science 40* (2009), 241–255.

[23] Doran, J. C., and Horst, T. W. An evaluation of guassian plume-depletion models with dual-tracer field measurements. *Atmospheric Environment 19* (1985), 939–951.

[24] Dupont, S., and Brunet, Y. Influence of foliar density profile on canopy flow: A large-eddy simulation study. *Agricultural and Forest Meteorology 148* (2008), 976–990.

[25] Endalew, M., Hertog, M., Verboven, P., Baetens, K., Delele. M. A., Ramon, H., and Nicolai, B. M. Modelling airflow through 3d canopy structure of orchards. *Aspects of Applied Biology 77* (2006), 465–472.

[26] Finnigan, J. Turbulence in plant canopies. *Annual Review of Fluid Mechanics 32* (2000), 519–571.

[27] Finnigan, J. J., Shaw, R. H., and Patton, E. G. Turbulence structure above a vegetation canopy. *Journal of Fluid Mechanics 637* (2009), 387–424.

[28] Harman, I. N., and Finnigan, J. J. A simple unified theory for flow in the canopy and roughness sublayer. *Boundary-Layer Meteorology 123* (2007), 339–363.

[29] Holtslag, A. A. M., and Nieuwstadt, F. T. M. Scaling the atmospheric boundary layer. *Boundary-Layer Meteorology 36* (1986), 201–209.

[30] Jarosz, N., Loubet, B., Durand, B., McCartney, A., Foueillassar, X., and Huber, L. Field measurements of airborne concentration and deposition rate of maize pollen. *Agricultural and Forest Meteorology 119* (2003), 37–51.

[31] Katul, G. G., and et al. Mechanisitc analytical models for long-distance seed dispersal by wind. *The American Naturalist 166* (2005), 368–381.

[32] Klein, E. K., Lavigne, C., Foueillassar, X., Gouyon, P.-H., and Laredo, C. Corn pollen dispersal: Quasi-mechanistic models and field experiments. *Ecological Monographs 73* (2003), 131–150.

[33] Legg, B. J. Turbulent dispersion from an elevated line source: Markov chain simulations of concentration and flux profiles. *Quarterly Journal of the Royal Meteorological Society 109* (1983), 645–660.

[34] Legg, B. J., and Powell, F. A. Spore dispersal in a barley crop: A mathematical model. *Agricultural Meteorology 20* (1979), 47–67.

[35] Lin, J.-S., and Hildemann, L. M. A generalized mathematical scheme to analytically solve the atmospheric diffusion equation with dry deposition. *Atmospheric Environment 31* (1997), 59–71.

[36] Marcolla, B., Pitacco, A., and Cescatti, A. Canopy architecture and turbulence structure in a coniferous forest. *Boundary-Layer Meteorology 108* (2003), 39–59.

[37] McCartney, H. A. Dispersal of spores and pollen from crops. *Grana 33* (1994), 76–80.

[38] McCartney, H. A., Fitt, B. D. L., and West, J. S. *Dispersal of Foliar Plant Pathogens.* Springer, 2006.

[39] Nelson, M. A., Pardyjak, E. R., Brown, M. J., and Klewicki, J. C. Properties of the wind field within the oklahoma city park avenue street canyon. part ii: Spectra, cospectra, and quadrant analyses. *American Meteorological Society 46* (2007), 2055–2073.

[40] Nelson, M. A., Pardyjak, E. R., Klewicki, J. C., Pol, S. U., and Brown, M. J. Properties of the wind field within the oklahoma city park avenue street canyon. part i: Mean flow and turbulence statistics. *American Meteorological Society 46* (2007), 2038–2054.

[41] Overcamp, T. J. A general gaussian diffusion-deposition model for elevated point sources. *Journal of Applied Meteorology 15* (1976), 1167–1171.

[42] Pahlow, M., Parlange, M. B., and Porte-Agel, F. On monin-obukhov similarity in the stable atmospheric boundary layer. *Boundary-Layer Meteorology 99* (2001), 225–248.

[43] Poggi, D., Katul, G., and Albertson, J. Scalar dispersion within a model canopy: Measurements and three-dimensional lagrangian models. *Advances in Water Resources 29* (2006), 326–335.

[44] Poggi, D., Porporato, A., Ridolfi, L., Albertson, J. D., and Katul, G. G. The effect of vegetation density on canopy sub-layer turbulence. *Boundary-Layer Meteorology 111* (2004), 565–587.

[45] Ramamurthy, P., Pardyjak, E. R., and Klewicki, J. C. Observations of the effects of atmospheric stability on turbulence statistics deep within an urban street canyon. *Journal of Applied Meteorology and Climatology 46* (2007), 2074–2085.

[46] Raupach, M. R., Coppin, P. A., and Legg, B. J. Experiments on scalar dispersion within a model plant canopy part i: The turbulence structure. *Boundary-Layer Meteorology 35* (1986), 21–52.

[47] Raupach, M. R., Finnigan, J. J., and Brunet, Y. Coherent eddies and turbulence in vegetation canopies: The mixing-layer analogy. *Boundary-Layer Meteorology 78* (1996), 351–382.

[48] Raynor, G., Hayes, J., and Ogden, E. Experimental data on ragweed pollen dispersion and deposition from point and area sources. 1–33.

[49] Seinfeld, J. H., and Pandis, S. N. *Atmospheric Chemistry and Physics: From Air Pollution to Climate Change.* John Wiley and Sons, Inc., Somerset, NJ, 2006.

[50] Sorbjan, Z. On similarity in the atmospheric boundary layer. *Boundary-Layer Meteorology 34* (1986), 377–397.

[51] Steven P. Oncley, C. A. F., and John C. Larue, Joost A. Businger, E. C. I. S. S. C. Surface-layer fluxes, profiles, and turbulence measurements over uniform terrain under near-neutral conditions. *American Meteorological Society 53* (1996), 1029–1044.

[52] Stull, R. B. *An introduction to boundary layer meteorology.* Kluwer Academic Publishers, The Netherlands, 1988.

[53] Su, H.-B., Schmid, H., Vogel, C., and Curtis, P. Effects of canopy morphology and thermal stability on mean flow and turbulence statistics observed inside a mixed hardwood forest. *Agricultural and Forest Meteorology 148* (2008), 862–882.

[54] Tarara, J., Ferguson, J., Hoheisel, G.-A., and Pena, J. P. Asymmetrical canopy architecture due to prevailing wind direction and row orientation creates an imbalance in irradiance at the fruiting zone of grapevines. *Agricultural and Forest Meteorology 135* (2005), 144–155.

[55] Thomas, C., and Foken, T. Flux contribution of coherent structures and its implications for the exchange of energy and matter in a tall spruce canopy. *Boundary-Layer Meteorology 123* (2007), 317–337.

[56] Walker, E. R. A particulate diffusion experiment. *Journal of Applied Meteorology 49* (1965), 614–621.

[57] Weiss, A., and Jr., L. H. A. Air-flow patterns in vineyard rows. *Agricultural Meteorology 16* (1976), 329–342.

[58] Wilson, J. D. Trajectory models for heavy particles in atmospheric turbulence: Comparison with observations. *Journal of Applied Meteorology 39* (2000), 1894–1912.

[59] Wyngaard, J. C., Cote, O. R., and Izumi, Y. Local free convection, similarity, and the budgets of shear stress and heat flux. *Journal of the Atmospheric Sciences 28* (1971), 1171–1182.

[60] Yi, C. Momentum transfer within canopies. *Journal of Applied Meteorology and Climatology 47* (2008), 262–275.

[61] Yue, W., Parlange, M. B., Meneveau, C., Zhu, W., van Hout, R., and Katz, J. Large-eddy simulation of plant canopy flows using plant-scale representation. *Boundary-Layer Meteorology 124* (2007), 183–203.